

**DEVELOPMENT OF AN EXPERIMENT FOR INVESTIGATING  
THE MAGNETOHYDRODYNAMIC RICHTMYER–MESHKOV INSTABILITY**

---

A Dissertation  
presented to  
the Faculty of the Graduate School  
at the University of Missouri

---

In Partial Fulfillment  
of the Requirements for the Degree  
**Doctor of Philosophy**

---

by  
ROY C. ALLEN IV

---

Dr. Jacob A. McFarland, Dissertation Supervisor

JULY 2019

**© COPYRIGHT BY ROY C. ALLEN IV 2019**

**ALL RIGHTS RESERVED**

The undersigned, appointed by the dean of the Graduate School, have examined the dissertation entitled

**DEVELOPMENT OF AN EXPERIMENT FOR INVESTIGATING THE  
MAGNETOHYDRODYNAMIC RICHTMYER–MESHKOV INSTABILITY**

presented by Roy C. Allen IV, a candidate for the degree of Doctor of Philosophy, and hereby certify that, in their opinion, it is worthy of acceptance.

Approved by:

Chair of Committee,

Dr. Jacob A. McFarland \_\_\_\_\_  
College of Engineering - Department of Mechanical & Aerospace Engineering  
*University of Missouri – Columbia*

Committee Members,

Dr. Gary L. Solbrekken \_\_\_\_\_  
College of Engineering - Department of Mechanical & Aerospace Engineering  
*University of Missouri – Columbia*

Dr. Robert A. Winholtz \_\_\_\_\_  
College of Engineering - Department of Mechanical & Aerospace Engineering  
*University of Missouri – Columbia*

Dr. Randy D. Curry \_\_\_\_\_  
College of Engineering - Department of Electrical Engineering & Computer Science  
*University of Missouri – Columbia*

Dr. Karl D. Hammond \_\_\_\_\_  
College of Engineering - Department of Chemical Engineering  
*University of Missouri - Columbia*

Date Approved: [MAY 8, 2019]

## DEDICATION

*To my late Uncle Cecil W. Dinan who was a surviving combat veteran of the D-Day Landing at Omaha Beach, World War II, and one of the finest people I have ever had the pleasure of knowing.*

*To my second cousin Lynn Exposito who is a surviving “Tunnel Rat” combat veteran of the Vietnam War. I think about your phenomenal courage and heroism daily.*

*To my friend and thesis advisor, the late Steve R. Nagel, former NASA astronaut and Space Shuttle Commander. – “It really is rocket science”*

*To my Uncle Richard L. Wollschlager, for showing me how to design and build anything I set my mind to. I never would have thought race cars, houses, and sailboats would turn into a supersonic shock tube, a 25,000° F plasma torch, and a magnetic field capable of suppressing magnetohydrodynamic instability.*

*Most important, to my wife, Colleen, and my parents, Roy and Gail. Your relentless love and support in every sense has allowed me to achieve all of this, even if you still don't understand what I am talking about.*

## ACKNOWLEDGMENTS

A decade-long academic endeavor is not sustained or successfully completed without significant help and support along the way. I would like to acknowledge and thank as many people as possible for their generosity and support while I completed mine. I honestly feel blessed to have been provided the opportunity to pursue this dissertation and Ph.D. degree and could not have done so without them.

First, I thank my advisor, Dr. Jacob A. McFarland, for giving me a chance as a Ph.D. research assistant and believing that I really could build anything; for shaping me into the experimentalist I have become, for having faith and trusting me when things were still not fully understood even the day before crucial deadlines, and for challenging me to the fullest extent to be the best scientist I could be. It is through his guidance and mentoring that I have embarked on the most significant project I have ever had the opportunity and pleasure to work on.

I thank Dr. Paul M. Rutherford for encouraging and preparing me as a high school student at Summit Technology Academy to embark on this collegiate engineering journey. I also thank Dr. Kyle Anderson for his tremendous teaching efforts and for putting up with me in as an International Baccalaureate student in high school.

My lab mates have played such a vital role in my success at the Missouri Fluid Mixing and Shock Tube Lab (FMSTL) and I could not have done this without them. John Middlebrooks has been such a crucial member of the FMSTL and the extra set of hands necessary to complete the experiments presented in this dissertation. In particular I thank

Wolfgang Black, my good friend and partner in crime. Wolfgang has always helped me work through not only the problems and perils of this dissertation but through coursework and the emotional stress induced by high-level research. I am truly grateful we got to spend all ten years at Mizzou together.

I thank Dr. Randy D. Curry and the research personnel at the Center for Physical and Pulse Power Electronics, who have provided me with what amounts to a blank check through the loaning of their research equipment, lab space, time, ideas, and effort to complete the various tasks required to finish this project. Generating atmospheric plasma on an extremely limited budget, for example, would otherwise have been nearly impossible without their generous contributions.

One of the most critical and difficult parts of this project could not have been able to be completed without the help of Dr. Karl Hammond. He has taught me a great deal about statistical thermodynamics and helped me understand the necessary components of the theory developed for the 2D Monochromatic Imaging Method used to characterize the plasma torch for my dissertation. He is one of the smartest and most dedicated professors I know; someone that truly cares about the success of students both inside and outside his lab. I can't express enough how much I appreciate all the time and assistance Dr. Hammond has provided to me.

I also thank Dr. Gary L. Solbrekken, Dr. Robert A. Winholtz, Dr. Craig A. Kluever, and all my professors for teaching me and preparing me, both inside and outside the classroom. Your efforts will culminate in success and are appreciated by me with the utmost gratitude.

At Mizzou, many staff members helped me with obtaining and manufacturing the materials and parts needed to complete the experiments performed and presented in this dissertation. Marilyn Nevels is such an excellent administrative assistant and the MU College of Engineering wouldn't run so successfully without her working tirelessly to do anything and everything to help students such as myself. Ghassan Al Bahhash and Matthew Marciniak have helped me machine, construct, and fix nearly every component of the plasma torch. Their efforts are unmatched when it comes to helping not only me but any and all other students in any way they can. They're always a positive influence and they make machining and fixing anything a blast.

I sincerely thank my family for the love and support they have provided to me all my life and for helping me become the person I am today. My Aunt Barb, who has always been like a second mother to me, for providing me with my first engineering job after earning my Bachelor's Degree, which allowed me to do some pretty amazing things. The opportunity she provided ultimately inspired me to go back to school and learn how to do more. Uncle Richard, who was my first boss when I started working at age 12, for teaching me how to build virtually anything, how to do it right, and to "be in control of my environment." My sister Katie, who is the most gifted and dedicated elementary school teacher I know and one of the best people I know. I can definitively say that I can perform at the highest levels of research because she is such a phenomenal little sister who inspired me greatly as we were growing up. I owe more to her than she knows. Additionally, I thank my grandparents, Buck & Wilma Allen and Keith & Ginger Goeglein, for all their support of my academic goals and for naming me their favorite (#1) grandchild!

Of course, the people I owe everything in this world to are my parents. I can't think of a time when they were unable or unavailable to help me in whatever way was necessary throughout my life. They have provided the financial backing for everything from my undergraduate degree to completing six more years of school without having to stress about whether I could afford a meal or gas to get back to the lab. I have inherited everything from their analytical and managerial skills to their humor and humility. No matter what I am interested in or what the cost, they never waiver or hesitate to support me in any and every way they can. I only hope that now that I am completing this chapter of my life, I can begin to repay them.

Finally, I thank my best friend, my biggest fan, and the most important person to me in life, my wonderful wife Colleen. What a phenomenal rollercoaster ride it has been. All the late nights and early mornings of wondering where I was and then remembering you are married to a Ph.D. candidate studying magnetohydrodynamic instabilities were very tough, to say the least. I appreciate so much how Colleen chose to forgo date nights and weekend trips and so much more so that I could continue to work, and she still had a hot meal ready for me when I finally did come home. She has kept me grounded, dedicated, and focused on being the best researcher I can be, on being the greatest husband I can be, and on being the person I was born to become.

# TABLE OF CONTENTS

<b>ACKNOWLEDGMENTS</b> .....	<b>ii</b>
<b>LIST OF TABLES</b> .....	<b>x</b>
<b>LIST OF FIGURES</b> .....	<b>xi</b>
<b>LIST OF SYMBOLS AND ACRONYMS</b> .....	<b>xxiii</b>
<b>ABSTRACT</b> .....	<b>xxiii</b>
<b>CHAPTER 1. INTRODUCTION</b> .....	<b>1</b>
1.1 Theory of Hydrodynamic Instabilities .....	3
1.1.1 Hydrodynamic Instabilities in the Traditional Sense .....	4
1.1.2 The Richtmyer–Meshkov Instability (RMI) .....	7
1.1.3 Magnetohydrodynamic Instabilities .....	10
1.1.4 The Magnetohydrodynamic Richtmyer–Meshkov Instability .....	12
1.2 Applications of the Magnetohydrodynamic Richtmyer–Meshkov Instability....	16
1.3 Section Outline .....	22
<b>CHAPTER 2. COMPUTATIONAL WORK</b> .....	<b>24</b>
2.1 MHD–RMI Simulation Motivation .....	24
2.2 The MHD–RMI Simulation Background .....	25
2.3 FLAG Software Description .....	28
2.4 Simulation Parameters and Initial Conditions used in FLAG .....	29
2.4.1 Explanation of FLAG Simulation Studies Applicable to MHD–RMI Experiments .....	32
2.4.2 FLAG Simulation Test Cases and Varied Parameter Explained .....	34
2.5 Simulation Results of the MHD–RMI in FLAG .....	36
2.5.1 Magnetic Field Orientation Simulation Results .....	37
2.5.2 Magnetic Field Strength Simulation Results .....	40

2.5.3	Mach Number Simulation Results .....	45
2.6	Conclusions of the Simulation Results of the MHD–RMI in FLAG .....	51
<b>CHAPTER 3.</b>	<b>EXPERIMENTAL APPARATUS AND METHODS DEVELOPED .....</b>	<b>54</b>
3.1	Background on Plasma Generation .....	55
3.1.1	Generating Atmospheric-Pressure Plasma .....	57
3.1.2	Torch Operational Conditions .....	60
3.2	Plasma Generation Method .....	62
3.2.1	Apparatus Design .....	62
3.2.2	Mechanical Design Considerations of the APPT.....	66
3.3	Diagnostic Methods .....	70
3.3.1	Background on Plasma Diagnostic Methods .....	70
3.3.2	The 2D Monochromatic Imagery Method .....	71
3.3.3	Validity of the 2D Monochromatic Imagery Method .....	74
3.3.4	Experimental Requirement of the 2D Monochromatic Imagery Method .....	82
3.3.5	Solid Particle PIV Apparatus Design .....	91
3.3.6	PIV Data Processing in Insight 4G and PIVlab .....	95
3.3.7	PIV Data Processing Background .....	96
3.3.8	Processing PIV Data in Insight 4G .....	101
3.3.9	Processing PIV Data in PIVlab .....	104
3.4	Magnetic Field Interactions with a Plasma Flow Field .....	106
3.4.1	Theory on Magnetic Field Interactions with a Plasma Flow Field .....	107
3.4.2	Theory on Magnetic Field Modeling .....	114
3.4.3	Test Cases Used to Visualize and Verify Plasma – Magnetic Field Interaction .....	118
<b>CHAPTER 4.</b>	<b>EXPERIMENTAL RESULTS .....</b>	<b>121</b>
4.1	Operating Conditions of a Nitrogen APPT .....	122
4.2	2DMIM Plasma Temperature and Degree of Ionization .....	128
4.3	Plasma-Particle Field Interface Imaging via PIV apparatus .....	135

4.3.1	Imaging the $r\theta$ -Plane for Future MHD–RMI Experiments.....	135
4.3.2	PIV Data Processing of the $rz$ -plane in Insight 4G.....	138
4.3.3	PIV Data Processing of the $rz$ -plane in PIVlab.....	144
4.4	Magnetic Field – Plasma Flow Field Deflection and Suppression .....	148
4.4.1	Model of the Externally Applied Magnetic Field .....	150
4.4.2	Magnetic Field Interactions with a Plasma Flow Field .....	156
<b>CHAPTER 5.</b>	<b>SUMMARY AND CONCLUSIONS .....</b>	<b>164</b>
5.1	Motivation Summarized.....	164
5.2	Important Computation Environmental Parameters .....	166
5.3	New Methods for Determining Plasma Characteristics and Parameters .....	167
5.4	Future Work.....	170
<b>FUNDING ACKNOWLEDGMENTS .....</b>		<b>172</b>
<b>BIBLIOGRAPHY .....</b>		<b>173</b>
<b>APPENDIX A. DEVELOPMENT, INSTRUMENTATION, AND CONTROL OF THE PLASMA TORCH .....</b>		<b>180</b>
A.1	Preliminary Plasma Torch Development .....	180
A.2	HVAC Starter Circuit .....	181
A.3	HCDC Power Supply .....	184
A.4	APPT Power Resistor Bank Construction .....	187
A.5	LABJACK and LABVIEW DAQ Wiring .....	188
A.6	PIV Supplementary Data .....	189
<b>APPENDIX B. PLASMA TORCH COMPONENTS REPAIR .....</b>		<b>199</b>
B.1	Machining the Anode and Cathode Sections .....	199
B.2	Replacement of Tungsten Cathode Rod .....	200
B.3	Transferred Arc Plasma Torch for Calibration Purposes .....	201

B.4	Initial Plasma Torch Operational Results .....	202
<b>APPENDIX C. CONSTRUCTION OF SUPPLEMENTARY MHD-RMI EXPERIMENTAL COMPONENTS.....</b>		<b>203</b>
C.1	PIV Solid Particle Seeder and Mock Section Apparatus .....	203
C.2	Emission of the APPT .....	205
C.3	Magnetic Field Apparatus .....	208
C.4	The Missouri Fluid Mixing and Shock Tube Laboratory .....	209
<b>VITA</b>	.....	<b>211</b>

## LIST OF TABLES

<b>Table</b>		<b>Page</b>
2-1	FLAG simulation initial conditions. ....	30
4-1	Parameters varied to produce a long, laminar, stable APPT.....	122
A-1	Keysight N8932A power supply characteristics.....	185

## LIST OF FIGURES

Figure		Page
1.1	The Kelvin Helmholtz instability rendered visible by clouds <i>ex Ref.</i> [8].....	4
1.2	Simulation (left) and experiment (right) observation of single-mode KHI in a supersonic flow from the work of Wan <i>et al.</i> [9]. .....	5
1.3	Large Eddy Simulation of Rayleigh–Taylor instability morphology performed in MIRANDA [10]. .....	6
1.4	Visual represnetation of the three stages of the RMI development. Image from Black <i>et al.</i> [12]. .....	9
1.5	Geometry of an Alfvén wave propagating along $\vec{B}$ (left), and a magnetosonic wave propagating at right angles to $\vec{B}$ (right). Image from Chen [15]. . .....	15
1.6	Visual representation of the stages of the MHD–RMI development. Image from Black <i>et al.</i> [12]. .....	15
1.7	NIF indirect-drive hohlraum and capsule schematic from Ref. [28]. Reproduced with permission from IOP Publishing. All rights reserved. ....	19
1.8	MagLIF experiment in Z machine at Sandia National Laboratories. Image courtesy of Randy Montoya, Sandia. All rights reserved. ....	20
1.9	The ITER Tokamak net energy magnetic fusion device core. Image courtesy of ITER from Ref. [30]. All rights reserved. ....	21
2.1	Two-dimensional schematic of species pseudocolor representing the intial conditions utilized in FLAG simulations at $t = 0$ . .....	31
2.2	Concept of MHD–RMI shock tube experiment with A) the $\vec{B}$ generated perpendicular to the shock’s transit direction, B) the $\vec{B}$ generated parallel to the shock wave’s direction. Interchangable diaphragms for Mach number variation are also displayed. ....	33

2.3	$\vec{B}$ orientation study simulation results showing species concentration. ....	38
2.4	Magnetic field strength simulations showing species concentration, $Y_p$ , with respect to $\tau$ . .....	42
2.5	Late time ( $\tau \approx 15$ ) species concentration and vorticity plots for incident shock wave strength variation study from FLAG. ....	48
3.1	Paschen curves generated for various gases. ....	58
3.2	V–I characteristics for pre- (left of peak) and post-arc (right of peak) conditions of an atmospheric pressure plasma. ....	59
3.3	Custom high-voltage alternating current (HVAC) starter circuit. ....	63
3.4	Circuitual schematic representing the electrical components of the custom HVAC starter circuit used to generate a spark in APPT. ....	63
3.5	Image of: (A) APPT cut-out diagram, (B) top view of tangential gas component, and (C) isometric cut-out representation of axial (blue) and tangential (red) gas flow paths. ....	68
3.6	Diagram for converting radial intensity to radial emissivity for axisymmetric cylindrical plasma source via Abel Inversion. ....	83
3.7	Visualization of variables in Equation (3.23) used for Abel transformation. ....	85
3.8	N-I and N-II nitrogen line emissions wavelength vs. intensity profile. ....	88
3.9	The APPT’s emission spectrum in the filter range as acquired by the Ocean Optics USB4000 VIS-NIR spectrometer. ....	89
3.10	Transmittance vs. wavelength of Andover $532 \pm 10$ nm bandpass filter and Thor Labs $532 \pm 1$ nm laser line filter. ....	90
3.11	Conceptual representation of negative image solid particle Particle Image Velocimetry Mock Tube apparatus with $rz$ -plane illuminated by the laser..	94
3.12	Constructed Mock Tube apparatus for PIV application. ....	94
3.13	Particle Image Velocimetry capture timing setup diagram. ....	99

3.14	Schematic representing particle flux direction and notation for plasma – magnetic field interaction. ....	113
3.15	Tangential magnetic field apparatus concept to show single-axis deflection of the plasma flow field.. ....	118
3.16	Tilted magnetic field apparatus concept showing multiaxis deflection of plasma flow field. ....	120
4.1	Calibration image (left) and APPT image (right) showing ionized region jet length (Region 1) at 20 cm and total jet length (Region 2) at 80 cm in length. ....	123
4.2	V–I characteristics of APPT with nitrogen gas flow rates of 1 SLM tangential and 5,7, and 10 SLM axial. ....	125
4.3	Ionized region jet length and total jet length vs. varying axial gas flow rate at constant tangential gas flow rate of 1 SLM and constant power of 15 kW. ....	126
4.4	Ionized region jet length and total jet length vs. percent of tangential gas flow rate for total gas flow rates of 3 and 5 SLM. ....	127
4.5	Theoretical normalized total line emission coefficient vs. temperature for 528.12 nm N-I emission line. ....	128
4.6	Mole fractions of molecular nitrogen ( $N_2$ ), atomic nitrogen (N), singly ionized nitrogen ( $N^+$ ), doubly ionized nitrogen ( $N^{++}$ ), and electrons ( $e^-$ ) vs. temperature. ....	129
4.7	Images of: A) APPT transferred arc apparatus close-up, and B) transferred arc RAW data CCD image taken for calibration of the optical system. ....	130
4.8	RAW data CCD image taken (left), plasma temperature plot in <i>rz</i> -plane (middle), and degree of ionization plot (right) for 2DMIM applied to APPT at 2.1 SLM axial, 0.9 SLM tangential gas flow rates, and an arc current of 200 A. ....	133
4.9	Radial temperature distribution profile at nozzle exit for APPT as shown in Figure 4.8. ....	134

4.10	CCD images of $rz$ -plane taken as shown in: a) without any bandpass filter present, b) with the $523 \pm 10$ nm bandpass filter present, c) with the $523 \pm 1$ nm laser line filter present, and d) in $r\theta$ -plane taken with $523 \pm 1$ nm laser line filter present. ....	136
4.11	The desired hydrodynamics and morphology PIV goal of MHD–RMI experiment in the $r\theta$ -plane. ....	138
4.12	The desired hydrodynamics and morphology PIV goal of MHD–RMI experiment in the $r\theta$ -plane as applied to an SDMI interface produced in the FMSTL. ....	139
4.13	ns-PIV Case 1: 1.6 SLM axial gas flow rate PIV image pair. ....	140
4.14	ns-PIV Case 2: 3.2 SLM axial gas flow rate PIV image pair. ....	141
4.15	ns-PIV Case 3: 4.8 SLM axial gas flow rate PIV image pair. ....	141
4.16	ns-PIV Case 2: 3.2 SLM axial flow rate PIV velocity vector field with particle speed colormap. ....	143
4.17	RAW image 2 of 2 (left), filtered image (center), ROI [as green line] masked area [in red] (right) for Case 2 as processed in custom MATLAB script and then in PIVlab’s GUI. ....	145
4.18	PIV data before post-processing (left), and after post-processing (right) for Case 2. ....	145
4.19	ns-PIV Case 2: PIV data velocity vector field as computed using $16 \times 16$ final interrogation size [red area indicates masked section]. ....	146
4.20	ns-PIV Case 2: 3.2 SLM axial flow rate PIVlab velocity vector field. ....	147
4.21	2D representation of the magnetic flux density (left), magnetic force vectors (middle) and resulting magnetic field lines (right) produced by permanent magnet apparatus as generated in custom MATLAB script. ....	151
4.22	Depection of the 3D magnetic flux density produced by the cylindrical permanent magnet apparatus with the outline of the plasma flow field cross-section shown in purple as generated in MATLAB. ....	152

4.23	3D magnetic field lines produced by permanent magnet apparatus as generated in custom MATLAB script. ....	154
4.24	Magnetic flux density broken into the $r$ -component (left), $z$ -component (middle), and total $\vec{B}$ field strength (right) produced by magnetic field apparatus as generated in MATLAB. ....	155
4.25	DSLR images of plasma deflection and suppression from test case one. ...	156
4.26	Deflection angle and plasma flow field height obtained from DSLR image's data presented in Figure 4.25. ....	157
4.27	CCD images with $523 \pm 10$ nm bandpass filter of tilted magnetic field interaction with plasma flow for: (a) $\vec{B} \sim 0$ T, (b) calibration image with magnet $N$ -pole edge in red, $S$ -pole in green, magnets center axis blue dashed line, (c) $\vec{B} \angle -30^\circ$ CW at 30 mm, (d) $\vec{B} \angle -30^\circ$ CW at 60 mm, and (e) $\vec{B} \angle 30^\circ$ CW at 30 mm. ....	161
4.28	DSLR side view image with $523 \pm 10$ nm bandpass filter of tilted $\angle 15^\circ$ magnetic field interaction with plasma flow. ....	163
A.1	Image of: (A) plasma generating apparatus proof of concept, and (B) preliminary APPT apparatus during operation. ....	180
A.2	Image of: (A) spark plug producing spark, and (B) spark plug plasma generating torch apparatus during operation. ....	181
A.3	Preliminary development of custom HVAC starter circuit. ....	182
A.4	National Instruments Multisim 12 HVAC–HCDC circuit simulation. ....	182
A.5	Image of: (A) aerial rear view of constructed HVAC starter circuit, (B) aerial front view of constructed HVAC starter circuit, and (C) isometric view of HVAC starter circuit with Faraday cage. ....	183
A.6	Keysight N8932A autoranging 15 kW power supply voltage–current relationship power curve. ....	184
A.7	Image of: (A) quick-disconnect fuses being installed, and (B) proper powering on of quick-disconnect fuse box. ....	186

A.8	Image of (A) 33 parallel wired power resistors for APPT’s HCDC circuit, and (B) resistors placed on recirculated water cooling bath tank. ....	187
A.9	Image of: (A) LABJACK I/O wiring, and (B) LabVIEW I/O wiring. ....	188
A.10	ns-PIV Case 1: 1.6 SLM axial gas flow rate particle speed histogram. ....	189
A.11	ns-PIV Case 2: 3.2 SLM axial gas flow rate particle speed histogram. ....	190
A.12	ns-PIV Case 3: 4.8 SLM axial gas flow rate particle speed histogram. ....	190
A.13	ns-PIV Case 1: 1.6 SLM axial gas flow rate particle speed (0–3 m/s) histogram. ....	191
A.14	ns-PIV Case 2: 3.2 SLM axial gas flow rate particle speed (0–3 m/s) histogram. ....	191
A.15	ns-PIV Case 3: 4.8 SLM axial gas flow rate particle speed (0–3 m/s) histogram. ....	192
A.16	PIV velocity vector field with particle speed from 0–25 m/s (left), and 0–3 m/s (right). ....	193
A.17	ns-PIV Case 1: 1.6 SLM axial flow rate PIV velocity vector field with particle speed colormap. ....	194
A.18	ns-PIV Case 2: 3.2 SLM axial flow rate PIV velocity vector field with particle speed colormap. ....	195
A.19	ns-PIV Case 3: 4.8 SLM axial flow rate PIV velocity vector field with particle speed colormap. ....	196
A.20	ns-PIV Case 1- 1.6 SLM axial flow rate PIVlab velocity vector field. ....	197
A.21	ns-PIV Case 3: 4.8 SLM axial flow rate PIVlab velocity vector field. ....	198
B.1	The anode section of the APPT: A) as a used and degraded component and B) as a freshly machined component. ....	199
B.2	Dissassembly of the cathode section from the APPT. ....	200

B.3	The transferred arc APPT used for calibrating the imaging system when performing the 2DMIM. ....	201
B.4	Jet length vs. arc current of the preliminary APPT design that used shorter nozzle length section. ....	202
C.1	The ns-PIV particle seeder (top left, A), the MT section (top right, B), and a visual schematic of the PIV system apparatus (bottom, C). ....	203
C.2	Photographs of the PIV system while operational. ....	204
C.3	Ocean Optics USB4000 VIS-NIR spectrometer setup to measure emissions present during 2DMIM diagnostic method. ....	205
C.4	The transmittance vs. wavelength of Andover $532 \pm 10\text{nm}$ bandpass filter and Thor Labs $532 \pm 1 \text{ nm}$ laser line filter as acquired by a Shimadzu UV $2401 \pm 0.3\text{nm}$ spectrophotometer. ....	206
C.5	Spectrometer emission measurement of the APPT with and without bandpass filter present accompanied by filter transmittance. ....	207
C.6	Magnetic field apparatus' traversing, positioning, and tilting system. ....	208
C.7	The first complete assembly of the FMSTL's shock tube. ....	209
C.8	The Fluid Mixing and Shock Tube Laboratory. ....	210

## LIST OF SYMBOLS AND ACRONYMS

<b>Symbol</b>	<b>Meaning</b>	<b>Typical Units</b>
2D	Two-Dimensional	
2DMIM	2D Monochromatic Imagery Method	
3D	Three-Dimensional	
AC	Alternating Current	
ALE	Arbitrary Lagrange Eulerian	
APPT	Atmospheric-pressure Plasma Torch	
CCD	Charge-Coupled Device	
CFD	Computational Fluid Dynamics	
DC	Direct Current	
DCC	Direct Cross-Correlation	
DFT	Discrete Fourier Transform	
DT	Deuterium–Tritium	
EMI	Electromagnetic Interference	
FFT	Fast Fourier Transform	
FMSTL	Fluid Mixing and Shock Tube Laboratory	
HCDC	High Current Direct Current	
HED	High Energy Density	
HI	Hydrodynamic Instability	
HVAC	High Voltage Alternating Current	
ICF	Inertial Confinement Fusion	
KHI	Kelvin–Helmholtz Instability	
LES	Large Eddy Simulation	
LSM	Laser Scattering Method	
LST	Laser Scattering Techniques	
LTE	Local Thermodynamic Equilibrium	
MagLIF	Magnetized Linear Inertial Fusion	
MHD	Magnetohydrodynamic	
NIF	National Ignition Facility	

<b>Symbol</b>	<b>Meaning</b>	<b>Typical Units</b>
NS	Navier–Stokes	
ns-PIV	Negative Image Solid Particle Image Velocimetry	
PCHIP	Piecewise Cubic Hermite Interpolating Polynomial	
PIV	Particle Image Velocimetry	
PLMS	Planar Laser Mie Scattering	
RBI	Rayleigh–Bernard Instability	
RHS	Right hand side	
RMI	Richtmyer–Meshkov Instability	
RNG	Recursive Nyquist Grid	
ROI	Region of Interest	
RS	Raman Scattering	
RTI	Rayleigh–Taylor Instability	
SDMI	Shock-Driven Multiphase Instability	
SIT	Series Injection Transformer	
SLM	Standard Liters per Minute	
STP	Standard Temperature and Pressure	
TS	Thomson Scattering	
UHV	Ultra High Voltage	
V–I	Voltage–Current	
WCPR	Water Cooled Power Resistor	
$A_c$	Saturation ionization constant	[atm <sup>-1</sup> m <sup>-1</sup> ]
$A$	Area	[m <sup>2</sup> ]
$A$	Atwood number, $A = (\rho_2 - \rho_1)/(\rho_2 + \rho_1)$ ; page 8.	
$A_l$	Alfvén number, $A_l = v(\rho\mu)^{\frac{1}{2}}B$ ; page 13.	
$A_{nm}$	Spontaneous emission transition probability	[s <sup>-1</sup> ]
$a_i$	Thermodynamic activity of component (species) $i$	
$\vec{B}$	Magnetic induction vector, (magnetic flux density)	[T]
$B$	Magnitude of $\vec{B}$ , ( <i>i.e.</i> , $B =  \vec{B} $ )	[T]
$B_c$	Surrounding gas breakdown constant	[V atm <sup>-1</sup> m <sup>-1</sup> ]
$c$	Speed of light in vacuum	[m s <sup>-1</sup> ]

Symbol	Meaning	Typical Units
$c_p$	Specific heat at constant pressure, $(\partial h_m / \partial T)_p$	[J kg <sup>-1</sup> K <sup>-1</sup> ]
$c_v$	Specific heat at constant volume, $(\partial u / \partial T)_v$	[J kg <sup>-1</sup> K <sup>-1</sup> ]
$D$	Diffusion coefficient	[m <sup>2</sup> s <sup>-1</sup> ]
$D_i$	Cross-sectional diameter of interface	[m]
$D_j$	Diffusion coefficient of species $j$	[m <sup>2</sup> s <sup>-1</sup> ]
$d$	Electrode gap distance	[mm]
$\vec{E}$	Electric field vector	[V m <sup>-1</sup> ]
$E_m$	Energy level of state $m$	[eV]
$e$	Electron charge	[C]
$\check{e}$	Total energy per unit volume	[kg m <sup>-1</sup> s <sup>-2</sup> ]
$\hat{f}_i$	Fugacity of pure component $i$ in the mixture	
$f_i$	Fugacity of pure component $i$ at $[T, p]$	
$f_i^\circ$	Fugacity of pure component $i$ at $[T, p^\circ]$	
$G^\circ$	Standard Gibbs energy	[J mol <sup>-1</sup> ]
$G_i^\circ$	Standard Gibbs free energy of formation for component $i$	[J mol <sup>-1</sup> ]
$G_j^\circ$	Standard Gibbs free energy of reaction $j$	[J mol <sup>-1</sup> ]
$g_m$	Statistical weight	
$h_m$	Enthalpy per unit mass	[J kg <sup>-1</sup> ]
$h$	Planck's constant	[J s]
$I$	Arc current	[A]
$I$	Chord-integrated intensity	
$\vec{j}$	Current density	[A m <sup>-2</sup> ]
$K_j$	Equilibrium constant of $j^{\text{th}}$ reaction	
$k$	Wavenumber	[m <sup>-1</sup> ]
$k_B$	Boltzmann's constant	[J K <sup>-1</sup> ]
$M$	Mach number	
$m_j$	Mass of $j^{\text{th}}$ species	[kg]
$n$	Kernel size	[pixels]
$n_i$	Number density of $i^{\text{th}}$ species	[m <sup>-3</sup> ]
$p$	Pressure	[kg m <sup>-1</sup> s <sup>-2</sup> ]

Symbol	Meaning	Typical Units
$p^\circ$	Standard pressure, reference pressure at STP	[atm]
$Q$	Fusion energy gain factor	
$Q_j$	Atomic partition function	
$q$	Elementary charge	[C]
$R$	Universal gas constant	[J mol <sup>-1</sup> K <sup>-1</sup> ]
$r$	Radial distance	[m]
$r_m$	Radius of magnet	[m]
$St$	Stokes number	
$T$	Temperature	[K]
$T_e$	Electron temperature	[eV]
$t$	Time	[s]
$\vec{U}$	Fluid velocity vector	[m s <sup>-1</sup> ]
$U_{px}$	PIV velocity in $x$ -direction	[pixels]
$u$	Internal energy per unit mass	[J kg <sup>-1</sup> ]
$\vec{V}$	Plasma flow field velocity vector	[m s <sup>-1</sup> ]
$V$	Arc voltage	[V]
$v$	Specific volume	[m <sup>3</sup> kg <sup>-1</sup> ]
$V_{BD}$	Breakdown voltage	[V]
$V_{py}$	PIV velocity in $y$ -direction	[pixels]
$v$	Velocity	[m s <sup>-1</sup> ]
$v_A$	Alfvén velocity	[m s <sup>-1</sup> ]
$v_s$	Acoustic velocity (speed of sound)	[m s <sup>-1</sup> ]
$w_i$	Shock wave transit speed	[m s <sup>-1</sup> ]
$Y_i$	Mole fraction of species $i$	
$Z$	Charge state, $Z = q/e$	
$\alpha_d$	Degree of dissociation	
$\alpha_i$	Degree of ionization	
$\alpha_{2i}$	Degree of second ionization	
$\beta$	Dimensionless magnetic strength, $\beta = 2p\mu_0/B^2$ ; page 26.	
$\Gamma$	Particle mass flux	[kg m <sup>-2</sup> s <sup>-1</sup> ]

<b>Symbol</b>	<b>Meaning</b>	<b>Typical Units</b>
$\epsilon_{nm}$	Total line emission coefficient	
$\epsilon(r)$	Radial emissivity	[J s <sup>-1</sup> m <sup>-1</sup> ]
$\epsilon$	Tolerance criterion for PIVlab	
$\eta$	Perturbation amplitude	
$\lambda$	Wavelength	[m]
$\lambda_{nm}$	Wavelength between states $n$ and $m$	[nm]
$\mu_i$	Chemical potential of species $i$	[J mol <sup>-1</sup> ]
$\mu_j$	Mobility of species $j$	[m <sup>2</sup> V <sup>-1</sup> s <sup>-1</sup> ]
$\mu_0$	Vacuum permeability, permeability of free space	[T m A <sup>-1</sup> ]
$\nu$	Collisional frequency	[s <sup>-1</sup> ]
$\nu_i^{(j)}$	Stoichiometric coefficient of the $i^{th}$ species of $j^{th}$ reaction	
$\xi_j$	Extent of reaction $j$	
$\rho$	Mass density	[kg m <sup>-3</sup> ]
$\sigma$	Standard deviation	
$\sigma_e$	Electrical conductivity	[ $\Omega^{-1}$ m <sup>-1</sup> ]
$\tau$	Dimensionless time	
$\hat{\phi}_i$	Dimensionless fugacity coefficient of $i^{th}$ component	
$Y_p$	Species concentration	
$\gamma$	Ratio of specific heats, $\gamma = c_p/c_v$ ; page 26.	
$\gamma_{se}$	Secondary emission coefficient	
$\Omega$	Angular frequency of wave	[rad s <sup>-1</sup> ]
$\omega$	Vorticity	[s <sup>-1</sup> ]
$\omega_b$	Baroclinic vorticity	[s <sup>-1</sup> ]
$\omega_c$	Cyclotron frequency	[s <sup>-1</sup> ]

# DEVELOPMENT OF AN EXPERIMENT FOR INVESTIGATING THE MAGNETOHYDRODYNAMIC RICHTMYER–MESHKOV INSTABILITY

Roy C. Allen IV

Dr. Jacob A. McFarland, Dissertation Supervisor

## ABSTRACT

Collaboration by some of the world’s brightest minds of the 21<sup>st</sup> Century pinpointed fourteen Grand Engineering Challenges that face humankind today. At the top of this list is “Provide Energy from Fusion”; a requirement deemed crucial for humankind to thrive flourish. Scientists from all over the globe have risen to this challenge in many ways; most recognizably by attempting to succeed at performing inertial confinement fusion (ICF). However, ICF currently remains unsuccessful at providing net-positive energy production, largely due to hydrodynamic instabilities, such as the shock-driven Richtmyer–Meshkov instability (RMI), which occur within the fusion reaction process, creating detrimental mixing. Applying magnetohydrodynamic approaches however, can mitigate these instabilities and reduce fluid mixing. It is precisely this problem that necessitates the research on magnetohydrodynamic instabilities presented in this dissertation to aid in solving the challenge to “Provide Energy from Fusion”; specifically the development of an experiment for investigating the magnetohydrodynamic Richtmyer–Meshkov instability (MHD–RMI).

The goal of this dissertation work is to develop a low-energy laboratory experiment to explore the MHD suppression of the RMI for validation of simulations. To achieve the goal of this dissertation and provide necessary aid towards solving the world

energy crisis, a new experiment was designed to examine the MHD–RMI. To do so, considerable computational efforts and a multitude of experimental efforts, apparatuses, and components were employed or developed that will be utilized in harmony in the MHD–RMI shock tube experiment. The author is unaware of any experimental studies performed on the MHD–RMI to date. However, there are groups who have begun to investigate the MHD–RMI through computational approaches. To design this new experiment, a simulation study was first undertaken to predict the required conditions (magnetic field strength and orientation, and shock wave strength) necessary to suppress the MHD–RMI. Next, to create a MHD active interface, a non-transferred, direct current (DC) arc, atmospheric-pressure plasma torch (APPT) was developed. Finally, new diagnostic methods were developed to measure/verify the plasma initial conditions, and to track the MHD–RMI growth over time.

Simulations of the MHD–RMI were performed and analyzed using the hydrodynamics software FLAG. By implementing a range of magnetic field strengths, magnetic field orientations, and incident shock wave Mach numbers, the results of the simulations provided unique insight into the physical phenomena, such as Alfvén waves, that are responsible for the suppression of the MHD–RMI. Additionally, the simulations provided predictions of the necessary MHD conditions (*e.g.*, plasma ionization degree and magnetic field strength) to be generated by the new experiment.

The experimental work presented herein consists of the development and diagnosis of an atmospheric-pressure, non-transferred, direct current (DC) arc plasma torch (APPT) for investigating magnetohydrodynamic experiments. The ability to generate a stable, laminar, atmospheric-pressure plasma torch, with a jet length of over

80 cm (~3 ft.) under ideal operating conditions, was achieved. In doing so, one of the longest laminar jet lengths of a non-transferred APPT was produced. One major contribution to the scientific community that resulted from the experimental work was the development of the 2D Monochromatic Imagery Method (2DMIM). The 2DMIM is able to acquire the plasma's electron temperature and degree of ionization profile with an order of magnitude greater in resolution than traditional spectroscopic methods like the well-known Fowler–Milne method it is based on. Electron temperatures of up to 14,000 K and degree of ionization of up to 27% at the torch exit were obtained.

To visualize the plasma interface in magnetohydrodynamics experiments, a technique was developed to image the cylindrical plasma jet in both the  $rz$ -plane (axial) and the  $r\theta$ -plane (cross-sectional) using planar-laser Mie scattering (PLMS) from particles added to the surrounding gas deemed the negative image solid particle image velocimetry technique, or ns-PIV for short. Once the plasma source was developed and diagnosed, an externally applied magnetic field was imposed on the plasma flow field at various magnetic field strengths and orientations. The interaction between the magnetic field and the plasma flow field provided the ability to observe, qualify and quantify the deflection and suppression effects that ensued and prove that the plasma generated was able to be significantly manipulated by an external magnetic field.

By developing and performing the computational and experimental efforts at the Missouri Fluid Mixing and Shock Tube Laboratory (FMSTL), the author has laid the groundwork to observe the suppression of the MHD–RMI in future shock tube experiments.

## CHAPTER 1. INTRODUCTION

Imagine our World with an endless supply of safe, clean and renewable energy. Air pollution virtually eliminated. Planet Earth saved from the ravages of nuclear waste and accidents, from coal mining, from natural gas fracking, from oil spills in the oceans and from so much more. Any threat of Global Warming being virtually eliminated

Now imagine a breakthrough in the decades old quest by our World's scientific community to produce this very supply of energy. President Abraham Lincoln once said "Determine that the thing can and shall be done, and then... find the way." What follows here is the roadmap of this author's journey to aid in achieving this breakthrough, to "find the way" and to help change our World.

To better understand the concept of magnetohydrodynamic instabilities, their role in the world energy crisis and how they factor into the challenge to "Provide Energy from Fusion" set forth in the National Academy of Engineering's Grand Engineering Challenges, the following framework for discussion is presented.

Magnetohydrodynamic (MHD) instabilities involve the coupling of hydrodynamic instabilities (HI) with magnetic field effects in a conducting fluid (*e.g.*, plasma). Hydrodynamic instabilities such as the Richtmyer–Meshkov instability (RMI) are ubiquitous in many high-energy-density (HED) applications. HED applications include areas such as astrophysics, thermonuclear weapons, and inertial confinement fusion (ICF). Fluid mixing present in these applications is instigated by HIs, which can result in a lower energy yield than what is necessary to achieve net-positive energy

production, (*s.c.*, fusion energy gain factor,  $Q > 1$ ). Studying these systems, however, is complicated due to the high energies involved. Thus the majority of large-scale HED research is performed at facilities such as the National Ignition Facility (NIF), located at Lawrence Livermore National Laboratory, the Omega Laser Facility at the University of Rochester, and the Z machine at Sandia National Laboratories.

Magnetic effects are being explored within the HED physics community as an option to increase the efficiency of inertial confinement fusion (ICF) [1]. The addition of externally applied magnetic fields can be found in experiments performed at the OMEGA Laser Facility at the University of Rochester using a spherical target as well as in Magnetized Linear Inertial Fusion (MagLIF), studied at Sandia National Laboratories [1–3]. In both experiments, plasmas are created during the compression of the fusion fuel, and fluid interfaces experience HIs, such as the Richtmyer–Meshkov (RMI, from impulsive/shock accelerations), Rayleigh–Taylor (RTI, from steady accelerations), and Kelvin–Helmholtz (KHI, from shear), which lead to fluid mixing and degrading the fusion yield [4–6]. The application of a magnetic field can limit/suppress the ability of HIs to develop detrimental mixing effects [7]. The ability to investigate MHD effects on HIs in a smaller, university laboratory (*i.e.*, in comparison to a HED facility) is highly beneficial. The FMSTL research group developed an approach to doing so by impulsively accelerating (shocking) atmospheric-pressure plasma with a cylindrical interface (*i.e.*, a plasma torch) using a low-energy shock tube facility while applying a strong external magnetic field to examine MHD effects on the RMI. Through an integrated endeavor of experimental efforts backed by computational work, the present study presents the development of an experiment suitable for studying MHD effects on

the RMI, setting the stage for future experiments to investigate MHD suppression of the RMI.

Before getting immersed in the specifics of MHD–RMI theory, providing the fundamentals of HI's is deemed necessary. Thus the following section is used to provide a brief background of, and highlight, what constitutes a hydrodynamic instability.

## **1.1 Theory of Hydrodynamic Instabilities**

Hydrodynamic instabilities, simply stated, are the mechanism by which a fluid makes a transition from a stable to unstable flow condition. HI theory has been developed since the early 1800's by such scholars as Lord Kelvin, Herman von Helmholtz, Lord Rayleigh, and Osborne Reynolds. HI's foundations are found in fluid mechanics and include the Reynolds number, Navier–Stokes equations (*i.e.*, Euler's equation neglecting viscosity), and the continuity equation. HIs are studied through a multitude of experiments and simulations for an extensive range of applications. HIs can also be seen all around us in nature. HI investigations can include effects as simple as constant acceleration or as complex as radiation. The RMI is an important member of a group of HIs which also includes the KH and RT instabilities. In the multitude of applications where the RMI occurs so too does the KHI, or the RTI, or both. Before diving into the specifics of the RMI in MHD, a review of these instabilities is presented.

### 1.1.1 Hydrodynamic Instabilities in the Traditional Sense

#### 1.1.1.1 Kelvin–Helmholtz Instability (KHI)

The KHI occurs when there is velocity shear in a single continuous fluid, or when there is a velocity differential across a two-fluid interface of equivalent density (absent buoyancy effects). As a shear layer develops, a vortex sheet is created between the two fluids which, if perturbed, causes vorticity to accumulate at points along the interface, and ultimately leads to the perturbation being amplified. Examples of this are seen in nature, such as when the wind blows over water to form a wave, or in “fluctus” clouds, as shown in Figure 1.1 [8].



**Figure 1.1.** The Kelvin Helmholtz instability rendered visible by clouds *ex* Ref. [8].

The KHI can be simulated using computational fluid dynamics (CDF) and compared to experiments to provide results such as the one shown in Figure 1.2 for a single-modal KHI in a supersonic flow.

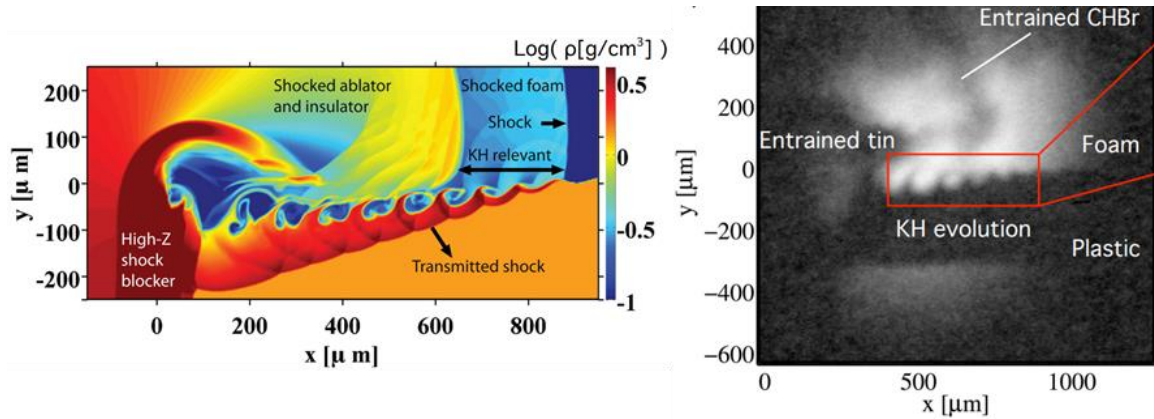


**Figure 1.2.** Simulation (left) and experiment (right) observation of single-mode KHI in a supersonic flow from the work of Wan *et al.* [9].

### 1.1.1.2 Rayleigh–Taylor Instability (RTI)

The next HI discussed is the RTI which is in the same family of HIs as the KHI and RMI. The RTI develops when two fluids of differing densities are uniformly accelerated constantly in the direction from the heavier fluid into the lighter fluid ( $\nabla p \cdot \nabla \rho < 0$ ). A pressure imbalance is generated when the two fluid interface is perturbed which causes the manifestation of vorticity and perturbation amplification. For example, the RTI is evident when cream is poured into coffee or when food coloring is dripped into water. Experimentation and simulation efforts on the RTI provide unique insight into the mixing transition and truly-asymptotic behavior of the RTI instability. One such example is of the Large Eddy Simulation (LES) simulation shown in Figure 1.3.

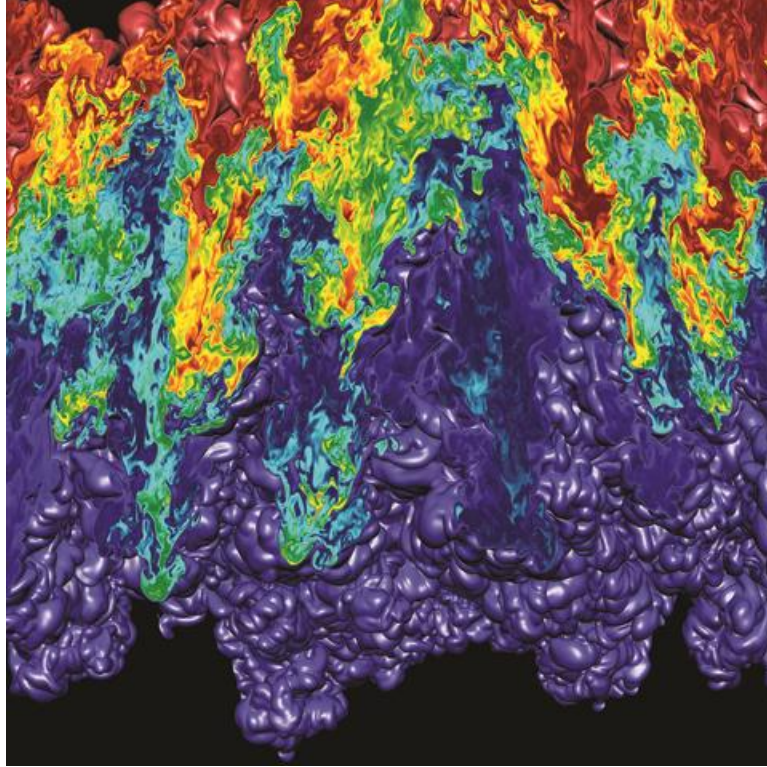


**Figure 1.3.** Large Eddy Simulation of Rayleigh–Taylor instability morphology performed in MIRANDA [10].

With the basis and specifics of the HIs discussed, the understanding of their evolution is now presented. The growth or morphology of these instabilities can be classified into various stages of development, where it is useful to consider the interface perturbations as a wave or sum of waves. Consideration of their perturbations as waves also helps tie MHD waves, which arise in the MHD–RMI, to the classical or traditional RMI specifically.

### *1.1.1.3 Hydrodynamic Instabilities Developmental Stages*

In the first stage, the instabilities begin to evolve in a linear growth regime where the amplitude of the perturbations,  $\eta$ , is much smaller than their wavelengths,  $\lambda$ , (*i.e.*,  $\eta/\lambda \ll 10^{-1}$ ). As the amplification of these perturbations progresses, their

amplitude begins to exceed their wavelength at which time they are considered to be in the non-linear regime (*i.e.*, when  $\eta/\lambda > 10^{-1}$ ). However, in the case of the RMI there is an initial non-linear regime or stage which precedes the linear regime due to compressibility effects [11]. Secondary instabilities, such as KHIs, can then develop as the interface continues to grow, which causes small-scale vertical features to be created in the interface. This process is evident through the bifurcation of the solutions to the Navier–Stokes (NS) equations as turbulence develops within the flow field. The final stages of the instability development and growth consist of it decaying into a turbulent mixing region. Specifically for the RMI, the classical criterion for turbulence is not necessarily met within the turbulent mixing region because the turbulence could be anisotropic. Therefore, further clarification of the classical RMI components and properties is presented in the following section.

### *1.1.2 The Richtmyer–Meshkov Instability (RMI)*

In the case of the classical RMI, the instability arises due to the interaction of an impulsive acceleration (usually in the form of a shock wave) misaligned with a density gradient created by a fluid interface. Three major ingredients are required for the RMI:

- 1) a density gradient, which is typically achieved by a gas interface, and quantified by the Atwood number  $A$ ,
- 2) a sharp pressure gradient (*i.e.*, a shock wave), which is accomplished and quantified by the Mach number  $M$ , and
- 3) a perturbed interface, which in the case of this study, is cylindrical in geometry.

The Atwood number,  $A$ , and can be calculated with Equation (1.1). The upstream and downstream fluid's densities are symbolized as  $\rho_1$  [ $\text{kg m}^{-3}$ ] and  $\rho_2$  [ $\text{kg m}^{-3}$ ], respectively. The Mach number,  $M$ , is a function of the fluid velocity,  $U$  [ $\text{m s}^{-1}$ ], the fluid sound speed  $v_s$  [ $\text{m s}^{-1}$ ], and can computed using Equation (1.2). Here, the sound speed is also expanded to be equivalent to the square root of the sum of the ratio of specific heats,  $\gamma$ , the gas constant,  $R$  [ $\text{J kg}^{-1} \text{K}^{-1}$ ], and temperature,  $T$  [K].

$$A = \frac{\rho_2 - \rho_1}{\rho_2 + \rho_1} \quad (1.1)$$

$$M = \frac{U}{v_s} = \frac{U}{\sqrt{\gamma RT}} \quad (1.2)$$

The Atwood number defines a dimensionless ratio of the difference in the density of two fluids over their sum, for the upstream and downstream fluids respectively. The Mach number relates the fluid velocity to the fluid sound speed. An essential characteristic of this is the larger the Mach number, the greater the vorticity deposition. Since Mach number and Atwood number represent the strength of the pressure and density gradients, respectively, a misalignment between the two is deemed the linearity of the interface (*i.e.*, the ratio of the perturbation amplitude to the wavelength,  $\eta/\lambda$ ). The lower this ratio, the more linear and developmentally weak the instability is that forms. This concept is discussed in greater detail in Richtmyer's linear model [4]. As the fluid interface is accelerated, it becomes distorted, during which its morphology develops in the direction of the acceleration impulse. The growth or development of the RMI's interface is realized through a three-stage process. The first stage consists of the shock

wave traversing the interface, where vorticity is deposited, and results in the growth of the interface's amplitude being linear in time. Vorticity deposited along the interface is termed the baroclinic vorticity  $\omega_b$  [ $s^{-1}$ ], which is a function of density,  $\rho$  [ $kg\ m^{-3}$ ], and pressure,  $p$  [ $kg\ m^{-1}\ s^{-2}$ ], and can be calculated with Equation (1.3).

$$\omega_b = \frac{1}{\rho^2} (\bar{\nabla} p \times \bar{\nabla} \rho) \quad (1.3)$$

During the mid-stage, a non-linear regime is evident in which the developments of small-scale structures (“rollups”) evolve that are created by subsequent (secondary) HI development, namely KHIs. Rollups are visible as bubbles when a lighter fluid penetrates a heavier fluid or as spike-like structures when a heavier fluid penetrates a lighter fluid. The final stage consists of a chaotic regime in which the non-linear growth structures decay into turbulent mixing at late-times. This process is visually represented in Figure 1.4.

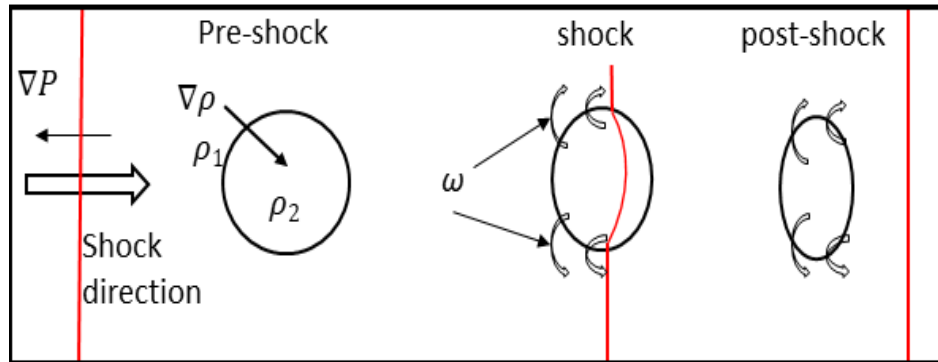


**Figure 1.4.** Visual representation of the three stages of the RMI development. Image from Black *et al.* [12].

The ability to predict, and more importantly control, the turbulent mixing created by the RMI is of paramount importance to the engineering field and scientific community. The ability to control and suppress the RMI motivates this dissertation.

### *1.1.3 Magnetohydrodynamic Instabilities*

Magnetohydrodynamics is a much newer field of physics compared to traditional hydrodynamics. MHD is the field of study on magnetic properties and the behavior of conducting fluids. The fundamentals of MHD were developed by Hannes Alfvén, for which he was awarded the Nobel Prize in Physics in 1970. The inclusion of magnetic fields,  $\vec{B}$ , and electric fields,  $\vec{E}$ , coupled with a conducting fluid at velocity,  $\vec{V}$ , when dependent on each other, goes beyond the two independent disciplines of electromagnetism and fluid mechanics, requiring the more general formalism of magnetohydrodynamics. The inclusion of these physical effects changes the study from classical hydrodynamics to magnetohydrodynamics, in which the effects are captured by Maxwell's Equations, and the Lorentz force, which plays a vital role in the fluid momentum equation. When these physical phenomena are strongly coupled (*i.e.*, a highly conducting fluid or a strong magnetic field or both are evident), spectacular phenomena can be observed, which will be seen in Sections 2.5 and 4.4.2 of this dissertation. One of the most prominent examples arises in the form of propagating Alfvén waves, which are based precisely on the strong coupling of the  $\vec{V}$  and  $\vec{B}$  fields. The description of the Alfvén wave and other MHD waves will be discussed in more detail in Section 2.4. The first of the coupled components to be discussed is the conducting fluid.

For a gas to become an electrically conducting fluid (*i.e.*, a plasma), it must be ionized. Astrophysical plasmas and thermonuclear fusion plasmas are perfect examples of highly electrically conducting fluids. However, certain aspects of their behavior are limited within traditional fluid models because the assumption of local thermodynamic equilibrium must be forgone, and interactions between elementary particles on one another must be considered. Laboratory plasma, such as the one generated for this work, is more amenable to being described by traditional fluid models, being that such plasmas are not as hot as stellar plasmas and are much less conductive. However, since laboratory plasmas are less dense, they are more susceptible to electromagnetic force effects. The significant contribution of the conducting fluid is that it changes what contributes to the density gradient as part of the RMI ingredients.

Astrophysical plasmas also possess much stronger magnetic fields than the ones able to be produced inside a traditional laboratory setting. Magnetars, for example, are estimated to generate magnetic field flux densities of 100 GT ( $10^{11}$  T) [13]. The strongest continuous magnetic field yet produced in a laboratory setting is 45 T, or  $\sim 1000$  times smaller than a magnetar (a type of neutron star) [14]. Achieving an understanding of these physical phenomena that arise when coupling magnetic and hydrodynamic effects at a small-scale university research facility through experiments and simulations can, in turn, be utilized to better understand the physical phenomena occurring in large-scale facilities research; and with next level thinking, can even be used to predict or better understand universal-sized phenomena. Now that the foundations of HI's, specifically the RMI, and what constitutes a magnetohydrodynamic instability have been portrayed, how these physical phenomena are tied together within the MHD–RMI is provided within the

following section. Specifically, the context of the MHD–RMI experiment as well as important parameters are provided; of which will become more important and evident in computational work Sections 2.4–2.5, and the experimental sections pertaining to the magnetic field within Sections 3.4, and 4.4.

#### *1.1.4 The Magnetohydrodynamic Richtmyer–Meshkov Instability*

The influential nature of an externally applied uniform magnetic field on an electrically conducting fluid commonly yields greater stability and induces a postponement of the appearance of turbulent effects. These effects are attributable to the fact that perturbations give rise to eddy currents whose energy is dissipated by the Joule heating effect. Investigational efforts on the MHD–RMI are not as progressed nor well-studied as the Rayleigh–Bernard instability (RBI) in the presence of a magnetic field, or those of the RTI in MHD. For the purposes of investigating the MHD–RMI, the treatment of the governing equations and relationships are restricted to their consideration in the ideal sense.\* The set of ideal MHD equations used are the continuity equation, momentum conservation equation, energy balance, Ampère’s law, Gauss’s law of magnetism, and the magnetic divergence constraint, as shown in Equations (1.4–(1.9). Additionally shown are the phase velocity of the hydrodynamic wave and the Alfvén velocity in Equations (1.10–1.11). The symbols presented in these equations are: density,  $\rho$  [ $\text{kg m}^{-3}$ ]; time,  $t$  [s]; velocity,  $\vec{U}$  [ $\text{m s}^{-1}$ ]; the speed of light in vacuum,  $c$  [ $\text{m s}^{-1}$ ], the current density,  $\vec{j}$  [ $\text{A m}^{-2}$ ], the magnetic field induction vector,  $\vec{B}$  [T], the permeability of free space,  $\mu_0$  [ $\text{T m A}^{-1}$ ]; the wave’s angular frequency;  $\Omega$  [ $\text{rad s}^{-1}$ ], wavenumber,

---

\* Ideal in this context means that all real physical effects are not captured within model, but reduced down to fluids operating as if they were perfect conductors, for example.

$k$  [ $\text{m s}^{-1}$ ]; acoustic velocity,  $v_s$  [ $\text{m s}^{-1}$ ]; Alfvén velocity,  $v_A$  [ $\text{m s}^{-1}$ ]; vorticity,  $\omega$  [ $\text{s}^{-1}$ ]; magnitude of the magnetic field,  $B$  [T], and Alfvén number,  $A_l$ . Equation (1.6) includes  $\check{e}$  [ $\text{kg s}^{-1} \text{m}^{-2}$ ], the total energy per unit volume (*i.e.*, energy density) within the energy equation (not to be confused with  $e$  [C], the electron charge).

$$\frac{\partial \rho}{\partial t} + \vec{\nabla} \cdot (\rho \vec{U}) = 0 \quad (1.4)$$

$$\rho \left( \frac{\partial}{\partial t} + \vec{U} \cdot \vec{\nabla} \right) \vec{U} = \vec{J} \times \vec{B} - \vec{\nabla} p \quad (1.5)$$

$$\frac{\partial \check{e}}{\partial t} + \vec{\nabla} \cdot \left[ \left( \check{e} + p + \frac{B^2}{2} \right) \vec{U} - \vec{B} \cdot \vec{U} \vec{B} \right] = 0 \quad (1.6)$$

$$\vec{J} = \frac{\vec{\nabla} \times \vec{B}}{\mu_0} \quad (1.7)$$

$$\vec{J} \times \vec{B} = \frac{(\vec{B} \cdot \vec{\nabla}) \vec{B}}{\mu_0} - \vec{\nabla} \frac{B^2}{2\mu_0} \quad (1.8)$$

$$\vec{\nabla} \cdot \vec{B} = 0 \quad (1.9)$$

$$\frac{\Omega}{k} = \sqrt{c^2 \frac{v_s^2 + v_A^2}{c^2 + v_A^2}} \quad (1.10)$$

$$v_A = \frac{B}{\sqrt{\mu_0 \rho}} \quad (1.11)^*$$

$$A_l = \frac{B}{\omega \sqrt{\mu_0 \rho}} = \frac{v_A}{\omega} \quad (1.12)$$

---

\* Shown in Equation (1.11) is the Alfvén number which is the ratio of magnetic to inertial forces.

The continuity equation, Equation (1.4), is the only one of these governing equations that remains unchanged from the classical RMI.\* The inclusion of electromagnetic forces is present in the momentum equation (Euler’s eq.), Equation (1.5) as the cross product of the current density  $\vec{j}$ , and the magnetic flux density  $\vec{B}$ . This term is the Lorentz force without an additional externally applied magnetic field. Ampère’s law expands the Lorentz force as given in Equation (1.7) to produce Equation (1.8). In this form of the Lorentz force equation, the right hand side (RHS) of the equation’s first term represents the magnetic tension force, which acts to straighten any disturbed magnetic field lines. This gives rise to the MHD waves that develop as well as the magnetic pressure which results.

The dispersion relationship for the interaction of the motion of charge that brings about the production of MHD waves, is able to be easily derived for both the perpendicular and parallel magnetic field orientations [15]. In turn, the dispersion relationship for each respective magnetic field orientation is used to find the MHD wave propagation velocity. MHD waves, which propagate perpendicular to the magnetic field with Alfvén velocity,  $v_A$ , as shown in Equation (1.11), are deemed “hydromagnetic waves”, or “Alfvén waves”. MHD waves that propagate along the magnetic field lines (*i.e.*, in parallel to the magnetic field) are termed “magnetosonic waves” (a.k.a. fast hydromagnetic waves because  $\Omega/k \gtrsim v_A$ ) and have phase velocity  $\Omega/k$ , which can be computed by utilizing Equation (1.10). A geometric visualization of both of these waves’ propagation patterns is shown in Figure 1.5.

---

\* The classical RMI is also governed by the continuity, momentum and energy conservation equations, Equations (1.4)–(1.6), with  $\vec{B}$  identically equal to zero.

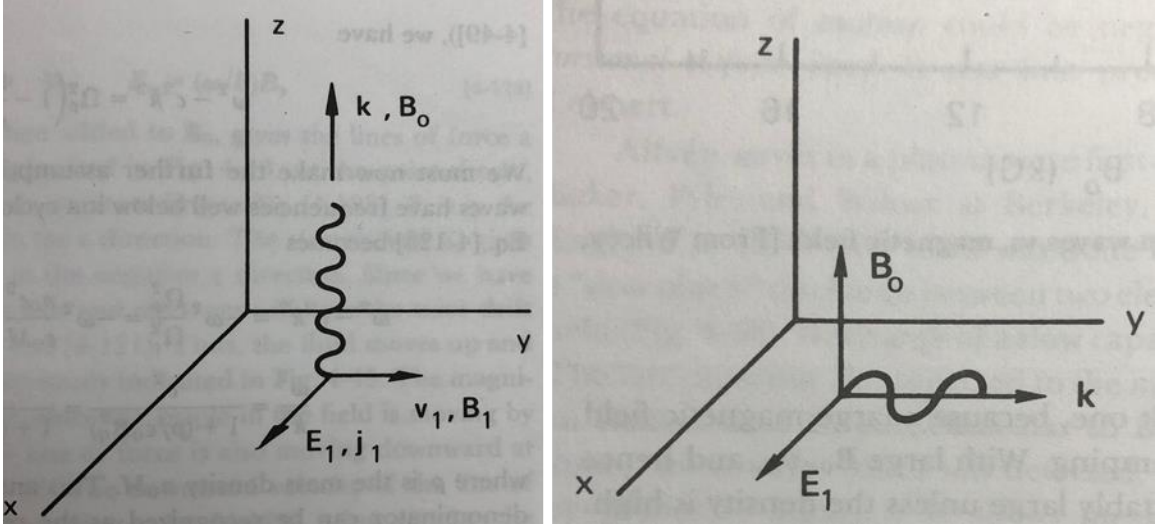


**Figure 1.5.** Geometry of an Alfvén wave propagating along  $\vec{B}$  (left), and a magnetosonic wave propagating at right angles to  $\vec{B}$  (right). Image from Chen [15].

In the limit  $\vec{B} \rightarrow 0, v_A \rightarrow 0$  the magnetosonic wave becomes an ordinary ion acoustic wave, propagating at a velocity equivalent to the acoustic velocity,  $v_s$ . The understanding and distinction between magnetosonic and Alfvén waves is quintessential because it is the Alfvén waves which provide the mechanism to suppress the RMI in MHD. This is explained in greater detail in the results Section 2.6 of Chapter 2. A visualization of all three stages of the RMI in MHD is shown in Figure 1.6. To better understand why the theory on MHD–RMI is presented, application’s where it is used is presented in the following section.

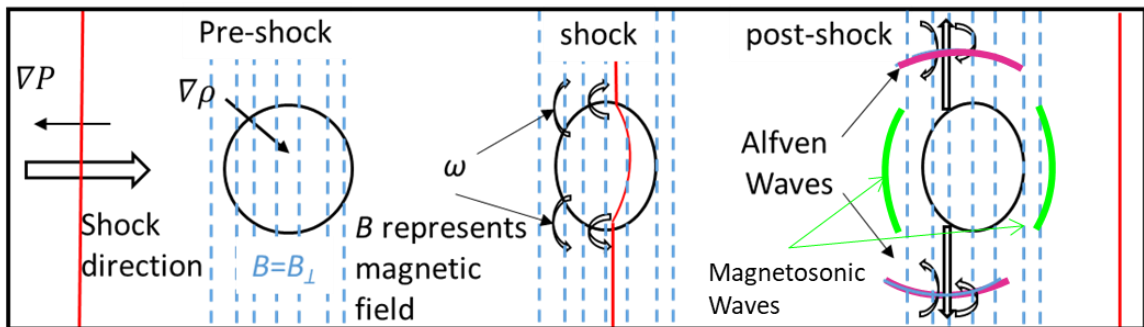


**Figure 1.6.** Visual representation of the stages of the MHD–RMI development.

## 1.2 Applications of the Magnetohydrodynamic Richtmyer–Meshkov Instability

The MHD–RMI occurs in a myriad of human-made and astrophysics (stellar) systems and has various important and useful applications in the scientific community. The study of the RMI is currently being applied to the astrophysics field, where its inclusion further increases the accuracy of modeling the behavior of supernovae remnant formation [16]. Another example is found in stellar phenomena, where large gaseous clouds, which have density inhomogeneities are subjected to everything from stellar winds, to convection, accretion, and, notably, strong shock waves (*i.e.*, “shocks”), created by supernovae [17]. In these celestial phenomena, the strong shock’s interaction with the gaseous media present is: (1) the likely driving mechanism (*i.e.*, force) by which stars are formed, (2) that which governs their respective temperatures and density due to fluid mixing, (3) shown to be the cause of the lack of stratification in the products of supernovae 1987A, and (4) even how solar systems are organized [18–21].

The MHD–RMI also arises in combustion systems such as hypersonic air-breathing engines [22, 23]. In these systems shock-flame interactions have been shown to occur [24]. Within these combustion systems, enhancement of the fuel–air mixing is achieved, where the RMI is significant in deflagration-to-detonation transition [21]. In scram-jet engine combustion analyses, circulation deposition is deemed the dominant fluid dynamical process in the early-time RMI environment [25]. Utilizing a plasma torch to assist supersonic combustion system, has shown promising ignition enhancement capabilities, and increased efficiency, both numerically and experimentally [26, 27]. Although this is not a direct goal of suppressing MHD–RMI development, it does show

how various aspects of the work produced in this dissertation, have a multitude of applications.

The most pertinent application of MHD–RMI research is ICF being performed at large-scale high-energy-density (HED) facilities. HED research is currently being conducted in astrophysics, thermonuclear weapons, and inertial confinement fusion (ICF). Fluid mixing present in these applications is encouraged by HIs in which the RMI is evident, ultimately increasing mixing and reducing energy yield. However, studying these systems is complicated due to the high energies involved. The most recognizable large-scale HED research is performed at facilities such as the National Ignition Facility (NIF), located at Lawrence Livermore National Laboratory, the Omega Laser Facility at the University of Rochester, and the Z machine at Sandia National Laboratories.

To increase the efficiency of inertial confinement fusion (ICF), magnetic effects are being explored for which the RMI arises [1]. ICF at the NIF utilizes 192 lasers in a semi-spherical orientation, which provide 1.8 MJ of laser energy at 500 TW, to compress deuterium and tritium (isotopes of hydrogen) fuel by several orders of magnitude. The fusion fuel is contained within what is termed, a hohlraum. The deuterium-tritium (DT) fuel, located within the hohlraum, is then fuse into a heavier element (helium), and releases energy. As the fuel undergoes this fusion process, it is plasmized (*i.e.*, becomes plasma). DT fuel is chosen due to it being the reaction elements with the lowest cross-section for achieving fusion. One of the side effects of this process is the releasing of free neutrons, which contain extraordinary amounts of energy. This energy can be harnessed by slowing down the neutrons in ocean water, for example, or utilized to convert fertile material into fission-reactor fuel.

During the ICF process, the hohlraum is struck by four, sequential, high-precision laser pulses, where it absorbs the lasers' energy and emits thermal energy back to the DT fuel target (DT ice capsule) in the form of X-rays. This method of ICF is termed indirect-drive. Employing multiple, sequential, laser pulses is attributed to the ability to better control the acceleration of the compressing fuel, as well as control the timing of the shock waves (forming HIs) that are created from the beryllium ablator shell that encasing the DT fuel target. That is, indirect-drive ICF is executed in a way, outside of utilizing magnetic fields, in an attempt to control the formation of RMIs and RTIs that arise within the fuel target. Specifically, RMIs develop for two reasons: (1) as a result of the perturbations generated within the fuel target due to manufacturing inaccuracies, and (2) from perturbations which arise due to the heat increase from the X-radiation incident on the DT fuel's beryllium ablator shell. As the RMIs continue to develop, the amplification of the perturbations results in the high-density DT fuel mixing with the lower density ablator material, ultimately causing reduction in the fusion yield, which is an undesirable effect. Consequently, the ability to control the development of the RMI (and the RTI) using suppression techniques is critical to the success of reliable power from ICF. A visual representation of the hohlraum and the respective components within it as used at the NIF's ICF research facility is shown in Figure 1.7.

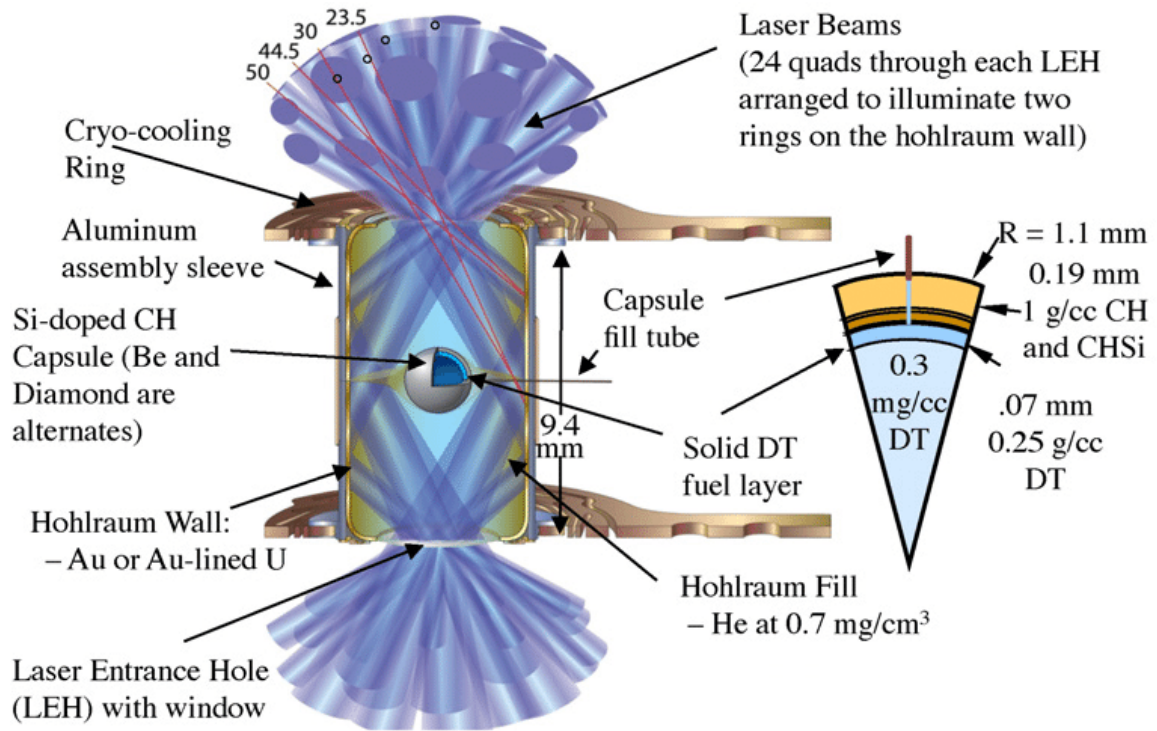


**Figure 1.7.** NIF indirect-drive hohlraum and capsule schematic from Ref. [28]. Reproduced with permission from IOP Publishing. All rights reserved.

The addition of externally applied magnetic fields can be found in the OMEGA Laser Facility's experiments, which utilize a spherical target similar to that used in Magnetized Linear Inertial Fusion (MagLIF) as studied at Sandia National Laboratories [2, 3]. In the OMEGA laser experiments, the application of an external magnetic field has been shown to increase thermal confinement and fusion yield on targets similar to those used by the NIF. MagLIF is performed in the Z machine experiment at Sandia, where a target undergoes magnetically-driven compression in a Z-pinch. The target is laser-heated and magnetically confined to generate fusion. Shown in Figure 1.8 is an aerial isometric view of the MagLIF experiment during operation where a colossal electric pulse generator creates tens of millions of amperes and generates what looks like a spider web of lighting (plasma).

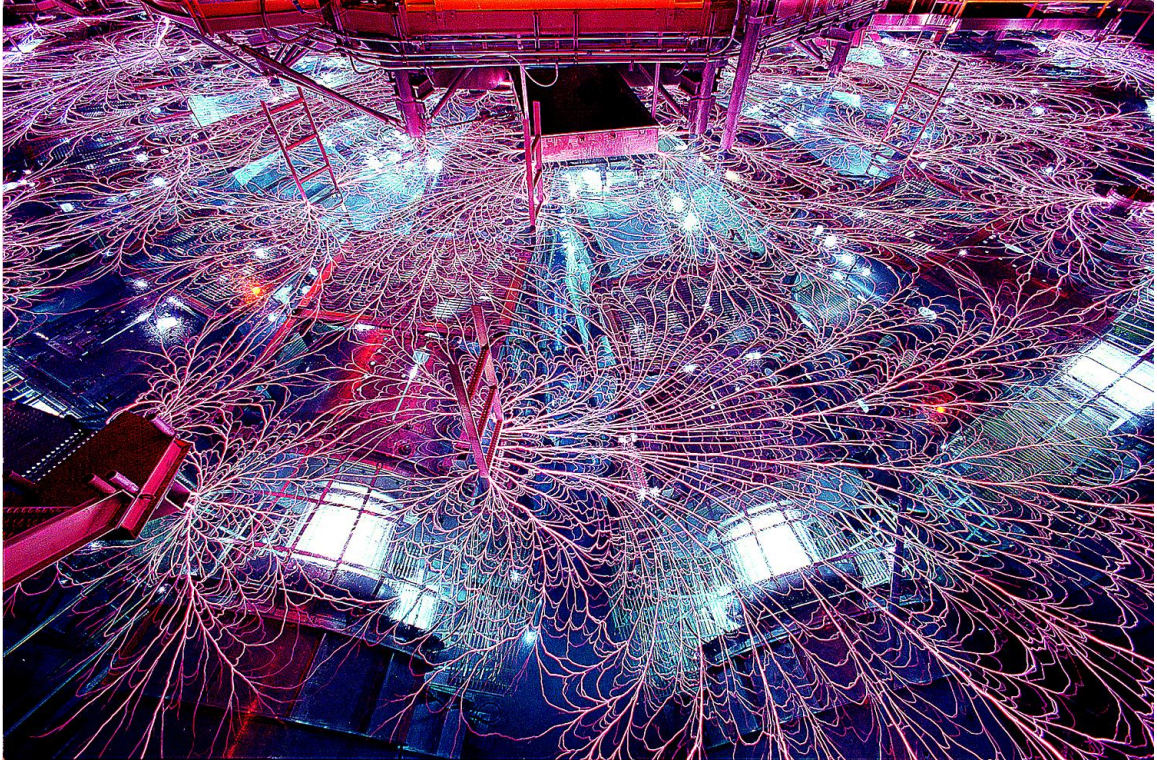


**Figure 1.8.** MagLIF experiment in Z machine at Sandia National Laboratories. Image courtesy of Randy Montoya, Sandia. All rights reserved.

In both the MagLIF and OMEGA experiments, plasmas are formed during the compression of the fusion fuel, and fluid interfaces experience HIs such as the RM (from impulsive/shock accelerations), RT (from steady accelerations), KH (from shear) instabilities, leading to hot/cold fluid mixing and degradation of the fusion yield [4–6]. The application of a magnetic field can limit/suppress the ability of HIs to develop detrimental mixing effects [7].

The newest internationally-recognized large-scale HED project that exhibits MHD–RMIs is the ITER project tokamak fusion reactor. Tokamaks prior to ITER have carried magnetic fusion reactors closer to the realm of break-even energy achievement ( $Q = 1$ ). Translating into the full ignition operational mode, ITER aims to be the world’s largest magnetic confinement plasma physics experiment, designed to produce 500 MW

of thermal output power sustained for ~20 minutes, as only 50 MW of thermal power is required to be injected into the tokamak [29]. This would yield an order of magnitude energy gain, ( $Q \approx 10$ ), should the multinational cooperative project be successful once completed and fully operational. ITER has stated that it is capable of generating magnetic fields with a flux density of up to 13 T, which is deemed enough to confine the toroidal plasma fusion reaction and yield net positive energy gain, even if HIs are initiated. Figure 1.9 shows a CGI cutout representation of the ITER core with plasma evident.



**Figure 1.9.** The ITER tokamak net-energy magnetic fusion device core. Image courtesy of ITER from Ref. [30]. All rights reserved.

Developing and performing research at each of these three large-scale research facilities requires a substantial amount of tax payer's dollars. The NIF's ICF research has accumulated over a 1.1 billion dollar financial requirement and ITER is estimated to cost upwards of 20 billion dollars once completed and operational [31, 32]. Therefore, by developing an experiment to investigate the MHD-RMI at a small-scale university laboratory, a more cost-effective aid is provided to the scientific community attempting to achieve net-positive energy yield from fusion where the MHD-RMI arises.

### 1.3 Section Outline

The remaining sections of this dissertation are divided into one minor section and two main sections, which is comprised of the research efforts performed in this dissertation. The minor section being the computational work performed; the first major section being the experimental apparatus and methods developed (*i.e.*, experimental work); and the second major section being the experimental results. The computational work presents simulations that were performed of the MHD–RMI and is examined first, as it provides assistance for understanding the goal of the dissertation research efforts. Not only do the simulations provide an idea of what the MHD–RMI experiment should look like, the results obtained were used to design various aspects of the experimental components and apparatuses the author developed. The computational work section is organized as follows: (1) a description of the CFD hydrodynamics software FLAG and input parameters used to perform simulations on the RMI in MHD, (2) the test cases implemented, which vary the magnetic field orientation, magnetic field strength, and Mach number; and (3) the results of the simulations and how they are applied to the experiments conducted in this dissertation.

The experimental work comprises the main body of research presented in this dissertation and is presented after the computational work. The experimental work routinely calls upon parameters and results presented in the computational work, specifically Section 2.5, as a way to better understand and analyze the experimental data obtained. Within the experimental work is the Experimental Apparatus and Methods Developed chapter, Chapter 3, and contains information that covers the background, theory, and design of the experimental apparatuses; as well as the methods utilized to

obtain the experimental data. Within the Experimental Results chapter, Chapter 4, is the data that was gathered and analyzed from performing the experiments themselves. The experimental apparatus and methods developed chapter is organized as follows: (1) how to generate plasma, specifically at atmospheric-pressure, and the parameters required to do so, (2) an experimental investigation on how to diagnose an atmospheric-pressure plasma, first by means of characteristics such as temperature and degree of ionization and second, through planar laser Mie scattering (PLMS) and particle image velocimetry techniques, and finally (3) the experimental development is concluded by developing the theory, and the apparatus, to qualify and quantify how a magnetic field interacts with a plasma flow field. Following the Experimental Apparatus and Methods Developed chapter is the Experimental Results chapter. The Experimental Results chapter is outlined as follows: (1) an analysis of the operating conditions which produce the optimal plasma torch, (2) the data obtained on the plasma characteristics through the development and implementation of the 2DMIM, (3) the planar laser Mie scattering (PLMS) results and negative image solid particle image velocimetry (ns-PIV) velocity field results in the  $rz$ -plane and the  $r\theta$ -plane, and finally (4) the resulting suppression and deflection effects from the interaction of the externally applied magnetic field with the plasma flow field; concludes the Experimental Results chapter.

## CHAPTER 2. COMPUTATIONAL WORK

### 2.1 MHD–RMI Simulation Motivation

Because it is the overall goal of this dissertation to supply the means to experimentally suppress the MHD–RMI, it became critical to develop simulations, prior to experimentation, to show that this goal was, in fact, achievable. Simulations provide the visual confirmation of what the MHD–RMI experiment should look like; and that it is possible to suppress the MHD–RMI. Additionally, designing a new, unique, large experimental apparatus, like the MHD–RMI shock tube experiment, requires a great deal of time and financial investment. By performing the simulations portrayed in this section, a refinement of the experimental parameters necessary to achieve the overall goal of suppressing the MHD–RMI results. Thus simulations reduce the burdens of time and cost that would otherwise be required to achieve the same outcomes, should they attempt to be completed by experimentation alone. Results from this computational work led to pinpointing major design parameters required of the plasma generating apparatus (*i.e.*, plasma torch), discussed in Section 3.2.2, as well as the magnetic field apparatus, which is discussed in Section 4.4.2. Additionally, the simulations show what the resulting PIV measurements, discussed in Section 4.3.1, should look like when executed in the full MHD–RMI shock tube experiment. Before divulging into the simulation results, a summary of the current status of computational research efforts on the MHD–RMI is presented in the next section.

## 2.2 The MHD–RMI Simulation Background

While the author of this work is unaware of any experiments performed to suppress the MHD–RMI to date, there have been several groups who have published computational results on the MHD–RMI. However, these groups have only begun publishing their efforts since the early 2000’s.

Research efforts have already established that the linear regime growth rate of the Rayleigh-Taylor instability (RTI) is mitigated at high wavenumbers in the presence of a magnetic field [33]. However, Samtaney is recognized as the first person to have investigated the effect of a magnetic field on the Richtmyer-Meshkov Instability (RMI) [34]. Samtaney demonstrated, through simulation efforts, the suppression of the inclined MHD–RMI interface’s growth [34]. The suppression of the MHD–RMI was later determined, by Wheatley *et al.*, to be a result of the changes in the interface’s shock refraction process, where the application of a magnetic field produces a vorticity-free interface [35]. Using analytical linear analysis, the stability of an impulsively accelerated, sinusoidally-perturbed, density interface, imposed on by a normal magnetic field, was also investigated by Wheatley *et al.* [36]. The results of this study were achieved by solving the linearized initial value problem (the numerical model utilized for the RMI) [36]. The work performed by Wheatley *et al.* portrayed that the initial growth rate of the perturbed interface is virtually unaffected by the presence of a magnetic field. However, in the case of a finite magnetic field, the amplitude of the interface asymptotes to a constant value, preserving the stability of the interface. The results produced from Wheatley’s *et al.* analytical analysis were in good agreement with results of both linearized and nonlinear compressible simulations [37]. Additionally, the results showed

the successful modeling of the MHD–RMI interface morphology for weak shocks and magnetic fields [37]. Alternative interface geometries, such a sinusoidal interface in: (1) planar, (2) converging cylindrical, (3) and spherical geometries, have also been examined by Wheatley *et al.* [36–38] and Mostert *et al.* [39, 40], as a continuation of Samtaney’s work [34].

Through the several articles published by these authors (and others) on their computational efforts, a full parametric study on the MHD–RMI has been accumulated. This includes: (1) the effects of the magnetic field orientation, (2) the effects of increasing magnetic field strength, (3) Atwood number effects, (4) the ratio of perturbation amplitude,  $\eta$ , to wavelength,  $\lambda$ , and (5) the effects of nondimensional number analysis such as magnetic strength number,  $\beta$ .<sup>\*</sup> The accumulation of the parametric studies’ information leads to the conclusion that Mach number  $M$ , and Atwood number  $A$ , effects are similar to those exhibited in classical hydrodynamics. However, through varying the magnetic field orientation (*i.e.*, normal or traverse relative to the interface), the MHD–RMI exhibits different qualitative evolution and morphology characteristics as well as varying suppressed growth rates. Ultimately, this compilation of simulation research concludes that increasing the strength of the magnetic field further dampens or suppresses the instability development.

---

<sup>\*</sup> Magnetic strength number is computed by  $\beta = 2p\mu_0/B^2$ , and represents the ratio of thermodynamic pressure to magnetic pressure.

The simulations presented in this computational work section are provided for three main reasons:

- (1) To aid the reader in understanding what the morphology of the MHD–RMI experiment in the FMSTL shock tube (a cylindrical interface, not examined in previous scholarly works) should look like based on ideal single fluid ideal MHD simulations.
- (2) To show how the author of this dissertation expects an externally applied magnetic field to influence the plasma flow field within the experiments performed. With magnetic field and plasma flow field experimental parameters being based on the parameters used in the simulations and the results that they provide.
- (3) What the magnetic field, plasma, and Mach number parameters need to be when executing the MHD–RMI experiment in the future through combining the experimental efforts published in this dissertation.

Because the main focus of this dissertation is on developing the experiment for suppressing the MHD–RMI in a shock tube setting, the simulations and results provided in Chapter 2 are summarized. The results are reproduced in part from Ref. [12] “Magnetohydrodynamic effects in a shock-accelerated gas cylinder” *Physical Review Fluids* **4**, 043901 (2019) to which the author of this dissertation was a co-author of the journal article published as well as the location where the full simulation results and analysis can be found. Before going into the simulation predictions of the MHD–RMI experiment, a brief discussion on the numerical software used to produce them will be presented.

### 2.3 FLAG Software Description

The 2D simulations presented in this work were performed using the fully unstructured grid mesh hydrodynamics software FLAG, developed at Los Alamos National Laboratories.\* FLAG is a multi-material, multi-physics, arbitrary Lagrangian–Eulerian (ALE) software which solves the Euler equations using a Lagrangian hydrodynamic step with mesh relaxation and remapping. A Laplacian-type smoothing relaxation algorithm is also performed during every cycle. The remapping step implements the flux corrector transport (FCT) algorithm developed by Boris and Book and achieves smoothing solutions with second-order accuracy while monotonicity at discontinuities is preserved and conservation is ensured [41]. The time step is normally second-order and uses a predictor–corrector method. FLAG currently supports multi-fluid ideal MHD equations provided in Eqs. (1.4–1.9); however, FLAG only considers conducting fluids via bulk properties and does not include resistive effects (resistivity), diffusivity, reabsorption, Hall effects, or collision effects. These effects, when included, provide greater simulation results accuracy however, are much more complex to include within the simulations and have not yet been fully implemented in FLAG. The simulations performed in FLAG utilize a Poisson solver algorithm for divergence control. Supplementary to the fact that the materials utilized in the ideal MHD simulations presented are treated as perfect conductors, FLAG additionally solves the  $\gamma$  law equation of state, where  $\gamma$  is the ratio of specific heats (*i.e.*,  $\gamma = c_p/c_v$ ), and utilizes the fluid’s internal energy  $\check{\epsilon}$  per unit volume. The equation of state is computed by Equation (2.1).

---

\* FLAG is restricted access software provided only to users who are authorized by Los Alamos National Laboratory (LANL). The simulations themselves were performed by Wolfgang J. Black, who was granted this access by LANL.

$$p = \rho(\gamma - 1)\check{e} \quad (2.1)$$

Now that the description of the hydrodynamics software FLAG has been outlined, the specific input parameters and initial conditions used to perform the computational efforts of this dissertation are presented in the following section.

## 2.4 Simulation Parameters and Initial Conditions used in FLAG

When performing simulations, one of the major parameters that need to be defined is the geometry of the physical phenomena that is to be simulated. All simulations performed herein consider a cylindrical interface geometry. This geometry was chosen because it represents the cross-sectional geometry of the atmospheric-pressure plasma torch (APPT) experimental apparatus the author constructed, discussed in Section 3.2.1. The simulated cylindrical interface utilizes a cross-sectional diameter of 2 cm. However, the interface's cross-sectional diameter that was simulated is larger than the 0.4–1.0 cm nozzle diameter of the APPT the author developed (the simulations were begun first to guide the development of this experiment). Again, the APPT experimental apparatus design will be discussed in greater detail in Section 3.2.1. The interface was treated as perfectly conducting nitrogen (*i.e.*, zero resistance to current) for the working gas and was initially set to a bulk temperature of 2,500 K. This is a temperature that was later found to be much lower than the plasma temperature achieved by the APPT, but it provides a good minimum baseline to quantify the results that could be expected in the future MHD–RMI experiment. Surrounding the nitrogen interface is perfectly conducting air at atmospheric-pressure and 300 K prior to being shocked.

**Table 2-1.** FLAG simulation initial conditions.\*

Parameter		RMI	MHD-RMI					
		$\vec{B} = \mathbf{0}$	$B_{\parallel}$			$B_{\perp}$		
$B$	(G)	0	100	250	500	100	250	500
$\beta$			2550	410	100	2550	410	100
$P_0$	(Pa)	101,325	101,325			101,325		
$T_1$	(K)	300	300			300		
$T_2$	(K)	2,500	2,500			2,500		
$\rho_{air}$	(kg·m <sup>-3</sup> )	1.12	1.12			1.12		
$\rho_{N_2}$	(kg·m <sup>-3</sup> )	0.136	0.136			0.136		
$A$		0.79	0.79			0.79		
$D_i$	(cm)	2	2			2		
$M$		1.2	1.66			2.2		
$U_{ps}$	(m s <sup>-1</sup> ) ± 1%	108	311			514		

The simulation parameters for all cases are provided in Table 2-1 and the description of each simulation test case is discussed in detail in Section 2.4.1 and Section 2.4.2.

Figure 2.1 shows an annotated pseudocolor (false color) schematic of plasma mass fraction (species two per the definition of Atwood number  $A$ ) given as,  $Y_p$ , and shows the initial configuration and conditions consistent with all simulations performed in FLAG. The initial conditions are for when time  $t = 0$ .

\* The resolution of the simulations, which utilize the information presented in Table 2-1, is 100 nodes per cm (200 nodes per cm for the diameter). Pressure, temperature, density, Atwood number, and diameter were initially held constant through these simulations.

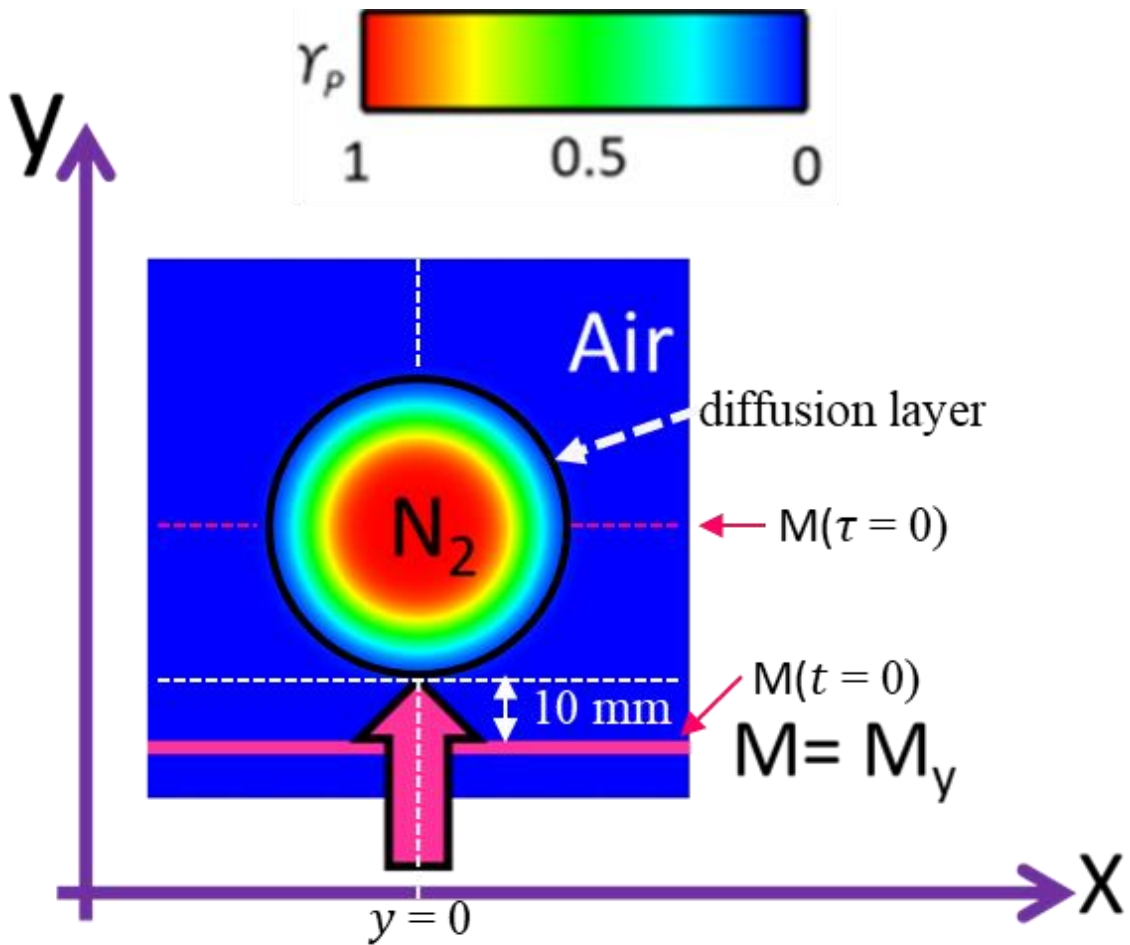


**Figure 2.1.** Two-dimensional schematic of species pseudocolor representing the initial conditions utilized in FLAG simulations at  $t = 0$ .

As shown in Figure 2.1, the computational domain is centered about  $y = 0$ . The shock wave propagates in the  $+y$ -direction and is represented as a line (pink) with the arrow (pink) showing the propagation direction of the shock wave. The magnetic field, if present, can be oriented along the  $y$ -direction (parallel) or the  $x$ -direction (perpendicular) relative to the shock transit direction.

A diffuse interface was chosen since there is a large temperature difference between the plasma interface  $T_2$  and the surrounding air  $T_1$ , (*i.e.*,  $T_2 \gg T_1$ ). This is represented in Figure 2.1 is a thin (black) line which represents the 5% plasma species

contour line; this is consistently visible in all figures presented in the results section of this chapter for comparative purposes. Not visible in Figure 2.1 are the computational boundaries in the  $x$ -direction and the  $y$ -direction where the full computational domain is a  $20\text{ cm} \times 2000\text{ cm}$  region with reflecting boundaries in both directions, respectively. These initial conditions serve as the foundation for the computations performed. The next step taken was to define the test cases used to simulate the MHD–RMI in FLAG which is presented in the following section. Within the next section, an explanation of how their parameters could be implemented in future MHD–RMI experiments is also presented.

#### 2.4.1 *Explanation of FLAG Simulation Studies Applicable to MHD–RMI Experiments*

To investigate and evaluate the effects of a prescribed magnetic field on the RMI in MHD, three simulations (studies) were performed, each with a wide range of parameters (test cases). The parameters that were altered within these simulation studies were chosen based on those that could be achieved in future MHD–RMI shock tube experiments. The three studies presented are on: (1) the magnetic field orientation, (2) the magnetic field strength, and (3) the Mach number, (*i.e.*, shock wave strength). Figure 2.2 is provided to conceptually visualize these parameters in reference to future MHD–RMI shock tube experiments. The specific details of the experimental apparatuses shown in Figure 2.2 will be discussed in much greater detail throughout the remainder of this dissertation, after the computational work section is concluded.

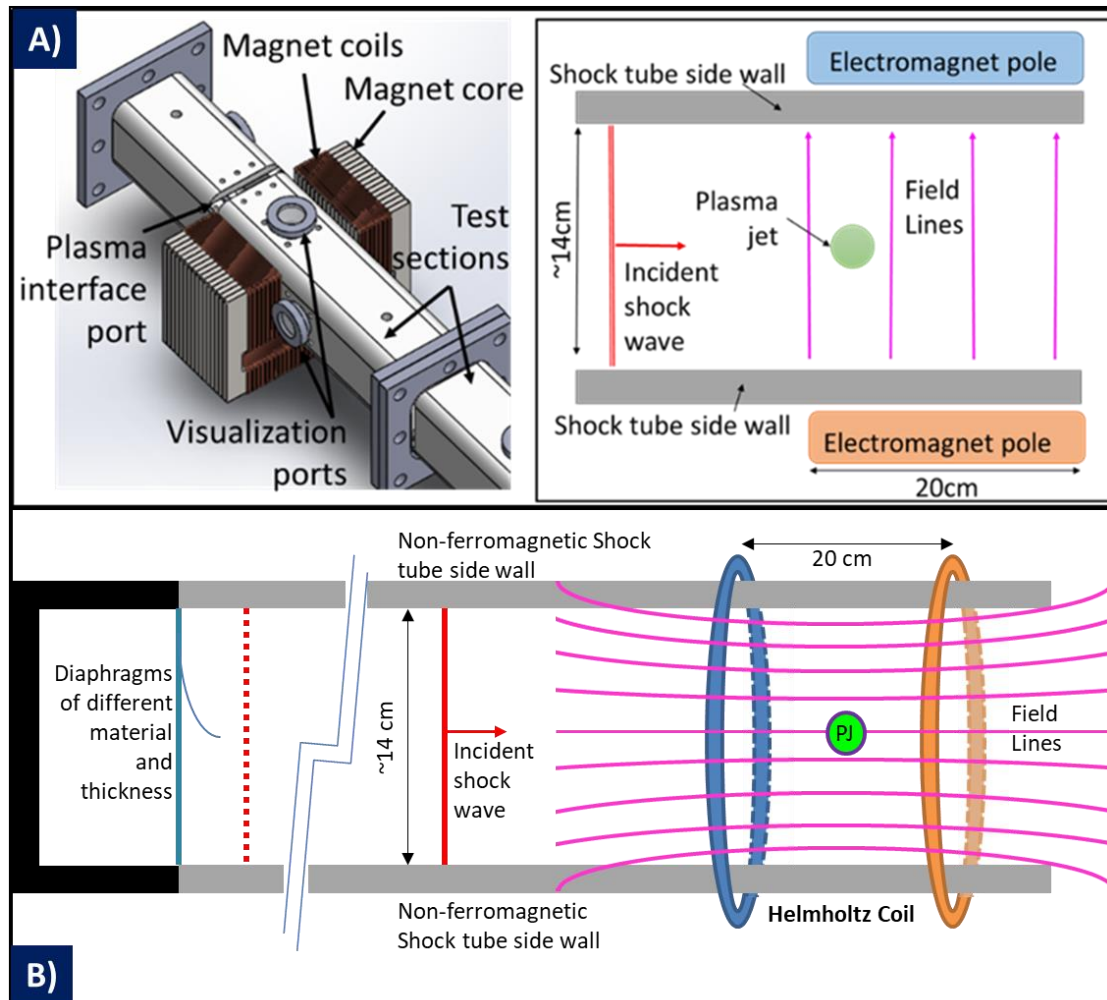


**Figure 2.2.** Concept of MHD–RMI shock tube experiment with A) the  $\vec{B}$  generated perpendicular to the shock’s transit direction, and B) the  $\vec{B}$  generated parallel to the shock wave’s direction. Interchangeable diaphragms for Mach number variation are also displayed.

The first study simulating magnetic field orientation effects can be achieved in the MHD–RMI shock tube experiment as shown in: Figure 2.2 A) using a “C” shaped iron core DC electromagnet to generate an approximately uniform magnetic field oriented perpendicular to the shock transit direction, or Figure 2.2 B) using a Helmholtz coil to generate an approximately uniform magnetic field oriented parallel to the shock wave transit direction. Both of these types of magnetic field apparatuses are capable of producing a wide range of magnetic field strengths, consistent with the second simulation

study performed. The magnetic field strength parameter range was also limited to realistic values which could be achieved by the magnetic field apparatus, discussed in Section 3.4.3. The last simulation study on Mach number utilizes realistic values achievable by the FMSTL shock tube. Mach number is considered the simplest of the three simulation studies' parameters to vary experimentally because it is the one that the author and FMSTL research group already has experience with by means of investigating shock-driven multiphase instability (SDMI) [42]. To increase the Mach number in these experiments, all that is required is to utilize a different diaphragm material or thickness, which ruptures to generate the desired shock wave Mach number. In order to understand how these three studies will affect the MHD–RMI experiment, their respective test cases and specific simulation parameters need to do so is define which is discussed in the next section.

#### 2.4.2 *FLAG Simulation Test Cases and Varied Parameter Explained*

The first study's parameter that was varied was the orientation of the magnetic field. The first test case within this study utilized  $\vec{B} = 0$  [G] (*i.e.*, the traditional RMI case), the second test case utilized a perpendicular magnetic field where  $\vec{B} = B\hat{e}_x = B_{\perp} = 500$  [G], and the third test case implemented a magnetic field parallel to the direction of the shock wave where  $\vec{B} = B\hat{e}_y = B_{\parallel} = 500$  [G]. All three test cases shared equivalent Mach numbers of  $M = 1.66$ . This Mach number was chosen since it has previously been achieved in the FMSTL shock tube while performing shock driven multiphase instability (SDMI) experiments [42]. The Atwood number for these three cases was set to  $A = 0.79$ .

The second study's parameter that was varied was the magnetic flux density, where three test cases of 100, 250, and 500 G were simulated for both magnetic field orientations. Since these values are experimentally achievable, the main reasoning behind the choice was to verify whether observable suppression effects occurred at small  $\vec{B}$  values. If suppression effects occur, then it would be possible that a strong magnetic field would not be an absolute necessity even with resistivity effects included. The Mach number and Atwood number for these test cases were kept consistent with those used the first simulation study for analysis congruency.

The final study's parameter that was varied while performing these simulations was the Mach number. Since the two previous studies focused strictly on magnetic field effects, the third study aims to analyze how the one of the hydrodynamic parameters (a variable independent of the magnetic field) can affect the evolution, morphology, and suppression of the MHD–RMI interface. For the first (base) test case on the traditional RMI, the magnetic field strength was set to  $\vec{B} = 0$  [G]. The second and third test cases set  $B_{\perp} = 500$  [G] and  $B_{\parallel} = 500$  [G] for the MHD–RMI cases, respectively. The Mach numbers utilized were  $M = 1.2, 1.66, \text{ and } 2.2$  for each of these three cases respectively; all achievable within the FMSTL shock tube. Incidentally, the post shock velocity  $U_{ps}$ , increases  $\approx 200$  [m s<sup>-1</sup>] for this range as the Mach number is increased.

The inclusion of MHD effects requires modifications to the shock jump equations due to the additional magnetic pressure term as derived and explained by Wheatley *et al.* [35]. However, the unidirectional orientation of the initial magnetic fields does not meaningfully alter the post-shock conditions: the scalar fields of pressure and

temperature vary by less than 3% from their anticipated conditions. The post-shock velocities vary even less, by less than  $\leq 2\%$ . Should the post-shock conditions be significantly altered, it would otherwise not be possible to attribute the morphological effects to the magnetic field alone. It is therefore reasonable to assume that comparing the traditional RMI simulation test case to the parallel and perpendicular MHD–RMI simulation test cases at various Mach numbers is acceptable.\* Having examined the simulation parameters that can be achieved in the MHD–RMI experiment, the next section presents the results of performing the three simulation studies.

## 2.5 Simulation Results of the MHD–RMI in FLAG

The results presented in this section provide the visual confirmation of what is expected when performing the MHD–RMI experiment. In addition to this, the results provided will be routinely called upon in the experimental work sections as they are used to inform on the design of the experimental apparatuses themselves. It is important to note that the results presented utilize a consistent and standard temporal scale across all three simulation studies and their respective test cases, as is often done in the RMI literature. This temporal scale is a dimensionless time,  $\tau$ , and computed by Equation (2.2). Dimensionless time,  $\tau$ , is a function of the variables: time,  $t$  [s], shock wave transit speed,  $w_i$  [ $\text{m s}^{-1}$ ], and the interface diameter,  $d$  [m].

$$\tau = \frac{t w_i}{d} \quad (2.2)$$

---

\* The naming convention used in the results of the studies performed follows  $M\#B_{dir}\#$ . Here,  $M$  is followed by  $\# = 1.2, 1.7, \text{ or } 2.2$  and  $B$  is followed by  $\# = 10, 25, \text{ or } 50$  for simplicity's sake.

Traditionally utilized in the denominator of Equation (2.2) is the initial interface amplitude,  $\eta_0$ , when simulating the sinusoidal RMI interface. However, in the cylindrical sense (*i.e.*, the MHD–RMI plasma interface geometry), this is replaced by the interface diameter,  $d$ ,

(*i.e.*,  $\eta_0 = d$ ). To clarify the relationship between initial time,  $t = 0$ , and when dimensionless time  $\tau = 0$ ; the shockwave’s position at initial time, is 10 mm in front of the leading edge of the interface. When dimensionless time  $\tau = 0$ , the shockwave is located at the center of the interface, in reference to the  $y$ -direction (*i.e.*, with equal distance between the leading and trailing edge of the interface) as seen in Figure 2.1. The results of the first simulation study on the magnetic field orientation, provided at dimensionless time intervals, are analyzed and presented in the following section.

### 2.5.1 Magnetic Field Orientation Simulation Results

The first simulation study results presented in this work compare the traditional RMI test case,  $M1.7B0$  to the MHD–RMI test cases,  $M1.7B_{\perp}50$ , and  $M1.7B_{\parallel}50$ . The results of the three test cases used in this simulation study are presented as a visual “matrix” of images in Figure 2.3. Specifically, there are nine pseudocolor (false color) images representing species concentration,  $Y_p$ , at  $\tau \approx 3, 7$ , and 15 {rows} for each of the three cases {columns} respectively. The three rows of images that compose Figure 2.3 are centered about the  $y$ -domain, and are respective to  $y(\tau \approx 3) = 3.11$  [cm],  $y(\tau \approx 7) = 7.64$  [cm], and  $y(\tau \approx 15) = 15.55$  [cm].

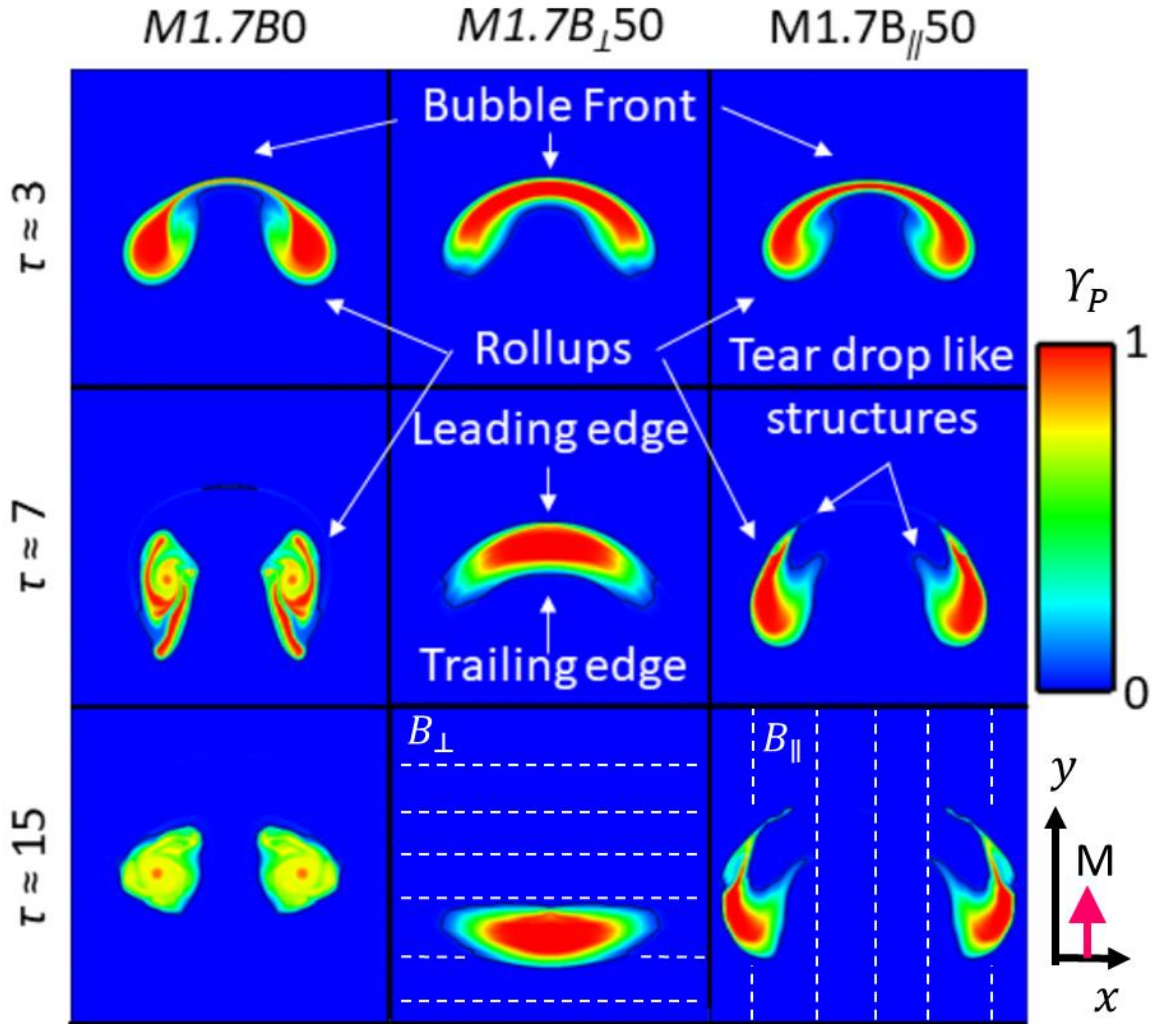


**Figure 2.3.**  $\vec{B}$  orientation study simulation results showing species concentration.<sup>§</sup>

As seen in left column of Figure 2.3, the traditional RMI case ( $M1.7B0$ ) has an interface that develops two large vortices and a thin bubble front. As time progresses, (*i.e.*,  $\tau \approx 7$ ), dissipation of the bubble front occurs and the two vortices undergo mixing. At later times, (*i.e.*,  $\tau \approx 15$ ), significant mixing has caused the pure plasma species concentration,  $Y_p = 1$ , (shown as the color red) to nearly completely diminish. The case which produced the most similar morphology to the traditional RMI was the  $M1.7B_{\parallel 50}$

<sup>§</sup> Figure reprinted with permission from “Magnetohydrodynamic effects in a shock-accelerated gas cylinder” by W. Black, R. Allen, W. Maxon, N. Denissen, J. McFarland, 2019. *Physical Fluids Review*, 4, 043901, Copyright © 2019 American Physical Society.

case, which investigated the MHD–RMI with a magnetic field parallel to the direction of the shock. As shown in the right column within Figure 2.3, early time development of this case parallels the traditional RMI case. However, the  $M1.7B_{\parallel}50$  case has a noticeable reduction in vorticity evolution and more of the pure plasma species is contained within the bubble front. As time progressed, (*i.e.*, at  $\tau \approx 7$ ), the large vortices (which are evident in the  $M1.7B_0$  case) show a reduction in fluid mixing and a larger cross sectional area in which the pure plasma species is preserved for the  $M1.7B_{\parallel}50$  case, resulting in teardrop-like structures to be formed on the interface’s leading edge. At late time, (*i.e.*, at  $\tau \approx 15$ ), the spiked teardrop-like structures are stretched as the evolution of the interface morphology continues without a significant difference or noticeable reduction in the concentration of the plasma species. This result is indicative of the reduction in the mixing of the plasma interface with the surrounding gas as the MHD–RMI evolved.

The last simulation test case analyzed was the  $M1.7B_{\perp}50$  case for the magnetic field orientation simulations. As the middle column in Figure 2.3 shows, there is a substantial difference in the interface morphology of the three test cases as time progressed. At early time, (*i.e.*, at  $\tau \approx 3$ ), the thickest bubble front on the leading edge of the  $M1.7B_{\perp}50$  interface is evident between all three cases. At mid-time, (*i.e.*, at  $\tau \approx 7$ ), evidence of vortices developing is absent; instead, there is a bubble front present that is propagating towards the trailing edge of the interface. A large concentration and localization of pure plasma species is also maintained in which nearly all fluid mixing is avoided. At late time, (*i.e.*, at  $\tau \approx 15$ ), the concave trailing edge and convex leading edge of the bubble front is inverted and the preservation of fluid mixing prevention is maintained.

The results of this simulation study's three test cases show: by altering the orientation of the magnetic field in both the parallel and perpendicular directions to the shock wave direction, a significant reduction in fluid mixing results in comparison to the traditional RMI where no magnetic field is present. Ultimately, it is the perpendicular  $M1.7B_{\perp 50}$  case that shows the best results in suppressing the evolution of the MHD-RMI between the three cases. It is precisely this result that led to developing the conceptual direct current (DC) electromagnetic device, as represented in Figure 2.2 (A), and the development of the externally applied magnetic field apparatus that was imposed perpendicular on the plasma flow field, as discussed in Section 3.4.3. By applying a magnetic field perpendicular to the shock wave transit direction within the MHD-RMI shock tube experiment; images of the interface morphology used to perform experimental PIV data acquisition should closely resemble the images shown in the middle column of Figure 2.3.

### 2.5.2 *Magnetic Field Strength Simulation Results*

It has been determined that the presence and orientation of the magnetic field ultimately affect the morphological evolution of the MHD-RMI. The next set of simulations will show how varying the strength of the initial magnetic field (increasing the magnetic flux density) controls the dispersion of the MHD waves via the Alfvén velocity. This section presents the results of increasing the magnetic field strength from 100, 250, and 500 G for both orientations of the magnetic field while keeping the Mach number constant ( $M = 1.66$ ). It was expected that utilization of a weaker magnetic field would result in the MHD-RMI's morphology to become more and more similar to the traditional RMI's and, the stronger the magnetic field strength, the more suppressed the

development of the MHD–RMI will be for both magnetic field orientations. This is attributed to the fact that vorticity is removed from the interface at a slower rate and thus the baroclinic vorticity has more time to cause mixing effects [12]. The results of this simulation parameter variation study are shown in Figure 2.4.

The analysis of the simulation results provided in this section and visualized in Figure 2.4 will be broken into three parts: (1) variation of the parallel-oriented magnetic field strength in comparison to the traditional RMI, (2) variation of the perpendicularly-oriented magnetic field strength in comparison to the traditional RMI, and (3) a comparative analysis between the two orientations; all with respect to how their morphology develops as a function of dimensionless time,  $\tau$ .

As shown by the simulation results presented in Figure 2.4 and previously discussed in Section 2.5.1, at early times,  $M1.7B_{\parallel}50$  exhibits similar vortex-like features to  $M1.7B0$ . As the magnetic field was reduced to 250 G and 100 G for the  $M1.7B_{\parallel}25$  and  $M1.7B_{\parallel}10$  cases, respectively, the morphology becomes nearly identical to  $M1.7B0$  and the bubble front shape bore closer and closer resemblance to  $M1.7B0$  at  $\tau \approx 3$ . As  $\tau$  increased, the midtime development results show more noticeable morphology effects as the magnetic field strength was reduced. The spiked teardrop-like structures that were evident in the  $M1.7B_{\parallel}50$ , are reduced in the  $M1.7B_{\parallel}25$  and  $M1.7B_{\parallel}10$  cases, in which their organization is more similar to the  $M1.7B0$  (traditional RMI) case. Specifically, the spike-like teardrop structure is not evident, but the interface development still remains more organized than the  $M1.7B0$  (traditional RMI) case.

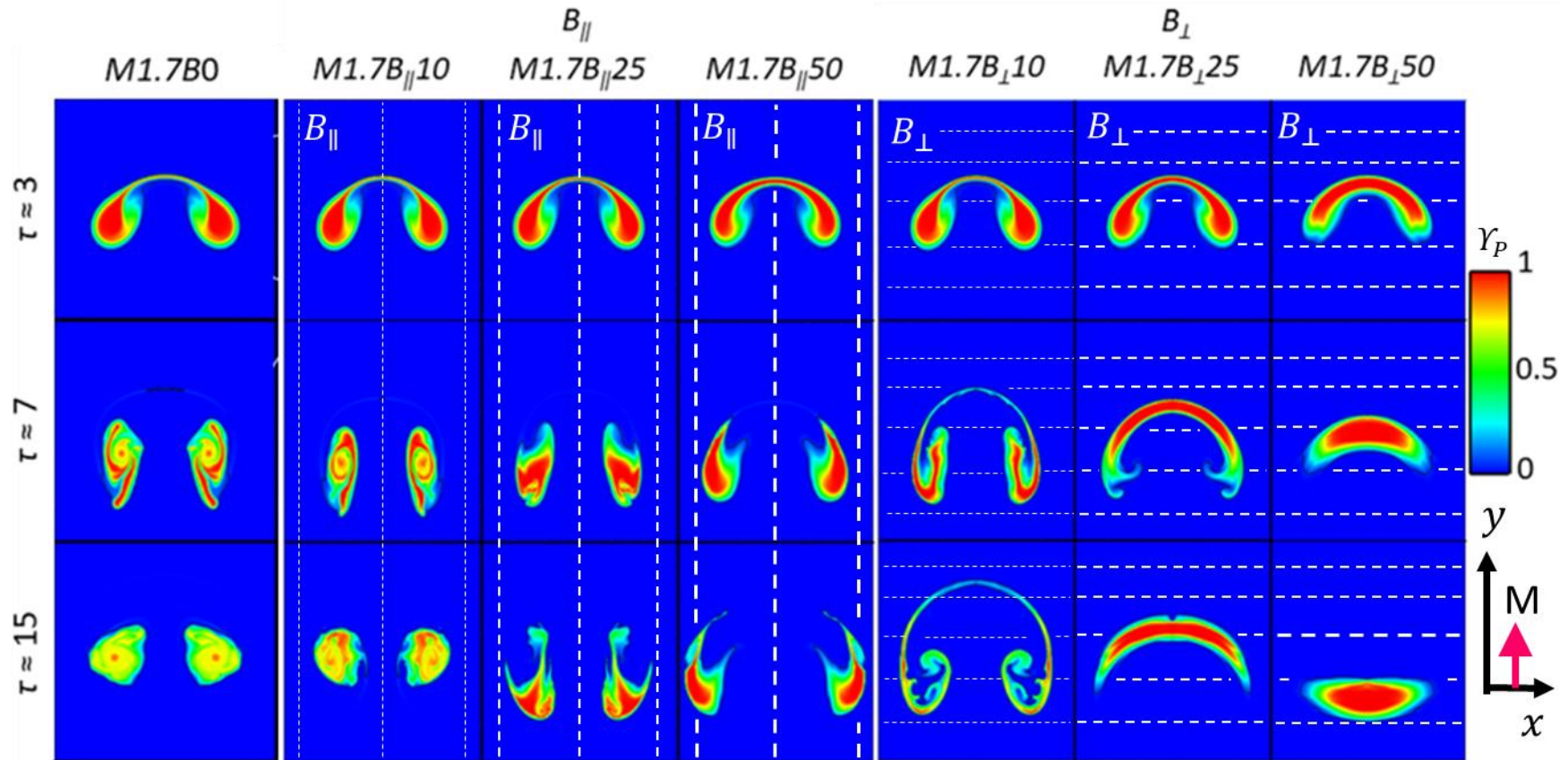


**Figure 2.4.** Magnetic field strength simulations showing species concentration,  $Y_P$ , with respect to  $\tau$ .\*

\* Figure reprinted with permission from “Magnetohydrodynamic effects in a shock-accelerated gas cylinder” by W. Black, R. Allen, W. Maxon, N. Denissen, J. McFarland, 2019. *Physical Fluids Review*, **4**, 043901, Copyright ©2019 American Physical Society.

At later time  $\tau \approx 15$ , the interface morphology remains more organized than that of the  $M1.7B0$  case, and although the evolution of the  $M1.7B_{\parallel 25}$  and  $M1.7B_{\parallel 10}$  cases show closer resemblance to the  $M1.7B0$  case, there remains a higher pure-plasma species concentration, suggesting that suppressed fluid mixing still results even at low magnetic field strengths. Again, these results are visible when comparing the parallel-oriented magnetic field simulation results shown in columns 2–4 of Figure 2.4, to the results shown in column 1 (the traditional RMI simulation results).

When comparing the results of progressively decreasing the strength of the perpendicularly-oriented magnetic field to that of the traditional RMI case, additional interesting results are found. Similar to the  $M1.7B_{\parallel}$  cases, at early times, the  $M1.7B_{\perp 50}$ ,  $M1.7B_{\perp 25}$ , and  $M1.7B_{\perp 10}$  show strong similarity to the  $M1.7B0$  case, where clear vortex features are evident and a noticeable, thin bubble front is visible. As the perpendicular magnetic field strength is decreased, the thickness of the bubble front decreases. However, the width (in the  $x$ -direction) of the interface for the three perpendicular cases remains nearly constant as magnetic field strength is reduced and is smaller than the traditional RMI  $M1.7B0$  case.

At moderate times, a thin bubble front is still evident for the  $M1.7B_{\perp 25}$  and  $M1.7B_{\perp 10}$  cases. The bubble fronts that are still visible for the perpendicular cases are not evident in the  $M1.7B0$  case. As magnetic field strength is reduced, the thickness of the bubble front is reduced at intermediate times for the  $M1.7B_{\perp 25}$  and  $M1.7B_{\perp 10}$  cases. Additionally, as the strength of the magnetic field is reduced, the thickness of the vortex

structures themselves increase (most noticeably in the  $M1.7B_{\perp}10$  case) and the length (in the  $y$ -direction) of the interface is increased.

At later times, the bubble front is still evident in all three perpendicular cases. Except for the  $M1.7B_{\perp}10$  case, the bubble front is significantly stretched out and diffuse, in which it most closely resembles the  $M1.7B_0$  case. At later times, the bubble front inversion that is apparent in the  $M1.7B_{\perp}50$  is not evident in the  $M1.7B_{\perp}25$  case. Instead, finger-like structures are formed where any evidence of vortex structures beginning to form at midtime are reduced or reversed back to a more organized state. This is likely the same mechanism that works to invert the interface for the higher magnetic field strength case, although, it is not as noticeable of a result due to a reduction of the field strength itself. The vortices structural morphologies for the perpendicular cases presented show increased thinning and greater fluid mixing as magnetic field strength is reduced. However, overall mixing and suppression of the MHD-RMI is achieved even at low magnetic field strengths for the perpendicular cases. This can be seen in columns 5–7 (perpendicularly-oriented magnetic field cases) of Figure 2.4 in comparison to columns 1 (the traditional RMI case) and 2–4 (parallel-oriented magnetic field cases).

In comparing the results of the parallel and perpendicular magnetic field cases at similar time and magnetic field strength, additional and noteworthy qualitative results are found, most of which are evident at mid- and late- development. Unlike the  $M1.7B_{\parallel}10$  cases at intermediate times, the  $M1.7B_{\perp}10$  case shows significant departure from the traditional RMI. At long times, the  $M1.7B_{\parallel}10$  case and the  $M1.7B_{\perp}10$  case are completely different from one another. The  $M1.7B_{\parallel}10$  case shows the closest

resemblance to the  $M1.7B_0$  case, where tight organizations of the vortex structures are evident. Conversely, the  $M1.7B_{\perp}10$  case has the least-organized vortex structures, and the interface appears to be a long, thin bubble front; this is completely opposite to the  $M1.7B_{\parallel}10$  case at long times. Qualitatively, fluid mixing, based on the visual decrease in pure plasma species concentration, is not able to be verified accurately on a case by case comparison. Again, further analysis of these results and other parameters are discussed in greater detail within Ref. [12].

Ultimately, the results of the magnetic field strength simulations show that mixedness is more concentrated and reduced at higher magnetic field strengths; specifically, in the perpendicular magnetic field case.\* This is attributed to the vortices being stretched and weakened by the magnetic field, which stretches the interface without leading to the interface's bubble front being broken down and the ability of the vortices to organize fully. Thus, the larger surface area of mixing in the traditional RMI case is reduced for the MHD-RMI cases, leading to a reduction in fluid mixing with the application of a magnetic field.

### 2.5.3 Mach Number Simulation Results

The previous two sections displayed the results of varying the magnetic field strength and orientation while keeping the Mach number  $M=1.66$ . The results of this study show how changing this hydrodynamic parameter affects the overall development of the interface for the MHD-RMI while keeping the magnetic field strength constant. The results are shown in comparison to the traditional RMI. Mach numbers of

---

\* Mixedness is defined as the ratio of mixing to fluid entrainment (*i.e.*, reduction in species concentration).

$M = 1.2$ ,  $M = 1.66$  (denoted 1.7), and  $M = 2.2$ , were each used to simulate both the traditional RMI, and the perpendicular MHD–RMI. Again, these Mach number was chosen since a  $M = 1.66$  shock wave has already been utilized in SDMI experiments at the FMSTL and thus would be easily replicated in MHD–RMI experiments [42]. To decrease or increase the shock wave Mach number for future MHD–RMI experiments, a simple decrease or increase in the diaphragm thickness or a different diaphragm material would be needed. Therefore, these Mach numbers were simulated because they can be achieve by the FMSTL shock tube.

Only the perpendicular magnetic field MHD–RMI was simulated because, as previously shown at high magnetic field strengths, it shows the strongest deviation from the traditional RMI resulting in greater instability suppression and reduced mixedness. Additionally, only late time development  $\tau \approx 15$  is shown because it presents: (1) the greatest deviance from the traditional RMI case, and (2) the greatest morphological development difference used to comparatively analyze the Mach number input parameter for the two orientations of the MHD–RMI magnetic field scenarios. In literature, it is common to vary the Mach number to better understand how interface evolution and morphology results due to variations in impulsive accelerations. As previously stated, Mach number provides the important pressure gradient ingredient for the RMI which is necessary to deposit baroclinic vorticity. As Richtmyer’s linear model states, the amplitude growth of the RMI instability is directly proportional to the shock jump velocity, or more simply stated, an increase in Mach number results in a stronger instability to ensue [4]. Thus the Mach numbers chosen were selected for their respective increase in shock jump velocity by  $\approx 200$  [ $\text{m s}^{-1}$ ]. Additionally, an increase in Mach

number alters the post shock conditions that influence the evolution of the interface (*e.g.*, density) and, in the case of the MHD–RMI, the resulting wave velocities. The simulation results, presented in Figure 2.5 , show not only the effect of varying the MHD parameters alone (magnetic field orientation) but also on an important traditional hydrodynamic parameter (*i.e.*, variable) which has resulting MHD consequences. Species concentration shown as pseudocolor plots (odd columns) utilize same scale which is shown above image for each three cases presented. Even columns show vorticity, are Mach number specific, and are shown below each respective group.

The pseudocolor images and vorticity plots shown in Figure 2.5 are centered about  $y$ , respective to  $M$  at:  $y(M = 1.2) = 7.60$  cm,  $y(M = 1.66) = 15.55$  cm, and  $y(M = 2.2) = 19.40$  cm. The simulation results of varying the Mach number for the traditional RMI case, shown in the top row of the species concentration and vorticity plots of Figure 2.5, exhibit classic RMI development and morphology behavior. These results compare to the results described in an extensive collection of other works on RMI. Thus, for brevity, it is only stated that as Mach number is increases, increased baroclinic vorticity is deposited unto the interface resulting in mixing occurring at a faster rate. Hence  $M2.2B0$  has an increased evolution rate which exhibits increased mixing which yields stronger vorticity than  $M1.7B0$  and even more than  $M1.2B0$  respectively. All three traditional RMI cases share similar interface organizational structure for species concentration and vorticity field at the late time presented.

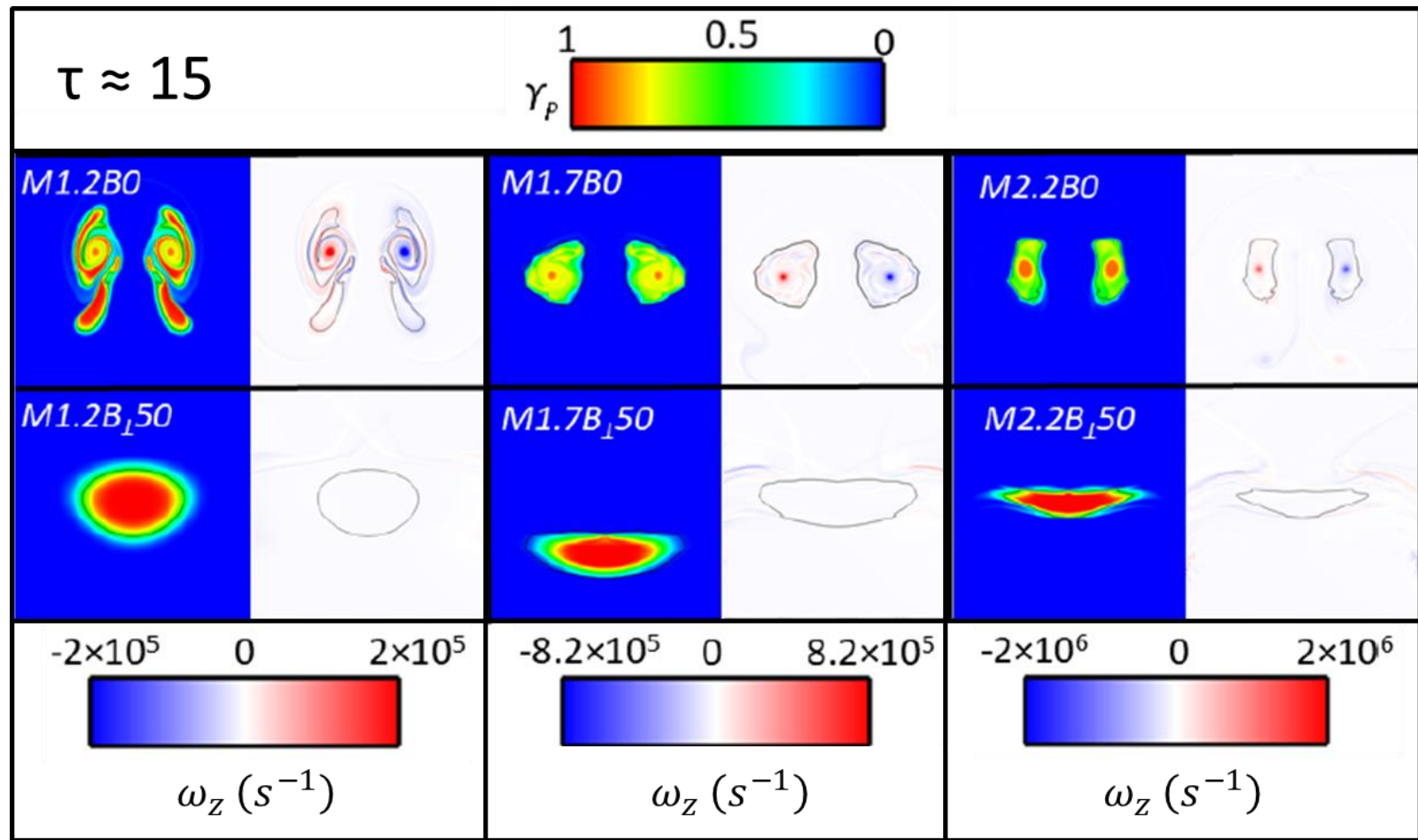


**Figure 2.5.** Late time ( $\tau \approx 15$ ) species concentration and vorticity plots for incident shock wave strength variation study from FLAG.\*

\* Figure reprinted with permission from “Magnetohydrodynamic effects in a shock-accelerated gas cylinder” by W. Black, R. Allen, W. Maxon, N. Denissen, J. McFarland, 2019. *Physical Fluids Review*, **4**, 043901, Copyright © 2019 American Physical Society.

Consideration of the late time evolution of the MHD–RMI at varying Mach numbers is shown in the second row of data present in Figure 2.5. At late time  $\tau \approx 15$ ,  $M1.2B_{\perp}50$  shows a large round interface with nearly no mixing evident. Here, the interface is lightly compressed but otherwise left undisturbed and preserves its initial geometry in comparison to its initial condition. Specifically, a thick, clear, and unmixed diffusion layer remains intact. When looking at its vortex field, shown in row 2, column 2 of Figure 2.5, almost no vorticity is evident on the surface of the interface. The extent of what vorticity is evident in this case is of negligible extent to be deemed incomparable to the magnitude of vorticity when considering the  $M1.2B0$  case’s vorticity. As Mach number is increased, the MHD–RMI interface exhibits greater compression and leads to greater mixing of the diffusion layer present. For example, considering the  $M1.7B_{\perp}50$  with respect to its lower Mach number neighbor  $M1.2B_{\perp}50$ , the interface shows a more compressed interface. In the case of the higher Mach number,  $M2.2B_{\perp}50$  case, an even more highly compressed interface which exhibits significantly less mixing is evident and bears no resemblance to its traditional RMI magnetic-field-free counterpart  $M2.2B0$  case. The vorticity field for both the  $M2.2B_{\perp}50$  and  $M1.7B_{\perp}50$  cases are similar in which they present negative and positive vorticity layers to the left and right sides of the interface and neither case shows signs of vorticity active on the interface itself.

To summarize how this has occurred, one should recount the mechanisms which work to remove vorticity from the interface which are a function of the Alfvén velocity. While the magnetic field is initialized at 500 G for these three Mach number cases, the Alfvén velocity also refers to the density of the species in its denominator. Thus two effects must be considered when analyzing the variation of the Mach number simulation

results. The first of which is the postshock density which is proportional to the Mach number. The second is the Alfvén velocity which is inversely proportional to the density. Ergo, there are two competing effects at play. Since the magnetic field is also function of the density of the conducting fluid, as shown in Equation (1.7), the Alfvén velocity then goes as  $\rho^{1/2}$ . Thus, as  $M$  increases,  $v_A$  increases as well. Increasing Mach number also results in a higher vorticity deposition on the interface. Thus at higher Mach numbers, a stronger vorticity deposition acts on the interface for a shorter amount of time. This resulted in lower mixedness resulting for the magnetic field MHD–RMI cases. Again, mixedness is the ratio of mixing to fluid entrainment. The entrainment area between the MHD–RMI cases is similar but at stronger Mach numbers, a greater  $v_A$  results, where there is less time for the vorticity to act on the interface and results in greater fluid mixing. This, paired with a smaller diffusion layer, leads to the reduction of mixing width, which in turn, leads to a decrease in mixedness. To summarize this, despite an increase in compression of the interface as Mach number was increased, the higher the Mach number, the less the mixedness resulted. Therefore, when performing the MHD–RMI experiment, to produce a more qualitatively suppressed interface, a lower Mach number should be utilized (*i.e.*, one that is visibly and noticeably different than the traditional RMI). To produce a more quantitatively suppressed interface in an MHD–RMI shock tube experiment, a stronger Mach number should be utilized.

Now that the third and final simulation study’s results have been analyzed, the following conclusion section is presented on the computational work performed on the MHD–RMI in FLAG.

## 2.6 Conclusions of the Simulation Results of the MHD–RMI in FLAG

The simulation results presented here were on the cylindrical MHD–RMI through variation of the magnetic field orientation, magnetic field strength, and incident shock wave Mach number (impulsive acceleration strength). The cylindrical interface geometry was chosen as the evolution of the interface is independent of the magnetic field orientation or the direction of the incident shock wave. Instead, the evolution was dependent only on the orientation of the shock transit direction relative to the magnetic field. The parameters of the magnetic field were chosen to explore the resulting effects on vorticity advection caused by MHD waves, and the variation of the Mach number was done so to explore how increased deposition of baroclinic vorticity effected the growth and morphology of the MHD–RMI. It was shown that interface mixing is a function of the amount of vorticity deposition (*i.e.*, the rate at which vorticity is advected), and the direction of the advection via Alfvén waves. In MHD the suppression of the RMI is evident when an externally applied magnetic field is present. This is attributed to the fact that vorticity,  $\omega$ , is advected from the interface via Alfvén waves. The orientation of the magnetic field affects the direction the Alfvén waves transport vorticity and the strength of the magnetic field affects the Alfvén velocity. Simply stated, the faster vorticity is removed from the interface, the more suppressed the RMI is which is proportional to the magnetic field strength. This result was shown for both the parallel and perpendicular cases performed. The vorticity was shown to be stretched significantly in the direction of the magnetic field. Specifically, vorticity is stretched along the magnetic field lines, along the direction of the shock wave in the parallel magnetic field case and vice versa for the perpendicular magnetic field case. Furthermore, vorticity is able to traverse the interface

more rapidly in the perpendicularly applied magnetic field case, resulting in positive and negative vorticity from opposing sides of the interface to interactively compete with one another [12].

Magnetic fields, and their respective strength and orientation, are shown to be the driving mechanism by which vorticity is transported. As the magnetic field strength was increased, so to was the suppression of the MHD–RMI interface evolution. Though analyzing the increase of magnetic field strength for both orientations, two nonobvious effects were discovered. First, there is a limit to the effectiveness of the magnetic field on the mixedness. Simply increasing the magnetic field strength did not result in significant decreases in mixedness. However, the species and vorticity fields displayed vary different morphology as magnetic field strength increased. Second, a competing effect was observed when analyzing the 100 G perpendicular field case where vorticity was unable to be removed from the interface but still resulted in significant morphological differences to be portrayed. Thus, while strong magnetic fields can be used to suppress the RMI in MHD, there may exist a regime in which magnetic fields can be utilized to redistribute vorticity through an interface, resulting in an increase in mixing. One of these scenarios would be to increase fluid mixing in the engines of hypersonic vehicles.

While the magnetic field is shown to drive the resulting MHD effects in these simulations, the Mach number effect is shown to drive the hydrodynamics. Again, for traditional RMI exploration, an increase in Mach number results in an increase of interface mixing due to the increase in baroclinic vorticity deposition. The opposite was observed however for the MHD–RMI cases presented here. The higher Mach number cases resulted in further compression of the MHD–RMI interface which lowered the

mixedness by compressing the diffusion layer (*i.e.*, area where mixing could ensue). As stronger vorticity deposition worked to compress the interface, it was ultimately advected away at higher Alfvén velocities as a result of higher postshock densities. Despite this, stronger vorticity deposition resulted in less mixing of the interface.

It is these three simulation studies, including their respective test case parameters and the resulting analysis that ensued, which (1) provided direct insight into designing the experiments performed in this dissertation, and (2) will be implemented in the future to experimentally investigate the MHD–RMI within the FMSTL at the University of Missouri. These experimental apparatus and methods developed are presented in the next chapter.

## **CHAPTER 3. EXPERIMENTAL APPARATUS AND METHODS DEVELOPED**

Developing the experiment to investigate the MHD–RMI was a challenging task due to the novelty of the application and the limited amount of published knowledge on the methods for atmospheric-pressure plasma torch construction. In the following sections, the astounding details of the designs, instrumentation, and operation of the apparatuses, used to conquer this challenge, is presented. Teddy Roosevelt once said, “Far and away, the best prize that life has to offer is a chance to work hard at hard work worth doing.” And I would add what makes hard work worth doing, is getting to do it, for the greater good of humanity. These sections also serve as a record of the over 10,000 hours of hard work, led by the author of this dissertation, with the invaluable assistance of fellow FMSTL lab members, that were undertaken to complete the development of this experiment and accomplish this very important goal.

This chapter describes the theory and design of the experimental apparatuses and diagnostics used to develop the MDH–RMI experiment to be performed in the FMSTL shock tube. A majority of the experimental work (and results) provided in this chapter, has already been published in scholarly journals [41, 42]. As discussed in the computational work Section 2.1, the development of a plasma source and the ability to manipulate its flow field by an externally applied magnetic field offers many unique advantages that are essential to achieving the overall goal of suppressing the MHD–RMI within a shock tube experiment. Specifically, the necessary parameters, outlined previously in Section 2.4, provide the means to achieve this overall goal. This chapter’s

sections are broken out as follows: (1) theoretical description, background, and design of the APPT developed, (2) how the APPT constructed by the author was characterized via the new diagnostic method developed, called the 2DMIM, and through modification of traditional PIV experimental techniques, and finally (3) the theory on how a magnetic field interacts with a plasma flow field and the corresponding apparatus developed to show deflection and suppression results. To better understand what a plasma torch is, a brief background and a short literature review on commonly used methods to generate and diagnose plasma at atmospheric pressure is presented in the following section.

### **3.1 Background on Plasma Generation**

Since the mid-1950's, plasma torches have been studied for a wide variety of applications, including material processing for surface modification, biomedical treatment for wound healing and sterilization, metallurgy, metal cutting, waste management, laser and space technology, and scientific research of plasma chemistry and physics [44]. An extensive amount of research has been performed on plasma torch devices, their design, and the conditions in which they operate under, which not only portrays their adaptive capabilities, but their unique ability to be used for a multitude of plasma related scientific, industrial, and commercial uses.

Many applications of plasma torches require that they operate at atmospheric pressure, at which it is more difficult to ionize gases due to the substantial increase in required breakdown voltage and current necessary to initiate and sustain the plasma. Previous studies on plasma torches have focused on the development and characterization of laminar atmospheric-pressure plasma torches (APPTs) and focused on issues

pertaining to optimal voltage–current (V–I) relationships, gas flow rates, and torch design parameters [45]. Understanding the roles these parameters play is imperative when developing and producing an optimal (*i.e.*, long, laminar) APPT. A comparison of plasma characteristics may be evaluated using similarity theory, in which one experimental property is used to determine the effect of others without performing additional experimentation [45, 46]. Plasma jet velocity measurements have also been taken using particle imaging methods by injecting particles into the plasma to better understand plasma flow conditions [47, 48].

A variety of optical methods has also been used to diagnose APPTs. Methods such as laser scattering techniques (LST) via Thomson, Rayleigh, and Raman scattering to obtain plasma characteristics have been performed [49, 50]. Additional methods include quantitative shadowgraphy, Schlieren imagery, spectroscopic methods, and the atomic Boltzmann method, each of which provides unique insights to various plasma characteristics such as plasma temperature [51–55]. Significant contributions to our understanding of the nature of atmospheric-pressure plasma through optical emission spectroscopic methods have been provided by Murphy [57], Haidar and Farmer [58], and Scott *et al.* [59]. These studies measured the temperature and composition of single-element or multi-element thermal plasmas by the implementation and modification of the Fowler–Milne spectroscopic method using the Abel inversion technique. Although traditionally applied to free-burning arcs, this method proves to be an excellent diagnostic for non-transferred APPTs after some modifications [59, 60]. Specific details on the diagnostic techniques developed to diagnose the APPT generated in this work, will be discussed later in Section 3.3. However, before a plasma source can be diagnosed, it must be

designed and generated. Information on how to generate an APPT is provided next in the following section.

### 3.1.1 *Generating Atmospheric-Pressure Plasma*

One method to produce a plasma, formed by ionizing a gas, is to use electrical current passed through a normally insulating fluid. This current is induced by an electric potential between two electrodes, forming a discharge. A discharge occurs due to the transfer of electrons, which in turn creates ions from the medium in which it flows, and results in the formation of plasma. To induce a discharge, a self-sustaining spark (arc) must first be generated between the electrodes, termed the anode (positive electrode) and cathode (negative electrode). The electric breakdown potential required for this spark depends on: the distance between the electrodes (electrode gap distance),  $d$  [mm], the gas pressure,  $p$  [atm], the surrounding gas breakdown constant,  $B_c$  [V atm<sup>-1</sup>m<sup>-1</sup>], the saturation ionization constant,  $A_c$  [atm<sup>-1</sup>m<sup>-1</sup>], and the secondary electron emission coefficient,  $\gamma_{se}$ .\*

This is a complex process called dielectric breakdown [43, 61]. The electric potential, or breakdown voltage,  $V_{BD}$  [V], of a gas is governed by Paschen's Law, defined in Equation (3.1).

$$V_{BD} = B_c(pd) / \left( \ln[A_c(pd)] - \ln \left[ \ln \left( 1 + \frac{1}{\gamma_{se}} \right) \right] \right) \quad (3.1)$$

---

\* The units provided here are chosen as an alternative to SI units in an effort to provide a better understanding of how Equation (3.1) is directly related to the experimental parameters of the APPT. Specifically, since the torch is operated at atmospheric pressure,  $p$  is given in [atm] and its respective electrode gap distance,  $d$  is provided in [mm].

Using Equation (3.1) and the numerical parameters specific to a particular gas, the required breakdown voltage as a function of the combined gas pressure and electrode spacing, commonly known as Paschen Curves, matches the plots shown in Figure 3.1.

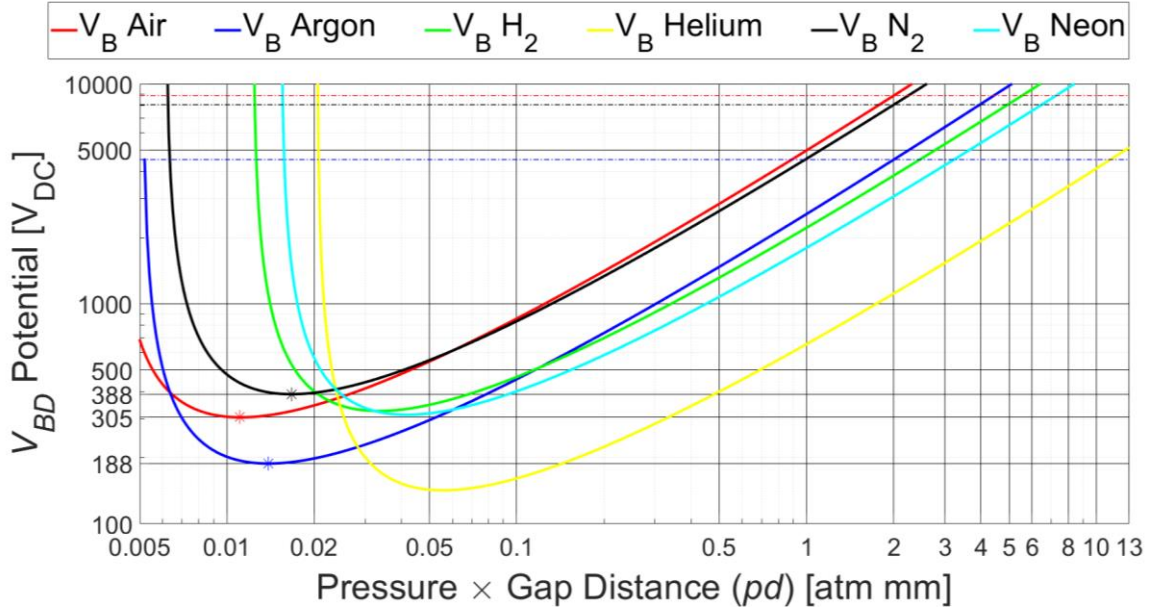


**Figure 3.1.** Paschen curves generated for various gases.

Figure 3.1 shows the minimum breakdown voltage for a specific gas at a given pressure and electrode spacing distance. The gap distance resembles the cross-sectional diameter of the interface utilized in the MHD–RMI simulations previously discussed in Section 2.4. It can be seen that the higher the pressure, or the larger the gap spacing between the electrodes, the higher the minimum breakdown voltage requirement. Once the required breakdown voltage is achieved, a spark forms. A transition from spark to arc must then be achieved. The spark-to-arc transition is achieved nearly instantaneously at atmospheric-pressure when a large current is induced between the electrodes, resulting in a self-sustaining arc discharge that ionizes the fluid and forms plasma. This electron emission process is often thermionic in nature. Thermionic emission is driven by a

current, which is supplied by a high-current DC (HCDC) power supply to the electrodes after spark formation. The voltage–current (V–I) characteristics pertaining to the regions of electric breakdown, spark formation, and arc establishment are shown in Figure 3.2.

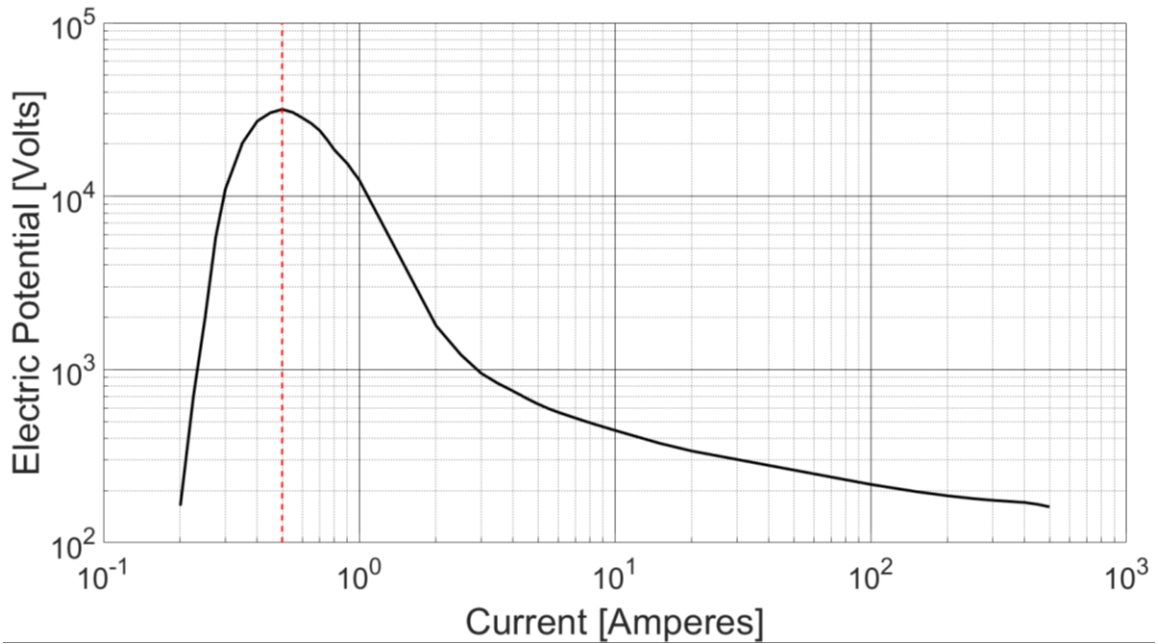


**Figure 3.2.** V–I characteristics for pre- (left of peak) and post-arc (right of peak) conditions of an atmospheric pressure plasma.

For atmospheric-pressure plasmas, the electric potential between the anode and cathode increases to the threshold value of the breakdown voltage, from the left to the peak of the curve in Figure 3.2. The working gas then becomes ionized and thus readily conducts current supplied by the HCDC power supply. Once the transition to an arc occurs, the required voltage decreases rapidly as the current increases rapidly [44].

Different methods have been used to produce atmospheric-pressure plasma, such as RF induction coils, transferred arcs (*i.e.*, free-burning arc), non-transferred arcs (*e.g.*, atmospheric-pressure plasma torches), and plasma arc heaters, all of which can be traced back to the governing conditions necessary for dielectric breakdown [44]. Because the

plasma torch developed for this work was designed to be implemented inside a shock tube, the plasma jet produced by the torch must be sustained in an unobstructed atmospheric environment and is desired to possess a minimum length of 14.5 cm (a length sufficient to cross the FMSTL's shock tube cross-section) [42]. Since non-transferred arc plasma torches provide the largest free (requiring no additional support components) plasma jet length, this method was selected for the plasma generation device. In order to generate the plasma, the operating conditions of the plasma generating apparatus must be defined. These operating conditions are defined in the next section.

### 3.1.2 Torch Operational Conditions

Many different gases and mixtures of gases have been utilized in the study of atmospheric-pressure plasmas. In particular, argon, air, helium, and oxygen have been popular choices. For the author's purposes, nitrogen is ideal due to its inherent physical properties in the ionized state. Additionally, nitrogen was the interface working gas used to perform the simulations described in Chapter 2. Nitrogen's limited and ideally located emission lines enable convenient diagnostics (discussed later in more detail in Section 3.3). For nitrogen, a breakdown potential upwards of 10kV is required at atmospheric-pressure with an electrode gap distance of 2 mm, as is needed for the APPT torch that is designed to interface well with future MHD-RMI shock tube experiments.

The voltage-current (V-I) characteristics of the torch must also be considered in the APPT's design. Many studies have been performed on atmospheric-pressure plasma torches specific to the voltage-current characteristic of the arc. Pan *et al.* examined the V-I characteristics of a laminar argon DC APPT utilizing arc voltages of 33–50 V, and

arc currents of 75–220 A [45]. Planche *et al.* implemented arc currents from 200–600 A with arc voltages of 50–80 V to investigate plasma jet velocities [48]. Das *et al.* measured the V–I characteristics of DC arc plasma utilizing arc voltages of 20–50 V and arc currents of 150–400 A [63]. It is known that as arc current increases, the arc voltage and plasma jet length also increase. Thus, an arc voltage of up to 100 V, and an arc current of up to 200 A was chosen to develop a laminar plasma jet with sufficient length to be implemented within the FMSTL shock tube for future investigation of the MHD RMI.

Of equally importance to the V–I characteristics of the arc, the gas flow rates also govern the length and stability of the plasma jet. Both axial and tangential gas flows are used in the torch to achieve laminar flow operating conditions. The tangential gas flow rotates the arc attachment around the nozzle to ensure even erosion of the anode material. Previous works used gas axial flow rates in the range of 5–27 SLM (standard liters per minute) for generating a long laminar atmospheric-pressure plasma jet [64]. Digital mass flow regulators were used to vary the ratio of axial and tangential gas flow as well as the total gas flow rate supplied to the torch.

As plasma is generated within the torch, the respective cathode and anode materials are subjected to extreme temperatures, beyond the melting point of all metals. Therefore, it is necessary to quickly remove heat from the anode and cathode components. A water cooling system can provide efficient and rapid cooling of these components, but requires additional electrical isolation considerations. Previous works utilized water cooling flow rates of 10–20 SLM while observing plasma torch electrical characteristics [45, 62]. Valincius *et al.* investigated thermal characteristics of a plasma torch finding that the temperature rise of the cathode was much smaller than that of the

anode [65]. To cool the anode and cathode, individual and electrically isolated water cooling systems were designed into the respective sections of the APPT. With the necessary parameters to be used in the APPT design provided, the following section presents the specifics of how these parameters were achieved by the APPT developed.

## **3.2 Plasma Generation Method**

### *3.2.1 Apparatus Design*

Although much research has been published on APPTs, the process of coupling a high voltage starter circuit, necessary to meet the gases minimum breakdown voltage and initiate a spark, with a high-current direct current (HCDC) power source, needed to sustain the arc, is seldom discussed. For this work, a high-voltage alternating-current (HVAC) source is used to initiate the spark since it is easy to achieve voltages of over 10 kV with AC, and the spark is only a temporary state that is unaffected by the fluctuating nature of AC. Typically, combined AC/DC signals is undesirable in electrical circuits due to fault currents arising that are harmful to the power sources and subsequent circuit components. However, the ability to transition seamlessly from spark to arc requires the integration of HVAC and HCDC signals. Thus, a custom, in-house fabricated, HVAC starter circuit was designed, developed, and constructed by the author. The HVAC starter circuit is comprised of the following major components: capacitors, resistors, an ignition coil, a spark gap switch, and a transformer. The constructed starter circuit is shown in Figure 3.3 and the corresponding circuit diagram is shown in Figure 3.4. Supplementary details on the starter circuit can be found in Appendix A.

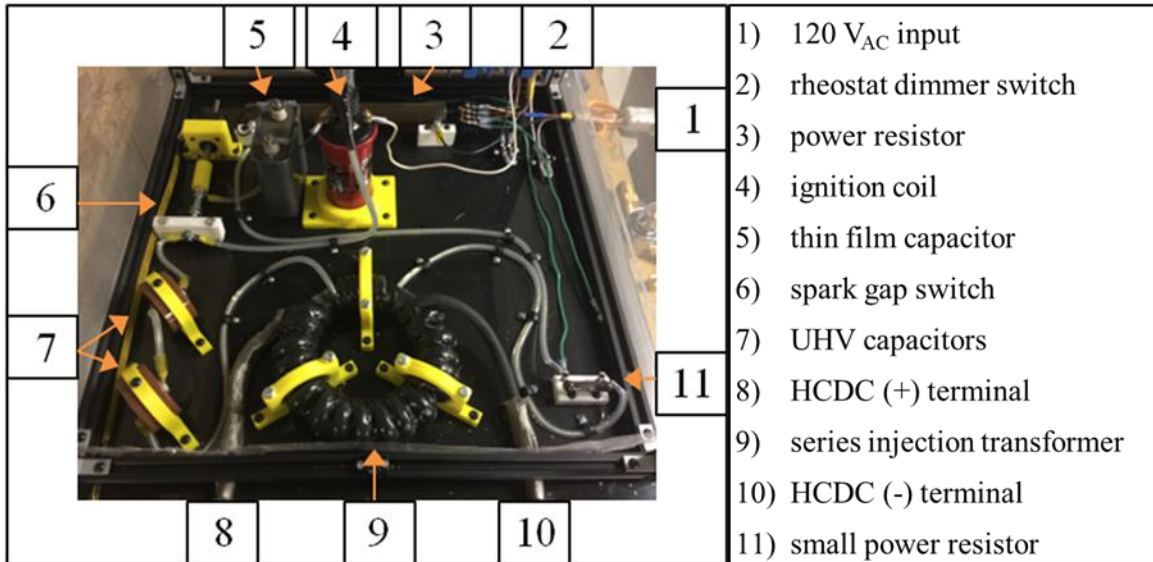


**Figure 3.3.** Custom high-voltage alternating current (HVAC) starter circuit.

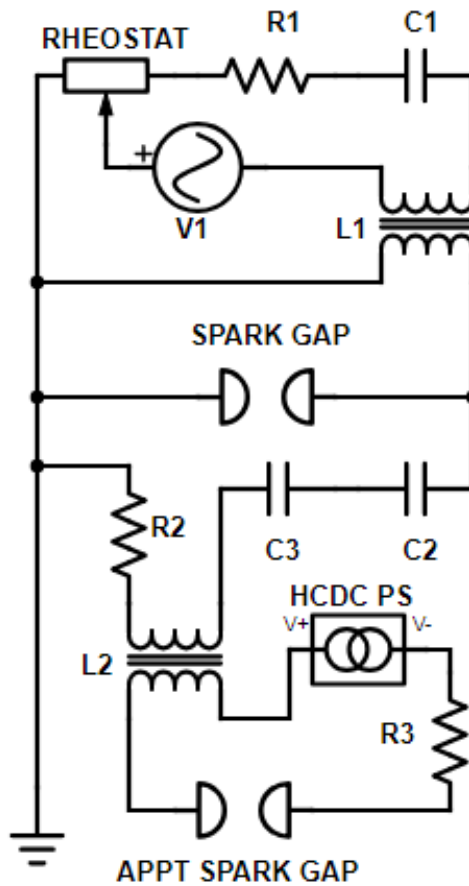


**Figure 3.4.** Circuitual schematic representing the electrical components of the custom HVAC starter circuit used to generate a spark in APPT.

To generate the spark, 120 V<sub>AC</sub> is supplied from a wall outlet, controlled by a rheostat, and is sent to a power resistor and thin film capacitor before entering an ignition coil transformer which steps up the voltage to 50 kV. The thin film capacitor is discharged into the ignition coil such that the intrinsic resistances in the discharge path reduce the capacitor discharge rate; thus, discharging into a positive resistance. Once the peak voltage of the ignition coil is achieved, the ignition coil “fires”, and a large potential between the spark gap switch is generated whilst simultaneous discharging of the ultra-high voltage (UHV) capacitors occurs. As the spark gap switch is broken down (HVAC spark induced between the spark gap switch electrodes), the UHV capacitors discharge their stored energy through the primary side of the series injection transformer (SIT) completing the circuit loop. The HVAC signal is injected to the secondary side of the SIT providing an electric potential to the anode and cathode of the torch (APPT spark gap) that is sufficient to meet the breakdown voltage within the APPT.

The use of a MetGlas™ core within the SIT was chosen because of its high magnetic permeability and extremely low core loss properties. Additionally, due to the high frequency of the starter circuit spark gap switching, UHV capacitors were implemented to help sustain the breakdown potential. The signal from the UHV capacitors is injected into the secondary side of the SIT, and therefore to the torch spark gap, resulting in a nearly instantaneous discharge since this path has little to no resistance. The capacitor’s current increases rapidly such that the current impulse is ultimately higher than conventional predictive methods allow for; thus, producing a greater degree of electrons to flow. The HCDC signal (from DC power supply) is preset to provide the desired arc current and allows the spark-to-arc transition to occur within

the torch. In essence, the HVAC signal crosses the breakdown potential initiating a spark that provides a path for current to flow from the HCDC signal creating the sustained arc within the APPT.

An Agilent Technologies N8932A, 15 kW DC autoranging power supply was used to provide, control, and vary the HCDC signal. This HCDC supply was selected based on parameters reported in previous APPT works. Pan *et al.* used an arc current of 200 A to produce a long, laminar, stable plasma jet with similar torch geometry and working gas [64]. The HCDC power supply selected can produce up to 200 VDC and 200 A. More detailed specifics on the HCDC power supply can be found in Appendix A.

To ensure the power supply would deliver 200 A to the torch during operation, water cooled power resistors (WCPRs) were implemented in series with the torch electrodes. The WCPRs themselves were selected and wired in parallel such that they were capable of handling a 200 A current with an equivalent total resistance of 0.23  $\Omega$ . The WCPRs stabilized the V–I requirements of the torch during the spark-to-arc transition where there is a sharp, instantaneous, decrease in voltage that is beyond the slew rate (change in V–I per unit time) of the HCDC power supply that would otherwise result in a low  $V_{DC}$  potential and failure of the spark-to-arc transition occurring.

Both the spark gap (in the HVAC starter circuit) and torch spark in the APPT generate large electromagnetic fields, leaving the data acquisition and torch control electronics susceptible to electromagnetic interference (EMI). To alleviate this, a Faraday cage was constructed to house the HVAC starter circuit and reduce EMI from the starter spark gap by the author. All non-HCDC supply lines were fitted with iron core electrical

chokes and grounding sheaths, and twisted wire techniques were used, where applicable, to further reduce EMI. Additionally, high-frequency high-voltage silicon rectifiers and DC electrolytic capacitors were wired in parallel with the HCDC power supply's terminals to protect it from the HVAC signal. After countless hours of refining and testing the starter circuit to render it safe and ensure its repeatability, it was deemed ready to be implemented within the overall APPT plasma generating apparatus.

As previously discussed in Section 3.1.2, and shown within the simulations initial conditions in 2.4; utilizing this starter circuit to produce atmospheric-pressure plasma, results in the generation of extremely high plasma temperatures. This is one of the many reasons why the APPT's mechanical design considerations required intricate and specific components to ensure it would be dependable and reusable within future MHD-RMI shock tube experiments. The details of these design considerations are presented in the following section.

### *3.2.2 Mechanical Design Considerations of the APPT*

When designing the plasma torch careful consideration was given to safety, repeatability, and efficiency. The major components of the torch are split into two sections, the anode (top) section and the cathode (bottom) section. The two sections were designed to be electrically isolated using alumina insulating disks. This ensured that electric breakdown occurred between the anode and cathode in the arc chamber section rather than spuriously occurring between other assembly components. As a point of safety, the entirety of the cathode section is housed inside the anode section, which is operated at the ground potential, such that during operation, only the ground potential

was physically accessible. Figure 3.5 shows a cross-sectional cutout of the torch designed by the author.

Material properties are important to arc generation and specific materials are desired for the anode and cathode components. The use of materials with low boiling points and thus higher current densities will aid in the transmission of electrons through the arc as the anode and cathode sections are heated. Additionally, materials with higher electrical resistivity result in faster material erosion rates [62]. This can be counteracted by high gas flow rates which decrease cathode erosion. A thoriated tungsten rod was used for the cathode and the anode comprised of Copper 182 alloy. The remaining components of the torch body (not in contact with the arc) were fabricated from 6061-T6 aluminum alloy by the author.

Modular sections are used in the torch to allow for efficient design modifications and repair. To optimize the plasma jet length the modular design was leveraged to test different nozzle diameters of the anode, ranging from 4–10 mm, and nozzle lengths from 15–80 mm. These geometry parameters were also selected based on the simulation results performed as discussed in Section 2.4. Additionally, the copper alloy anode components were designed as press fit inserts to the top and bottom sections of the anode. Therefore, the anode components could be replaced easily, without having to replace the entirety of the anode section as a whole, to ensure repeatable operation as erosion occurred. A supplemental discussion on repairing the APPT components can be found in Appendix B.

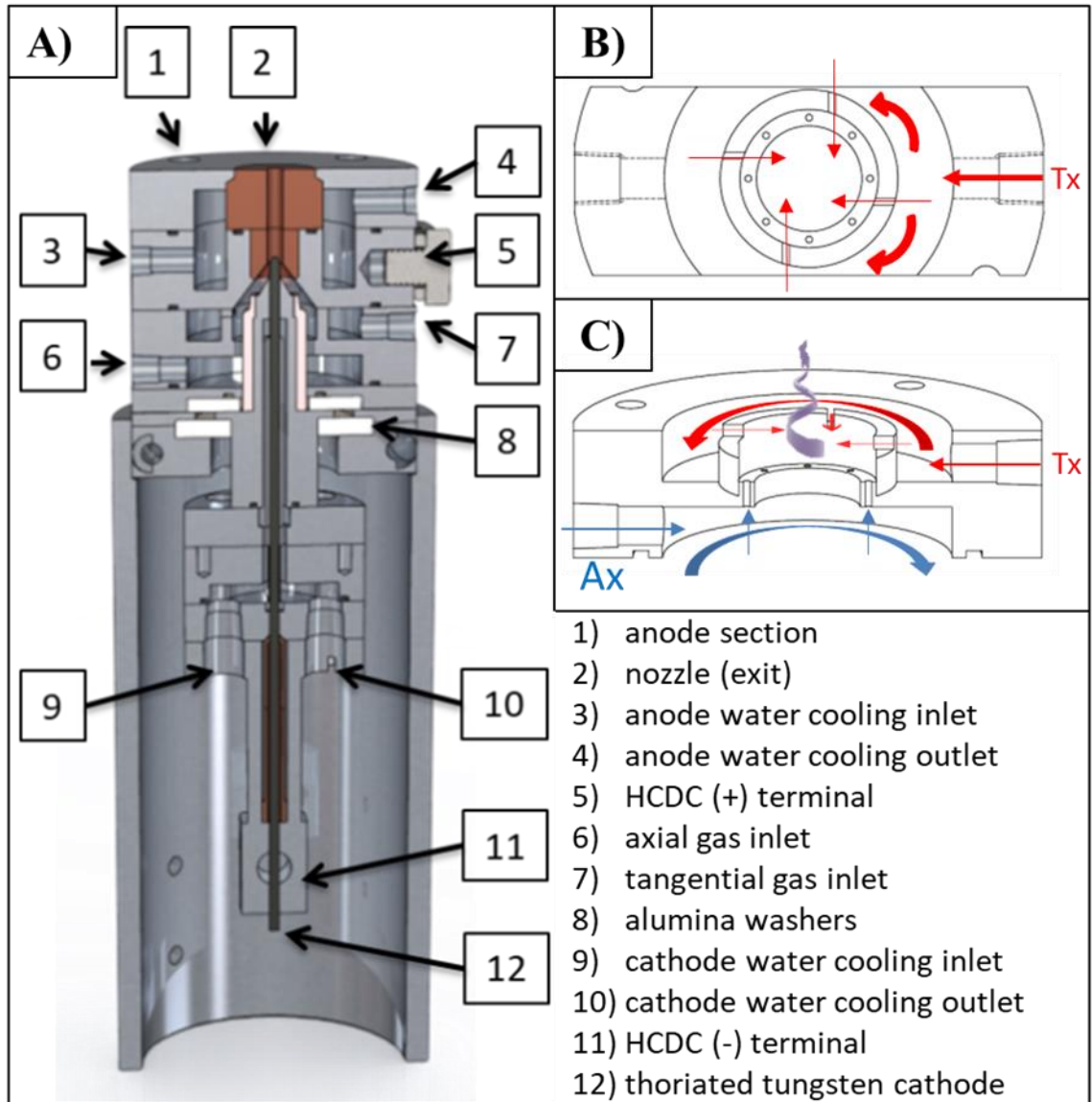


**Figure 3.5:** Image of: (A) APPT cut-out diagram, (B) top view of tangential gas component, and (C) isometric cut-out representation of axial (blue) and tangential (red) gas flow paths.

Given the large amount of heat transfer that occurs from the plasma to the anode and cathode components, it is impossible to operate the torch for long periods of time, given material limitations (*i.e.*, melting temperature), without an active cooling system. Active cooling is achieved within the APPT by water cooling loops implemented within both the anode and cathode sections. Since the anode section is driven to a ground

potential, a once-through cooling circuit is used where tap water is filtered, flowed through the anode section and dumped to a drain. The cathode section, at the HVAC or HCDC potential, requires a more sophisticated approach to cooling. An electrically isolated, closed-loop, deionized water cooling system, due to its lower electrical conductivity properties than tap water, is used to ensure that the electrical potential of the cathode is not transmitted through the water cooling loop, (*i.e.*, outside the cathode section). The selection of nitrogen as the working gas also provides additional cooling capacity, as nitrogen has a higher specific heat, due to its diatomic nature, than many other commonly used gases (*e.g.*, argon).

After much experimentation, a final torch design geometry was selected with a nozzle length of 30 mm and diameter of 4mm. For this dissertation, various gas (tangential and axial) flow rates and arc currents were tested to achieve the maximum plasma jet length by the author. A visualization aid differentiating how axial and tangential gas flow is supplied to the APPT can be seen in Figure 3.5 (b) and (c). A regiment of diagnostic techniques are discussed in the remaining sections of Chapter 3 that were used to quantify the effect on the plasma jet length and ionized region length. The most notable of the diagnostic methods presented in this dissertation was one of the author's major contributions to the scientific community; the 2D Monochromatic Imagery Method (2DMIM) which was developed by the author to estimate the degree of ionization and plasma temperature at the optimized flow conditions. Before discussing the diagnostic methods performed in this dissertation and the 2DMIM specifically, a brief background of diagnostic methods used to characterize plasma is presented first in the following section.

### 3.3 Diagnostic Methods

#### 3.3.1 Background on Plasma Diagnostic Methods

Many different diagnostic methods have been implemented to understand and characterize atmospheric-pressure plasmas over the past few decades. Each presents its own set of advantages and limitations. Invasive techniques such as Langmuir and Caloric probes have been used to accurately measure electron densities and temperatures, but are traditionally used on low pressure or low temperature plasmas [66]. These probes acquire 1D data so they must be moved through the plasma to acquire spatially measured data, and are therefore less reliable for temporally-varying plasmas. Additionally, they are intrusive and can alter the plasma flow field undesirably.

Many noninvasive techniques have been developed to overcome the disadvantages of intrusive probes. Quantitative shadowgraphy and Schlieren imaging have been used to determine the rotational temperatures of gas and visualize the hydrodynamic characteristics of plasma jets [52, 53]. Laser scattering methods (LSMs) are another type of nonintrusive optical diagnostic. LSMs have been used on atmospheric-pressure plasmas to investigate the gas temperature using Rayleigh scattering, electron temperature and electron density via Thomson scattering (TS), and molecular densities and rotational temperature by Raman scattering (RS) [52]. TS is also used to spatially and temporally resolve the electron density and energy distribution when the gas temperature is a few orders of magnitude less than the electron temperature [50]. Since atmospheric plasmas do not always operate within the laminar regime, plasma turbulence imaging has been performed using TS as well [67].

The spectroscopic determination of radial temperature distribution profiles is one of the most prevalent methods implemented for measuring atmospheric plasmas. Utilizing emission spectroscopy as a diagnostic technique is based on the observance of emitted light intensity pertaining to the spectral distribution of the plasma and is used to recover radial temperature distributions. The Fowler–Milne spectroscopic technique has been implemented by researchers such as Haddad *et al.* [68], Farmer *et al.* [69], Scott *et al.* [59], Haidar *et al.* [58], and Thornton [70], to name a few. The modified Fowler–Milne spectroscopic method can be used to determine both the composition and temperature of multi-element thermal plasmas as shown by Murphy [57]. Other methods utilizing a monochromator have been performed utilizing emission spectroscopy [71]. These non-invasive methods, however, can lack the ability to inquire space-time data instantaneously, simultaneously, or to a high degree of accuracy; radial profile temperature distributions traditionally require obtaining individual data points as a spectrometer or monochromator is incrementally swept across a plasma. This creates disadvantages similar to those of swept probes, thus data resolution is lost in both space and time. Moreover, these techniques have been traditionally implemented on free-burning arcs (transferred arcs). Therefore, the author sought to expand on these techniques to produce instantaneous 2D temperature profiles for the non-transferred APPT developed.

### 3.3.2 *The 2D Monochromatic Imagery Method*

To the authors knowledge, none of the spectroscopic methods used to diagnose and characterize an atmospheric-pressure plasma torch have attempted to fully define, in 2D, plasma characteristics such as temperature distribution, electron number density, and

degree of ionization simultaneously and instantaneously for a non-transferred thermal APPT. This was accomplished by the author for this dissertation by developing a 2D imaging technique, the 2D Monochromatic Imagery Method (2DMIM). The 2DMIM is based on a combination of monochromatic and spectroscopic techniques to measure the entirety of the plasma flow field at a single instant in time. The 2DMIM is based off the Fowler–Milne spectroscopic method and utilizes an atomic element’s total line emission coefficient to determine the radial temperature distribution profile as computed from the measured emission intensity profile produced by the APPT corresponding to axial height location.

Two components are needed to diagnose an atmospheric-pressure plasma spectroscopically. The first is to theoretically determine the total line emission coefficient of a specific emission line (wavelength) pertaining an atomic element of the working gas. The second component needed is to experimentally measure the intensity emitted by the plasma at that specific wavelength. Traditionally, intensity measurements are taken at specific spatial locations by spectrometers by scanning through a range of wavelengths. Additional points along the radial direction of the plasma are chosen and the process repeated to formulate a 1D intensity plot. Alternatively, the intensity at a specific wavelength can be measured by a monochromator as it spatially scans across one dimension of the plasma flow field. However, both methods lack the ability to be either highly spatially resolved, temporally resolved, or both. This is the foundation that the 2DMIM is built upon. By utilizing a high resolution charge-coupled device (CCD) camera affixed with a narrow bandpass filter to image a single emission line of the torch, an instantaneous 2D intensity measurement is acquired. The 2DMIM allows for a precise

depiction of the plasma flow field, with each pixel of data corresponding to the intensity of radiated light emitted from the torch both axially and radially.

As with the Fowler–Milne method, calculation of the theoretical total line emission coefficient,  $\epsilon_{nm}$ , must be performed. The emission coefficient is calculated by Equation (3.2).

$$\epsilon_{nm} = \frac{hc}{4\pi\lambda_{nm}} g_m A_{nm} \frac{n_j(T)}{Q_j(T)} \exp\left(-E_m/k_B T\right) \quad (3.2)$$

The emission coefficient relationship provided in Equation (3.2) is a function of the wavelength  $\lambda_{nm}$  [m] of the emitted radiation of species  $j$ . The wavelength of the emitted radiation species is proportional to the emission coefficient,  $\epsilon_{nm}$ , at a specific temperature  $T$  [K]. Specifically, the total line emission coefficient  $\epsilon_{nm}$  represents a transition of electrons from upper energy level  $m$  to a lower level  $n$ , where  $h$  [J s],  $c$  [m s<sup>-1</sup>],  $g_m$ ,  $A_{nm}$  [s<sup>-1</sup>],  $n_j$  [m<sup>-3</sup>],  $Q_j$ ,  $E_m$  [eV] and  $k_B$  [J K<sup>-1</sup>] are Planck's constant, the speed of light in a vacuum, the statistical weight of the upper energy level  $m$ , the spontaneous emission transitional probability from the upper to lower energy level, the number density of species  $j$ , the atomic partition function of species  $j$  [72], the excitation energy of upper level  $m$ , and Boltzmann's constant respectively. Equation (3.2) is used to calculate  $\epsilon_{nm}$  over a range of temperatures and normalized such that the maximum emission coefficient value is unity, occurring at a specific temperature deemed, the “normal temperature”. Utilization of Equation (3.2) assumes that the plasma is in local thermodynamic equilibrium (LTE) and has a maximum well-defined temperature corresponding to a peak emission coefficient. To validate the LTE

assumption and present the methods for determining the variables in Equation (3.2), the following theory is presented.

### 3.3.3 *Validity of the 2D Monochromatic Imagery Method*

Atmospheric-pressure plasmas are dominated by collisions. The fraction of energy transferred from particle to particle is dependent on the respective masses of elastically colliding particles. The more comparable the masses, the more effective the collisions (*i.e.*, the greater the energy transfer). Collisions are responsible for maintaining LTE, because it is the electrons that remove energy from the electric field and transfer it to the heavy particles, thus generating plasma. Inelastic collisions between atoms and electrons or electrons and ions govern the excitation and ionization processes as well as the respective inverse processes like recombination, de-excitation, and attachment. The energy exchange between heavy particles enforces a Maxwellian velocity distribution and results in a kinetic temperature deemed the gas temperature. The energy exchange between electrons enforces a Maxwellian velocity distribution of the electron velocities, establishing the kinetic temperature of the free electrons. Should the electron density be too low, there will be a temperature difference between the electrons or the ions due to the lack of collisions. Should the energy gain per mean free path be small in comparison to the thermal energy, both electrons and heavy gas particles obey a Maxwellian velocity distribution where the electron and heavy gas kinetic temperatures can be calculated.

The electron temperature possesses an important consequence for the excited state population of atomic (molecular) levels and the ionization (dissociation) process. A high number density of free electrons with electron temperature  $T_e$  causes the excited energy

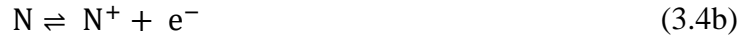
levels to follow a Boltzmann distribution, which is used in conjunction with the Saha equation to determine the ratio of the number density of heavy (neutral) particles, ions, or electrons to the total number density of all particles present as a function of temperature. Here, the ground state of the atom is included in the excitation-ionization equilibrium computations [73]. If the heavy particle gas temperature and the electron temperature are equal then the plasma is in LTE. Plasma in this state is fully described by the pressure and temperature of the gas as well as the relative concentrations of different atomic elements. For plasma with singly ionized charges present, the following equilibrium relationships are valid in conjunction with the Boltzmann and Saha equations. The equation of state (the ideal gas law) is provided in Equation (3.3). The equation of state is a function of the number density of all gaseous species, including free electrons, Boltzmann's constant, and the temperature, respectively.

$$p = n_{TOT}k_B T_e \quad (3.3)$$

The condition of net charge neutrality must also be satisfied for a plasma generated by an electrical arc.

Calculation of species composition and the degree-of-ionization profile produced by the APPT was performed for nitrogen plasma on a per-unit-volume basis by solving for equilibrium composition through minimization of the Gibbs free energy for the dissociation and first two ionization reactions. Further explanation of this procedure can be found in Ref. [74] with corresponding data presented in Ref. [75]. For nitrogen, the relevant reactions are the dissociation of molecular nitrogen ( $N_2$ ) into atomic nitrogen (N), followed by ionization into monovalent nitrogen cations ( $N^+$ ) and an electron ( $e^-$ ),

where ( $N^+$ ) is then ionized again into a divalent nitrogen cation ( $N^{2+}$ ) and an electron ( $e^-$ ), *vis.*,



Let  $\xi_a$  be the extent of dissociation, which is the number density of  $N_2$  molecules dissociated as in the reaction in Equation (3.4a). Let  $\xi_b$  be the extent of ionization, which is the number density of N atoms ionized in the reaction in Equation (3.4b). Let  $\xi_c$  be the extent of second ionization, which is the number density of ionized  $N^+$  (*i.e.*, monovalent cations) transformed to  $N^{2+}$  by the reaction in Equation (3.4c). The extents of reaction are related to changes in the amount of each species by Equation (3.5),

$$\Delta n_i = \sum_{j=a}^c \nu_i^{(j)} \xi_j . \quad (3.5)$$

The symbol  $\nu_i^{(j)}$  represents the stoichiometric coefficient of the  $i^{th}$  component in the  $j^{th}$  reaction. The stoichiometric coefficients themselves do not correspond to the numbers of moles (or number densities) of the components present, but rather their coefficients in Equation (3.4). The number density of the  $i^{th}$  component present is designated by  $n_i$ , and changes in the amount of the  $i^{th}$  component present are represented as  $\Delta n_i$ . The change in the extent of reaction  $j$  is designated as  $\xi_j$ .

The fraction of nitrogen molecules that have dissociated is quantified by the degree of dissociation,  $\alpha_d$ ,

$$\alpha_d = \frac{n_0 - n_{N_2}}{2n_0} = \frac{\xi_a}{2n_0} . \quad (3.6)$$

Here,  $\xi_a$  represents the number density of dissociated molecules of nitrogen ( $N_2$ ) and  $n_0$  represents the initial number density of  $N_2$  before any dissociation or ionization. The number density of molecular nitrogen ( $n_{N_2}$ ) is related to  $\xi_a$  and  $\alpha_d$  as shown in Equation (3.7),

$$n_{N_2} = n_0(1 - \alpha_d) = n_0 - \frac{1}{2}\xi_a . \quad (3.7)$$

Similar to  $\alpha_d$ , the degree of ionization,  $\alpha_i$ , is the ratio of monovalent nitrogen cations to neutral nitrogen atoms, that is,

$$\alpha_i = \frac{n_{N^+}}{n_N} = \frac{\xi_b - \xi_c}{\xi_a - \xi_b} . \quad (3.8)$$

Here,  $n_N$  represents the number density of atomic nitrogen (*i.e.*, number of moles of dissociated molecular nitrogen) before undergoing ionization and  $n_{N^+}$  represents the number density of monovalent nitrogen cations (*i.e.*, number density of ionized atomic nitrogen). Similarly, the second degree of ionization,  $\alpha_{2i}$ , is the ratio of divalent to monovalent nitrogen cations, that is,

$$\alpha_{2i} = \frac{n_{N^{2+}}}{n_{N^+}} = \frac{\xi_c}{\xi_b - \xi_c} . \quad (3.9)$$

Here,  $n_{N^{2+}}$  represents the number density of divalent nitrogen cations, (*i.e.*, the number density of ionized monovalent nitrogen cations). Rearranging the terms of Equations (3.6), (3.8), and (3.9) allows for the extents of reaction to be defined as functions of the degrees of dissociation, ionization, and second ionization, as well as the initial number of moles) of  $N_2$ , as in Equation (3.10).

$$\xi_a = 2\alpha_d n_0 \quad (3.10a)$$

$$\xi_b = \frac{2\alpha_d \alpha_i (1 - \alpha_{2i})}{1 - \alpha_i (1 - \alpha_{2i})} n_0 \quad (3.10b)$$

$$\xi_c = \frac{2\alpha_d \alpha_i \alpha_{2i}}{1 - \alpha_i (1 - \alpha_{2i})} n_0 \quad (3.10c)$$

Combining the dissociation, ionization, and second ionization reactions' resulting number densities, yields the total number density,  $n_{TOT}$ :

$$n_{TOT} = n_{N_2} + n_N + n_{N^+} + n_{N^{2+}} + n_{e^-} = n_0 - \frac{1}{2}\xi_a + \xi_b + \xi_c \quad (3.11)$$

The number densities of all respective species within the dissociation, ionization, and second ionization processes are then utilized to compute the mole fractions of each component. The mole fractions for each of the species are provided by Equation (3.12). The symbols  $Y_{N_2}$ ,  $Y_N$ ,  $Y_{N^+}$ ,  $Y_{N^{2+}}$ , and  $Y_{e^-}$ , are the mole fractions of molecular nitrogen, atomic nitrogen, monovalent nitrogen cations, divalent nitrogen cations, and electrons, respectively.

$$\begin{aligned}
Y_{\text{N}_2} &= \frac{n_{\text{N}_2}}{n_{\text{TOT}}} & Y_{\text{N}} &= \frac{n_{\text{N}}}{n_{\text{TOT}}} \\
Y_{\text{N}^+} &= \frac{n_{\text{N}^+}}{n_{\text{TOT}}} & Y_{\text{N}^{2+}} &= \frac{n_{\text{N}^{2+}}}{n_{\text{TOT}}}
\end{aligned} \tag{3.12}$$

$$Y_{\text{e}^-} = \frac{\sum n_{\text{e}^-}}{n_{\text{TOT}}} = \frac{\xi_b + \xi_c}{n_0 - \frac{1}{2}\xi_a + \xi_b + \xi_c}$$

The equilibrium composition can be determined using the equilibrium constants of all three reactions simultaneously. Equilibrium constants are used to compute the extents of the reaction, which are in turn used to determine the mole fractions. The equilibrium constant,  $K_j$ , of the  $j^{\text{th}}$  reaction is given by Equation (3.13),

$$K_j = \exp\left(\frac{-\Delta G_j^\circ}{R T}\right) = \prod_i a_i^{v_i^{(j)}} \ , \tag{3.13}$$

where  $\Delta G_j^\circ$  [J mol<sup>-1</sup>] is the standard Gibbs free energy of reaction  $j$ ,  $R$  [J mol<sup>-1</sup> K<sup>-1</sup>] is the universal gas constant, and  $T$  [K] is the temperature. The standard Gibbs free energy of reaction  $j$  is related to the standard Gibbs free energy of formation,  $G_i^\circ$ , of each species by

$$\Delta G_j^\circ = \sum_i v_i^{(j)} G_i^\circ \ . \tag{3.14}$$

The chemical potential,  $\mu_i$  [J mol<sup>-1</sup>] is related to the standard Gibbs free energy of formation, the thermodynamic activity,  $a_i$ , of the  $i^{\text{th}}$  component,

$$\mu_i = G_i^\circ + RT \ln a_i \quad . \quad (3.15)$$

Equation (3.13) holds true because of the relationship between the activity,  $a_i$ , and the chemical potential,  $\mu_i$  in Equation (3.15) and the reaction equilibrium criterion shown in Equation (3.16).

$$\sum_i \mu_i \nu_i^{(j)} = 0 \quad (3.16)$$

Equation (3.16) provides a relationship among the chemical potentials of a given reaction's species when the reaction is at equilibrium. The manner in which equilibrium is attained is of little importance. The thermodynamic activity,  $a_i$ , of component  $i$ , shown in Equation (3.17), is the ratio of the fugacity of component  $i$  in the mixture,  $\hat{f}_i$ , to the fugacity of component  $i$  in the standard state,  $f_i^\circ$ ; for gases, the standard state is the pure ideal gas at standard pressure ( $p^\circ$ ).

$$a_i = \frac{\hat{f}_i}{f_i^\circ} = \frac{Y_i \hat{\phi}_i p}{p^\circ} \quad (3.17)$$

The dimensionless fugacity coefficient,  $\hat{\phi}_i$ , of species  $i$  represents deviations from an ideal gas mixture.

Therefore, the extents of reaction defined in Equation (3.10), used to compute the mole fractions defined in Equation (3.12), are computed using the respective equilibrium constants for the dissociation ( $K_a$ ), ionization ( $K_b$ ), and second ionization ( $K_c$ ) reactions, as shown in Equations (3.18)–(3.20).

$$K_a = \exp\left(-\frac{\Delta G_a^\circ(T)}{R T}\right) = \frac{a_N}{a_{N_2}^{\frac{1}{2}}} = \frac{\xi_a - \xi_b}{\left(n_0 - \frac{1}{2}\xi_a\right)\left(n_{tot}^{\frac{1}{2}}\right)} \left(\frac{p}{p^\circ}\right)^{\frac{1}{2}} \left(\frac{\hat{\phi}_N}{\hat{\phi}_{N_2}^{\frac{1}{2}}}\right) \quad (3.18)$$

$$K_b = \exp\left(-\frac{\Delta G_b^\circ(T)}{R T}\right) = \frac{a_{N^+}a_{e^-}}{a_N} = \frac{\xi_b^2 - \xi_c^2}{(\xi_a - \xi_b)(n_{tot})} \left(\frac{p}{p^\circ}\right) \left(\frac{\hat{\phi}_{N^+}\hat{\phi}_{e^-}}{\hat{\phi}_N}\right) \quad (3.19)$$

$$K_c = \exp\left(-\frac{\Delta G_c^\circ(T)}{R T}\right) = \frac{a_{N^{2+}}a_{e^-}}{a_{N^+}} = \frac{\xi_c(\xi_b + \xi_c)}{(\xi_b - \xi_c)(n_{tot})} \left(\frac{p}{p^\circ}\right) \left(\frac{\hat{\phi}_{N^{2+}}\hat{\phi}_{e^-}}{\hat{\phi}_{N^+}}\right) \quad (3.20)$$

The assumption that the reacting species in Equation (3.4) behave like an ideal gas mixture is reasonable for this particular situation because the potential energy of the ions is much less than their kinetic energy (*i.e.*,  $PE \ll KE$  for intermolecular interactions). Additionally, because the plasma torch was operated at atmospheric pressure (*i.e.*, at  $p \approx p^\circ$ ), the pressure terms in Equation (3.17) are at unity.\*

Thus, three Equations, (3.18), (3.19), and (3.20), and three unknowns (extents of reaction),  $\xi_a$ ,  $\xi_b$ , and  $\xi_c$ , are simultaneously solved to compute the degrees of dissociation  $\alpha_d$ , ionization  $\alpha_i$ , and second ionization  $\alpha_{2i}$ , as a function of temperature  $T$ . The extents of reaction also allow us to find the number density,  $n_i$ , of each species and their mole fractions as a function of temperature. With the number densities computed for each species, they are utilized in Equation (3.2) as the final component to solve for the total line emission coefficient value,  $\epsilon_{nm}$ , vs. temperature,  $T$ .

---

\* The FMSTL in Columbia, MO is at an altitude above sea level = 231 m. This equates to an atmospheric pressure of 98,633.2 Pa or 0.986 bar. This average is sufficient to justify  $p \approx p^\circ$  in Equation (3.17) and allowing them to be ignored.

These equations together are a mathematical model for computation of the total line emission coefficient profile used for spectroscopic diagnosis of atmospheric pressure plasmas. As is evident in this section's discussion, computing the equilibrium mole fractions of the species concentrations alone is a complex process. Although some of the parameters in Equations (3.2) and (3.18)–(3.20) have been calculated [75], they are provided at large intervals between values (*e.g.*,  $T = 1000$  K intervals). Intermediate values were generated at much smaller (1 K) temperature intervals via a shape-preserving piecewise function using the Piecewise Cubic Hermite Interpolating Polynomial (PCHIP) function in MATLAB's curve fitting toolbox. The result of doing so is provided in Section 4.2.

With the first component (*i.e.*, the computed theoretical line emission component) needed to perform the 2DMIM described, the following section presents the second component, the experimentally-acquired emission coefficient component, required to perform the 2DMIM.

### 3.3.4 *Experimental Requirement of the 2D Monochromatic Imagery Method*

The second component needed to diagnose plasma spectroscopically via the 2DMIM is the measurement of the intensity profile produced by the plasma. The 2D, chord-integrated intensity profile is experimentally measured in the  $xy$ -plane using a charge-coupled device (CCD) camera. This profile is used to determine the normalized emission coefficient in the  $rz$ -plane by performing an Abel inversion. In this process, the measured chord-integrated intensity ( $xy$ -plane) is transformed into the radial distribution function of the emission coefficient. This process assumes that the plasma is optically

thin, rotationally symmetric, and that the emitted radiation is isotropic; thus, no absorption occurs within the plasma. Abel inversion recovers three-dimensional data from the measured chord-integrated two-dimensional data. Figure 3.6 illustrates the Abel inversion and relevant variables.

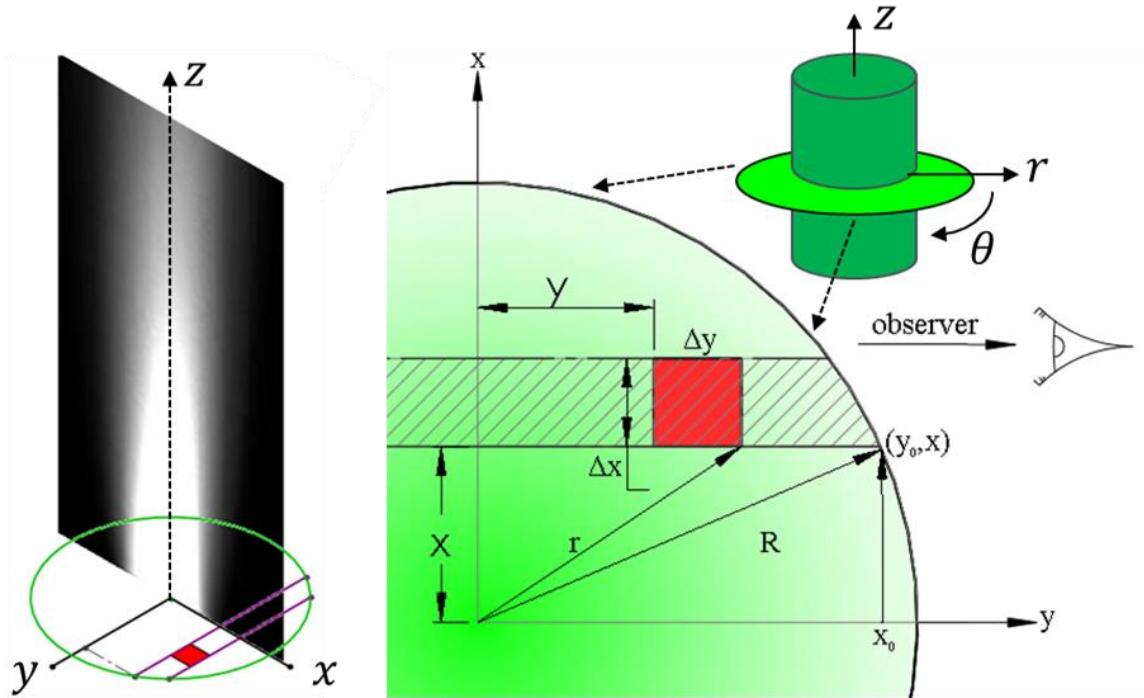


**Figure 3.6.** Diagram for converting radial intensity to radial emissivity for axisymmetric cylindrical plasma source via Abel Inversion.

The chord-integrated intensity,  $I(x)$ , must be expressed as a continuous function as,

$$I(x) = 2 \int_x^R \frac{\epsilon(r)r}{\sqrt{r^2 - x^2}} dr, \quad (3.21)$$

which is analytically inverted to obtain the radial emission coefficient,  $\epsilon(r)$ ,

$$\epsilon(r) = -\frac{1}{\pi} \int_r^R \frac{I'(x)}{\sqrt{x^2 - r^2}} dx. \quad (3.22)$$

Once the radial emission coefficient is recovered from the intensity data, it is then normalized. Various methods to recover the radial emission profile from the 2D intensity data have been performed, including curve fitting and Fourier transform methods [76]. These methods can result in considerable fitting errors and inaccuracies. Because it is the goal of the 2DMIM to recover a 2D  $rz$ -profile of the emission from the APPT, the method incorporated Abel inversion through generation of an upper triangular area matrix constructed by geometric relationships, as developed by Cho *et al.* [77]. This method allows for traditional Abel inversion fitting errors and inaccuracies to be forgone. The matrix, given in Equation (3.23), shows how the emissivity profile is recovered from each row of pixel intensity data gathered by the CCD camera:

$$\left[ \begin{pmatrix} S_{11} & S_{12} & \cdots & S_{1n} \\ 0 & S_{22} & \cdots & S_{2n} \\ \vdots & \vdots & \ddots & \vdots \\ 0 & 0 & \cdots & S_{nn} \end{pmatrix} \right] \begin{bmatrix} \epsilon_1 \\ \epsilon_2 \\ \vdots \\ \epsilon_n \end{bmatrix} = \frac{d}{2} \begin{bmatrix} I_1 \\ I_2 \\ \vdots \\ I_n \end{bmatrix} \quad (3.23)$$

As a visual representation of the variables used in Equation (3.23), Figure 3.7 is provided.

With the normalized radial distribution of emission coefficient per row of pixel data, and the theoretical line emission coefficient vs. temperature profile computed, 2D spectroscopic measurements of temperature can be made.

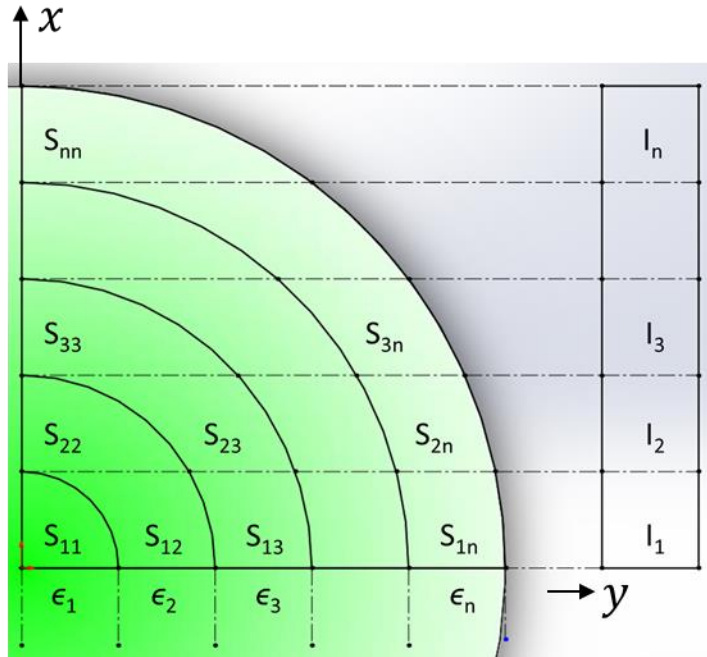


**Figure 3.7.** Visualization of variables in Equation (3.23) used for Abel transformation.

Careful considerations must be taken into account when utilizing the measured emission profile of an APPT for deriving temperature. For an atmospheric-pressure plasma in local thermodynamic equilibrium (LTE), the spectral line intensity increases initially with an increase in temperature. This is a result of the increase in number density of atoms making transitions to the upper energy state. As the plasma continues to ionize and expand, the number density then decreases. This is governed by the balance of the number density,  $n_j(T)$ , term and the temperature,  $T$ , term in the exponent of Equation (3.2). That is, as temperature continues to increase and the gas achieves a higher degree of ionization, there is a reduction in the theoretical line emission coefficient as the gas continues to ionize. This results in a peak in the total line emission coefficient profile corresponding to the normal temperature and provides a point where the curve of the experimentally-determined normalized emission coefficient passes through a maximum (*i.e.*,  $\epsilon_{nm}'(T) = \epsilon'(r) = 0$ ). For the case of free-burning arcs, the plasma temperature on

the arc axis exceeds this normal temperature. Therefore, experimentally determined emission coefficients can be calibrated to temperature using a point at the normal temperature.

For non-transferred APPTs, however, the normal temperature occurs very near the plasma torch body and is difficult to measure optically. The maximum temperature occurs at the center axis for much of the observable torch length and does not satisfy the off-axis criterion for the Fowler–Milne technique. To overcome this, the non-transferred APPT was temporarily converted into a transferred arc plasma apparatus to allow optical measurement of the normal temperature. This allowed the imaging system to be calibrated against this intensity value (radial emission coefficient), and for the temperature to be determined (see Section 4.2 for further explanation).

To validate the correlation between the data of the experimentally-acquired emission coefficient in the  $rz$ -plane and the theoretically computed emission coefficient values using Equation (3.2), observation of the plasma emitting photons at the respective theoretical emission wavelength must be achieved. Observation of these wavelengths emitted by the plasma implies that a known energy transition, from an upper to a lower energy state, is occurring as a result of the ionized plasma undergoing diffusion, recombination, and de-excitation, resulting in the emission of photons. It is this energy transition and photon emission process that connects the intensity values emitted by the plasma at a specific wavelength to the corresponding temperature relationship governed by Equations (3.2)–(3.23).

To determine the best wavelength to use for the 2DMIM, the emission line spectral distribution intensity plot, shown in Figure 3.8, was generated from the tabulated values from the NIST for singly and doubly ionized nitrogen [78]. To measure a single wavelength from the spectral distribution of the APPT, all other line emissions must be filtered out. Thus the line must be completely isolated to ensure that the emission coefficient is not influenced by neighboring emission lines (either singly-ionized or doubly-ionized emission lines). From Figure 3.8, the 528.12 nm line from singly-ionized nitrogen plasma is a good choice based on its spectral isolation. The closest neighboring emission lines are for doubly ionized plasma and are sufficiently far away (~20 nm) to be eliminated by optical bandpass filters. The 528.12 nm line corresponds to the transition ( $2s^22p^2(^3P)4p$  [13.2709 eV]  $\rightarrow$   $2s2p^4$  [10.9239 eV]) with a transition probability of  $A_{nm} = 0.00245 \times 10^{-8} \text{ s}^{-1}$  and an oscillator strength  $f_{mn}$  of 0.00103.

Other authors implementing the Fowler–Milne spectroscopic technique have used the 746.83 nm line for nitrogen while performing temperature measurements for free burning arcs [58]. Performing the spectroscopic techniques described here proves to be more difficult if examining the 528.12 nm line compared to the 746.83 nm line. This can be attributed to the fact that the 746.83 nm emission line has decreased upper energy state [11.99 eV] and lower energy state [10.33 eV] quantities and that the respective energy states' difference is less than that for the 528.12 nm line (1.66 eV vs. 2.35 eV). Additionally, the transition probability and oscillator strength is greater for the 746.83 nm line, ( $A_{nm} = 0.196 \times 10^{-8} \text{ s}^{-1}$ ,  $f_{mn} = 0.109$ ), than for the 528.12 nm line.

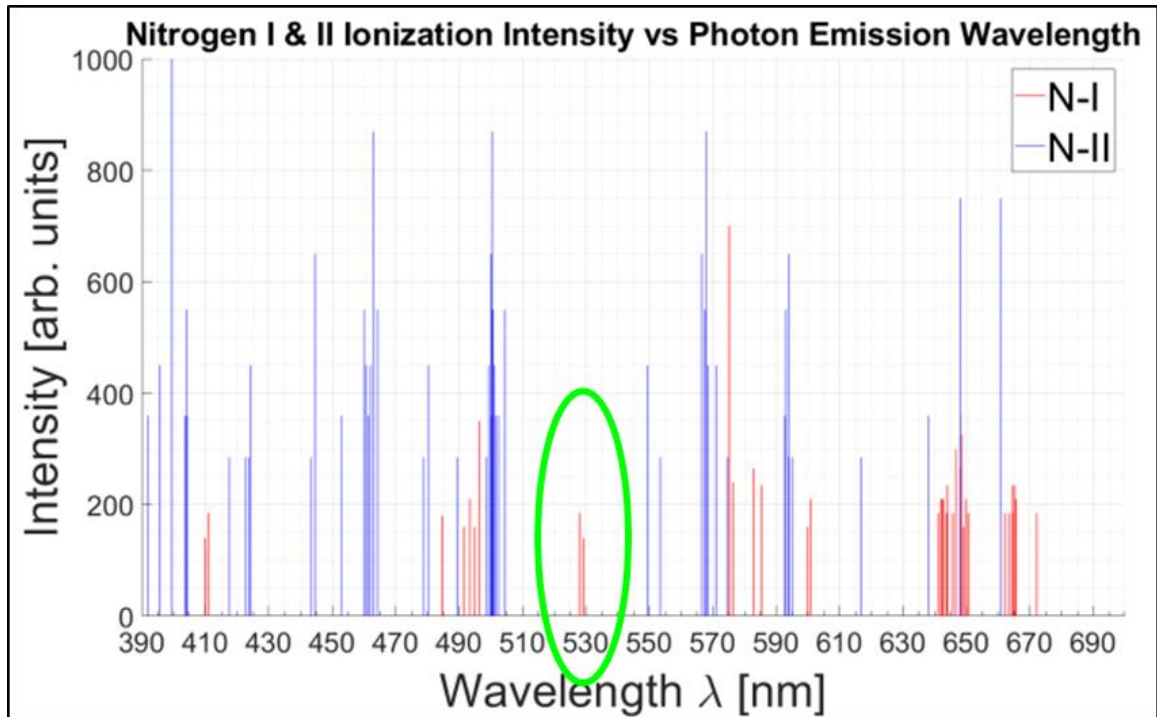


**Figure 3.8.** N-I and N-II nitrogen line emissions wavelength vs. intensity profile.

Although the 528.12 nm line appears to be well isolated from all other N-I (dissociated nitrogen) lines and N-II (singly ionized nitrogen) lines, emissions from other elements may be present near these lines that are utilized in the APPT. Thus the need to verify the actual spectrum of emissions from the APPT is a must. The emission spectrum produced by the APPT, taken by a spectrometer, can be seen in Figure 3.9.

However, due to the need to image both the plasma emissions and 532 nm laser illuminated particles simultaneously (within one filtered image) and the availability of sufficient (center wavelength and bandwidth) bandpass filters, the 528.12 nm line was chosen by the author. The final necessity that needs to be addressed to perform spectroscopic investigation of plasma is that the plasma must be considered optically thin (*i.e.*, that plasma-emitted blackbody radiation is not absorbed by the plasma).

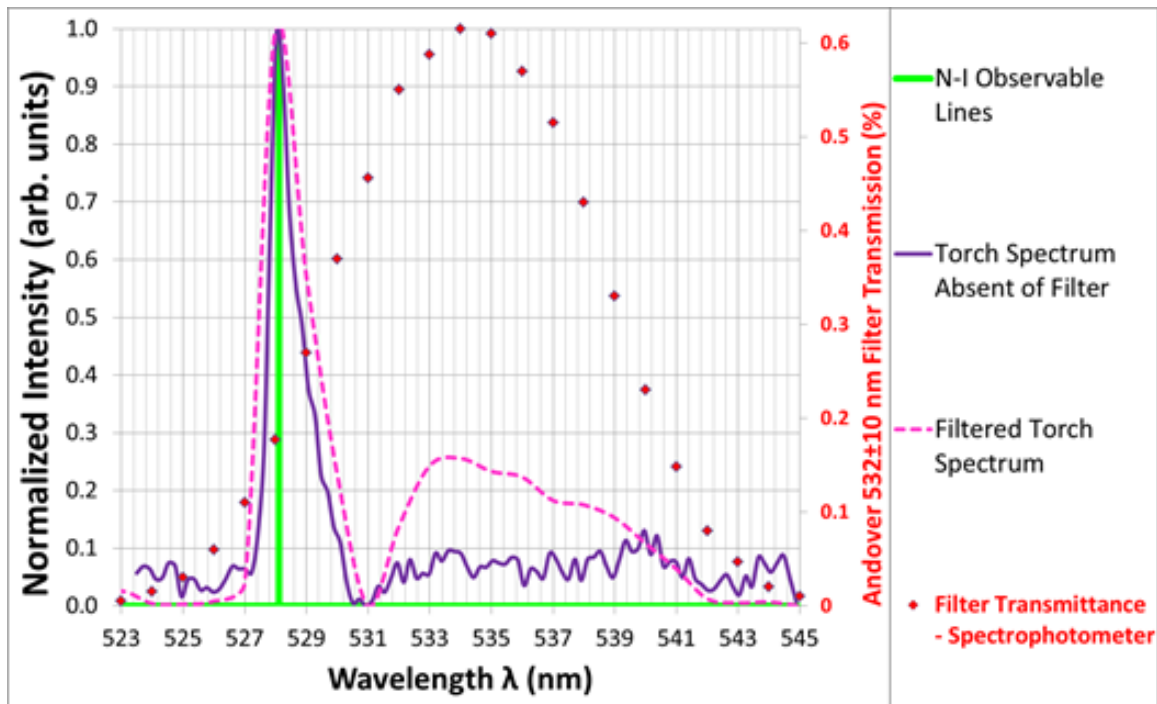


**Figure 3.9.** The APPT’s emission spectrum in the filter range as acquired by the Ocean Optics USB4000 VIS-NIR spectrometer. Additionally, the red points show transmittance data from Figure 3.10 (Shimadzu UV-2401 spectrophotometer) for comparison.

This is also achieved through neglecting the self-absorption of the 528.12 nm emission line, consistent with other researchers’ spectroscopic temperature measurements (*e.g.*, Ref. [58]).

To acquire the 2D chord-integrated intensity emitted by the APPT, a CCD camera was effectively converted into a 2D monochromator. The CCD camera utilized was a TSI, Inc. 29MP camera affixed with an AF Nikkor 50mm lens with aperture set to  $f/22$ . The aperture stop was chosen since the CCD camera’s imaging sensor is extremely sensitive to light and the emissions produced by the camera are powerful enough to damage the equipment, even for a short time period. Additionally, the aperture stop chosen provides a longer depth of field, thus the entirety of the plasma flow field would be in focus. The camera was operated in 12 bit RAW mode and affixed with diopter

lenses and an Andover Corporation 532 nm bandpass filter with a  $\pm 10$  nm FWHM wavelength range. This filter transmitted the 528.12 nm emission line while reducing all other lines by a factor of  $10^4$  or greater (OD4). For reference, spectrophotometry data on the filters used can be seen in Figure 3.10.

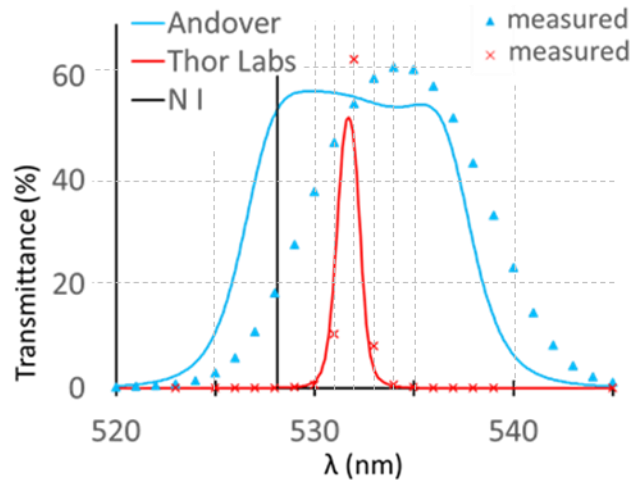


**Figure 3.10:** Transmittance vs. wavelength of Andover  $532 \pm 10$  nm bandpass filter and Thor Labs  $532 \pm 1$  nm laser line filter. Solid lines indicate manufacturers' data; data points with corresponding colors indicate measured data as acquired by a Shimadzu UV-2401  $\pm 0.3$  nm spectrophotometer.

This optical system was implemented to ensure that a maximum amount of the CCD camera's sensor gathered intensity data produced by the torch while still satisfying the parallel ray projection criterion, in order to achieve the highly spatially-resolved motivation for 2DMIM. The camera was controlled by utilizing the imaging software Insight4G and the image exposure time was limited to  $100 \mu\text{s}$ . Both the aperture and exposure were chosen to prevent overexposure whilst achieving a high signal to noise ratio.

Having developed a method to measure the plasma ionization, the next section presents a method to observe the hydrodynamic development of the plasma interface and

the velocity field of the surrounding, non-ionized, gas species, entrained in the MHD–RMI. This method provides a means to qualitatively compare experimental to simulation results using a laser illuminated passive particle field in the surrounding gas, and is similar to previous, well-validated, methods for classical RMI experiments.

### 3.3.5 *Solid Particle PIV Apparatus Design*

Another optical method used to determine characteristics of a flow field (in this case for a plasma's) is particle imaging velocimetry (PIV). PIV is a non-intrusive, non-invasive, correlation-based diagnostic technique which uses light reflected from a particle field that follows the gas to track the motion of groups of particles. A pair of singly-exposed images of the flow field is acquired at two times and statistical spatial correlation is performed to determine the local instantaneous particle velocity vector fields within the fluid. Imaging can reveal unfavorable conditions which can affect the RMI. This diagnostic method requires particles to be injected either into the working gas (plasma), pre-ionization, or into the surrounding non-ionized gas (passive). PIV uses planar laser Mie scattering from an illuminated passive particle-laden flow field and provides both qualitative information, morphology of the interface (growth or suppression of the RMI), as well as quantitative information, *e.g.*, two-dimensional planar velocity and vorticity fields. The velocimetry data is then used to quantitatively verify the suppression of MHD–RMI interface in comparison to the traditional RMI (without a magnetic field), and is also used to validate the computational simulation results obtained in Section 2.5. By doing so, a more accurate model can be utilized when performing simulations on the MHD–RMI. Other methods to measure plasma flow velocity have been implemented such as laser scattering techniques, and laser Doppler anemometry. Similar methods have

been previously performed to examine velocity distributions of the plasma flow field and have applications such as the surface treatment of materials [49].

In this work, the author adapted previous PIV techniques to visualize the plasma interface. The previous work this technique is adapted from is provide in Ref. [42] which was co-authored by this dissertation's author. In the future, development of this method will need to be performed further to acquire velocities of the interface for the MHD–RMI shock tube experiment. Acquisition of velocity profiles of the interface during the MHD–RMI experiment allow quantitative data to be gathered on the interface's morphological development within the shock tube experiment to prove suppression results.

For now, the author only required a method to image the plasma interface morphology in the  $r\theta$ -plane within the FMSTL shock-tube facility for future shock-driven MHD–RMI experiments. To develop this diagnostic technique, visualization of both the axial ( $rz$ ) and cross-sectional ( $r\theta$ ) planes was performed by imaging the particle-laden flow field surrounding the plasma while filtering out the plasma's emissions. Filtering is normally not required to acquire traditional PIV data on flow systems. However, since the light captured by the camera for this system consists of the laser light as well as the light emitted by the plasma due to ionization, elimination of any other wavelength of light, other than that produced by the laser, is required to perform PIV. The plasma's emissions were blocked by fitting a TSI 29 MP CCD camera with a ThorLabs  $532 \pm 1$  nm laser line filter that transmitted only 532 nm Nd:YAG laser light reflected from the neutrally buoyant particles. CCD cameras convert electrical charge from the incident light (photons) to a voltage in a common output structure rather than at each individual pixel. This results in a loss of frame rate capability in comparison to

complementary metal oxide semiconductor (CMOS) imaging sensor cameras which convert voltage on an individual pixel basis. Nonetheless CCD cameras possess greater resolution with lower signal-to-noise ratios.

Particles entrained in the fluid flow field are considered to be “ideal” if they meet the following criterion: (1) they follow the exact motion of the fluid flow, (2) they do not significantly alter the fluid flow or its properties, and (3) they do not interact with one another. Thus titanium dioxide particles of 0.3–1.0  $\mu\text{m}$  diameter (manufacturer specifications) were chosen based on their ability to survive near the plasma (high melting and vaporization temperatures – of  $\sim 2,116$  K and  $\sim 3,245$  K respectively). Additionally, these small diameter particles entrained in the gas surrounding plasma were determined to have a sufficiently small Stokes number (*i.e.*,  $St \ll 1$ ). The particles follow the flow of the surrounding gas with minimal error of flow lag (response to fluid) due to their small volume and light mass, sufficient to propagate at the same velocity as the bulk fluid motion.

To illuminate the particles, a Litron NanoPIV Nd:YAG laser, frequency doubled to 532 nm ( $\approx 200$  mJ/pulse), was used with supplementary external optics to generate a thin laser sheet to illuminate either the axial or cross-sectional plane. The laser pulse duration is  $\sim 4$  ns which allow the flow to be effectively “frozen” in time when it is imaged. The particle-laden flow field was confined in a volume with equivalent cross section to the FMSTL shock tube ( $0.146 \text{ m} \times 0.146 \text{ m} \times 1.0 \text{ m}$ ) termed the Mock Tube (MT). The MT was constructed of polycarbonate sheets to allow for optical access. The APPT nozzle was mounted flush with the inside of the bottom wall of the MT and a circular exit was cut out in the top wall to allow the high temperature plasma to escape.

Particles were supplied to the MT by a solid particle generator system (TSI model 9309). The MT and a schematic of the experiment are shown in Figure 3.11 and Figure 3.12.

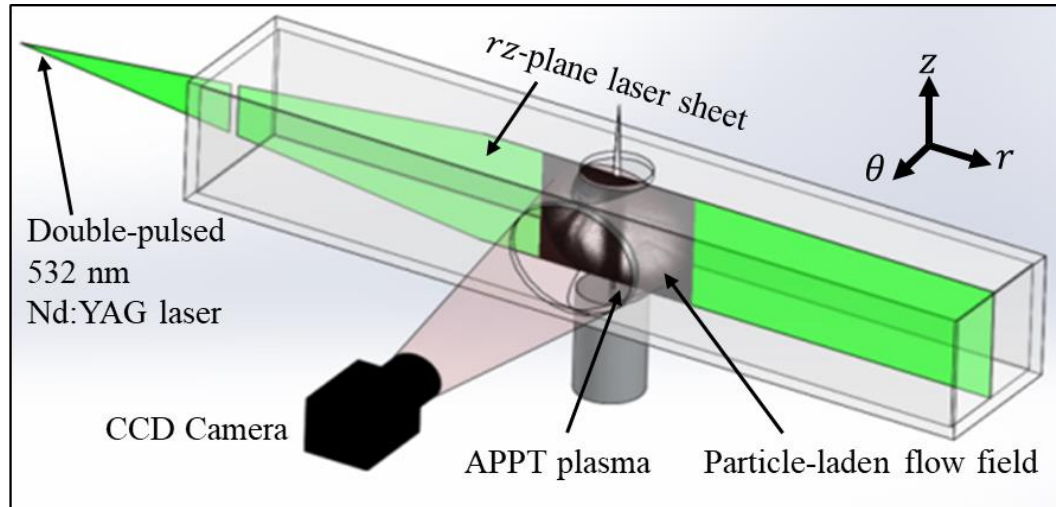


**Figure 3.11.** Conceptual representation of negative image solid particle Particle Image Velocimetry Mock Tube apparatus with  $rz$ -plane illuminated by the laser.



**Figure 3.12.** Constructed Mock Tube apparatus for PIV application.

To image the  $r\theta$ -plane, a similar setup was implemented when imaging the  $rz$ -plane. However, the camera was oriented slightly off-axis of the plasma torch to ensure that the plasma itself would not come into contact with the CCD camera, thus resulting in damage to the equipment. More details on this can be found in Section 4.3.1 which discusses the results of the images acquired while implementing this diagnostic method.

In order to utilize these experimental PIV apparatuses to obtain accurate PIV data, the use of PIV data acquisition instrumentation and software is required which is discussed in the next section.

### *3.3.6 PIV Data Processing in Insight 4G and PIVlab*

Two different software platforms were used to process the acquired PIV data from image pairs captured by the CCD camera. This was done to obtain velocity fields generated by the particle-laden flow field surrounding the plasma's flow field. The first, and most predominately utilized software, was TSI's Insight 4G®. The PIV software Insight 4G is used to automate the process of acquiring and analyzing global images (velocity fields, particle images, or scalar image fields). Insight 4G allows for the displaying of the global properties of said fields, and their respective statistics, obtained by a digital camera. The data acquired is processed within the program and can be easily exported to other secondary software programs such as MATLAB and Excel. This is done so that the data acquired can be easily visualized according to user specifications.

The second PIV program used was PIVlab. PIVlab is a time-resolved GUI based add-on app or toolbox used in MATLAB to visualize, process, analyze, validate, and

post-process PIV data [79]. Although Insight 4G and PIVlab are separate programs which are independent of one another, the same PIV image pairs are able to be processed by both programs. The corresponding PIV data generated by each software can be processed by a MATLAB script written by the author of this dissertation. The results are thus able to be compared for likeness and similarity. PIV data processing by each of these software programs was done to not only to validate the results of the two codes independently, but to see how the results of commercial PIV software code, Insight 4G, and open-source software, PIVlab, compared. In order understand how the image pairs were processed (for both methods), the following sections are provided.

### *3.3.7 PIV Data Processing Background*

Analyzing sequential digital image pairs of particles via PIV measurements to determine the motion (velocity) of the flow is achieved through spatial cross-correlation where the images are divided into interrogation regions (sub-windows) that yield a displacement vector. Spatial cross-correlation of an interrogation region can be performed directly (DCC) or through using a discrete Fourier transform (DFT). Computing the cross-correlation directly however, is computationally expensive. To avoid this, transformation of images into the frequency domain is achieved using the fast Fourier transform (FFT). During this procedure, an interrogation region within each of the two images is utilized to “search” for the initial and final location of the particles and uses statistical cross-correlation to measure their most probable locations (displacement). A correlation engine is used to compute the correlation function and returns its corresponding correlation map. By calculating the correlation coefficient, the location of the peak correlation coefficient is found within the interrogation region for the particles

of interest, and thus their displacement is realized. This is done through utilizing an algorithm that sums the particle image matches at all pixel displacements within the prescribed pixel range. Post transformation, the cross-correlation plane becomes the product of the two images complex conjugate, where its inverse FFT is computed to transform it back into the spatial domain.

Cross-correlation itself only possesses the capability to predict the particle field's displacement to an integer value which leads to  $\pm 0.5$  pixel uncertainties and thus error. Thus using smaller sized interrogation regions, (*e.g.*, in an effort to increase the resolution of the velocity vector field), would so too increase in the error that results. Therefore, sub-pixel accuracy estimation algorithm methods are used to minimize this effect where fractional displacement of the particles can be obtained using the distribution of less intense grey values around the peak correlation-coefficient. Particle image intensities are well approximated by a Gaussian distribution and the most prevalent sub-pixel distribution estimator algorithm used is the Gaussian 3-point curve estimator where the minimum resolvable velocity is  $\sim 0.1$  pixels.

By repeating this process multiple times, through utilizing multi-pass image-shifting processing, a more refined and precise definition of the displacement field is computed. This is achieved through analyzing the image pair with a large grid of interrogation regions on the first pass, and refining the interrogation region (normally by a factor of one half) during subsequent passes. The particles peak displacement values calculated within each interrogation region on the first pass are then utilized to predict the peak correlation locations for subsequently refined passes. Utilizing a  $16 \times 16$  square pixel interrogation regions with 50 % overlap is standard for multi-pass processing.

Smaller interrogation regions (*e.g.*,  $8 \times 8$  pixels<sup>2</sup>) is possible but the flow must be *ideal*. Incorporating image-shifting into the processing scheme allows the uniformly arranged first pass interrogation regions to be shifted by values predicted from the peak correlation locations of the first pass (or the prior pass). The relationship between these is, when the area of the interrogation region decreases, spatial resolution is increased; however, the velocity range decreases. Multi-pass processing is not affected by in-plane loss of particle image pairs as spatial resolution is increased because the particles themselves can propagate into, and out of, the illumination plane of the laser.

Once the cross-correlation analysis is completed through utilizing the multi-pass image shifting FFT cross-correlation algorithm, the resulting velocity vector fields are classified into one of two distinct categories: (1) correct measurements with a certain level of uncertainty, or (2) spurious (false) velocity measurements. Spurious vectors are the result of random errors that arise either during image acquisition or during computation of the correlation coefficients peak locations. To combat this issue, statistical analysis of vector validation is utilized through post-processing schemes, local vector filtering, and global filtering techniques. Filtering techniques are not limited to occur within the post-processing stage of PIV analysis, and are often utilized during the processing of the image pairs themselves. Typically mean and median filtering are the more commonly utilized. These filters aid in eliminating unreasonable spurious outliers in the data.

Although PIV is a proven robust means to acquire velocimetry data measurements of a fluid in motion, the specifics and characteristics of the equipment utilized exhibits limiting factors. The camera's resolution and frame rate, the laser's power and pulse

duration, and the supplementary timing setup initialized when these pieces of equipment are utilized in harmony, are examples of these equipment limitations. To effectively capture a highly turbulent fluid's motion, or a fluid moving at greater than sonic flow speeds, both the laser's repetition rate and both the camera's resolution and frame rate are required to resolve the fluid's motion down to the Kolmogorov scales, to acquire accurate data. Generally an increase in a camera's frame rate results in a decrease in its resolution. To effectively keep up with a camera's frame rate, the laser pulse frequency must also increase which generally results in a loss of laser power. A decrease in laser power can result in a decrease of spatial resolution of the image acquired by the camera. Ultimately, by utilizing the correct equipment with the appropriate specification and the correct timing scheme between these two, results in the ability to accurately capture the fluid's motion and thus the resulting velocity on a per system basis. To better understand how these characteristics are utilized in tandem, the following diagram in Figure 3.13 is presented.

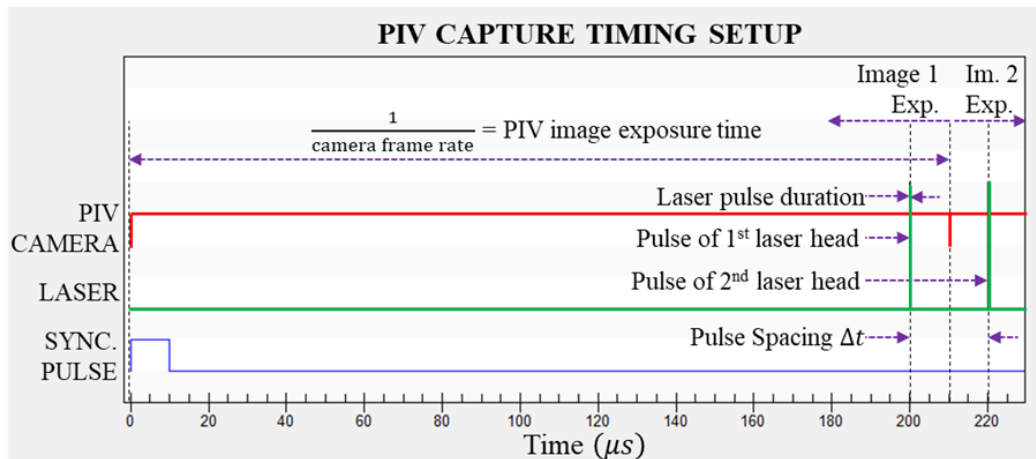


**Figure 3.13.** Particle Image Velocimetry capture timing setup diagram.

As shown in Figure 3.13, acquiring the two images for PIV measurement is based on the timing setup. Initially, it is seen that the camera is on (shutter is open) to capture

the first frame of intensity data per pixel. This is shown as the first horizontal red line. The PIV image exposure time dictates how long the camera is allowed to acquire the first frame's data. During the first image's exposure, the laser is turned on (pulsed) to illuminate the particle-laden flow field, providing the intensity data (*i.e.*, the particles location) to the camera. This is shown as the first green vertical line (*i.e.*, spike), which lasts on the order of nanoseconds. After the laser is pulsed, the camera's frame grabber (image exposure control device) closes the camera's shutter a short time thereafter. This completes the first image exposure of the PIV data acquisition. Next, the second image is acquired by exposing the camera's pixels again. This is shown as the second horizontal red line. A short time after, the laser is pulsed again to illuminate the particle field. This is shown as the second green spike. The time differential between laser pulses is termed the pulse spacing ( $\Delta t$ ). The time between laser pulses dictates how long the time is between image exposures. Small pulse spacing allows for studying higher velocity flows as well as capturing highly-varying flow morphology. Because the repetition rate of the Litron laser used for this diagnostic technique is quite low, the necessity to utilize its dual-heads, consisting of two laser cavities pumped at the same frequency and equivalent power, allows for the demand of small pulse spacing to be met. This criterion is commonly used in many PIV systems which use a Nd:YAG laser. Specifically, this technique is termed frame straddling and allows for the cameras repetition rate to be operated with frame rates as small as twice the frequency of the laser.

The details on how these processing procedures and timing setups are implemented in each of the two PIV programs are presented in the following two sections.

### 3.3.8 Processing PIV Data in Insight 4G

As with any PIV software, two main ingredients are required: (1) displacement (length scale) of particle motion, and (2) time (interval between image pairs). To setup the Insight 4G software, the first step was to obtain a calibration image of a ruler to determine the pixels per centimeter (length scale). The second was to set the time differential of when the image pairs would be taken. For the purposes of the data presented where PIV data is acquired in the  $rz$ -plane, the pulse spacing time differential  $\Delta t$  was set to 20  $\mu\text{s}$ , the laser pulse delay to 200  $\mu\text{s}$ , and the PIV exposure time was set to 210  $\mu\text{s}$ . These parameters were chosen as they paralleled previous PIV setup timing schemes used in turbulent round jet experiments and SDMI experiments performed at the FMSTL in the past by the author [42]. As the results will show in Section 4.3.2, this produced good velocity profiles considering the time scale the particles travel during these specific experiments.

With the length calibration and time scale initialized, the next step was to setup the image pre-processing pipeline (procedure). The pre-processing pipeline for the data presented consisted of an image filter and region of interest (ROI) as well as masking areas unfit for processing (if necessary). The image filter chosen was a Gaussian (low-pass) filter since it utilizes a rotationally symmetric kernel of size  $n = 5$  [pixels<sup>2</sup>] (filter size) and standard deviation  $\sigma = 0.5 = 50\%$  (parameter). A filter kernel width of 5 [pixels] was chosen since it was the width of a particle and the filter overall aids in smoothing and reducing unwanted noise in each image. The ROI and mask implemented for the  $rz$ -plane data acquired are shown later in Section 4.3.

Once the image preprocessing pipeline was setup, the next step was to setup the PIV processor itself within the program. The algorithm chosen to do so was Classic PIV because ensemble averaging was not performed. The grid engine used was a Recursive Nyquist Grid (RNG). The grid engine breaks the input image up into smaller sections for processing capabilities where the vector field is initialized. The RNG was chosen because it processes an image's vector field in two or more passes. The first processing pass computes the vector field at the starting spot sizes where the RNG utilizes a 50% overlap between grid spacing.

Next, the calculated vector field is revised via pass validation, in which the first pass results are used in optimizing the spot offsets for the second pass of processing. The spot offsets are equal to the displacement of the integer pixel measured during the first pass such that subsequent passes show a peak location within half a pixel of the correlation center. Should the final spot size be smaller than the starting spot size, they are reduced by half and the rows and columns are doubled, resulting in four times the number of vectors with each and every pass. Should the former and latter pass spot size be the same, the final pass uses the optimized window offsets to recompute the vector field with the same number of vectors.

In an effort to prevent the generation of additional noise within the images, no spot mask engine was implemented. The correlation algorithm used was the Fast Fourier Transform (FFT) correlation engine. Specifically, the FFT correlation engine was used because it computes the correlation function using the Fast Fourier Transform algorithm due to its high degree of correlation accuracy. Utilizing the FFT correlation engine requires the spots A and B to be square powers of two and spot A must be the same size

as spot B. Should this condition not be met, a decrease in signal-to-noise ratio and correlation accuracy will result. Using the FFT correlation engine ensures that the particle tracing and tracking is optimized and the resulting PIV field generated is accurate. To do so, a peak engine is used to find the correlation peak with sub-pixel accuracy. The peak engine utilized was the Gaussian peak plugin, which finds the sub-pixel correlation peak by fitting a Gaussian curve to the highest pixel and its four local nearest neighbors by 3-point fitting the left and right pixel in the  $x$ -direction and the top and bottom pixel in the  $y$ -direction. It is also the recommended peak engine to be used with the FFT correlation engine. The starting spot size chosen was  $64 \times 64$  [pixels] and the final spot size was  $32 \times 32$  [pixels] with a maximum displacement of  $dx = dy = 0.49$ .

Pass validation settings were also implemented within the PIV processor setup for local vector validation and vector field conditioning. The local vector validation setup consisted of using a Median Test method with a neighborhood size of  $7 \times 7$  [pixels], bad vector replacement by local median, and a velocity tolerance of  $dU = dV = 2$  [pixels]. Local median vector validation is the most commonly utilized validation method where vectors in the neighborhood are known to be within a certain tolerance and limit. Conditioning of the vectors are done post vector validation to fill any “holes” in the velocity data field as well as to aid in smoothing the data field itself. A local mean recursive filling conditioning method was used to condition the vectors within a neighborhood size of  $5 \times 5$  [pixels] and standard deviation  $\sigma = 0.8$ , (*i.e.*, 80% of the kernel). No additional smoothing was performed since the initial preprocessing image was already Gaussian filtered and smoothed prior to this step in an effort to preserve the accuracy of the data computed. Thus if there are missing vectors within a local

neighborhood of good data vectors that are outside of the 80% correlated value, they are forced to the mean value of the neighborhood vector field.

Once an image pair's PIV data was computed and processed, they are then post-processed. During the post-processing procedure, the same local vector validation method is performed as a redundant check once the velocity field is computed in its entirety. After undergoing local vector validation, the velocity field is globally validated as a whole. During this global validation process, any velocity that is found to be  $\pm 2 U_{px}$  or  $\pm 2 V_{py}$  [pixels] is filtered out. Once the data are globally filtered they are conditioned using the same setup as before to fill the missing data. The resulting velocity vector field is then produced and ready for analysis.

In order to compare the results generated by using the PIV software Insight 4G to the results obtained by using the second PIV software PIVlab, the processing parameters used within PIVlab must first be defined which is discussed in the following section.

### *3.3.9 Processing PIV Data in PIVlab*

The second software utilized in obtaining and analyzing the image pair PIV data was PIVlab. The setup of PIVlab is similar to that of Insight 4G. The parameters were kept consistent (where possible) between the two software platforms to ensure accuracy of data obtained and ability to compare the data generated plausible. The same ROI and mask area/locations were kept consistent when using PIVlab, to those used in Insight 4G. PIVlab utilizes the superior processing speed of a fast Fourier transform cross-correlation (FFT-CC) algorithm for each image pair processing. Image pairs were then correlated utilizing PIVlab's multi-pass FFT-CC function where a window-shifting technique and

sub-pixel interpolation methods were employed. An initial pass interrogation area of  $64 \times 64$  [pixels] with a step size of 32 (*i.e.*, 50%), and a final pass interrogation area of  $32 \times 32$  [pixels] with a step size of 16 were implemented in PIVlab so that the results were comparable to those obtained by Insight 4G. The sub-pixel estimator employs the two pass 3-point Gaussian window-shifting technique along with a  $5 \times$  repeated correlation within PIVlab. This is similar to the vector validation correlation engine implemented in Insight 4G. The vector validation method used a standard deviation filter with a threshold,  $n \times \sigma = 1$ , a local median filter with a threshold of 7, and standard deviation filter threshold (tolerance criterion) of  $\varepsilon = 7$ . Post processing vector validation was mimicked in the PIVlab settings from that of the Insight 4G setup. Since PIVlab does not automatically know the time differential between the two images like Insight 4G does, it had to be specified at  $20 \mu\text{s}$  and a pixel-to-centimeter calibration needed to also be performed. Once the processing of the data was complete in PIVlab, the results were obtained and are discussed in Section 4.3.3.

In order to capture PIV data on the suppression of the MHD–RMI interface experimentally, the ability to suppress the instability by an externally-applied magnetic field must first be achieved. Specifically, verification that an externally-applied magnetic field would influence the plasma flow field, produced by the APPT, must be performed; because the plasma produced by the APPT will be used to create the interface within the MHD–RMI experiment. The third and final experimental method developed to diagnose the plasma torch was its interaction with a magnetic field apparatus. This was method was developed to investigate deflection and suppression of the plasma flow field and

presented in the next section. This diagnostic method will, in turn, be used develop the magnetic field applied within the future MHD–RMI shock tube experiment.

### **3.4 Magnetic Field Interactions with a Plasma Flow Field**

Magnetic fields and their interaction with physical phenomena have been a major impetus in the physics community since the discovery of their principles by Maxwell and Faraday. How magnetic fields interact with a conducting fluid’s hydrodynamics (*e.g.*, a plasma) is coupled in the field of magnetohydrodynamics (MHD), was first introduced by Hannes Alfvén. Investigation of varying alignments and strength of magnetic fields induced on various types plasma flow fields have been performed both experimentally and via numerical simulations. Both show deflection and suppression of plasma flow field due to the presence of an externally applied magnetic field. Specifically, the suppression of the RMI in MHD has been shown possible by simulation efforts as discussed in Chapter 2. Therefore, how an externally-applied magnetic field influenced the plasma flow and ultimately caused deflection and suppression of the flow field to result, was investigated and analyzed to diagnose the plasma.

A plasma’s interaction with a magnetic field is particularly difficult to analyze because plasma is a multi-species fluid of intermediate density. Fluids, like water for example, are sufficiently dense such that the motion of individual particles does not require consideration since they are collision-dominated and the basic fluid dynamics equations are sufficient in describing the effects of flow propagation. Extremely low density devices such as particle accelerators (*e.g.*, the Alternating-Gradient Synchrotron at Brookhaven National Labs) only require individual particle trajectories to be

considered because collective effects are often inconsequential. Plasmas, on the other hand, behave sometimes like collections of individual particles and sometimes like a single fluid: individual particle effects as well as bulk flow effects must be considered. Should an externally-applied magnetic field's prohibit its treatment to be reduced to a 1-D component, only increases the difficulty of analyzing magnetic field interaction with plasma. Thus, the goal of performing this diagnostic method is to visualize and analyze that magnetic field interacting with plasma flow field, and thus qualify and quantify the results that are obtained.

#### *3.4.1 Theory on Magnetic Field Interactions with a Plasma Flow Field*

An external magnetic field's interaction with an APPT fluid flow profile is a topic that is traditionally investigated using transferred arc plasmas, non-thermal plasma jets, or collisionless plasmas. To the author's knowledge, the effects of an external magnetic field applied to a non-transferred APPT have yet to be investigated experimentally. Similar studies such as the investigation of non-thermal, RF generated, APPT interaction with an applied DC magnetic field, where parallel and traverse magnetic field interactions with the plasma flow field were discussed quantitatively showing intensified or reduced plasma flow fields, respectively [80]. Monochromatic imaging techniques used to study transferred-arc plasma behavior in the presence of a transverse magnetic field where a relatively small, sinusoidal, transverse magnetic field showed arc elongation effects due to the external magnetic field, have also been investigated [81]. 3D numerical modeling of transferred-arc plasma deflected by an external magnetic field has been performed with deflection results similar in nature to experiments previously listed [82]. Most easily stated, alteration of the plasma's flow is due to its magnetic

influenceability where its individual species are repelled (diamagnetic) or attracted (paramagnetic) by an externally applied magnetic field. Nonetheless, the conclusion is that external magnetic fields do interact with plasmas.

Due to the nature of the non-transferred thermal arc plasma produced by the APPT developed by the author, which differs from transferred arcs or non-thermal arcs, so too will its respective interaction results with an external magnetic field differ. There are specific considerations that must be taken into account when deducing, both quantitatively and qualitatively, what effects should arise for this specific experimental setup. When a non-transferred APPT's plasma is ejected out of the nozzle and is absent of any external magnetic field interaction, there is no space charge because there is a uniform spatial distribution of the number of ions and electrons and the plasma is assumed to be isotropic. Once an external magnetic field is applied on the plasma flow field, the plasma becomes spatially anisotropic and a space charge electric field develops. Additionally, the arc itself is confined within the nozzle of a non-transferred APPT which is not the case with transferred arc plasma torches where the electric field, generated by the electrodes electric potential difference, must be taken into consideration. This is also important when examining the self-induced electric field that arises due to the external magnetic field interacting with the plasma flow field velocity profile. Additionally, since the plasma generated by the APPT is only partially ionized, consisting of ions, electrons, and neutral particles, charged particles collide with neutral particles and result in momentum exchange, thus the collisionless assumptions must be forgone as well as utilizing only Coulomb collision equations between charged particles.

These effects, interactions, and considerations, in conjunction with others, are applied within the MHD fluid equations used to describe the fluid's equations of motion of a singly-ionized gas medium and are as follows. The respective continuity and momentum equations for a particular species  $j$  are,

$$\partial_t n_j + \nabla \cdot (n_j \vec{V}_j) = 0 \quad (3.24)$$

$$m_j n_j \partial_t \vec{V}_j = -\nabla p_j \pm Z e n_j [\vec{E} + \vec{V}_j \times \vec{B}] + \vec{P}_{ei}, \quad (3.25)$$

where  $n_j$ ,  $\vec{V}_j$ ,  $m_j$ ,  $p_j$ , are the number density, velocity, mass, and pressure, of the  $j^{\text{th}}$  species, respectively, and  $Z$ ,  $e$ ,  $\vec{E}$ , and  $\vec{B}$  is the charge state, electron charge, electric field, and magnetic field, respectively. For a plasma with monovalent particles,  $Z = 1$ . The  $\vec{P}_{ei}$  terms in Equation (3.25) represents the particle collision drag term such that,  $\vec{P}_{ei} = -\vec{P}_{ie} \approx m_e n_e (\vec{V}_i - \vec{V}_e) \bar{\nu}_{ei}$ , where  $\bar{\nu}_{ei}$  is the electron-ion collisional frequency.

Again, as discussed in Section 3.3.3, the condition of local net charge neutrality must be met, *i.e.*,  $n_e = n_i$  for when only monovalent ions, electrons, and neutral particles are present. Additionally, the plasma must obey Dalton's law of partial pressures as prescribed in the equation of state given in Equation (3.3). To be considered a single fluid, the mass density,  $\rho$ , and hydrodynamic velocity,  $\vec{V}$ , are introduced as

$$\rho = m_i n_i + m_e n_e = n(m_i + m_e) \quad (3.26)$$

$$\vec{V} = \frac{m_i \vec{V}_i + m_e \vec{V}_e}{m_i + m_e} \quad (3.27)$$

where the subscripts  $i$  and  $e$  represent the ion and electron components respectively. A full derivation of the single fluid MHD equations can be found in Chen [15].

Ultimately, applying a transverse external magnetic field to a plasma flow field results in drift motions of the ions and electrons, charge separation, and thus bulk plasma flow deflection and/or suppression. As plasma propagates through a magnetic field, there arises an additional force term accounted for in the MHD momentum equation, Equation (3.25), known as the Lorentz force, which is perpendicular to both the magnetic field and the velocity field. Since energy cannot be imparted onto charged particles themselves by a magnetic field, associated with the magnetic field is an induced electric field based on  $\vec{V} \times \vec{B}$ . This induced electric field gives rise to charge separation and thus an induced current density governed by the generalized Ohm's law equation from MHD body force (*i.e.*, Lorentz force) as,

$$\vec{J} = \sigma_e [\vec{E} + \vec{V} \times \vec{B}] \quad (3.28)$$

where  $\vec{J}$  is the current density and  $\sigma_e$  is the electrical conductivity of the fluid.

The extent of the effect the Lorentz force has on plasma fluid motion is realized by evaluating the mobility, diffusion, electron collision frequency, and cyclotron frequency. Although the plasma is treated as a single fluid, there arises a difference in mobility,  $\mu_j$  [ $\text{m}^2 \text{V}^{-1} \text{s}^{-1}$ ], and diffusion coefficient of the  $j^{\text{th}}$  species,  $D_j$  [ $\text{m}^2 \text{s}^{-1}$ ], for the ions and electrons, which are governed by the relationships shown in Equation (3.29a). The symbols used to compute these transport coefficients are: the elementary charge,  $q$  [C],

the mass of the  $j^{th}$  species,  $m_j$  [kg], the collisional frequency of the  $j^{th}$  particle species,  $\nu_j$  [ $s^{-1}$ ], Boltzmann's constant,  $k_b$  [ $J s^{-1}$ ], and the temperature of species  $j$  is,  $T_j$  [K].

$$\mu_j = \frac{|q|}{m_j \nu_j} \quad (3.29a)$$

$$D_j = \frac{k_B T_j}{m_j \nu_j} \quad (3.29b)$$

Mobility is the measure of how easily a charged species propagates is influenced by an applied field, and the diffusion coefficient is a proportionality constant between the molar flux (due to molecular diffusion) and the species concentration gradient (*i.e.*, the number density gradient). These transport coefficients are connected by the *Einstein relation*:  $\mu_j = |q| D_j / k_B T_j$ .

Since the electrons have much smaller masses than the ions, they have a much higher mobility and diffusivity coefficient than that of the ions. As seen in Equation (3.29b), there is an inverse proportionality relationship between particle mass and diffusivity. Since the electrons diffuse at a higher rate than the ions, there is an excess of positively charged ions thus giving rise to space charge electric field. Additionally, these transport phenomena give rise to ion and electron particle fluxes, denoted as  $\Gamma_{j \parallel}$ , along the magnetic field lines.

The electron collision frequency for momentum transfer is energy dependent in atmospheric gases at atmospheric pressure and is governed by

$$\nu_m = \nu_{em} + \nu_{ei} + \nu_{ee} \quad (3.30)$$

where  $\nu_{em}$ ,  $\nu_{ei}$ , and  $\nu_{ee}$  are the electron–neutral, electron–ion, and electron–electron collisional frequencies, respectively [83]. It is known that collisions between like charged particles (ion–ion or electron–electron) give rise to small diffusion effects, whereas unlike particle collisions (ion–electron) are the dominating effect of diffusion [15]. The cyclotron frequency,  $\omega_c$  [ $s^{-1}$ ], of the  $j^{th}$  species is given by

$$\omega_{cj} = \frac{q_j \vec{B}}{m_j}, \quad (3.31)$$

which shows that an increase in the magnetic field intensity,  $\vec{B}$  [T] results in an increase in the cyclotron frequency. Therefore, the electrons, of smaller mass, will “gyrate” around magnetic field lines with a higher cyclotron frequency, than ions. Additionally, a charged particle will gyrate around the same magnetic field force line until a collision occurs.

By examining the perpendicular component of Equation (3.25), there also exist perpendicular mobility and diffusion coefficients, given by

$$\mu_{\perp} = \frac{\mu}{1 + (\omega_c^2/\nu_m^2)} \quad D_{\perp} = \frac{D}{1 + (\omega_c^2/\nu_m^2)}, \quad (3.32)$$

which give rise to particle fluxes, denoted  $\Gamma_{j\perp}$ , perpendicular to the tangential magnetic field. Noting that although  $\Gamma_{i\perp} > \Gamma_{e\perp}$ , the perpendicular ion and electron particle fluxes occur in the same perpendicular direction, away from the magnetic field. This concept

can be visualized in Figure 3.14, where the cross-section of a cylindrical plasma flow field is swept through the magnetic field, resulting in the aforementioned particle fluxes and the gyration of particles about a magnetic field line. Shown in Figure 3.14 are the boundaries of permanent cylindrical magnets shown in green, magnetic field lines shown as blue lines, plasma cross-sectional boundary shown as purple circle, electrons and ions within the plasma shown as red dots, and direction plasma flow field is propagated is shown by purple arrow. The experimental apparatus, for which this schematic represents, is discussed in Section 3.4.3.

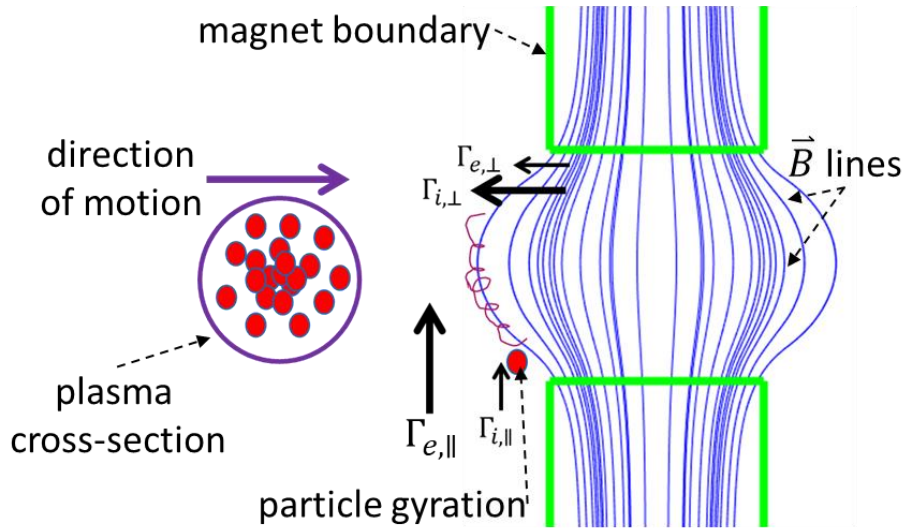


**Figure 3.14.** Schematic representing particle flux direction and notation for plasma – magnetic field interaction.

The relationship between the electron cyclotron frequency and electron collision frequency is utilized in determining the extent a magnetic field of known intensity will affect the plasma flow field. When  $\omega_c^2/\nu_m^2 \ll 1$ , the magnetic field has little effect on diffusion. Conversely, when  $\omega_c^2/\nu_m^2 \gg 1$ , the magnetic field hinders the rate of diffusion across  $\vec{B}$  significantly [15]. Additionally, when  $\omega_c^2/\nu_m^2 \ll 1$ , the collision-

dominated plasma transport phenomena are approximately isotropic in nature, as they are in the  $\vec{B} = 0$  case; mobility, diffusion, and electrical conductivity are important constituents [80]. Therefore, as  $\vec{B}$  increases,  $\omega_c$  increases, and the resulting impact of the mobility and diffusivity within the plasma is increased. It is these parameters that ultimately predict the behavior of the flow field when influenced by an externally applied magnetic field.

### 3.4.2 Theory on Magnetic Field Modeling

To analyze the externally applied magnetic field,  $\vec{B}$ , generated by the cylindrical and axially-coincident permanent magnets used in constructing the magnetic field apparatus, the following model is presented. The model is based on an ideal solenoid of finite length, which serves as an excellent basis for cylindrical permanent magnets after some modifications, provided that the permanent magnet's magnetization is sufficiently uniform. Should the externally applied magnetic field be static, it would satisfy two of Maxwell's equations. The first is Ampère's circuital law given as:

$$\vec{\nabla} \times \vec{B} = \mu_0 \vec{J}, \quad (3.33)$$

and the second is Gauss's law for magnetism,

$$\vec{\nabla} \cdot \vec{B} = 0, \quad (3.34)$$

where  $\vec{J}$  [ $A\ m^{-2}$ ] and  $\mu_0$  [ $T\ m\ A^{-1}$ ] are the current density and vacuum permeability, respectively.

Gauss's law suggests the use of the magnetic vector potential,  $\vec{A}$ , defined such that

$$\vec{B} = \vec{\nabla} \times \vec{A}. \quad (3.35)$$

Because the divergence of the curl of a vector is zero, Equation (3.34) is guaranteed. If  $\vec{A}$  is chosen such that the divergence of  $\vec{A}$  is also zero, that is,

$$\vec{\nabla} \cdot \vec{A} = 0, \quad (3.36)$$

the magnetic vector potential satisfies the equation

$$\vec{\nabla} \times (\vec{\nabla} \times \vec{A}) = -\vec{\nabla}^2 \vec{A} = \mu_0 \vec{J}. \quad (3.37)$$

Because the magnetic field produced by the magnetic field apparatus' cylindrical magnets is axisymmetric, only the toroidal component in the  $rz$ -plane is of interest for calculation purposes. Thus, Equation (3.37) can be written

$$\vec{\nabla}^2 \vec{A}(r, z) = -\mu_0 \vec{J}(r, z) \quad (3.38)$$

and expanded to

$$\frac{1}{r} \frac{\partial}{\partial r} \left( r \frac{\partial A_\theta}{\partial r} \right) - \frac{A_\theta}{r^2} + \left( \frac{\partial^2 A_\theta}{\partial z^2} \right) = -\mu_0 J_\theta(r, z) \quad (3.39)$$

where  $A_\theta, J_\theta$  are the toroidal components of the magnetic vector potential and current density, respectively. In relation to fluid dynamics, Equation (3.38) is analogous to the vorticity equation, which is  $(\vec{\nabla}^2 \vec{A})_\theta = -\omega_\theta(r, z)$ . However, the vorticity equation is

constrained by the convection equation, whereas the current distribution,  $J_\theta(r, z)$ , is not restricted in the same manner.

From Equation (3.39) the magnetic field's radial and axial components are given by

$$B_r(r, z) = -\frac{\partial A_\theta(r, z)}{\partial z} \quad (3.40)$$

and

$$B_z(r, z) = \frac{1}{r} \frac{\partial}{\partial r} (r A_\theta(r, z)). \quad (3.41)$$

The toroidal component of the magnetic vector potential is expressed in Equation (3.42) with supplementary equations provided in Equations (3.43)–(3.47). The symbolic parameters used in Equations (3.42)–(3.47) are: the current,  $I$  [A], length of the magnet,  $L$  [m], radius of the magnet,  $r_m$  [m], the distance in the radial direction,  $r$  [m], and axial distance from the center of the magnet,  $z$  [m]. Shown in Equations (3.45)–(3.47) are the equations for the complete elliptical integrals of the first,  $K(m)$ , second,  $E(m)$ , and third kind,  $\Pi(n, m)$ , respectively.

$$A_\theta = \frac{\mu_0 I}{4\pi L} \sqrt{\frac{r_m}{r}} [\zeta k (C_1 K(k^2) - C_2 E(k^2) + C_3 \Pi(h^2, k^2))]_{\zeta_-}^{\zeta_+} \quad (3.42)$$

$$C_1 = \frac{k^2 + h^2 - h^2 k^2}{h^2 k^2} \quad C_2 = \frac{1}{k^2} \quad C_3 = \frac{h^2 - 1}{h^2} \quad (3.43)$$

$$\zeta_\pm = z \pm \frac{L}{2} \quad h^2 = \frac{4r_m r}{(r_m + r)^2} \quad k^2 = \frac{4r_m r}{(r_m + r)^2 + \zeta^2} \quad (3.44)$$

$$K(m) = \int_0^{\pi/2} \frac{1}{\sqrt{1 - m \sin^2 \theta}} d\theta \quad (3.45)$$

$$E(m) = \int_0^{\pi/2} \sqrt{1 - m \sin^2 \theta} d\theta \quad (3.46)$$

$$\Pi(n, m) = \int_0^{\pi/2} \frac{1}{(1 - n \sin^2 \theta) \sqrt{1 - m \sin^2 \theta}} d\theta \quad (3.47)$$

Substituting Equation (3.43)–(3.47) into Equation (3.42) and then into Equations (3.40)–(3.41) yields the magnetic flux density's radial and axial components,  $B_r$  and  $B_z$ ,

$$B_r = \frac{\mu_0 I}{4\pi L} \sqrt{\frac{r_m}{r}} \left[ \left( \frac{k^2 - 2}{k} K(k^2) + \frac{2}{k} E(k^2) \right) \right]_{\zeta_-}^{\zeta_+} \quad (3.48)$$

$$B_z = -\frac{\mu_0 I}{4\pi} \frac{1}{2L} \frac{1}{\sqrt{r_m r}} \left[ \zeta k \left( K(k^2) + \frac{r_m - r}{r_m + r} \Pi(h^2, k^2) \right) \right]_{\zeta_-}^{\zeta_+}. \quad (3.49)$$

To implement Equation (3.48) and Equation (3.49) into the model, the remnant flux density of the permanent magnet is used in place of the solenoid's residual field [84]. With the model of the magnetic field generated by the permanent magnets' magnetic field apparatus provided, a description of the test cases that were used to study the magnetic field interacting with the plasma flow field, as well as the apparatus itself, is provided in the following section.

### 3.4.3 Test Cases Used to Visualize and Verify Plasma–Magnetic Field Interaction

The two test cases that were implemented to measure the magnetic field's interaction with the plasma flow field are discussed. The first is the application of a tangential magnetic field applied to the plasma flow field as it traverses into the plasma flow field. A diagram of this is in Figure 3.15 where the red dashed lines indicate Cartesian coordinates of experiment in reference to simulations performed, green direction vectors represent polar cylindrical coordinates of plasma torch and magnetic field domain, black dashed line shows deflection direction on  $r\theta$ -plane (*i.e.*,  $yz$ -plane), and the  $z_m$ -axis shows magnetic field tilt orientation reference axis.

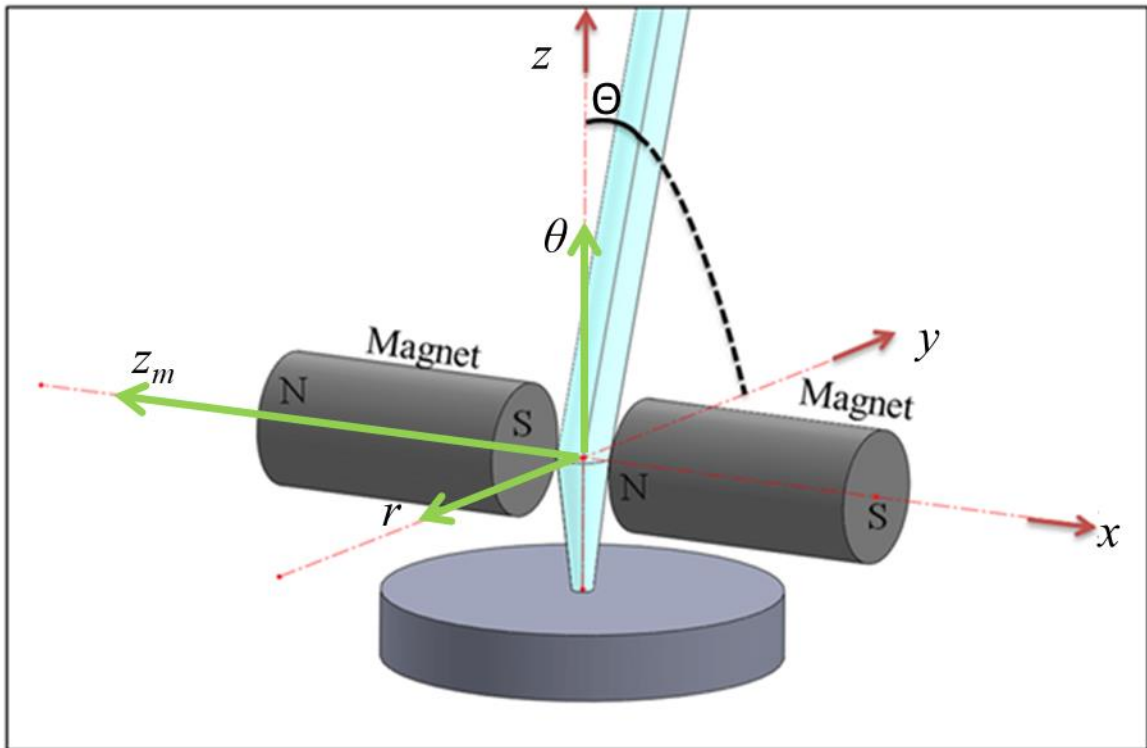


**Figure 3.15.** Tangential magnetic field apparatus concept to show single-axis deflection of the plasma flow field.

The first test case allows for a basic understanding of whether or not the APPT generated for this research is, in fact, able to be influenced by a magnetic field.

Additionally, the magnetic field was swept through the plasma flow field (in the  $y$ -direction) to determine how the resulting increase in magnetic field strength affected deflection and/or suppression results to ensue. The use of two coordinate systems within Figure 3.15 is done for two reason: (1) so the model used to generate the magnetic field data to would independent of the orientation of the magnetic field's tilt angle, and (2) it would not confuse the reader in understanding its referential coordinate system with that of the plasma flow field's coordinates, as well as the MHD–RMI simulations coordinates.

The second test case involved the same configuration of the magnetic field as the first; however its reference axis was tilted in the  $\phi$ -direction on the  $z_m\theta$ -plane. Additionally, the magnetic fields vertical location (in the direction of the  $z$ -axis) was varied in reference to the plasma torch nozzle exit. This was done to experimentally verify whether the ions or electrons are more or less attracted to the north or south poles of the magnets themselves. Also, the second test case was performed to determine how the resulting magnetic field strength affected various degrees of ionization within the plasma flow field at various angles and thus parallel the simulation study on magnetic field orientation, discussed in Section 2.4.2 and Section 2.5.1 . A visualization of this can be seen in Figure 3.16. The angles  $\theta$ ,  $\phi$  and  $\beta$  are analogous to pitch, roll, and yaw angles in flight mechanics.

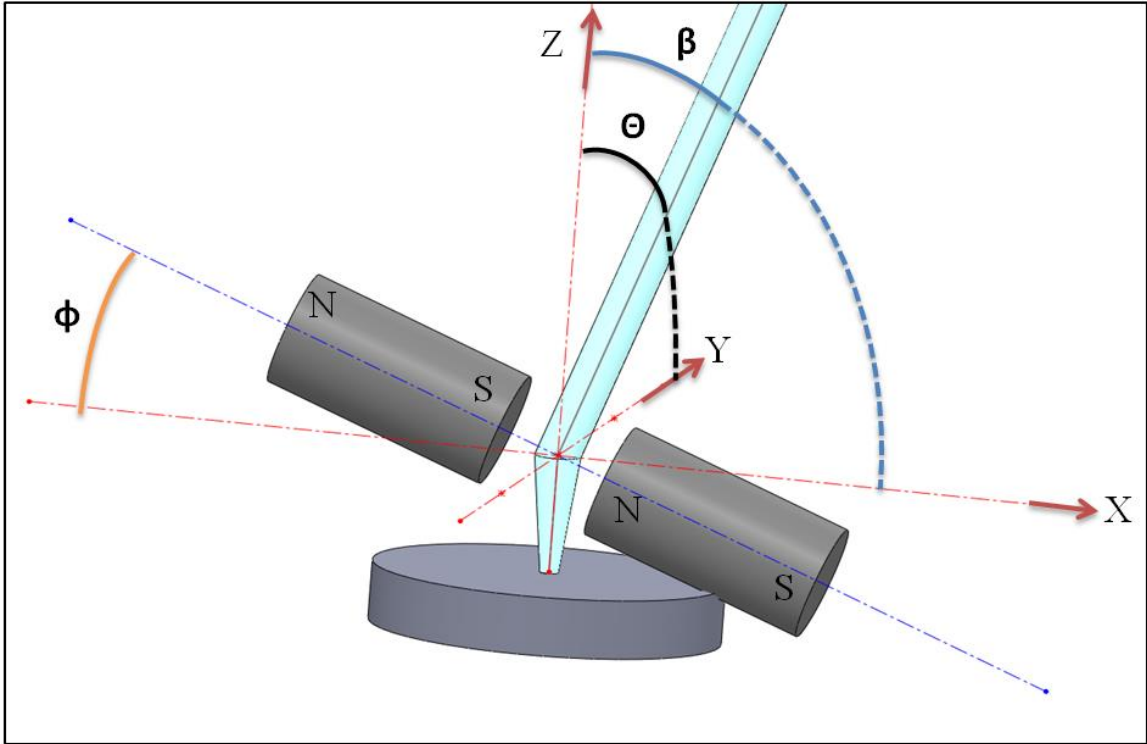


**Figure 3.16.** Tilted magnetic field apparatus concept showing multiaxis deflection of plasma flow field.

Between these two test cases, a basic understanding and analysis of the interaction between the plasma flow field and an externally applied magnetic field with various arrangements/ orientations is able to be determined. The results of these two experimental test cases are found in Section 4.4.2.

## CHAPTER 4. EXPERIMENTAL RESULTS

Having presented the development of the new experimental apparatus and methods, the purpose of this chapter is to now present the results of the experiments, showing the operating range and capabilities of the APPT apparatus, the properties of the plasma produced, degree of ionization and plasma temperature, particle image velocimetry, and the plasma–magnetic field interaction.

The major findings discussed within this chapter are: (1) the tallest APPT jet length able to be achieved is  $\approx 80$  cm, (2) the tallest APPT jet length does not directly indicate the tallest plasma containing region, (3) the plasma temperatures achieved reach upwards of 14000 K and a degree of ionization of  $\approx 27\%$ , (4) the ability to image both the  $rz$ -plane and  $r\theta$ -plane as well as acquire PIV data is achieved best with commercial software, and finally (5) an externally-applied magnetic field is able to influence the APPT plasma flow field significantly. This chapters sections are outlined as follows: (1) a discussion of the parameters utilized to develop and diagnose an APPT, (2) the results of performing the 2DMIM method to obtain the plasma temperature and degree of ionization, (3) PIV analysis of the Mie scattered particle fields and the ns-PIV measurements that were obtained, and (4) the deflection and suppression results of the plasma flow field due to the presences of various orientations and magnetic field strengths.

These results will finalize the achievement of the goal of this dissertation to develop the experiment to investigate the magnetohydrodynamic Richtmyer-Meshkov instability.

#### 4.1 Operating Conditions of a Nitrogen APPT

There are three basic parameters utilized when developing and diagnosing an APPT: arc voltage, arc current, and gas flow rate (both axial and tangential flow rates). The parameters used are shown in Table 4-1. These three parameters were optimized to produce a stable laminar APPT with the longest jet length possible.

**Table 4-1:** Parameters varied to produce a long, laminar, stable APPT.

Parameter	Value	Units
Nozzle Diameter	4	mm
Arc Voltage	40–60	V
Arc Current	100–200	A
Total Circuital Power	4-15	kW
Power Resistors	0.23	$\Omega$
Working Gas	nitrogen	
Total Gas Flow Rate	2–11	SLM
Axial Gas Flow Rate	1–10	SLM
Tangential Gas Flow Rate	10–50	%

The jet length was first measured using visible spectrum emissions, imaged by a DSLR camera. Figure 4.1 shows a visible spectrum emission image of the torch in operation (right) and a calibration image for measuring the torch height (left).

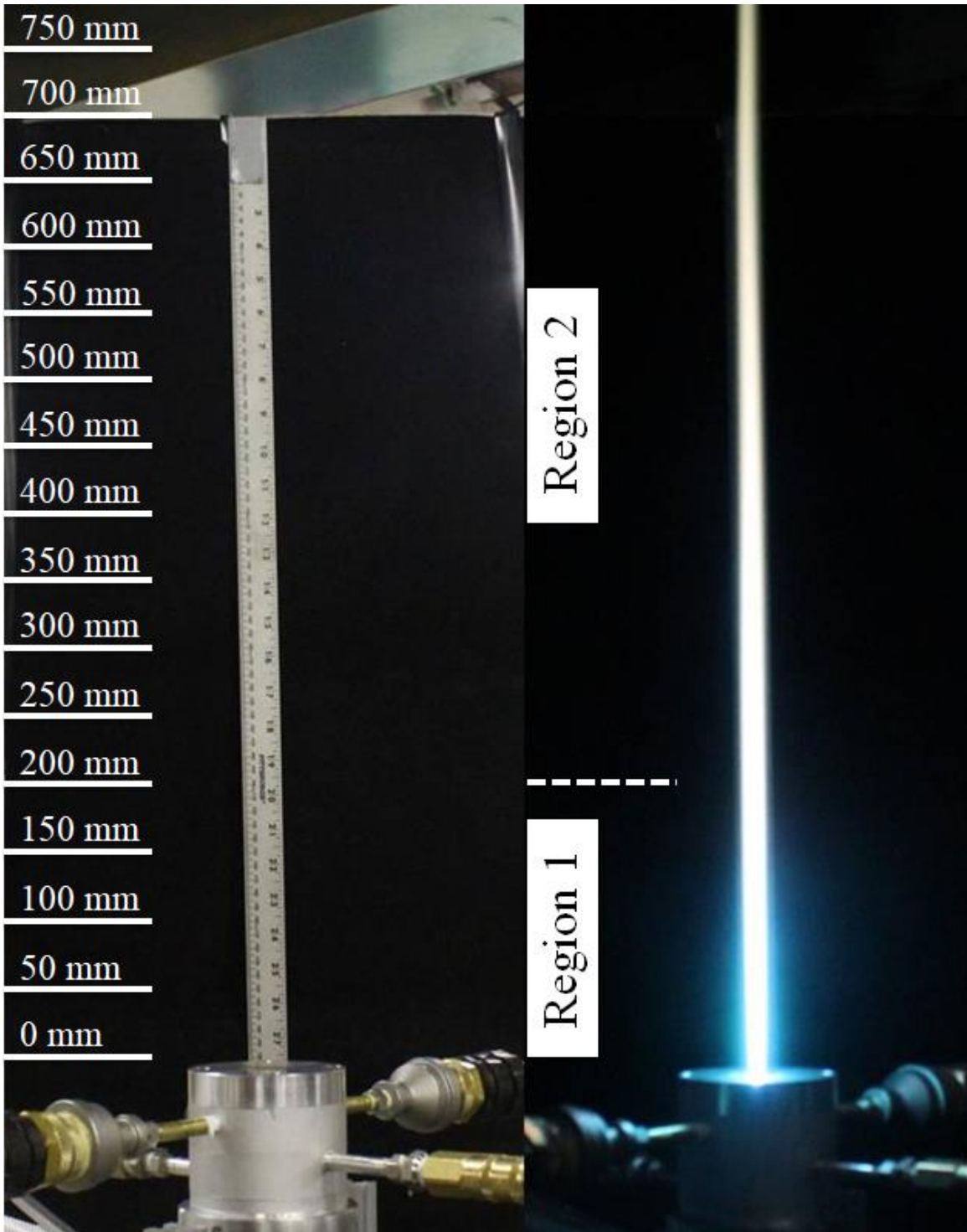


**Figure 4.1.** Calibration image (left) and APPT image (right) showing ionized region jet length (Region 1) at 20 cm and total jet length (Region 2) at 80 cm in length.

The image on the right of Figure 4.1 was taken when the torch was operated with an arc current of 170 A, an arc voltage of 49 V, and gas flow rates of 3.2 SLM axial and 0.6 SLM tangential. As shown in the right image of Figure 4.1, two distinct regions are visible. Region 1 is a highly luminous core surrounded by a luminous aureola termed, the “Ionized Region.” Region 1 contains both ions and electrons, and is dominated by various types of collisions obeying the local quasineutrality assumption; thus, a plasma. Region 2 hosts both excited atoms and collisions but does not constitute a plasma, as there are no longer photons emitted at wavelengths corresponding to the ionized emission spectrum because the electrons are no longer separated from their nuclei; rather, the hot gas is simply incandescent.

Often, distinguishing between what is truly plasma (Region 1) and what are merely thermal emissions from non-ionized hot gas (total jet length) is forgone, because total jet length is equated to plasma length. To separate these regions, images were taken with a DSLR camera for diagnosing the total jet length while simultaneously capturing images of isolated nitrogen emissions at 528.12 nm using a charge-coupled device (CCD) camera equipped with the  $532 \pm 1$  nm laser line filter to measure what is termed the ionized region jet length. For diagnostic purposes, the nozzle diameter of the APPT was set to 4 mm and the nozzle length was 28 mm. These two parameters were chosen based on preliminary experiments showing that a smaller nozzle diameter (vs. 6, 8, or 10 mm) and long nozzle length (vs. 18 or 23 mm) allowed for an adequate flow development region within the torch and eliminated turbulence. Longer nozzle lengths greater than 28 mm were also tested, but they reduced the ionized region jet length.

Shown in Figure 4.2 are the V–I characteristics of the APPT for three gas flow rates. The three gas flow rates used consisted of axial gas flow rates of 5, 7, and 10 SLM with the tangential flow rate kept constant at 1 SLM. The arc current was set by the HCDC power supply and the corresponding arc voltage was recorded.

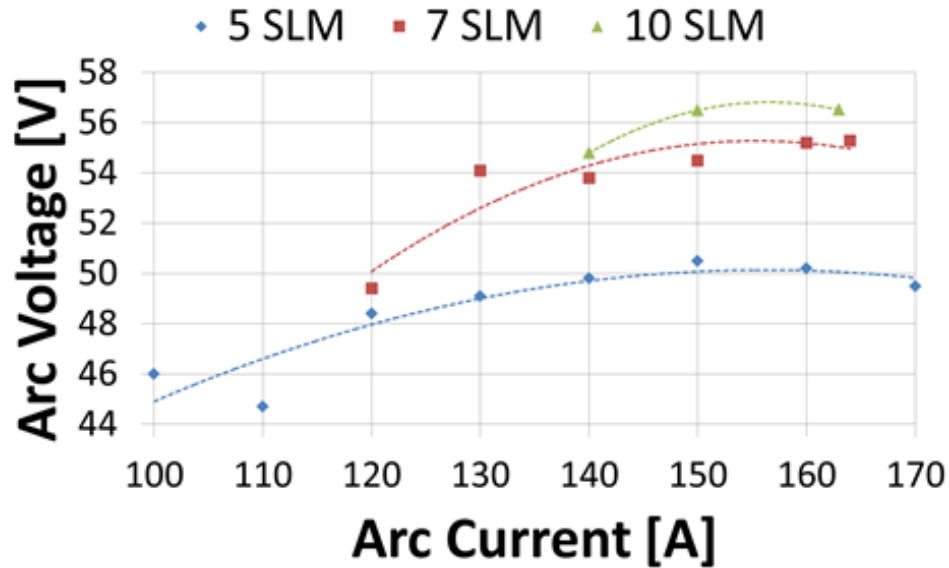


**Figure 4.2.** V–I characteristics of APPT with nitrogen gas flow rates of 1 SLM tangential and 5, 7, and 10 SLM axial.

As seen in Figure 4.2, keeping the gas flow rate constant and increasing the arc current increases the arc voltage. As the gas flow rate increases at a constant arc current, so too does the required arc voltage.

Figure 4.3 displays both the total jet length and the ionized region jet length as the axial gas flow rate was increased. The tangential gas flow rate and the power delivered to the arc were both held constant at 1 SLM and 15 kW, respectively. The power was held constant by operating the HCDC power supply in constant power mode. As the axial gas flow rate increased, the total jet length increased up to 3 SLM, followed by a decrease

thereafter. This was visually determined to be the result of a transition between laminar, transitional, and turbulent flow.

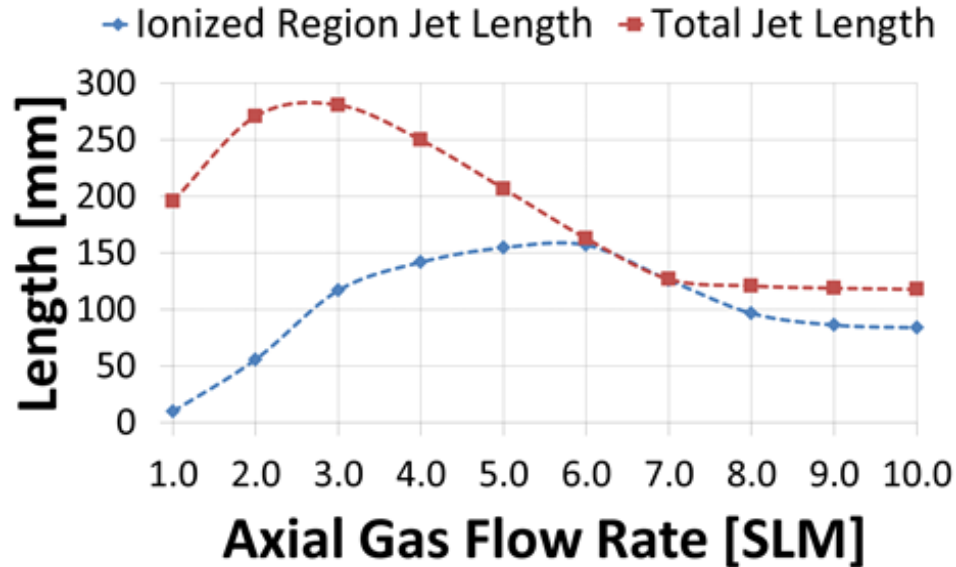


**Figure 4.3.** Ionized region jet length and total jet length vs. varying axial gas flow rate at constant tangential gas flow rate of 1 SLM and constant power of 15 kW.

Interestingly, although the overall jet length began to decrease as the axial flow rate increased past 3 SLM, the ionized region jet length increased until it became nearly equivalent to the overall jet length at axial flow rates of 6–7 SLM. Axial flow rates of 7 SLM or greater resulted in turbulent effects dominating the flow, and thus a slow decrease of both the ionized region jet length and the total jet length. Thus the conclusion made, is the tallest jet length doesn't indicate the tallest plasma-containing region length.

The last study performed when developing the APPT was to determine how the ratio of axial to tangential gas flow rates affected the total and ionized region jet lengths. This was accomplished by operating the torch's high current DC (HCDC) power supply in constant power mode (15 kW) and keeping the overall gas flow rate constant while varying the ratio of axial to tangential gas flow rates from 10% to 50%. The resulting plot

for using total gas flow rates of 3 SLM and 5 SLM is shown in Figure 4.4. As this plot shows, the jet length was not strongly affected by the flow ratio, though the longest jet lengths were achieved at a ratio of 70% axial to 30% tangential gas flow rate.

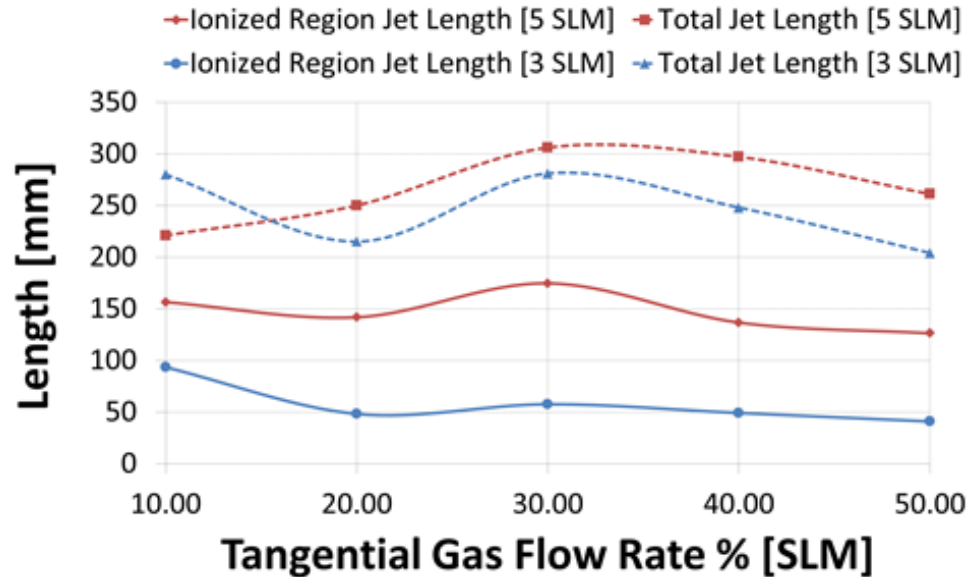


**Figure 4.4.** Ionized region jet length and total jet length vs. percent of tangential gas flow rate for total gas flow rates of 3 and 5 SLM.

While performing this diagnostic technique, other important factors, specifically repeatability of jet length observations, deserve consideration. The overall jet length as shown in Figure 4.1 does not coincide with the lengths portrayed in Figure 4.3 and Figure 4.4. This is attributed to the fact that a newly constructed nozzle anode section and cathode tip, not yet subjected to ablation and erosion effects, produces a much longer, laminar jet. As the APPT is operated, the initial jet length as observed in Figure 4.1 decreases, but over time ( $\approx 10$  min) settles into a stable condition where reproducible lengths are observable for many hours of operation. While the results portrayed in this diagnostic section are similar to results published in literature, installing fresh components for each jet length data point would be extremely arduous. Should new

components be installed, the results will scale accordingly; ultimately yielding the same overall trends for jet length optimization and ionized region versus total jet length. Future design modifications may allow for maintaining this initial longer total jet length. However, the ionized region, necessary for future MHD–RMI experiments, is not significantly affected by overall jet length, so constantly swapping fresh components may not be beneficial. Now that the plasma torch has been characterized, the results of diagnosing it, using the methods discussed in Sections 3.3.2–3.3.4, are presented in the following section.

## 4.2 2DMIM Plasma Temperature and Degree of Ionization

The results of computing the 528.12 nm emission line’s normalized theoretical total line emission coefficient over a range of temperature, governed by Equation (3.2), is shown in Figure 4.5. The tabulated values required to do so are presented by Capitelli *et al.* in Refs. [72], [75].

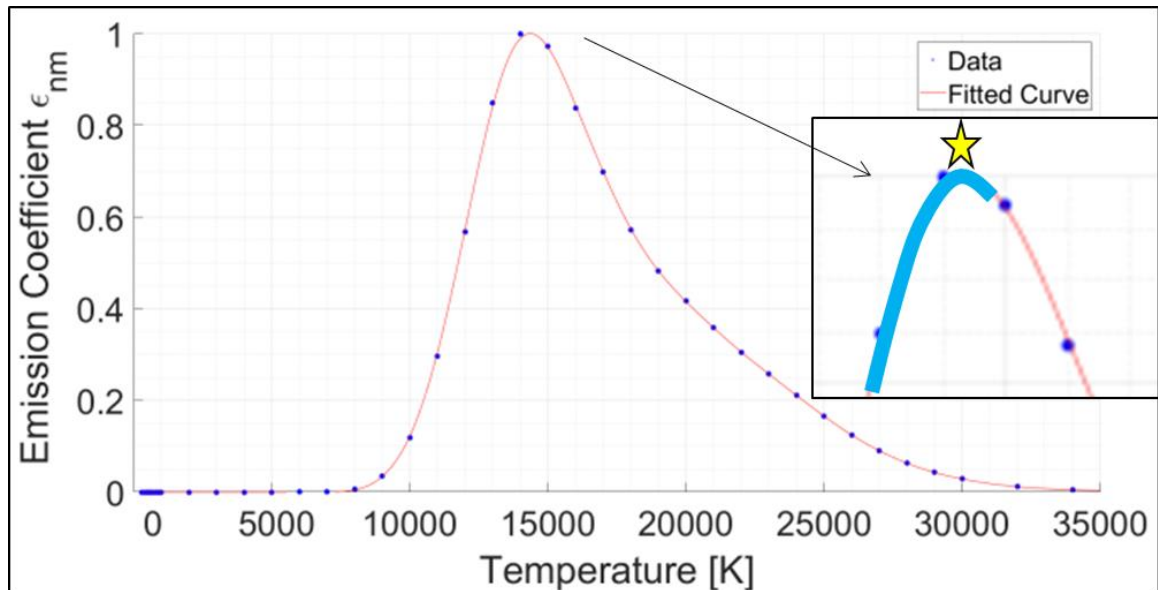


**Figure 4.5.** Theoretical normalized total line emission coefficient vs. temperature for 528.12 nm N-I emission line.

The tabulated values found in Ref. [75] are at  $T = 1000$  [K] intervals; thus the author developed a MATLAB script to curve-fit a shape-preserving smoothing-spline to this data; increasing the resolution accuracy by three orders of magnitude. As Figure 4.5 shows, there exists a peak emission coefficient value (yellow star) corresponding to the normal temperature value for singly ionized nitrogen emission. Figure 4.5 only shows the normalized emission coefficient for the 528.12 nm line for computational purposes and is comparable to other sources emission coefficient computation efforts [58]. Also shown in Figure 4.5 is a thick blue line which represents to desired “off-axis-maximum” required to perform the 2DMIM. The resulting mole fraction for each as computed from Equation (3.18)–(3.20), can be visualized in Figure 4.6 where the second ionization reaction, from Equation (3.4c), was also included to achieve better accuracy when computing the degree of single ionization in the APPT.

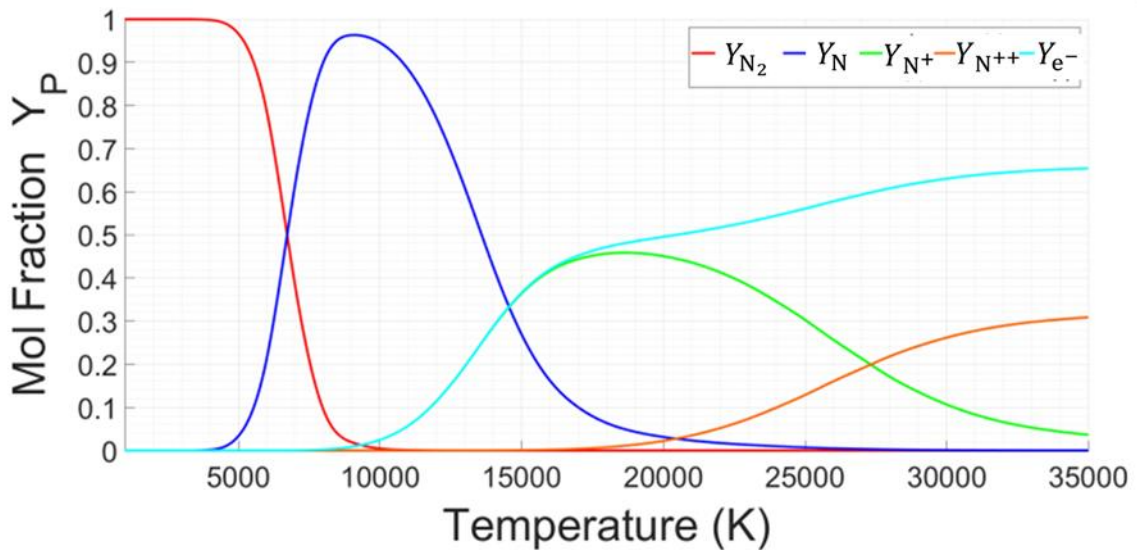


**Figure 4.6.** Mole fractions of molecular nitrogen ( $N_2$ ), atomic nitrogen ( $N$ ), singly ionized nitrogen ( $N^+$ ), doubly ionized nitrogen ( $N^{++}$ ), and electrons ( $e^-$ ) vs. temperature.

Calibration of the radial temperature distribution versus intensity was performed by first deriving the radial temperature distribution from the measured radial intensity

distribution of our APPT while temporarily converted into a transferred arc. As mentioned in Section 3.3.4, calibration required observation of the arc, where the normal temperature could be observed as an off-axis maximum in intensity. The calibration image used to do so is shown in Figure 4.7, where the arc current was set to 200 A, the gas flow rate was set to 3 SLM, and the distance between the cathode and anode was 3 mm. The yellow line indicates row of pixel data used for calibration of off axis maximum emission coefficient. The magenta line indicates central axis of arc.

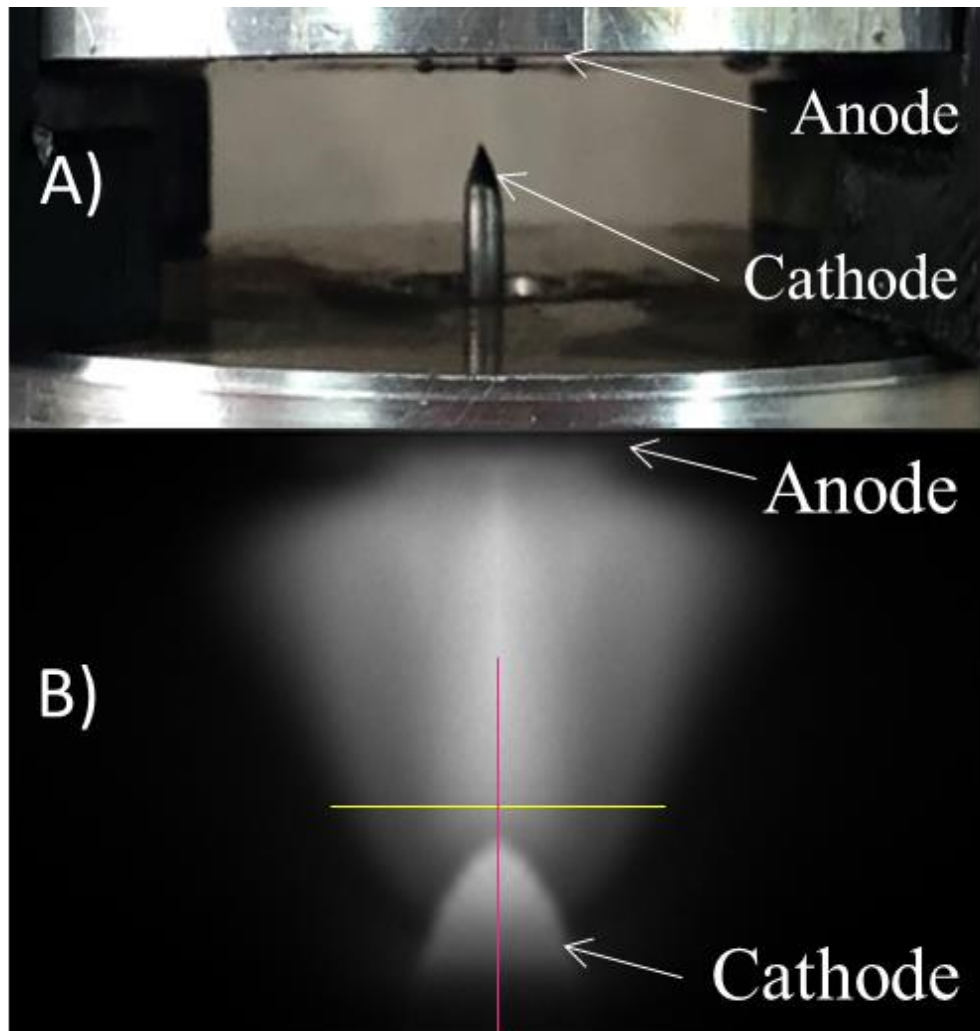


**Figure 4.7.** Images of: A) APPT transferred arc apparatus close-up, and B) transferred-arc RAW data CCD image taken for calibration of the optical system.

The off-axis maximum radial emission coefficient and normal temperature occurred 0.3 mm above the thoriated tungsten cathode tip. Although this observation fulfilled the Fowler–Milne-based 2DMIM implementation requirements, the decrease in the Abel inverted emission profile towards the centerline of the transferred arc (*i.e.*, off-axis maximum) was less pronounced when observing the 528.12 nm lines emission than previous observation of the 746.83 nm line reported by Haider and Farmer [58]. As previously mentioned in Section 3.3.4, this is attributed to the 746.83 nm line’s upper and lower energy levels being more readily achieved (satisfied), as well as the 746.83 nm line having an increased oscillator strength and transitional probability. Therefore, observation of the off-axis maximum normalized emission coefficient, where a more pronounced decrease in number density, corresponding to a higher temperature towards the center axis of the arc, is deemed easier to measure spectroscopically when observing the 746.83 nm line than for the 528.12 nm emission line of dissociated nitrogen.

With the optical system calibrated, spatially-resolved 2-D temperature and degree of ionization profiles were then produced for the APPT in the non-transferred arc configuration. Performing the Abel inversion on the non-transferred APPT’s intensity image was done for each row of data such that the maximum intensity value was taken to correspond to the centerline axis of the torch. The left and right side of the image acquired by the CCD camera (relative to the centerline of the torch) was then Abel inverted separately so as to preserve some of the torch asymmetry. The left image in Figure 4.8 shows the bandpass-filtered image (528.12 nm line emission), temperature (center), and degree of ionization (right) profiles of the APPT operated at 2.1 SLM axial and 0.9 SLM tangential gas flow rates with an arc current of 200 A. These parameters

were chosen to ensure that the entirety of the plasma-containing region would be captured and to ensure a high level of spatial resolution ( $540 \times 2100$  pixels) would be achieved. This level of spatial resolution is an order of magnitude greater than traditional spectroscopic or monochromatic plasma diagnostic techniques as well as it is instantaneously resolved, a condition not met by these traditional methods [58, 59].

Ionized region jet lengths greater than the one imaged in Figure 4.8, ultimately result in the entirety of the plasma containing region not being captured by the calibrated optical system. That is, the transferred arc, used for calibration, was set at a distance such that sufficient resolution could be achieved. Subsequent measurements of the non-transferred APPT must be kept in the same position, limiting the camera's field of view. Larger torches were imaged, but the entirety of the ionized region was not visible.

The total jet length achieved for these conditions was 280 mm. However, the ionized region jet length was only 64 mm for this specific case, as shown in Figure 4.8. As the plasma is ejected out of the nozzle, the intensity values measured decreases both axially and radially. This is due to recombination, de-excitation, and diffusion effects that return the ionized gas ( $N^+ + e^-$ ) to its dissociated (atomic nitrogen, N) and then initial (molecular nitrogen,  $N_2$ ) state. The maximum plasma temperature occurred at the exit of the nozzle and was found to be nearly that of the normal temperature,  $\sim 14,000$  K with a maximum degree of ionization of  $\sim 27\%$ . This is to be expected as arc root attachment within the nozzle is very close to the exit. Additionally, the radial temperature profile just above the nozzle exit is shown in Figure 4.9.

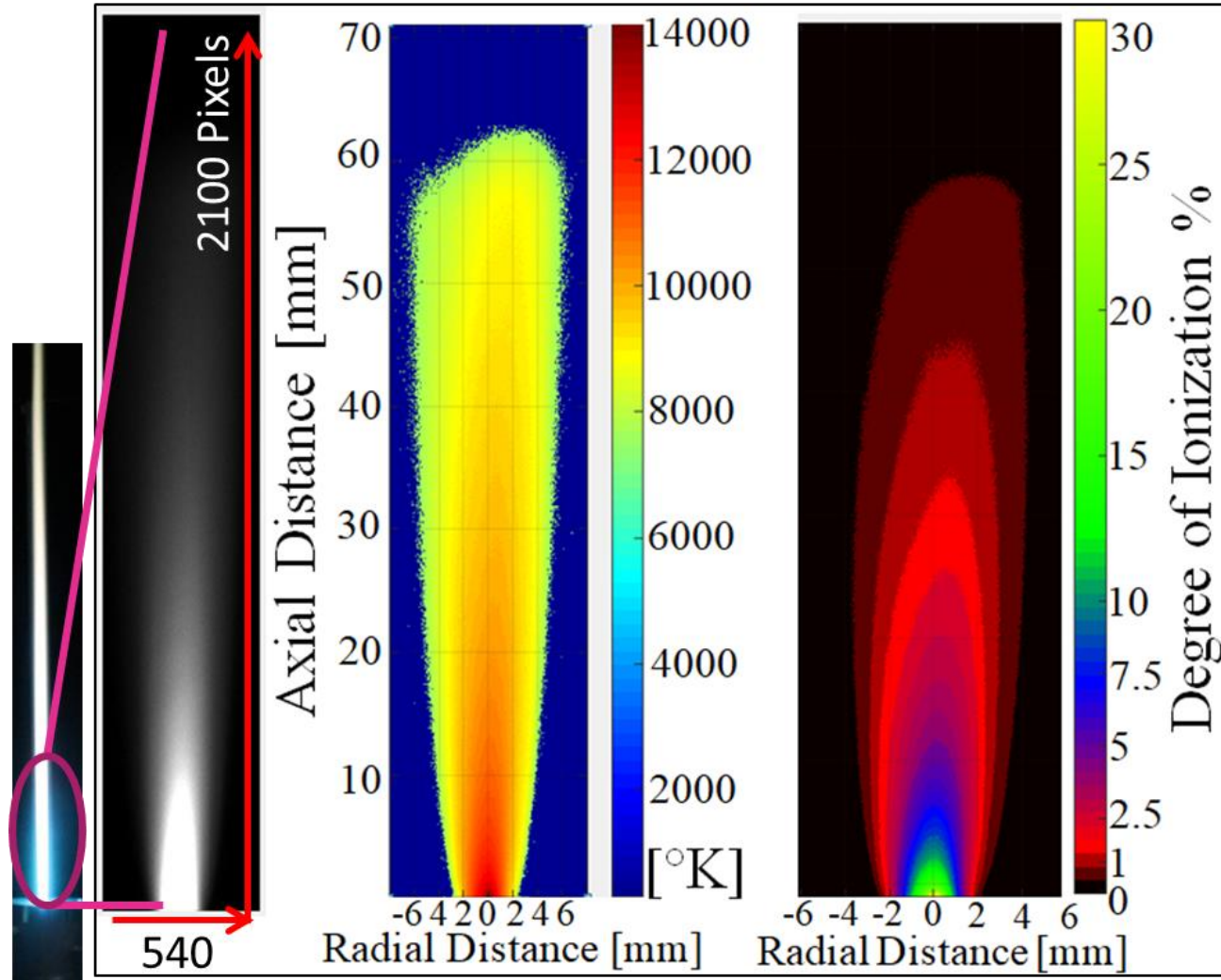


**Figure 4.8.** RAW data CCD image taken (left), plasma temperature plot in  $rz$ -plane (middle), and degree of ionization plot (right) for 2DMIM applied to APPT at 2.1 SLM axial, 0.9 SLM tangential gas flow rates, and an arc current of 200 A.

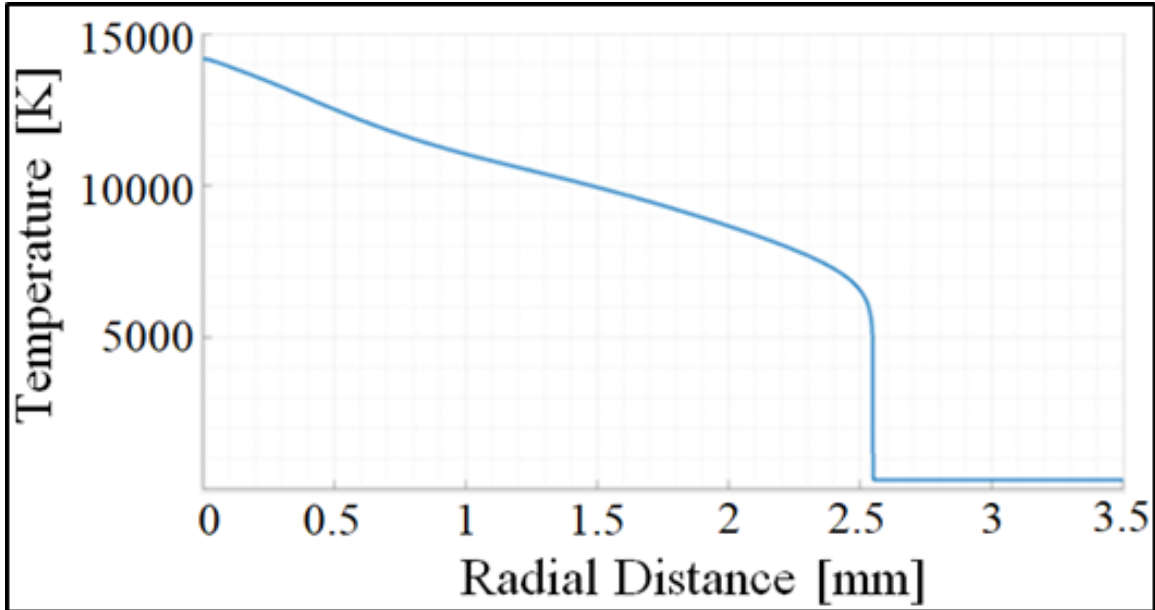


**Figure 4.9.** Radial temperature distribution profile at nozzle exit for APPT as shown in Figure 4.8.

Previous monochromatic and spectroscopic investigations of APPTs have depicted a Gaussian profile when examining the radial temperature distribution. Performing the 2DMIM however allows for more accurately defined profile to be achieved that shows the profile is, in fact, non-Gaussian. At the edge of the plasma-atmosphere interface there is a steep, noticeable, and clearly defined gradient where the temperature drops sharply from  $\sim 7450$  K to equilibrium with atmospheric (room) temperature  $\sim 300$  K. This is explained by comparing the results shown in Figure 4.6, with the results of Figure 4.8, where there is no longer any significant presence of electrons or ions able to be measured by the diagnostic equipment utilized, below this temperature, and thus no emission.

### 4.3 Plasma-Particle Field Interface Imaging via PIV apparatus

The main goal of implementing these experimental methods, as previously stated, was to develop the ability and capability to image the evolution of the MHD–RMI experimentally within the FMSTL shock tube. This section shows the results of first, the ability to visualize the plasma-particle interface by the use of a particle laden flow field in the  $rz$ - and  $r\theta$ -plane. Second, the results of obtaining PIV measurements of particle field in the  $rz$ -plane using Insight 4G. Third, shows the results of processing the image pairs and the resulting velocity vector fields as obtained using PIVlab. Finally, compares the  $rz$ -plane velocity vector field data between the two software platforms utilized.

#### 4.3.1 *Imaging the $r\theta$ -Plane for Future MHD–RMI Experiments*

The plasma emission was found to be much greater than the illuminated particle field over a longer exposure (100  $\mu$ s) as seen in Figure 4.10 (a) on pg. 136, necessitating the use of a narrow bandpass filter. Keeping the CCD camera exposure (duration of intensity data acquisition) to 100  $\mu$ s (near the limit of the camera) also minimized the continuous plasma emission intensity integrated over the duration of the exposure. Since the duration of the laser pulse, and thus particle field illumination time, are approximately 4 ns, the reflected laser signal compared to the plasma emissions will increase as the exposure time is decreased to 4 ns. From Figure 4.10 (b), it can be seen that plasma emission is still visible while using the  $532 \pm 10$  nm filter but that there is a large reduction in the illumination intensity of the plasma when compared to using no filter, Figure 4.10 (a). Here, the laser illuminated particle field intensity is on the same order to that of the plasma emission intensity.

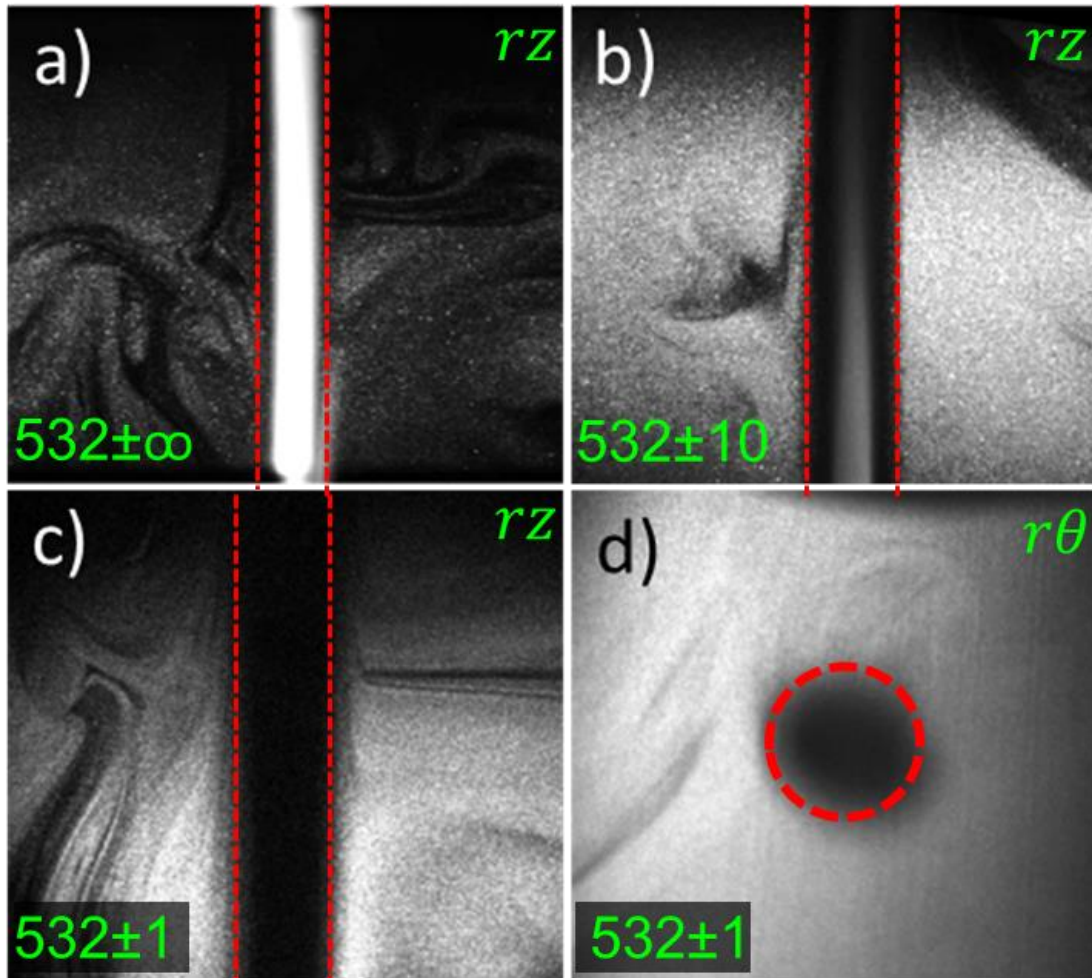


**Figure 4.10.** CCD images of  $rz$ -plane taken as shown in: (a) without any bandpass filter present, (b) with the  $523 \pm 10$  nm bandpass filter present, (c) with the  $523 \pm 1$  nm laser line filter, and (d) in the  $r\theta$ -plane taken with  $523 \pm 1$  nm laser line filter present. Red dashed lines indicate plasma boundary.

Additionally, there is a boundary layer evident between the plasma and the surrounding particle-laden atmosphere. This is consistent with the results shown in Figure 4.9 where the particles that would otherwise be present, have evaporated due to the high temperature imposed on them by the plasma. The  $\text{TiO}_2$  particles melting temperature is 2,116 K while the vaporization temperature 3,245 K. Using simple 1D calculation for particle heating and phase change the particle life is estimated to be on the order of 100  $\mu\text{s}$  [85, 86].

The elimination of the plasma emission is visible in Figure 4.10 (c), where the dark column in the middle of the figure is the plasma flow field region. Additionally, the illuminated particles appear only in a circular section of the camera field-of-view with the narrow bandpass filter affixed even though particles in the full field-of-view are illuminated by the laser sheet. This is attributed to the angle of incidence of scattered (reflected) light from the particles (rays), as the wavelengths passed by the narrow bandpass filter shift towards the blue spectrum (the center wavelength of 532 nm is blocked) as the angle of incident light decreases. Thus, less particle illumination (*i.e.* laser light reflected off the particles as convergent or divergent rays) is passed through the  $532 \pm 1$  nm laser line filter in regions away from the center of the field-of-view. Also seen in Figure 4.10 (a–c), are structures formed outside the plasma boundary (shown in dashed red lines) which occur due to particle injection into the atmospheric surroundings within the MT section.

To visualize the  $r\theta$ -plane, the laser sheet was rotated  $90^\circ$  and the following image shown in Figure 4.10 (d), resulted. As with many PIV experiments implemented to investigate hydrodynamic instabilities such as the RMI, a cross-sectional image of the  $r\theta$ -plane is desired to deduce the extent of the instability that arises, post shock conditions, as it evolves in time. Since the  $r\theta$ -plane is not able to be captured with the camera positioned directly above the plasma jet column, the image was acquired at an off-axis angle from the plasma column (perpendicular to the laser sheet) and the image was corrected using the Scheimpflüg principle. Therefore, developing this method can be used for PIV measurements in future MHD–RMI experiments once implemented in the FMSTL shock tube. Additionally, visualization of the  $r\theta$ -plane allows for confirmation

of the hydrodynamics and morphology that ensue and potentially the suppression of the HI itself where the mosaic below, in Figure 4.11, shows the desired result from simulations.

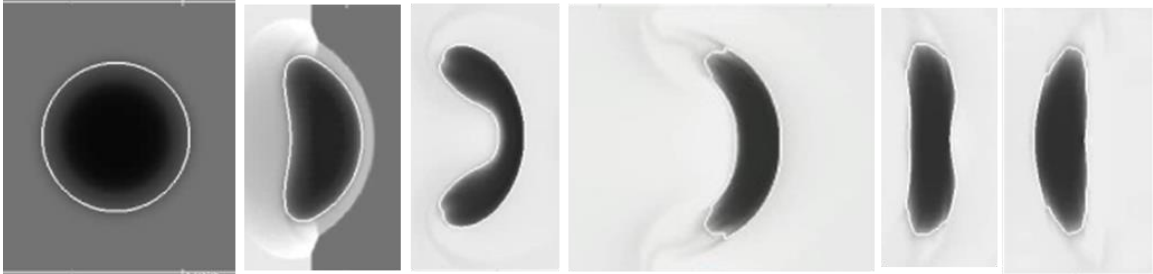


**Figure 4.11.** The desired hydrodynamics and morphology PIV goal of MHD–RMI experiment in the  $r\theta$ -plane.

#### 4.3.2 PIV Data Processing of the $rz$ -plane in *Insight 4G*

This section provides the results of the particle image velocimetry “tool” that was developed to acquire ns-PIV data on the interface morphological development within future shock-driven MHD–RMI experiments. Since the MHD–RMI has yet to be experimented in the FMSTL, the results provided in this section are from the PIV tool being applied on the plasma-atmospheric boundary in the  $rz$ -plane. The goal of this PIV tool is to produce PIV fields which will look similar to the one shown in Figure 4.12 which shows the morphology of a shock-driven multiphase instability (SDMI) shock tube experiment in the  $r\theta$ -plane. While this tool was being developed, SDMI experiments were occurring at the FMSTL. Thus, the author utilized this tool on a non-ionized gas SDMI interface image pair to verify, preliminarily, that if a cylindrical interface was shocked within the FMSTL shock tube, whether or not the tool developed would generate the appropriate velocity field associated with the instability and morphological development. By doing so, the conclusion was deduced that, if this PIV tool could be

implemented on a non-ionized gas interface in the  $r\theta$ -plane, and, if this tool could be utilized to acquire ns-PIV data on the plasma-atmospheric interface in the  $rz$ -plane, then it could ultimately be effectively used in future MHD–RMI experiments in the  $r\theta$ -plane.

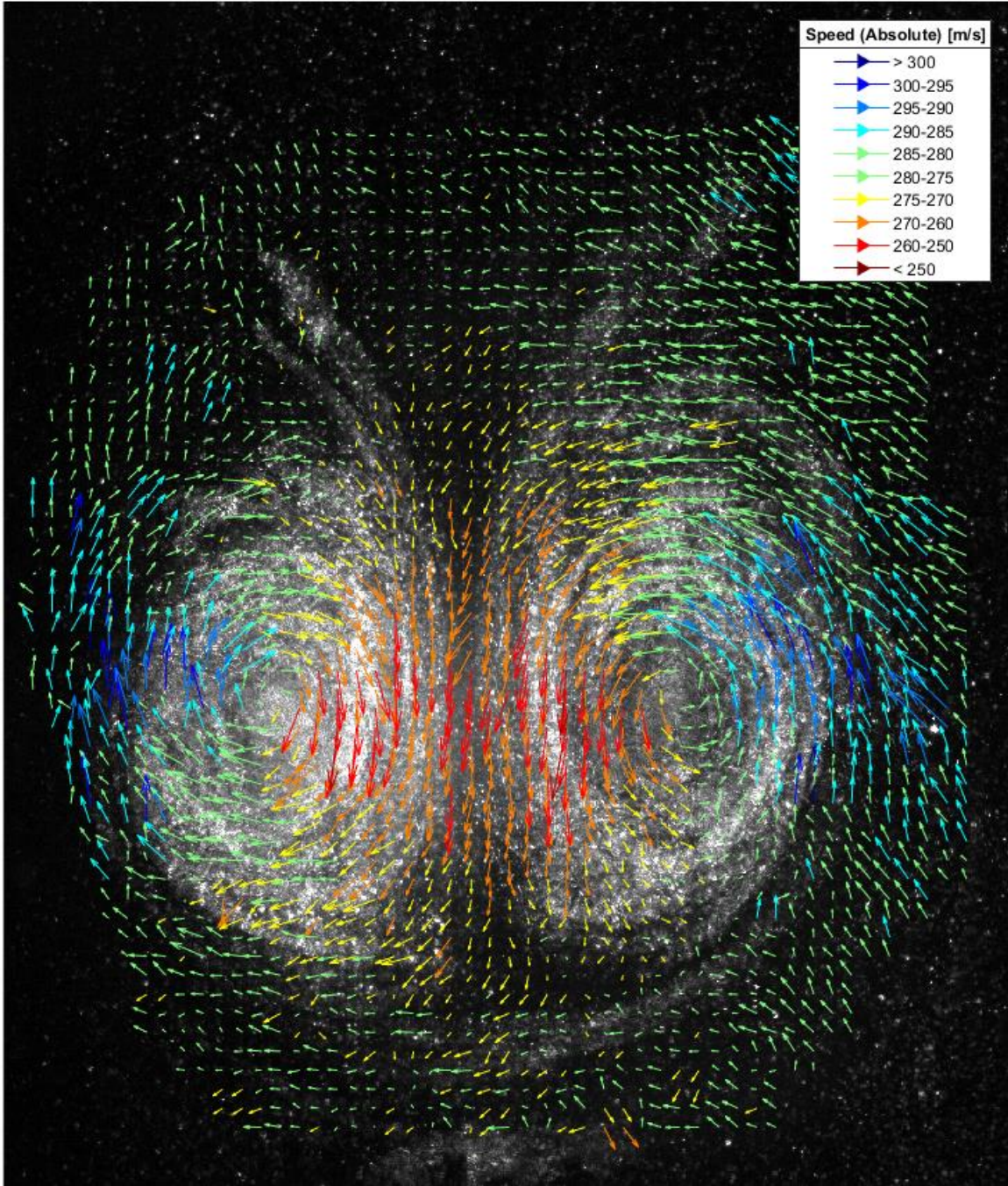


**Figure 4.12.** The desired hydrodynamics and morphology PIV goal of RMI–MHD experiment in the  $r\theta$ -plane as applied to an SDMI interface produced in the FMSTL.

Because this PIV tool could effectively be applied to the SDMI interface, the next step taken was to acquire plasma-atmospheric interface in the  $rz$ -plane. Thus three cases were tested to obtain PIV velocity field data of the particle laden flow field within the Mock Tube apparatus, described in Section 3.3.5, as the plasma flow field propagated through the particle-laden flow field, using Insight 4G. Keeping the tangential gas flow rate constant at 0.8 SLM, the arc current at 175 A, and the power at 15 kW, the APPT axial gas flow rate was varied from 1.6, 3.2, and 4.8 SLM, respectively. The CCD camera, affixed with the Thor Labs  $532 \pm 1$  nm laser line filter, obtained image pairs for each of the three cases. These image pairs are shown in Figure 4.13–Figure 4.15.

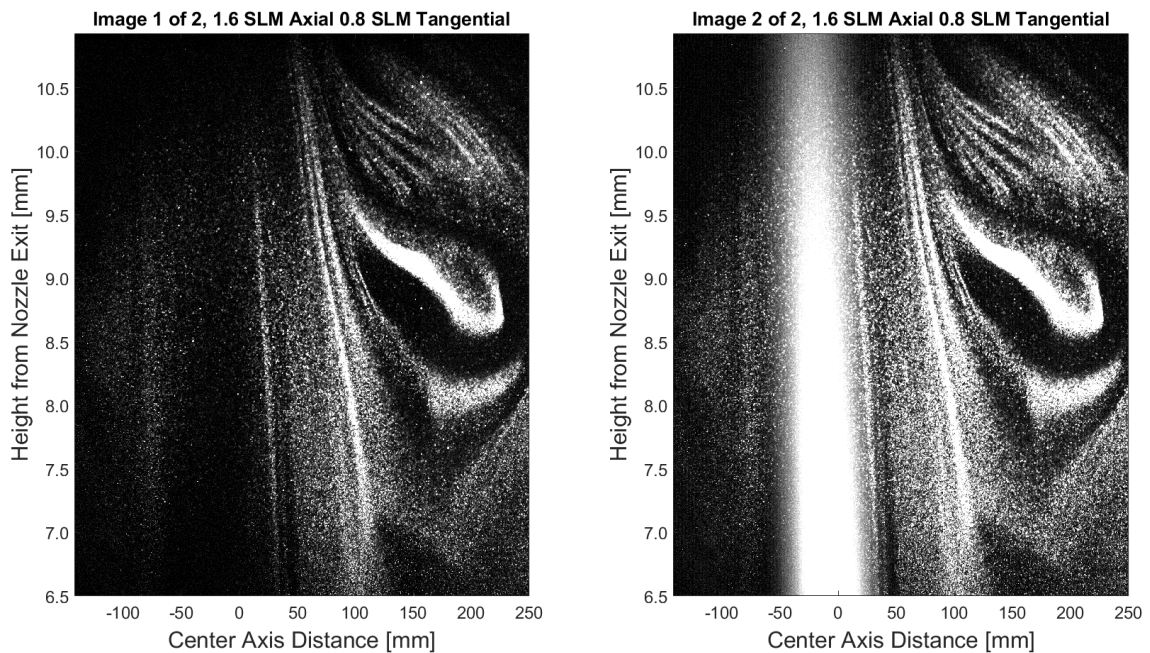


**Figure 4.13.** ns-PIV Case 1: 1.6 SLM axial gas flow rate PIV image pair.

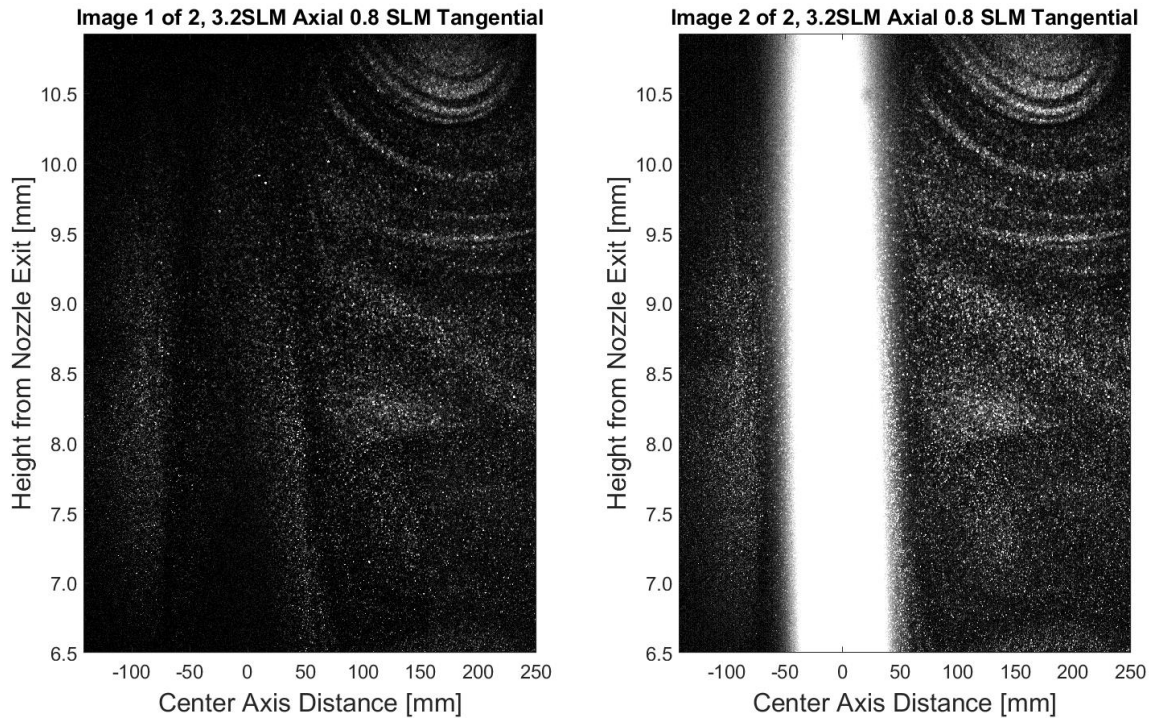


**Figure 4.14.** ns-PIV Case 2: 3.2 SLM axial gas flow rate PIV image pair.

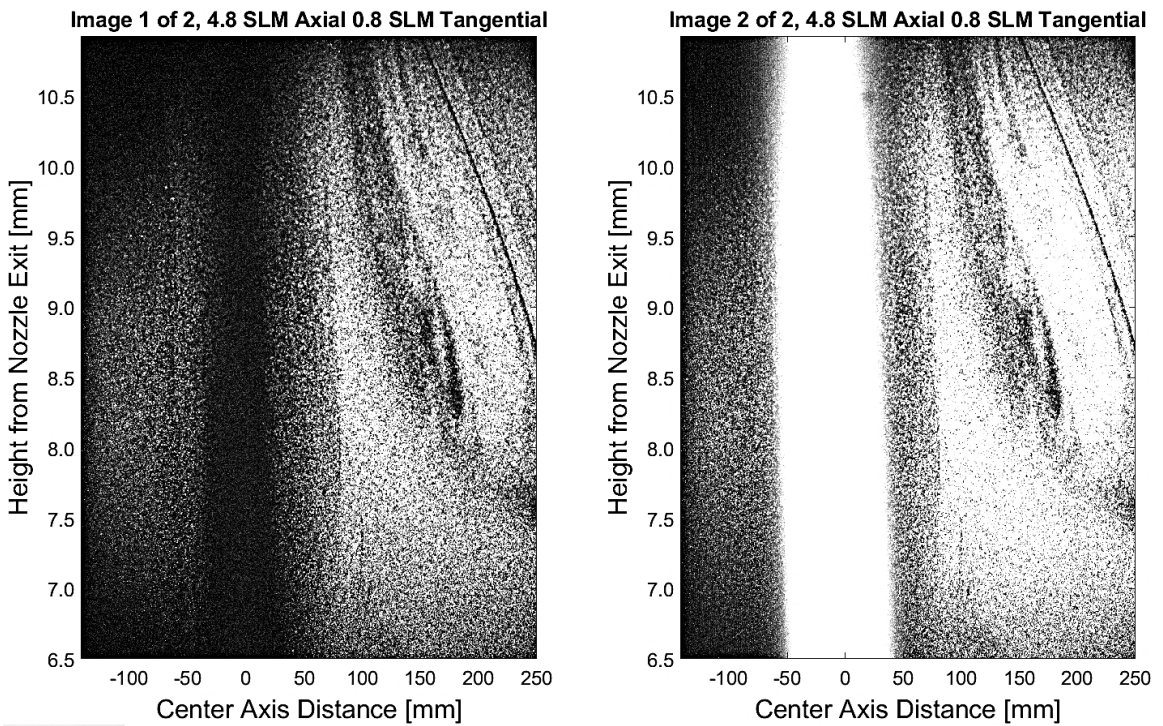


**Figure 4.15.** ns-PIV Case 3: 4.8 SLM axial gas flow rate PIV image pair.

As seen in these three figures, a saturated particle field surrounding the plasma flow field was generated. In each of the second images of the three figures, the emissions from the plasma are evident even with the filter present. The reasoning the plasma emissions are absent in the first of the two images for each of the three cases is because the plasma emissions are relatively weak when integrated over a short time while the laser is still strong (pulse length is only  $\approx 5$  ns). In the second frame of each set, the software is unable to correctly limit the exposure time, and more light (emissions) from the plasma is accumulated in the images. This undesirable effect can be eliminated with additional high-tech custom imaging components and filtering techniques to be developed for future MHD–RMI experiments. Fortunately, this error does not inhibit the ability to obtain and analyse PIV data accurately.

Once the image pair vector fields were filtered, processed, and post processed in Insight 4G as described in Section 3.3.6 the data was then processed in a custom MATLAB script developed by the author, to produce the histograms displaying the velocity magnitude (speed) of the particles for each respective case. These histograms can be seen in Appendix A.6. The histograms, were in turn used to fine tune the PIV processing algorithm implemented in Insight 4G. After obtaining many image pairs for each of the test cases, refinement of the PIV tool was achieved and utilizing image pairs, such as the ones shown in Figure 4.13–Figure 4.15, ns-PIV data was produced. For the sake of brevity, only ns-PIV data in the  $rz$ -plane for the second test case is presented within this section and is shown in Figure 4.16.

## PIV Particle Speed Analysis (1 of 2) 3.2 SLM Axial 0.8 Tangential Gas Flow Rate

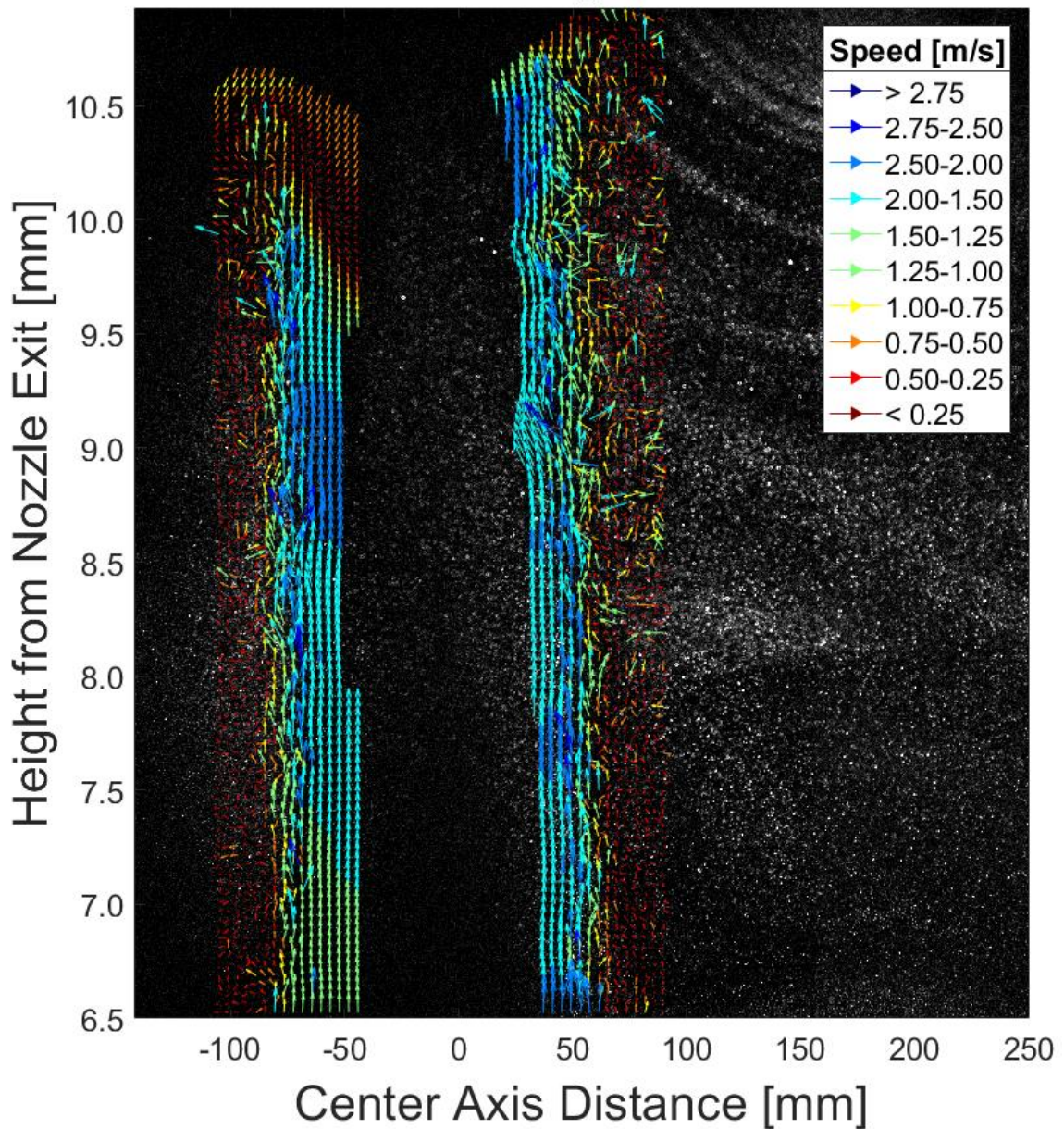


**Figure 4.16.** ns-PIV Case 2: 3.2 SLM axial flow rate PIV velocity vector field with particle speed colormap.

Between the three test cases studied, there is strong similarity between the resulting PIV velocity vector profiles. As axial gas flow rate was increased, the speed of the particles is increased as they translate closer to the plasma flow field. Additionally,

the width of the particles increasing in speed (relative to the plasma-atmospheric boundary) also increases. Thus not only is there a steeper velocity gradient at this boundary but the particles begin to gain momentum as they propagate closer to the plasma flow field.

Thus the ability to perform PIV data acquisition on a particle-laden flow field surrounding the plasma flow field at different velocities is achieved. This in turn would be the setup and baseline parameters utilized during future MHD–RMI experiments in the shock tube setting for both the  $rz$ -plane and subsequently, the  $r\theta$ -plane to determine the velocity fields of the interface morphology and quantify the resulting MHD–RMI instability’s development and suppression.

#### *4.3.3 PIV Data Processing of the R-Z plane in PIVlab*

The same three test cases (image pairs) used for obtaining PIV data via Insight 4G, were used in computing the resulting PIV velocity vector fields in PIVlab. Before doing so, manual intensity reduction filtering of the plasma emissions which evident within the second image of each case’s image set, was performed in a custom MATLAB script prior to PIVlab processing in order to reduce the high intensity emissions from producing errors in the resulting PIV data generated. This was achieved by analyzing the columns of intensity data of the second image where the plasma emissions were evident. Within this region a “for loop” was implemented such that any cell (pixel) with data that had a mean intensity value (within a  $5 \times 5$  pixel area) greater than the maximum intensity of the particle field surrounding the plasma emissions area was reduced by an order of magnitude. Setting the ROI and the masked region (area to exclude from computation)

was also done prior to PIV processing in the PIVlab's GUI. The original image, the resulting filtered image, and the ROI and masked area (constructed from a polyline in the mask area GUI) are shown in Figure 4.17 below. This same filtering scheme was implemented on all three test cases second images. The result of implementing the post-processing filters, as described in Section 3.3.6, is shown in Figure 4.18.

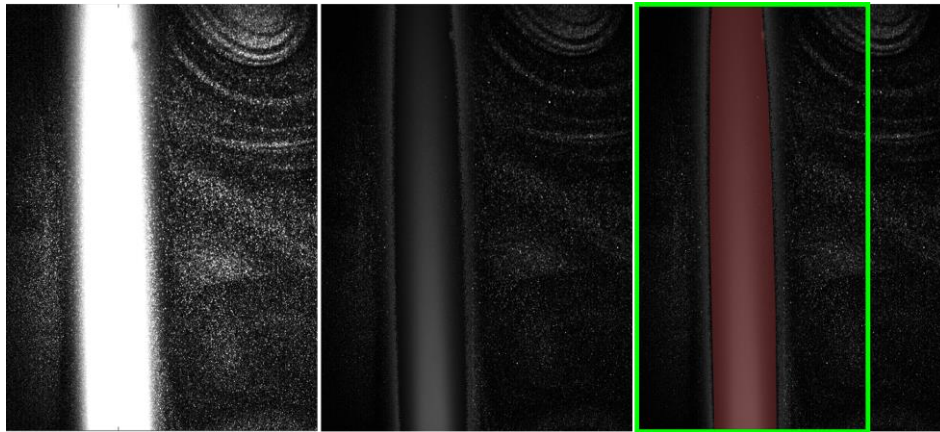


**Figure 4.17.** RAW image 2 of 2 (on the left), filtered image (in the center), and with the ROI [as green line] and masked area [in red region] (on the right) for Case 2 as processed in custom MATLAB script and then in PIVlab's GUI.

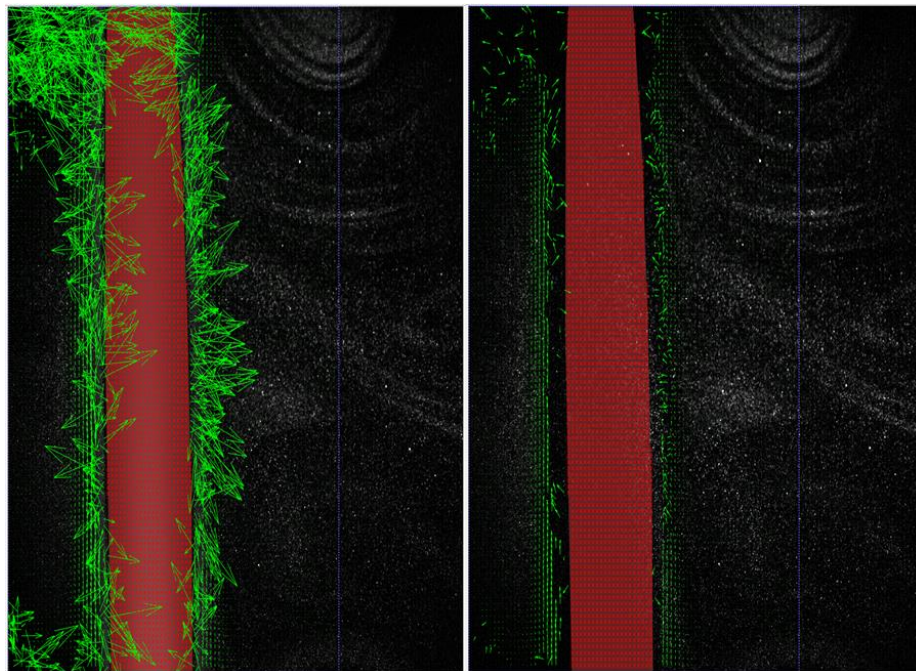


**Figure 4.18.** Case 2 data before post-processing (left), and after post-processing (right).

As seen in the right image of Figure 4.18, the elimination of a large majority of spurious velocity vectors is evident. This is important when finalizing the resulting PIV data that ensues while using PIVlab since it is not as powerful of a tool as an open source software add on in comparison to Insight 4G. Ensuring that the proper interrogation size utilized is also an important parameter when using any PIV software. To check whether a final size of  $32 \times 32$  pixel interrogation region was sufficient, the following vector field shown in Figure 4.19 was produced from Case 2 data which implemented a final interrogation size within a third pass of  $16 \times 16$  pixel interrogation region for comparison.

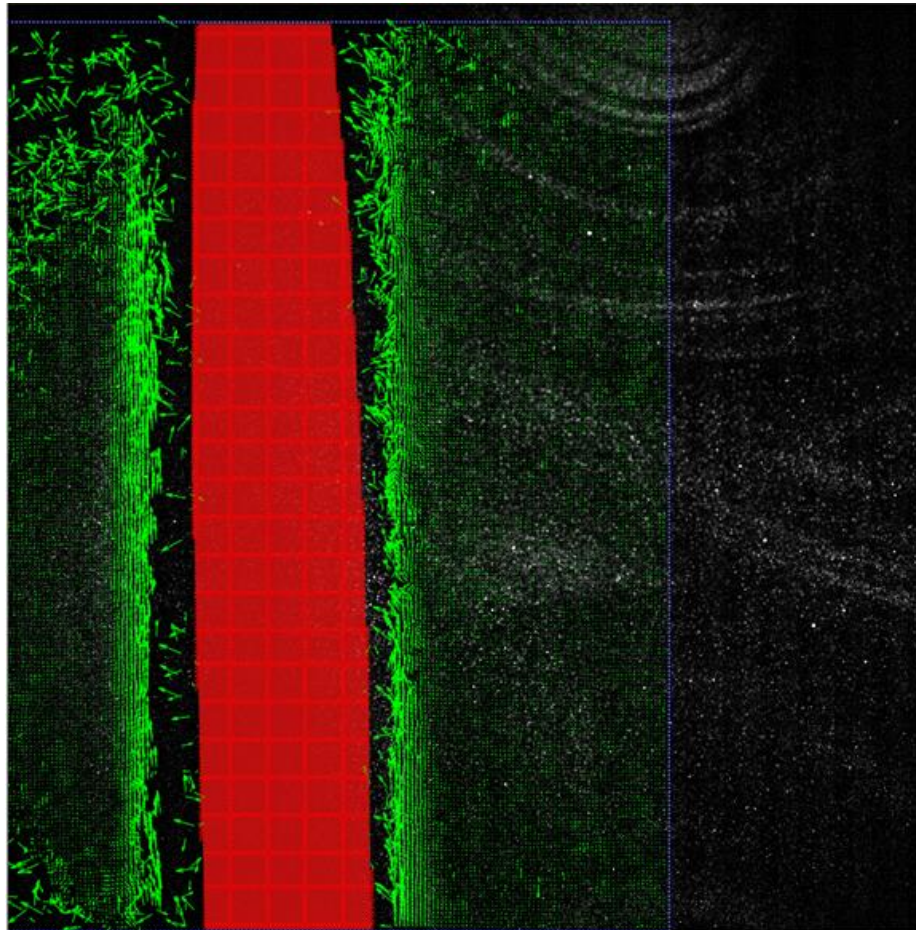


**Figure 4.19.** ns-PIV Case 2: PIV data velocity vector field as computed using  $16 \times 16$  final interrogation size [red area indicates masked section].

As the vector field displays in Figure 4.19, there is a much higher resolution vector field that is produced for a final interrogation size of  $16 \times 16$ . However, even when implementing the same post processing schemes, there are a large number of stray or spurious vectors that are computed near the plasma interface and at the edges/corners of the field itself. Thus the decision to keep the final interrogation size at  $32 \times 32$  was upheld. Of the three test cases studied, only Case 2, as analyzed using PIVlab, is shown in Figure 4.20, for brevity. Test case 1 and 3's resulting PIV velocity profile can be found in Appendix A.6.

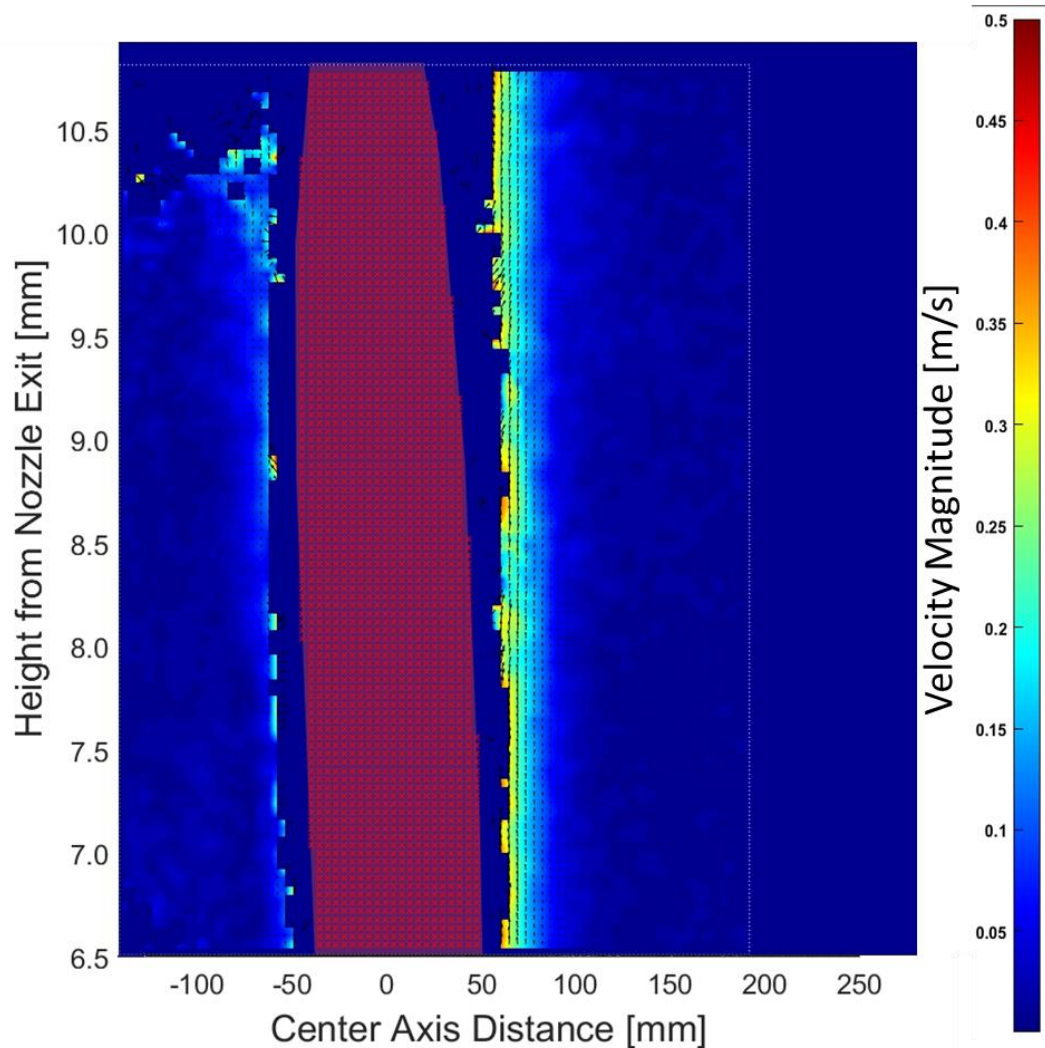


**Figure 4.20.** ns-PIV Case 2: 3.2 SLM axial flow rate PIVlab velocity vector field.

The result of these three test cases showed, as axial flow rate was increased, so too did the corresponding velocity of the particles as they neared the plasma flow field interface. These results parallel the velocity field results achieved using Insight 4G for all three cases.

The major difference between the velocity vector fields produced by PIVlab and Insight 4G was that PIVlab was only able to produce accurate velocity vectors an order of magnitude less than those produced in Insight 4G. This can be attributed to the more rigorous and powerfulness of computational algorithms and processing capabilities of Insight 4G than those of the open-source PIVlab software. However, when looking closely at the location of the velocity vectors produced by PIVlab, the location they are computed does compare to the resulting velocity field vectors produced by Insight 4G. This is important as a validation method although similar results are expected using the same image pairs and the same processing schemes between the two programs.

Ultimately, the results produced here, as by the custom generated MATLAB script used supplementary to the Insight 4G and PIVlab software generated data to show the velocity fields, are able to be easily incorporated into future MHD–RMI experiments to produce  $r\theta$ -plane PIV data through the ns-PIV method. They are in good agreement with the plasma-atmospheric boundary interface thickness results provided in Figure 4.9.

#### **4.4 Magnetic Field – Plasma Flow Field Deflection and Suppression**

To understand the intricacy of how an externally applied magnetic field is able to deflect and suppress the plasma flow field, the results of generating the magnetic field model are presented first. These results provide the details required to first, understand

how the magnetic field apparatus' 3D magnetic field interacts with the 3D axisymmetric-plasma flow field and second, how this experiment's magnetic field deviates from the magnetic field utilized in the work presented in Chapter 2 on MHD–RMI simulations.

The second set of results presented show the results of inducing the magnetic field perpendicular to the plasma flow field. This specific magnetic field orientation test case was performed for three reasons: (1) to show that an externally applied magnetic field does, in fact, interact with the plasma flow field generated by the APPT developed by the author, (2) to show the resulting deflection and suppression of the plasma flow field as the magnetic field strength (magnetic flux density) was increased, and (3) to compare the experimental results obtained when increasing the magnetic field strength, to the simulation results achieved in Section 2.5.2, from a qualitative analysis standpoint.

The third set of results presented shows the second test case's data of inducing a magnetic field at an orientation which is not perpendicular (*i.e.*, tilted), relative to the plasma flow field centerline. This was done to better understand how the individual plasma species themselves are affected by the orientation of the magnetic field (specifically the magnets' N-S pole alignment) and to compare these results to those obtained from the simulations presented in Section 2.5.1, at least, from a qualitative standpoint applicable to the future MHD–RMI experiment.

It is with these results that good baseline understanding of: (1) how the magnetic field interacts with the plasma flow field is developed, (2) how simulations and experimental results coincide or differ, and (3) what magnetic field's parameters should be utilized when performing future MHD–RMI experiments.

#### 4.4.1 *Model of the Externally Applied Magnetic Field*

To visualize the magnetic field, a custom MATLAB script was developed through utilization of Equation (3.48) and Equation (3.49) which allowed for the resulting figures of the magnetic field's properties to be generated. These figures provide the basis of understanding how the geometry and composition of the magnetic field, as generated by the concentric neodymium magnets, their respective magnetic flux intensity, force vectors, and field lines that result, can ultimately effect the plasma flow field.

The first figure shown is Figure 4.21 which is a 2D visualization of the magnetic field and its resulting characteristics that was used for the experimental analysis of the following section. The left image in Figure 4.21 shows the magnetic field flux density as generated by the two neodymium magnets where the plasma's cross-sectional boundary is represented as a purple circle. Evident in this image is a large variation in magnetic field strength with large gradients in both the  $r$ - and  $z$ -directions within the 2D image generated. The center image shows magnetic field force vectors produced from a quiver plot by the custom MATLAB script generated by the author. The quiver plot produced shows that the majority of the force vectors are nominally unidirectional about the centerline of the magnetic field. This is to be expected and parallels the magnetic field orientation simulations discussed in Section 2.4.2. However, when analyzing the right image of Figure 4.21 showing the field lines of the magnetic field as a whole, a different story is represented. The result of using the two neodymium magnetics shows a highly non-uniform magnetic field produced by the magnetic field apparatus utilized.

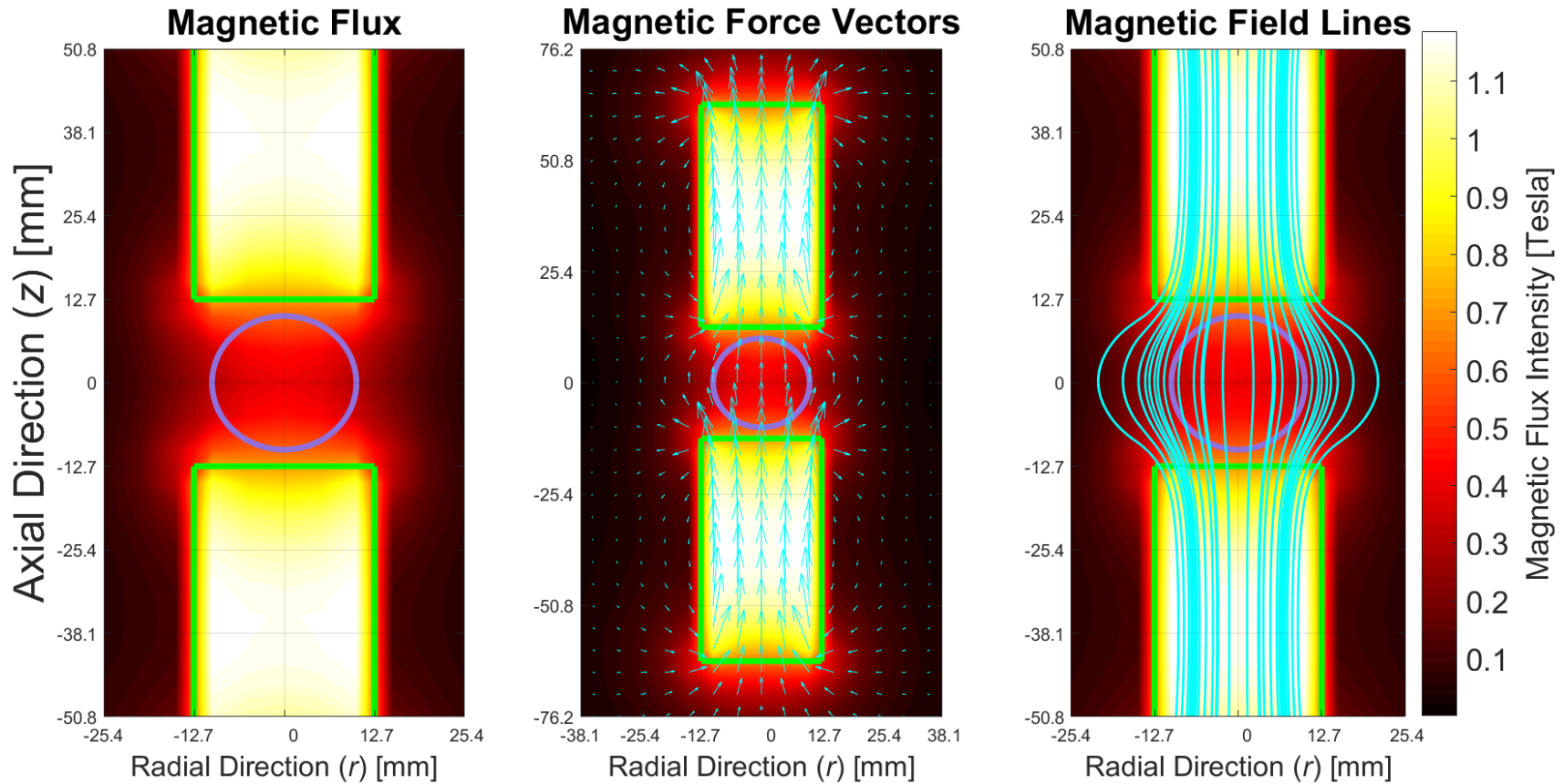


**Figure 4.21.** 2D representation of the magnetic flux density (left), magnetic force vectors (middle) and resulting magnetic field lines (right) produced by permanent magnet apparatus as generated in custom MATLAB script.\*

\* Axial position represents  $z$ -direction for the magnetic field model shown here. Radial position represents the  $x$ -direction and the  $y$ -direction (not denoted in the following figures) is equivalent to the  $\theta$ -direction. Not only does the magnetic field calculations presented here switch from Cartesian to polar cylindrical coordinates based on the data presented, but the orientation of the plasma flow field and the simulation results previously presented do not follow this specific coordinate system.

The difference between the magnetic field simulated in FLAG and the magnetic field generated by this experimental apparatus attributes to why simulations (especially *ideal* ones) can vary from real-world experiments which do not disallow the inclusion of physical phenomena or effects. The non-ideal nature of the experimentally generated magnetic field further complicated the analysis of the interaction of the magnetic field with the plasma flow field as described in Section 3.4.1 and results presented in Section 4.4.2.

Thus as the cylindrical permanent magnet apparatus interacts with the plasma flow field, it is considered an axisymmetric 3D magnetic field interacting perpendicular with an axisymmetric 3D plasma flow field. The next image presented in Figure 4.22 is a mid-plane 3D representation of the magnetic flux density to show how variable the magnetic field is in reference to the plasma flow field. Again, this figure was produced by the custom MATLAB script written by the author of this dissertation.

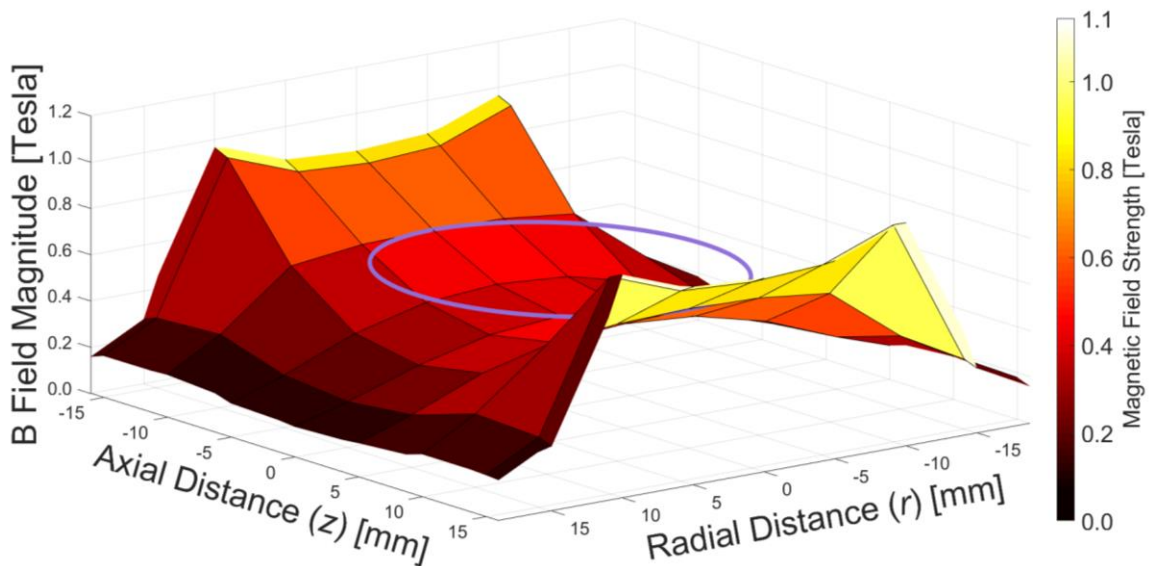


**Figure 4.22.** Depiction of the 3D magnetic flux density produced by the cylindrical permanent magnet apparatus with the outline of the plasma's cross-section shown in purple as generated in MATLAB.

As seen in Figure 4.22, there is a sharp, unequal gradient in both the  $r$ - and  $z$ -directions of the magnetic field's flux density. This plays an important role in the understanding of the results produced and analyzed in the following Section 4.4.2. To expand on this, Figure 4.23 on pg. 154 displays a 3D visualization of the magnetic field lines produced by the magnet field apparatus about the  $rz$ -plane.

The final figure produced in this results subsection is of the respective axial, radial, and total magnetic flux density components of the magnetic field. These components represent the  $r$ - and  $z$ -components, where the  $\theta$ -component is omitted for the axisymmetric magnetic field because it is negligible (*i.e.*,  $B_\theta \approx 0$ ). These components are visually represented in Figure 4.24 on pg. 155. As seen in Figure 4.24, not only is there a large variation in the  $x$ - and  $z$ -components of the magnetic field itself, but they possess both positive and negative values. The  $r$ -component of the magnetic field's flux density shows the greatest variation in positive and negative values. However, it is the  $z$ -component of the magnetic flux density that proves to be the driving component of the total magnetic flux density as shown in the right image of Figure 4.24.

With these 2D and 3D magnetic field representations, depictions, and corresponding components, a complete visualization and understanding of the magnetic field and its resulting components is formalized. These are in turn used to better understand the results of influencing the plasma flow field with an externally applied magnetic field presented in the following results section.

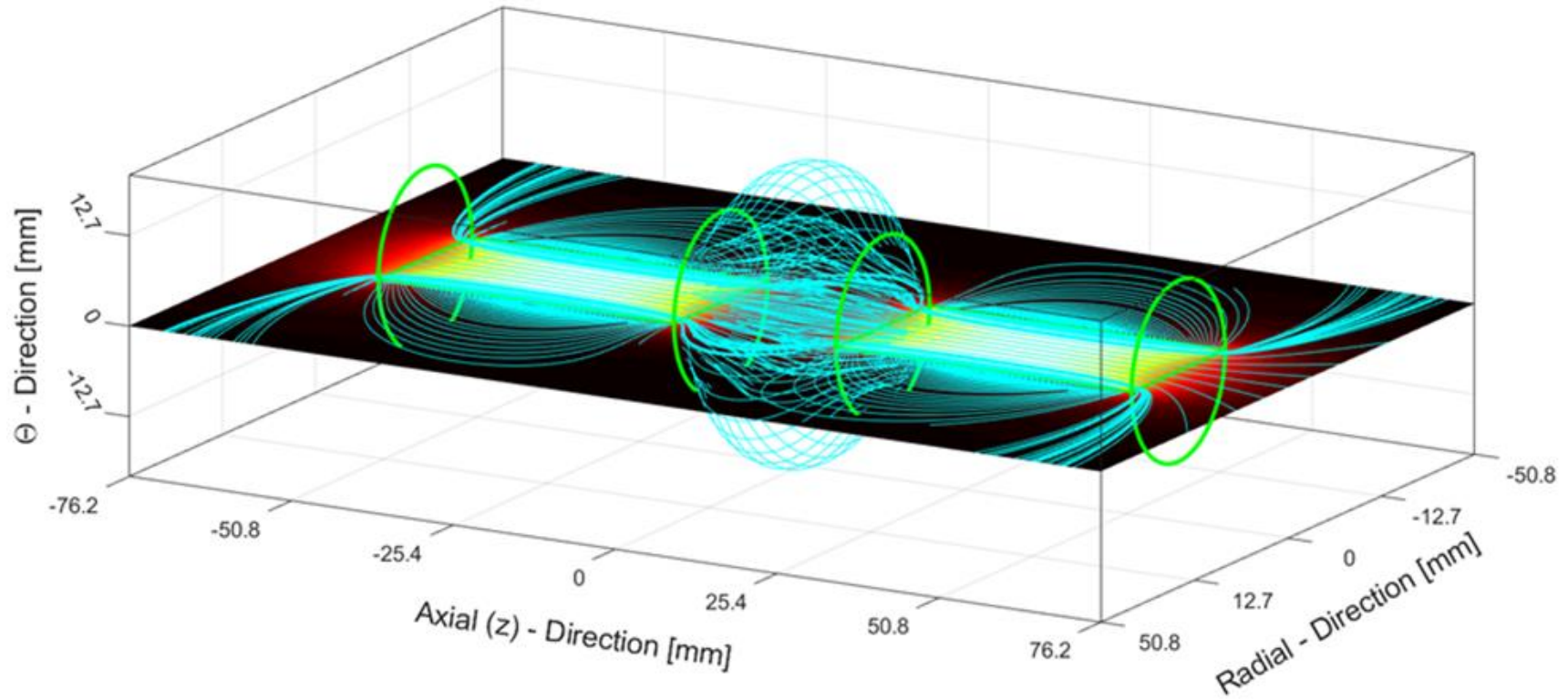


**Figure 4.23.** 3D magnetic field lines produced by permanent magnet apparatus as generated in custom MATLAB script.

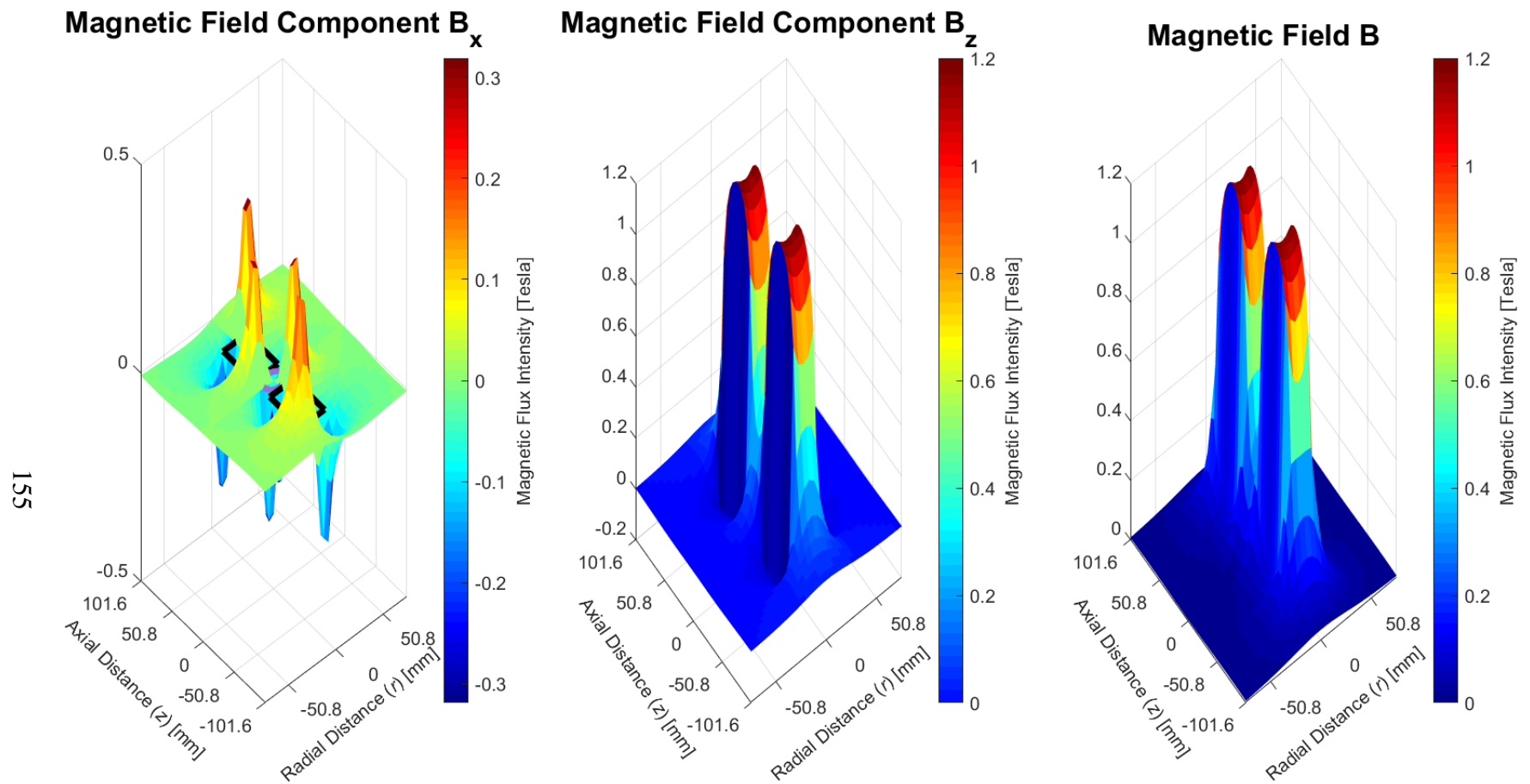


**Figure 4.24.** Magnetic flux density of the magnetic field broken into the  $r$ -component (left),  $z$ -component (middle), and total  $\vec{B}$  field strength (right), produced by the magnetic field apparatus as generated in MATLAB.

#### 4.4.2 Magnetic Field Interactions with a Plasma Flow Field

With the results of the magnetic field model presented, analysis of the results of the magnetic field interacting with the plasma flow field is provided for the first test case. The results of test case one, as described in Section 3.4.3, where the externally applied magnetic field was traversed through the plasma flow field to quantify and qualify the deflection and suppression of the plasma flow field, is shown in Figure 4.25.

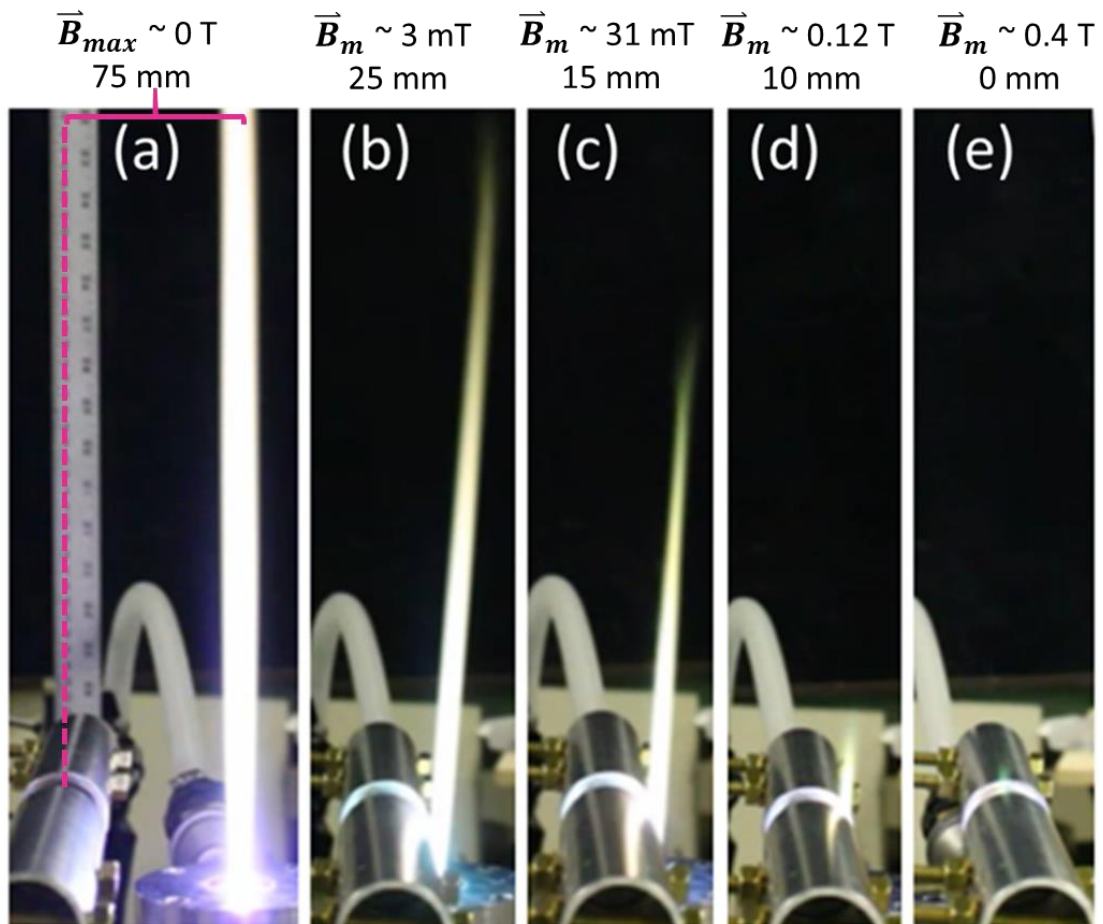


**Figure 4.25.** DSLR images of plasma deflection and suppression from test case one.

Initially, a long, laminar plasma jet can be seen (left image (a) in Figure 4.25) where there appears to be no deflection or suppression of the plasma flow given that the maximum magnetic flux density,  $\sim 0$  Tesla, imposed onto the plasma flow field is

substantially far away, ~75 mm between magnetic field centerline and velocity field centerline. As the magnet apparatus is traversed to the right (+y-direction in reference to the global coordinate system of the shock tube as described in Section 3.4.3), there results in a greater degree of deflection and suppression of the plasma flow field. Once the centerline of the magnetic field is tangentially aligned with the axis of the plasma flow field, the plasma no longer is deflected and only experiences severe flow suppression effects. The data that corresponds to the results presented here is portrayed in Figure 4.26 where the deflection angle and height of the plasma was measured using the calibration image and pixel location data corresponding to the center of the nozzle exit to the visible tip of the plasma.

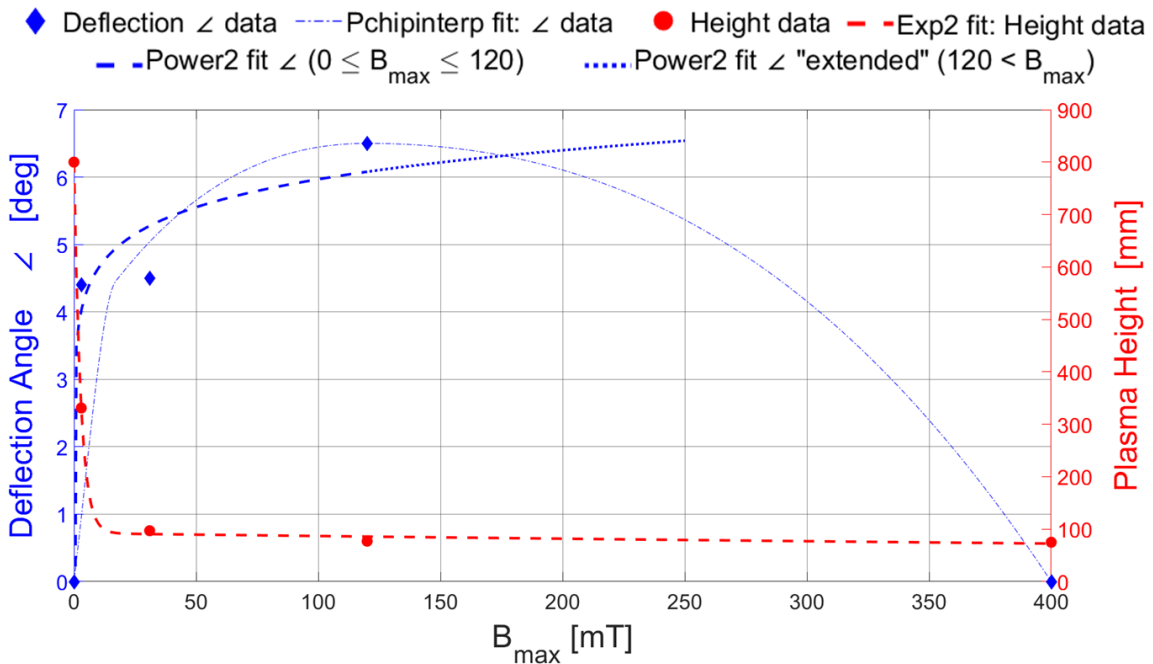


**Figure 4.26.** Deflection angle and plasma flow field height obtained from DLSR image's data presented in Figure 4.25.\*

\* Power2 fit is of the function  $f(x) = a \cdot x^b + c$  where  $a = 3.426, b = 0.1519, c = -0.8131$  and has a coefficient of determination,  $R^2 = 0.985$ . Exp2 is of the function  $f(x) = a \cdot \exp(b \cdot x) + c \cdot \exp(d \cdot x)$  where  $a = 694.9, b = -0.3734, c = 105.1, d = -0.002594$  and has an  $R^2 = 1$ .

From the data presented in Figure 4.26, it is seen that initially, when no magnetic field is present, no deflection or suppression of the plasma flow field results as previously discussed. There exists a peak in the maximum deflection angle of the plasma flow field near 120 mT which is preceded by a steep gradient and followed by a quasi-parabolic decay. When considering the deflection angle data from 0 to 120 mT, a second-order power law curve fit can be applied (an extended for reference) which better represents this sharp increasing gradient. Due to the limited data presented, these results are deemed accurate yet indefinite to precisely depict the true nature of deflection angle vs magnetic field strength.

There is a well-defined exponential decay, (shown as a second-order exponential curve fit) in the height of the torch versus magnetic field strength which shows that even at small amounts, the magnetic field imposed on the plasma flow field results in definitive deflection and suppression results to ensue. Since there is a second-order exponential function fit applied to the height vs magnetic field strength, the conclusion could be argued that there is an inverse relationship that exists between the two. However, further analysis must be performed in the future before definitive results could be concluded.

Deflection occurs as a result of the flux of electrons,  $\Gamma_{e \perp}$  being smaller than the flux of ions,  $\Gamma_{i \perp}$  due to their respective mass differing and the electrons being more readily “trapped” by the magnetic field. Again, because energy cannot be imparted onto the plasma’s charged particles themselves by a magnetic field, an induced electric field is generated. Additionally, the electric field that is generated can be short circuited by the imbalance of electron ion fluxes,  $\Gamma_{i \parallel} < \Gamma_{e \parallel}$ , along the magnetic field lines resulting in

negative charge being dissipated. That is to say that the electrons are initially and easily captured by the magnetic field, in which they undergo cyclotron motion and diffuse along magnetic field lines; As the heavier ions, although perturbed by a magnetic field, are less easily captured, they can escape or deflect off the magnetic field and diffuse radially, away from the magnetic field; As this occurs, space charge ensues; Thus the electrons are dragged out of the magnetic field by the ions resulting in bulk flow deflection of the plasma velocity profile. Additionally, since the magnetic field lines have a greater radius of curvature the further they are away from the magnet's centerline; the resulting Lorentz force imposed on the flow is greatest at the part of the magnetic field line that is perfectly tangential to both the velocity component and electric field component. The Lorentz force decays as the respective angle between the electric, magnetic, and velocity components decreases, as evaluated by Equation (3.28). Thus the edge of the plasma closest to the magnetic field experiences the greatest Lorentz force imposed upon it. Once the plasma is perfectly centered in the magnetic field, equal Lorentz forces are experienced across the flow field thus suppression is the only result observed.

In comparison to the simulation results provided in Section 2.5.2, the deflection angle experimental results shown here parallel the trends exhibited in the magnetic field strength simulation study versus vorticity or species concentration in FLAG. In both the experimental results and the simulation results, there is an immediate reaction of the plasma flow field when interacting with a magnetic field followed by an exponentially decaying trend of the results (physical phenomena) that occurs. None the less, the results provided here are on a broad scale and are comparable conceptually to the simulation results provided.

The next test case studied was the resulting effects that arise due to the magnetic field being tilted when imposed on the flow field. This test case was performed to verify the previous test case's analysis that it is in fact the ions that are the driving species behind the deflection experienced by the plasma flow field in the presence of an external magnetic field for the case of a non-transferred APPT.

Shown in Figure 4.27 are the resulting monochromatic images for test case 2, taken by a CCD camera affixed with a  $532 \pm 10$  nm filter, of the plasma flow field imposed on by a magnetic field tilted at a  $30^\circ$  angle. For comparison, images were taken with the center axis of the magnetic being aligned at different axial heights within the plasma flow field. For verification and additional analysis purposes, the tilt angle of the magnetic field was reversed, with the resulting image also displayed.

As seen in Figure 4.27 (c), suppression in the plasma flow field occurs when compared to (a) where no magnetic field is present. This coincides with the results achieved in the tangentially aligned magnetic field test case one previously discussed. As seen in Figure 4.27 (c–e), suppression of the plasma flow does not occur until the flow is nearing the outside edge of the circular face of the magnets, where the magnetic flux density is the greatest. Additionally, there is more deflection and less suppression of the plasma flow when the magnetic field is imposed at a greater axial height as shown in Figure 4.27 (d) compared to that of (c). The positively charged ions are more attracted to the south pole of the magnet and the negatively charged electrons are repelled by the north pole in (c) and (d) which coincides with the previous analysis made in the tangential magnetic field case regarding the parallel ion and electron flux as a result of cyclotron motion and drift effects.

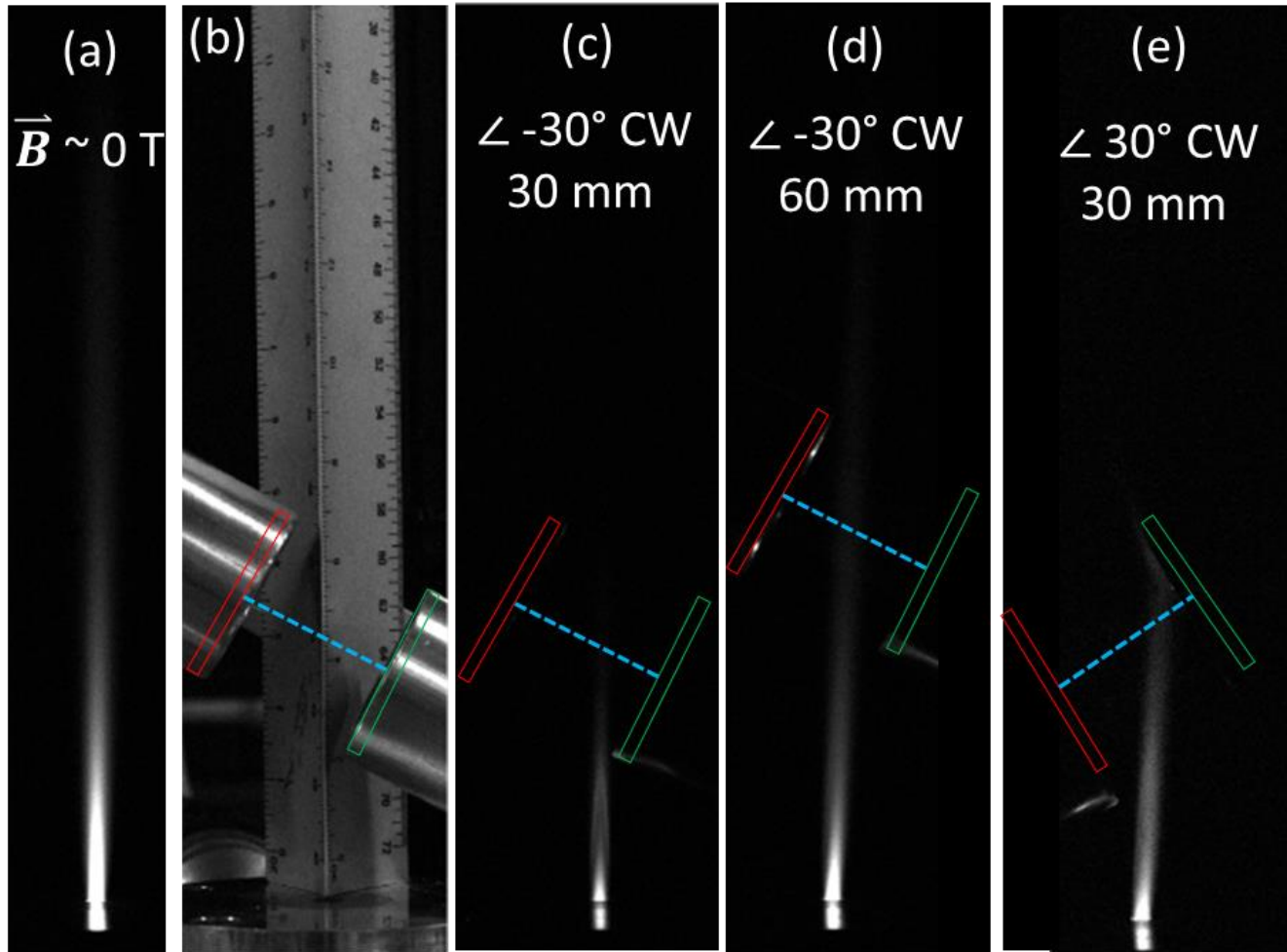


**Figure 4.27.** CCD images with  $523 \pm 10$  nm bandpass filter of tilted magnetic field interaction with plasm flow for: (a)  $\vec{B} \sim 0$  T, (b) calibration image with magnet *N*-pole edge in red, *S*-pole in green, magnets center axis blue dashed line, (c)  $\vec{B} \angle -30^\circ$  CW at 30 mm, (d)  $\vec{B} \angle -30^\circ$  CW at 60 mm, and (e)  $\vec{B} \angle 30^\circ$  CW at 30 mm.

With the magnetic field apparatus tilt angle reversed, there exists a greater degree of deflection and less degree of suppression as shown in Figure 4.27 (e) when compared to the image shown in Figure 4.27 (c) of which were examined at the same axial height. Thus it is the ions again, shown to be the driving species behind the deflection and suppression results experienced by the plasma flow field. When imaging the effects experienced by the plasma flow field in the presence of a tilted magnetic field with the CCD camera head on, loss of important information regarding the flow deflection can occur while ensuring to not over expose the sensitive CCD sensor.

Thus imaging of the plasma flow deflection was captured with a DSLR camera affixed with the same  $532 \pm 10$  nm filter to fully examine the deflection effects in full for the tilted magnetic field scenario. The following image shown in Figure 4.28 on pg. 163, displays the deflection of the plasma flow field propagating through the tilted magnetic field in its entirety. As seen in Figure 4.28, the tilted magnetic field results in the deflection of the plasma flow field in the same direction as the tilt angle of the magnetic fields central axis.

Thus the basis of an externally applied magnetic field, including its orientation and magnetic field strength, is shown to have differing deflection and suppression effects on the plasma flow field experimentally. These results are in good agreement with the simulation results provided such that different magnetic field strengths and orientations affect the MHD–RMI interface development differently.

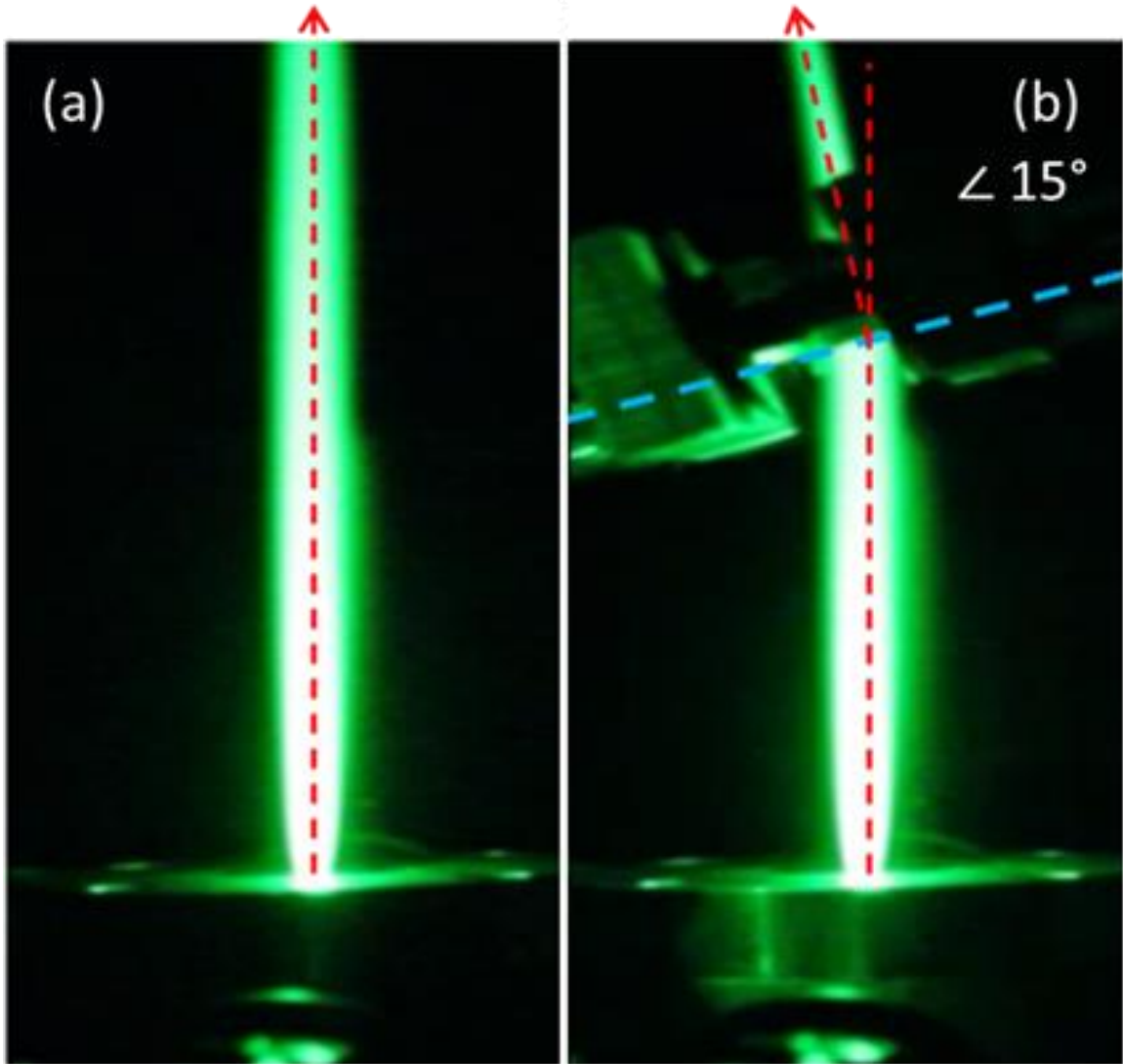


**Figure 4.28.** DSLR side view image with  $523 \pm 10$  nm bandpass filter of tilted  $\angle 15^\circ$  magnetic field interaction with plasma flow.

It is with these results that satisfy the reasoning of performing the magnetic field apparatus experiment: (1) that an externally applied magnetic field does, in fact, interact with the plasma flow field generated by the APPT developed by the author, (2) by increasing the magnetic field strength the resulting deflection and suppression of the plasma flow field was increased and (3), the experimental results obtained when increasing the magnetic field strength portray results that parallel the simulation results achieved in Section 2.5.2, from a qualitative analysis standpoint.

## CHAPTER 5. SUMMARY AND CONCLUSIONS

### 5.1 Motivation Summarized

The desire to generate reliable, clean, renewable, and sustainable energy sources is an ever increasing and vital field of interest linked to nearly all major problems facing our society currently and in the future. Inexorable emissions of heat-trapping gases continue to linger and endanger our planet where CO<sub>2</sub> emission levels have been reported to be at an all-time high for over 30 years in a row according to the World Meteorological Organization [87]. To counteract this problem, scientist from across the globe are joining together, seeking to develop new ways and technologies to generate fusion power as a viable, reliable, clean, and seemingly endless source of power which drives the world economy. The United States of America has been at the forefront of these efforts through supporting major campaigns such as Lawrence Livermore National Laboratory's National Ignition Facility which hosts the world's largest inertial confinement fusion (ICF) experiment, and multinational cooperative efforts such as the ITER project's tokamak fusion reactor located in France. ICF is making steady progress towards successful net-positive energy production from fusion. At the NIF's ICF experiment, the world's largest and most technologically advanced laser system is used to compress a droplet of fusion fuel to the extreme temperatures and densities required to fuse hydrogen isotopes into helium. In doing so, large amounts of energy are released. Through this process, hydrodynamic instabilities develop as a result as the fuel is compressed. His ultimately lead highly dense fusion fuel to mix with the low density media and inert material surrounding it which reduces the fusion yield so much, that it prevents the

economic viability of fusion power as a leading renewable energy source. Currently, NIF (formerly NIC) has resorted to material studies and is exploring additional supplementary ways to use the NIF technologies. Being that ICF performed at the NIF is a large-scale HED multibillion dollar project that is not currently a reliable net-positive energy source, the need for small-scale facilities to investigate effective and viable ways to reduce the HIs that develop is a cost-effective step towards achieving this goal. The Richtmyer-Meshkov instability is one of the major HIs that is responsible for this detrimental fluid mixing. The time and length scales alone associated with these processes makes it incredibly difficult even for the latest cutting edge technology to image and measure the HIs that arise and decouple the resulting effects that ensue.

For this reason, developing simulations and experiments at small-scale facilities such as the FMSTL at the University of Missouri are paramount to ICF's success. They are implemented such that the effects are able to be isolated and studied extensively and used to predict and improve future experiments on IFC. The important physics of the RMI and mixing in ICF can be studied in shock tube experiments which allows for larger time scales and length scales to be investigated and the results scaled to fit the NIF ICF experiment. Traditional RMI simulations and experiments only tell part of the story, which is also one of the fundamental reasons why MHD effects must be included to further increase the accuracy of scaling the results to prepare for more effective and successful ICF experiments.

Understanding the way the RMI differs from the MHD-RMI, though varying simulation parameters such as magnetic field orientation, magnetic field strength, and Mach number, aids in determining the important parameters which lead to not only the

development of the instability itself, but more importantly, how to suppress or prevent it. From an experimental standpoint, developing ways to validate that a plasma flow field, for example, can be manipulated by an externally applied magnetic field, provides the groundwork when developing the overall experiment for investigating the MHD–RMI at small-scale facilities such as the FMSTL. Should experiments like this be successful, the results in turn can then be scaled and applied towards achieving success at large-scale HED facilities like the NIF’s ICF.

## **5.2 Important Computation Environmental Parameters**

The simulation results presented were on the cylindrical MHD–RMI through variation of the magnetic field orientation, magnetic field strength, and incident shock wave’s Mach number. The parameters of the magnetic field were chosen to explore the resulting effects on vorticity advection caused by MHD waves. The variation of the Mach number was done so to explore how increased deposition of baroclinic vorticity effected the growth and morphology of the MHD–RMI. It was shown that interface mixing is a function of the amount of vorticity deposition, and the direction of the advection via Alfvén waves. The results showed that, in MHD, the suppression of the RMI is evident when an externally-applied magnetic field is present. This was attributed to the fact that vorticity is advected from the interface via Alfvén waves. The orientation of the magnetic field affects the direction the Alfvén waves transport vorticity and the strength of the magnetic field affects the Alfvén velocity. In other words, the faster vorticity is removed from the interface, the more suppressed the MHD–RMI’s interface is which is proportional to the strength of the applied magnetic field; a result shown for both the magnetic field orientations. However, vorticity was shown to traverse the interface more

rapidly in the perpendicularly-applied magnetic field case. Magnetic fields, and their respective strength and orientation, were shown to be the driving mechanism by which vorticity is transported. As the magnetic field strength was increased, so to was the suppression of the MHD–RMI interface evolution. While the magnetic field was shown to drive the resulting MHD effects in the simulation cases studied, the Mach number effect was shown to drive the hydrodynamics of the morphology of the MHD–RMI instability. Traditional RMI simulations showed that an increase in Mach number results in an increase of interface mixing due to the increase in baroclinic vorticity deposition. The opposite was observed however for the MHD–RMI cases where increased Mach numbers resulted in further compression of the MHD–RMI interface and lowered the mixedness by compressing the diffusion layer. As stronger vorticity deposition worked to compress the interface, it was ultimately advected away at higher Alfvén velocities as a result of higher postshock densities. Despite this, stronger vorticity deposition resulted in less mixing of the interface.

### **5.3 New Methods for Determining Plasma Characteristics and Parameters**

A non-transferred DC arc atmospheric-pressure plasma torch apparatus was created by constructed a custom HVAC starter circuit where it was coupled with a HCDC power supply as the spark initiation and plasma source power generation systems. Plasma characteristics such as V–I and gas flow rates were regulated to produce a long, laminar, stable plasma jet capable of achieving  $\approx 80$  cm in height. It was shown that the tallest jet height does not directly indicate the tallest plasma containing region. Diagnostics were performed utilizing the 2D Monochromatic Imagery Method (2DMIM), and a particle Mie scattering method (similar to particle image velocimetry). These diagnostic methods

were developed to provide observation of the magnetohydrodynamic Richtmyer–Meshkov instability (MHD–RMI) in future shock-driven fluid mixing experiments with an applied external magnetic field.

Developing the highly spatially resolved, nearly instantaneous, 2DMIM provided new insights to the plasma temperature and degree of ionization profiles for non-transferred APPT where traditional spectroscopic and monochromatic methods fall short. This method utilized the nitrogen 528.12 nm emission line’s normalized theoretical emission coefficient in comparison to the experimentally-acquired normalized radial emission coefficient obtained by analytically inverting the 2D intensity data produced by the torch, to generate 2D plasma temperature and degree of ionization profiles. By doing so, plasma temperatures of ~14000 K and degree of ionization of ~27% were acquired at the nozzle of the torch.

The particle Mie scattering method (PLMS method) allowed for visualization of the surrounding cold gas, and thus the interface of the plasma torch. Notably, this technique allows visualization in both the  $rz$ - and  $r\theta$ -planes, meaning the symmetry of the torch can be examined, and in future shock-driven experiments the MHD–RMI can be observed. The ns-PIV diagnostic method showed Insight 4G PIV data provided the best results in comparison to the open-source PIV software PIVlab. Qualitatively, the data produced was in good agreement with the interface thickness data produced in the 2DMIM section. Quantitatively, it was shown that although the interface thickness remains constant as axial gas flow rate was increased, the velocity gradient at the plasma–atmosphere boundary increases.

The results of applying an external magnetic field on the plasma flow field were also explored. It was shown within the first test case that as the magnetic field strength increased, the plasma flow field height decreased exponentially. Additionally, it was discovered that there was a maximum in the deflection angle curve fit that occurs near 120 mT. Both experimental and simulated results show good agreement that as magnetic field strength is increased, there is an increase in the suppressability of the plasma region. The second way this was accomplished was by varying the orientation of the applied magnetic field to observe the deflection and suppression results that ensued. It was discovered that the Lorentz force decays as the respective angle between the electric, magnetic, and velocity components decreases, where the edge of the plasma flow field closest to the magnetic field's centerline experiences the greatest Lorentz force imposed upon it. Once the plasma was perfectly centered in the magnetic field, equal Lorentz forces are experienced across the flow field thus suppression is the only result observed. The final conclusion was that it was the ions that are the driving species that determine the bulk flow suppression and deflection characteristic.

## 5.4 Future Work

A complete development of the necessary components needed to experimentally investigate the magnetohydrodynamic Richtmyer–Meshkov instability in a shock tube setting has been presented. This includes the three main ingredients being, (1) a conducting fluid (*i.e.* a plasma produced by the APPT), (2) a magnetic field and (3), a shock tube as constructed through the efforts led by the author of this dissertation. Despite the extensiveness of the information provided throughout this work, many of the extensions of the current work lay just beyond the reach of the author’s time of study.

The ground work has been provided but refining and continuing to investigate the APPT’s parameters via the 2DMIM at various flow rates and V–I operating conditions to formalize a complete parametric study should be performed. This will aid in providing better insight of the species composition of the plasma flow field and provide the necessary data that could in turn be directly imported into future computational efforts in FLAG.

A complete parametric study should also be performed to refine the data produced in the magnetic field interactions with the plasma flow field based on magnetic field strength as well as field orientation. Coupling the 2DMIM technique while performing experiments on magnetic field interacting with the plasma flow field will also provide an additional layer of knowledge on how the plasma flow field, temperature, and degree of ionization, is altered while undergoing deflection and suppression.

Since the magnetic field produced by the dual cylindrical permanent magnet apparatus utilized in the experimental efforts of this work is too small to be implemented

about the FMSTL shock tube, a large-scale pulse power or Helmholtz coil electromagnet capable of generating a steady state magnetic field for the duration of the MHD–RMI experiment should be developed. The author has laid the groundwork for this and conceptual idea can be seen in the Appendix section.

Lastly, future MHD simulations such as non-ideal, two fluid, resistive MHD simulations, in both 2D and even 3D, can be incorporated into FLAG and potentially compared to results obtained in FLASH (U. Chicago open source) and ARES (Lawrence Livermore National Laboratory), other valid and viable hydrodynamic simulation software as time and funding permits.

Overall, all that remains is to experimentally suppress the RMI in an MHD shock tube experiment.

## **FUNDING ACKNOWLEDGMENTS**

The author thanks the National Nuclear Security Agency – Stockpile Stewardship Academic Alliance Program for providing the major funding source required to complete this dissertation research (Grant No. DE-NA0003345)

## BIBLIOGRAPHY

- [1] S. A. Slutz and R. A. Vesey, “High-Gain Magnetized Inertial Fusion,” *Phys. Rev. Lett.*, vol. 108, no. 2, Jan. 2012, Art. no. 025003.
- [2] M. Hohenberger *et al.*, “Inertial Confinement Fusion Implosions with Imposed Magnetic Field Compression Using the OMEGA Laser,” *Phys. Plasmas*, vol. 19, no. 5, Mar. 2012, Art. no. 056306.
- [3] J. A. Fooks *et al.*, “Evolution of Magnetized Liner Inertial Fusion (MagLIF) Targets,” *Fusion Sci. Technol.*, vol. 73, no. 3, pp. 423–433, Apr. 2018.
- [4] R. D. Richtmyer, “Taylor Instability in Shock Acceleration of Compressible Fluids,” *Commun. Pure Appl. Math.*, vol. 13, no. 2, pp. 297–319, May 1960.
- [5] E. E. Meshkov, “Instability of the Interface of Two Gases Accelerated by a Shock Wave,” *Fluid Dyn.*, vol. 4, no. 5, pp. 101–104, Sept. 1969.
- [6] G. I. Taylor, “The Instability of Liquid Surfaces When Accelerated in a Direction Perpendicular to Their Planes. I,” *Proc R Soc Lond A*, vol. 201, no. 1065, pp. 192–196, Mar. 1950.
- [7] T. Sano, T. Inoue, and K. Nishihara, “Critical Magnetic Field Strength for Suppression of the Richtmyer-Meshkov Instability in Plasmas,” *Phys. Rev. Lett.*, vol. 111, no. 20, Nov. 2013, Art. no. 205001.
- [8] S. Sutherland, “Cloud Atlas Leaps into 21st Century with 12 New Cloud Types,” *The Weather Network*, Mar. 23, 2017. Accessed: Feb. 4, 2019. [Online]. Available: <https://www.theweathernetwork.com/news/articles/cloud-atlas-leaps-into-21st-century-with-12-new-cloud-types/80685/>
- [9] W. C. Wan *et al.*, “Observation of Single-Mode, Kelvin-Helmholtz Instability in a Supersonic Flow,” *Phys. Rev. Lett.*, vol. 115, no. 14, Oct. 2015.
- [10] “Rayleigh–Taylor Instability Simulation,” *Computation*, Nov. 12, 2012. Accessed: Apr. 3, 2019. [Online]. Available: <https://computation.llnl.gov/rayleigh%E2%80%93taylor-instability-simulation>
- [11] J. A. McFarland, “Experimental and Computational Study of the Inclined Interface Richtmyer-Meshkov Instability,” Ph.D. dissertation, Dept. Mech, Eng., Texas A&M Univ., College Station, TX, 2013.
- [12] W. J. Black, R. C. Allen, W. C. Maxon, N. Denissen, and J. A. McFarland, “Magnetohydrodynamic Effects in a Shock-Accelerated Gas Cylinder,” *Phys. Rev. Fluids*, vol. 4, no. 4, Apr. 2019, Art. no. 043901.

- [13] C. Kouveliotou, R. C. Duncan, and C. Thompson, “Magnetars,” *Scientific American*, vol. 288, no. 24, Feb. 2003.
- [14] J. Patten, “Mag Lab Press Release: World’s Most Powerful Magnet Tested Ushers in New Era for Steady High Field Research”, Dec. 17, 1999. Accessed: Apr. 3, 2019 [Online]. Available: <https://legacywww.magnet.fsu.edu/mediacenter/news/pressreleases.html>.
- [15] F. F. Chen, *Introduction to Plasma Physics and Controlled Fusion: Volume 1: Plasma Physics*, 2nd ed. New York, NY, USA: Springer, 1984.
- [16] J. Kane, R. P. Drake, and B. A. Remington, “An Evaluation of the Richtmyer-Meshkov Instability in Supernova Remnant Formation,” *Astrophys. J.*, vol. 511, no. 1, pp. 335–340, Jan. 1999.
- [17] D. Arnett, “The Role of Mixing in Astrophysics,” *Astrophys. J. Suppl. Ser.*, vol. 127, no. 2, p. 213, Apr. 2000.
- [18] J. Krebs and W. Hillebrandt, “The Interaction of Supernova Shockfronts and Nearby Interstellar Clouds,” *Astron. Astrophys.*, vol. 128, pp. 411–419, Dec. 1983.
- [19] R. I. Klein, C. F. Mckee, and P. Colella, “On the Hydrodynamic Interaction of Shock Waves with Interstellar Clouds. 1: Nonradiative Shocks in Small Clouds,” *Astrophys. J.*, vol. 420, no. 1, pp. 213–236, Jan. 1994,
- [20] R. Klein, K. Budil, T. Perry, and David R. Bach, “Interaction of Supernova Remnants with Interstellar Clouds: From the Nova Laser to the Galaxy,” *Astrophys. J. Suppl. Ser.*, vol. 127, no. 2, pp. 379–383, Dec. 2008.
- [21] V. Wheatley, R. Samtaney, D. Pullin, and R. Gehre, “The Transverse Field Richtmyer-Meshkov Instability in Magnetohydrodynamics,” *Phys. Fluids*, vol. 26, Jan. 2014, Art. no. 016102.
- [22] C. Park, U. B. Mehta, and D. W. Bogdanoff, “MHD Energy Bypass Scramjet Performance with Real Gas Effects,” AIAA, NASA Ames Research Center, Moffett Field, CA, USA, 2000.
- [23] M. F. Lindsey, “Assessing the Potential for Improved Scramjet Performance Through Application of Electromagnetic Flow Control,” Ph.D. dissertation, Dept. of the Air Force Air Univ., Air Force Institute of Technology, Wright-Patterson Air Force Base, OH, USA, 2006.
- [24] J. Yang, T. Kubota, and E. E. Zukoski, “Applications of Shock-Induced Mixing to Supersonic Combustion,” *AIAA J.*, vol. 31, no. 5, pp. 854–862, May 1993.
- [25] R. Samtaney, J. Ray, and N. J. Zabusky, “Baroclinic Circulation Generation on Shock Accelerated Slow/Fast Gas Interfaces,” *Phys. Fluids*, vol. 10, no. 5, pp. 1217–1230, May 1998.

- [26] K. Takita, N. Abe, G. Masuya, and Y. Ju, "Ignition Enhancement by Addition of NO and NO<sub>2</sub> from a N<sub>2</sub>/O<sub>2</sub> Plasma Torch in a Supersonic Flow," *Proc. Combust. Inst.*, vol. 31, no. 2, pp. 2489–2496, Jan. 2007.
- [27] R. Minato, T. Niioka, H. Sugiyama, and K. Mizobata, "Numerical Analysis of Supersonic Combustion by a Plasma Torch," in *AIAA/CIRA 13th International Space Planes and Hypersonics Systems and Technologies Conference*, in Session: HYTASP-27: Plasma Ignition Techniques, Capua, Italy, May 16–20, 2005.
- [28] O. L. Landen *et al.*, "Progress in the Indirect-Drive National Ignition Campaign," *Plasma Phys. Control. Fusion*, vol. 54, no. 12, Nov. 2012, Art. no. 124026.
- [29] R. Aymar, "The ITER project," *IEEE Trans. Plasma Sci.*, vol. 25, no. 6, pp. 1187–1195, Dec. 1997.
- [30] "Milestones around the world," *ITER*. Accessed: June 6, 2019 [Online]. Available: <http://www.iter.org/sci/beyonditer>.
- [31] W. H. Lowdermilk *et al.*, "The Nova Upgrade Facility for ICF Ignition and Gain," in *Laser Interaction and Related Plasma Phenomena: Volume 10*, G. H. Miley and H. Hora, Eds. Boston, MA: Springer USA, 1992, pp. 323–335.
- [32] D. Clery, "Panel Backs ITER Fusion Project's New Schedule, But Balks at Cost," *Science / AAAS*, Apr. 28, 2016. Accessed: Apr. 25, 2019 [Online]. Available: <https://www.sciencemag.org/news/2016/04/updated-panel-backs-iter-fusion-project-s-new-schedule-balks-cost>.
- [33] S. Chandrasekhar, *Hydrodynamic and Hydromagnetic Stability*, Oxford: Oxford University Press, 1961.
- [34] R. Samtaney, "Suppression of the Richtmyer–Meshkov Instability in the Presence of a Magnetic Field," *Phys. Fluids*, vol. 15, no. 8, pp. L53–L56, Jun. 2003.
- [35] V. Wheatley, D. I. Pullin, and R. Samtaney, "Regular Shock Refraction at an Oblique Planar Density Interface in Magnetohydrodynamics," *J. Fluid Mech.*, vol. 522, pp. 179–214, Jan. 2005.
- [36] V. Wheatley, D. I. Pullin, and R. Samtaney, "Stability of an Impulsively Accelerated Density Interface in Magnetohydrodynamics," *Phys. Rev. Lett.*, vol. 95, no. 12, Sep. 2005, Art. no. 125002.
- [37] V. Wheatley, R. Samtaney, and D. I. Pullin, "The Richtmyer–Meshkov Instability in Magnetohydrodynamics," *Phys. Fluids*, vol. 21, no. 8, Aug. 2009, Art. no. 082102.
- [38] V. Wheatley, R. Samtaney, D. I. Pullin, and R. M. Gehre, "The Transverse Field Richtmyer–Meshkov Instability in Magnetohydrodynamics," *Phys. Fluids*, vol. 26, Jan. 2014, Art. no. 016102.

- [39] W. Mostert, V. Wheatley, R. Samtaney, and D. I. Pullin, “Effects of Seed Magnetic Fields on Magnetohydrodynamic Implosion Structure and Dynamics,” *Phys. Fluids*, vol. 26, no. 12, Dec. 2014, Art. no. 126102.
- [40] W. Mostert, V. Wheatley, R. Samtaney, and D. I. Pullin, “Effects of magnetic fields on magnetohydrodynamic cylindrical and spherical Richtmyer-Meshkov instability,” *Phys. Fluids*, vol. 27, no. 10, p. 104102, Oct. 2015.
- [41] J. P. Boris and D. L. Book, “Flux-Corrected Transport. I. SHASTA, a Fluid Transport Algorithm that Works,” *J. Comput. Phys.*, vol. 11, no. 1, pp. 38–69, Jan. 1973.
- [42] J. B. Middlebrooks, C. G. Avgoustopoulos, W. J. Black, R. C. Allen, and J. A. McFarland, “Droplet and Multiphase Effects in a Shock-Driven Hydrodynamic Instability with Reshock,” *Exp. Fluids*, vol. 59:98, Jun. 2018.
- [43] R. C. Allen, W. J. Black, and J. A. McFarland, “Development and Diagnosis of an Atmospheric Pressure Plasma Torch for Investigating Magnetohydrodynamic Instabilities,” *J. Phys. Appl. Phys.*, vol. 52, no. 17, Apr. 2019, Art. no. 175201.
- [44] A. Schutze, J. Y. Jeong, S. E. Babayan, J. Park, G. S. Selwyn, and R. F. Hicks, “The Atmospheric-Pressure Plasma Jet: A Review and Comparison to Other Plasma Sources,” *IEEE Trans. Plasma Sci.*, vol. 26, no. 6, pp. 1685–1693, Dec. 1998.
- [45] W. Pan, W. Zhang, W. Ma, and C. Wu, “Characteristics of Argon Laminar DC Plasma Jet at Atmospheric Pressure,” *Plasma Chem. Plasma Process.*, vol. 22, no. 2, pp. 271–283, Jun. 2002.
- [46] A. M. Paingankar, A. K. Das, V. S. Shirodkar, K. P. Sreekumar, and N. Venkatramani, “Prediction of Electrical Characteristics of a Non-Transferred Arc-Plasma Torch Using Principles of Dynamic Similarity,” *Plasma Sources Sci. Technol.*, vol. 8, pp. 100–109, Feb. 1999.
- [47] G. Li, W. Pan, X. Meng, and C. Wu, “Application of Similarity Theory to the Characterization of Non-Transferred Laminar Plasma Jet Generation,” *Plasma Sources Sci. Technol.*, vol. 14, pp. 219–225, May 2005.
- [48] M. P. Planche, J. F. Coudert, and P. Fauchais, “Velocity Measurements for Arc Jets Produced by a DC Plasma Spray Torch,” *Plasma Chem. Plasma Process.*, vol. 18, no. 2, pp. 263–283, Jun. 1998.
- [49] A. Vardelle, P. Fauchais, B. Dussoubs, and N. J. Themelis, “Heat Generation and Particle Injection in a Thermal Plasma Torch,” *Plasma Chem. Plasma Process.*, vol. 18, no. 4, pp. 551–574, Dec. 1998.
- [50] S. Hübner, J. S. Sousa, J. van der Mullen, and W. G. Graham, “Thomson Scattering on Non-Thermal Atmospheric Pressure Plasma Jets,” *Plasma Sources Sci. Technol.*, vol. 24, no. 5, pp. 1–15, Aug. 2015.

- [51] K. Tomita, N. Bolouki, H. Shirozono, Y. Yamagata, K. Uchino, and K. Takaki, “Two-Dimensional Thomson Scattering diagnostics of Pulsed Discharges Produced at Atmospheric Pressure,” *J. Instrum.*, vol. 7, no. 02, pp. C02057–C02057, Feb. 2012.
- [52] A. F. H. van Gessel, E. A. D. Carbone, P. J. Bruggeman, and J. J. A. M. van der Mullen, “Laser Scattering on an Atmospheric Pressure Plasma Jet: Disentangling Rayleigh, Raman and Thomson scattering,” *Plasma Sources Sci. Technol.*, vol. 21, no. 1, Jan. 2012, Art. no. 015003.
- [53] G. de Izarra, N. Cerqueira, and C. de Izarra, “Quantitative Shadowgraphy on a Laminar argon Plasma Jet at Atmospheric Pressure,” *J. Phys. D: Appl. Phys.*, vol. 44, no. 48, Nov. 2011, Art. no. 485202.
- [54] Y. Zheng, L. Wang, W. Ning, and S. Jia, “Schlieren Imaging Investigation of the Hydrodynamics of Atmospheric Helium Plasma Jets,” *J. Appl. Phys.*, vol. 119, no. 12, Mar. 2016, Art. no. 123301.
- [55] B. Pokrzywka, K. Musiol, S. Pellerin, E. Pawelec, and J. Chapelle, “Spectroscopic Investigation of the Equilibrium State in the Electric Arc Cathode Region,” *J. Phys. D: Appl. Phys.*, vol. 29, no. 10, pp. 2644–2649, Oct. 1996.
- [56] N. K. Joshi, S. N. Sahasrabudhe, K. P. Sreekumar, and N. Venkatramani, “Variation of Axial Temperature in Thermal Plasma Jets,” *Meas. Sci. Technol.*, vol. 8, pp. 1146–1150, Oct. 1997.
- [57] A. B. Murphy, “Modified Fowler–Milne Method for the Spectroscopic Measurement of Temperature and Composition of Multielement Thermal Plasmas,” *Rev. Sci. Instrum.*, vol. 65, no. 11, pp. 3423–3427, Nov. 1994.
- [58] J. Haidar and A. J. D. Farmer, “Temperature Measurements for High-Current Free-Burning Arcs in Nitrogen,” *J. Phys. D: Appl. Phys.*, vol. 26, pp. 1224–1229, Aug. 1993.
- [59] D. A. Scott, P. Kovitya, and G. N. Haddad, “Temperatures in the plume of a dc plasma torch,” *J. Appl. Phys.*, vol. 66, no. 11, pp. 5232–5239, Dec. 1989.
- [60] B. Bachmann *et al.*, “High-Speed Three-Dimensional Plasma Temperature Determination of Axially Symmetric Free-Burning Arcs,” *J. Phys. D: Appl. Phys.*, vol. 46, no. 12, Mar. 2013, Art. no. 125203.
- [61] R. Kozakov *et al.*, “Change of Electrical Conductivity of Ar Welding Arc Under Resonant Absorption of Laser Radiation,” *J. Phys. D: Appl. Phys.*, vol. 48, no. 9, Mar. 2015, Art. no. 095502.
- [62] *Electrical Engineer’s Reference Book*, 16th ed., M. A. Laughton and D. F. Warne, Eds. Burlington, MA, USA: Elsevier Sci., 2003, Accessed: Aug. 15, 2018, [Online]. Available: <https://www.elsevier.com/books/electrical-engineers-reference-book/laughton/978-0-7506-4637-6>

- [63] A. K. Das, K. P. Sreekumar, and N. Venkatramani, "DC Plasma Torch Voltage and Current Characteristics Through Heat Balance Measurements," *Plasma Sources Sci. Technol.*, vol. 3, pp. 108–113, Feb. 1994.
- [64] W. Pan, X. Meng, C. Wu, and X. Chen, "Experimental Study on the Thermal Argon Plasma Generation and Jet Length Change Characteristics at Atmospheric Pressure," *Plasma Chem. Plasma Process.*, vol. 26, no. 4, pp. 335–345, Aug. 2006.
- [65] V. Valincius, V. Krusinskaite, P. Valatkevicius, V. Valinciute, and L. Marcinauskas, "Electric and Thermal Characteristics of the Linear, Sectional DC Plasma Generator," *Plasma Sources Sci. Technol.*, vol. 13, pp. 199–206, May 2004.
- [66] L. Prevosto, H. Kelly, and B. R. Mancinelli, "Langmuir Probe Diagnostics of an Atmospheric Pressure, Vortex-Stabilized Nitrogen Plasma Jet," *J. Appl. Phys.*, vol. 112, no. 6, Sep. 2012, Art. no. 063302.
- [67] S. J. Zweben *et al.*, "Edge Turbulence Imaging in the Alcator C-Mod Tokamak," *Phys. Plasmas*, vol. 9, no. 5, pp. 1981–1989, Apr. 2002.
- [68] G. N. Haddad and A. J. D. Farmer, "Temperature Determinations in a Free-Burning Arc. I. Experimental Techniques and Results in Argon," *J. Phys. D: Appl. Phys.*, vol. 17, pp. 1189–1196, Jun. 1984.
- [69] A. J. D. Farmer and G. N. Haddad, "Rayleigh Scattering Measurements in a Free-Burning Argon Arc," *J. Phys. D: Appl. Phys.*, vol. 21, pp. 426–431, Mar. 1988.
- [70] M. F. Thornton, "Spectroscopic Determination of Temperature Distributions for a TIG Arc," *J. Phys. D: Appl. Phys.*, vol. 26, pp. 1432–1438, Sep. 1993.
- [71] N. Singh, M. Razafinimanana, and A. Gleizes, "The Effect of Pressure on a Plasma Plume: Temperature and Electron Density Measurements," *J. Phys. D: Appl. Phys.*, vol. 31, pp. 2921–2928, Oct. 1998.
- [72] G. Colonna and M. Capitelli, "A Few Level Approach for the Electronic Partition Function of Atomic Systems," *Spectrochim. Acta*, vol. 64, pp. 863–873, Sep. 2009.
- [73] A. Fridman and L. A. Kennedy, *Plasma Physics and Engineering*, 2nd ed. New York, NY, USA: Taylor & Francis, 2011.
- [74] M. Capitelli, G. Colonna, and A. D'Angola, *Fundamental Aspects of Plasma Chemical Physics: Thermodynamics*. New York, NY, USA: Springer-Verlag, 2012.
- [75] M. Capitelli *et al.*, "Tables of Internal Partition Functions and Thermodynamic Properties of High-Temperature Mars-Atmosphere Species from 50K to 50000K," *ESA Sci. Tech. Rev.*, vol. 246, Oct. 2005.
- [76] K. Bockasten, "Transformation of Observed Radiances into Radial Distribution of the Emission of a Plasma," *J. Opt. Soc. Am.*, vol. 51, no. 9, pp. 943–947, Sep. 1961.

- [77] Y. T. Cho and S.-J. Na, “Application of Abel Inversion in Real-Time Calculations for Circularly and Elliptically Symmetric Radiation Sources,” *Meas. Sci. Technol.*, vol. 16, pp. 878–884, Mar. 2005.
- [78] A. Kramida, Y. Ralchenko, J. Reader, and NIST ASD Team (2018), “NIST: Atomic Spectra Database (version 5.5.6),” *NIST Atomic Spectra Database*. Accessed: Aug 15, 2018, [Online]. Available: <https://physics.nist.gov/asd>
- [79] W. Thielicke and E. J. Stamhuis, “PIVlab - Particle Image Velocimetry (PIV) Tool,” *J. Open Res. Softw.*, vol. 2, Oct. 2014.
- [80] R. Safari and F. Sohbatzadeh, “Effect of DC Magnetic Field on Atmospheric Pressure Argon Plasma Jet,” *Indian J. Phys.*, vol. 89, no. 5, pp. 495–502, May 2015.
- [81] M. M. Stoiljković, M. M. Pavlović, M. Kuzmanović, and J. J. Savović, “Monochromatic Imaging Technique used to Study DC Arc Plasma Under the Influence of a Transverse Magnetic Field,” *Plasma Sources Sci. Technol.*, vol. 18, no. 3, Aug. 2009, Art. no. 035005.
- [82] A. Blais, P. Proulx, and M. I. Boulos, “Three-Dimensional Numerical Modelling of a Magnetically Deflected DC Transferred Arc in Argon,” *J. Phys. Appl. Phys.*, vol. 36, no. 5, pp. 488–496, Mar. 2003.
- [83] M. H. Mentzoni, “Momentum Transfer Collisions in Oxygen for Thermal Electrons,” *J. Res. Natl. Bur. Stand. Sect. Radio Sci.*, vol. 69D, no. 2, p. 213, Feb. 1965.
- [84] E. E. Callaghan and S. H. Maslen, “The Magnetic Field of a Finite Solenoid,” NASA Lewis Research Center, Technical Report 19980227402, Oct. 1960.
- [85] W. J. Black, N. A. Denissen, and J. A. McFarland, “Evaporation Effects in Shock-Driven Multiphase Instabilities,” *ASME J. Fluids Eng.*, vol. 139, no. 7, pp. 071204-2–071204-15, Apr. 2017.
- [86] J. Dahal and J. A. McFarland, “A Numerical Method for Shock Driven Multiphase Flow with Evaporating Particles,” *J. Comput. Phys.*, vol. 344, pp. 210–233, Sep. 2017.
- [87] T. Miles, “CO<sub>2</sub> Levels Hit Record High for 30th Year in a Row,” *Scientific American*, Accessed: Apr. 19, 2019. [Online]. Available: <https://www.scientificamerican.com/article/co2-levels-hit-record-high-for-30th-year-in-a-row/>

## APPENDIX A. DEVELOPMENT, INSTRUMENTATION, AND CONTROL OF THE PLASMA TORCH

### A.1 Preliminary Plasma Torch Development

Starting from humble beginnings, generating a plasma is no easy feat. To do so, many preliminary measures were taken to generate the proof of concept that it was possible to generate plasma at atmospheric conditions. To start, a luminous tube (neon sign) transformer was used to generate spark breakdown between two tungsten electrode TIG welding rods. Then nitrogen gas was supplied to the system by flowing the gas across the spark that was generated to produce the first atmospheric-pressure plasma created in the FMSTL. Shown in Figure A.1 below is the first iteration plasma generating apparatus concept as well as it while operational.

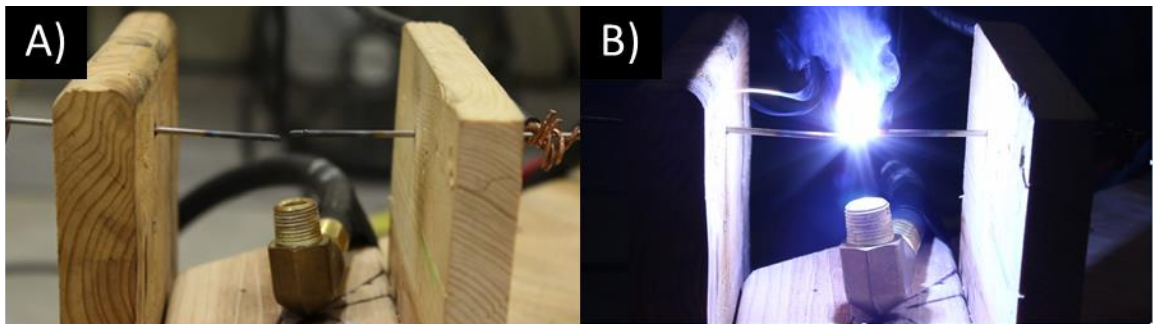


**Figure A.1.** Image of: (A) plasma generating apparatus proof of concept, and (B) preliminary APPT apparatus during operation.

Once the ability to produce atmospheric plasma in this manner was achieved, the next step taken was to construct a simple working model of a plasma torch. This was accomplished by retrofitting a automotive spark plug with custom machined

components which included a gas flow inlet to provide working gas to the spark plug plasma torch and is shown while operational in Figure A.2.

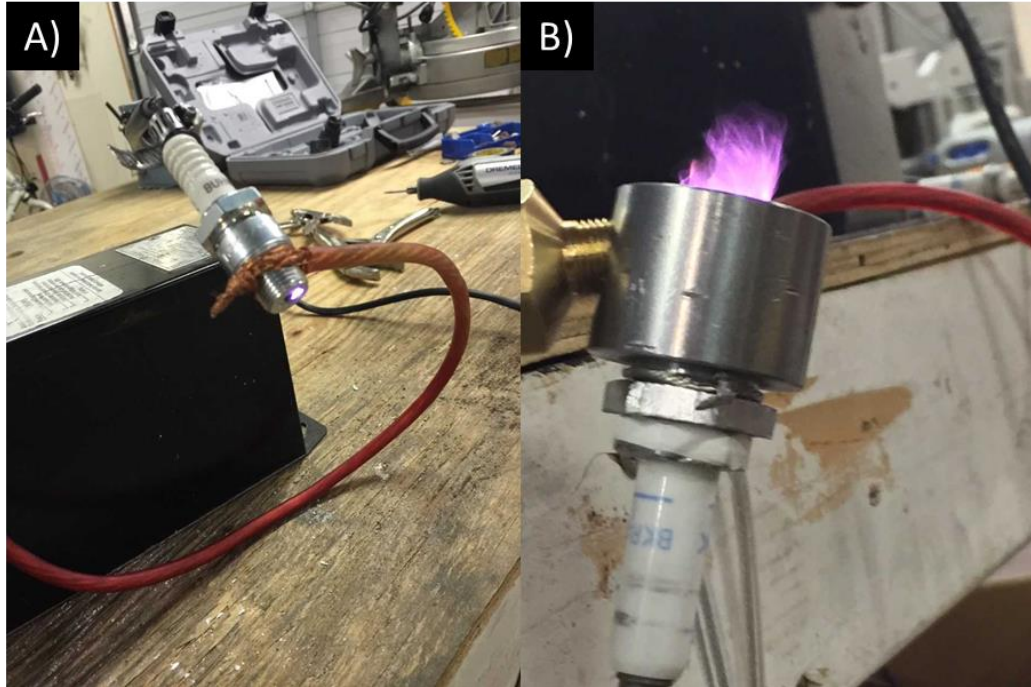


**Figure A.2.** Image of: (A) spark plug producing spark, and (B) spark plug plasma generating torch apparatus during operation.

Many hours were spent modifying and improving on these basic apparatuses and components before designing and fabricating the full APPT used in this dissertation and a lot of the foundations of the full design come from this preliminary investigation, specifically, how it failed, repetitively.

## **A.2 HVAC Starter Circuit**

A large amount of effort was also spent to adequately and safely generate the custom HVAC starter circuit utilized in this dissertation work as part of the APPT apparatus. The preliminary development of the HVAC starter circuit is shown in Figure A.3.



**Figure A.3.** Preliminary development of custom HVAC starter circuit.

To better understand how the individual components affected the operation of the HVAC starter circuit, the circuitual schematic was simulated in National Instruments' Multisim 12 Student Version transient circuit simulation program. The circuit diagram of the simulated HVAC starter circuit is shown in Figure A.4.

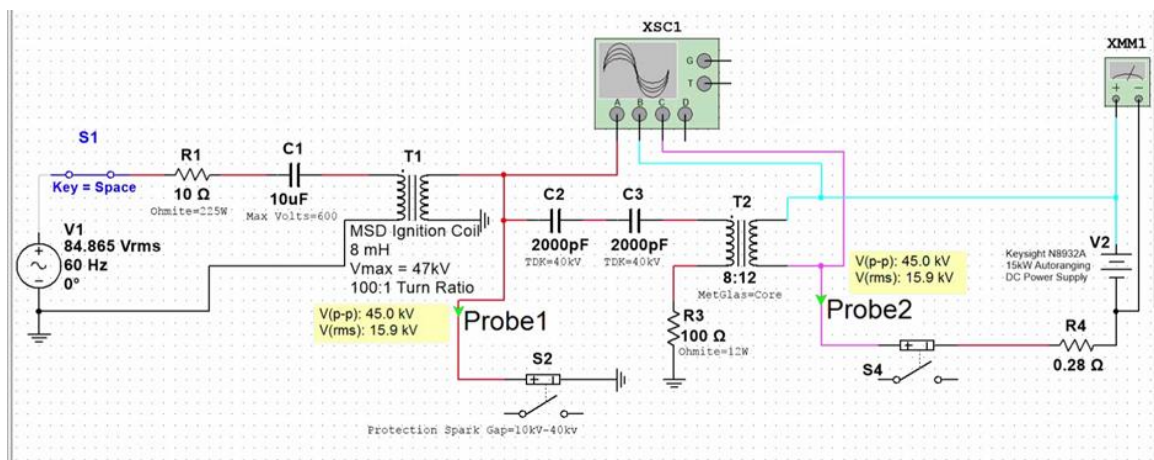


**Figure A.4.** National Instruments Multisim 12 HVAC–HCDC circuit simulation.

Through performing the circuit simulation of the HVAC starter circuit, the high-frequency oscillatory nature of the spark gap switch and plasma torch's electrode spark gap was able to be visualized. This portrayed the necessity to surround the HVAC circuit with a Faraday cage. Also, the circuit's transient V-I results were obtained and evaluated through performing this simulation. This allowed the proof that once the full HVAC starter circuit was constructed, the proper components with sufficient electrical parameters and ratings were being utilized.

After completing preliminary design reviews and simulation analysis, the HVAC starter circuit was constructed. Images of the during-construction and post-completion HVAC starter circuit and surrounding Faraday cage are shown in Figure A.5.

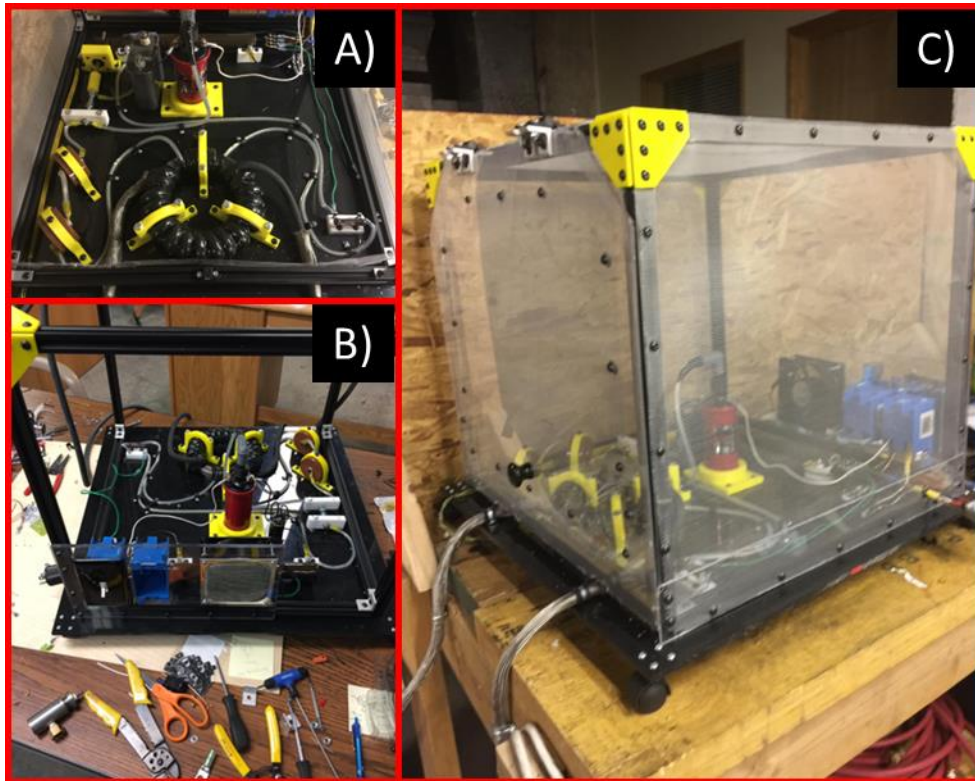


**Figure A.5.** Image of: (A) aerial rear view of constructed HVAC starter circuit, (B) aerial front view of constructed HVAC starter circuit, and (C) isometric view of HVAC starter circuit with Faraday cage.

Many of the supporting features such as brackets and electrical component holders were 3D printed by the author of this dissertation and are evident as yellow plastic components.

### A.3 HCDC Power Supply

The HCDC power supply utilized in providing the constant/consistent DC (steady-state) power to the APPT apparatus was a Keysight N8932A autoranging 15kW power supply. This particular DC power supply was chosen because it has the capability to be run in constant current, constant voltage, or constant power mode. It also has additional safety features that were applicable to and necessary for plasma generation. To that effect, it could withstand the brutalities of being conjoined with the HVAC starter circuit through a series injection transformer. How an autoranging power supply differs from similar HCDC power supplies, is best represented by the V–I curve shown in Figure A.6. The specifics of the N8932A power supply are provided in Table A-1.

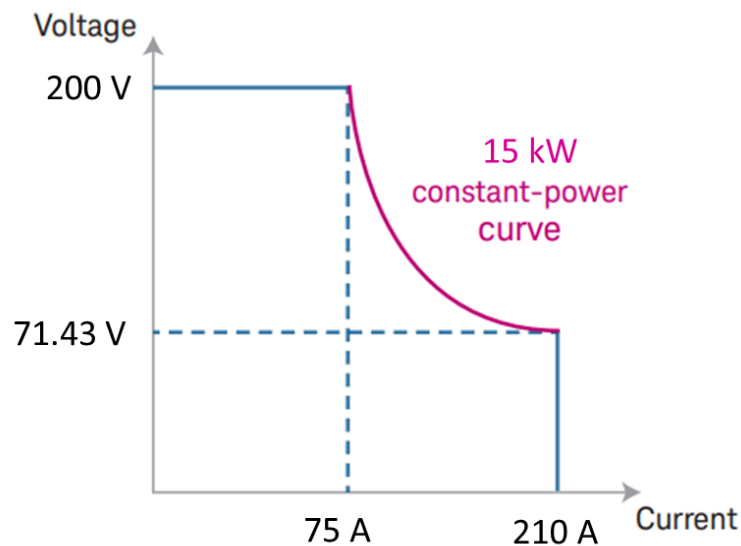


**Figure A.6.** Keysight N8932A autoranging 15 kW power supply voltage–current relationship power curve.

**Table A-1:** Keysight N8932A power supply characteristics.

<b>N8932A Performance Specifications</b>	
<b>DC output ratings</b>	
Voltage	200 V
Current	210 A
Power	15 kW
<b>Output voltage ripple and noise</b>	
$CV_{p-p}$	375 mV
$CV_{rms}$	40 mV
<b>Load effect (change from 0% to 100% of full load)</b>	
Voltage	100 mV
Current	315 mA
<b>Programming &amp; Measurement accuracy (23 °C ± 5 °C)</b>	
Voltage	≤ 200 mV
Current	≤ 420 mA
<b>Load transient recovery time</b>	
Time	≤ 1.5 ms
<b>Output response time:</b>	
Up, full load	≤ 30 ms
Down, full load	≤ 80 ms
Down, no load	≤ 10 s
Command response time	< 25 ms
Over-voltage protection	0 - 220 V
<b>Output current ripple and noise</b>	
$CC_{rms}$	66 mA
<b>Programming &amp; Measurement resolution</b>	
Voltage	9 mV
Current	9 mA
<b>Output terminal isolation</b>	
Positive terminal	+600 V
Negative terminal	±400 V
<b>208 VAC input</b>	
Nominal input voltage	208 VAC
Input range	Nominal ±10%
Frequency	45-65 Hz
Phase	3 phase
Input current	2 x 32 A, 1 x 56 A
Inrush current	97 A
Power factor	> 0.99
Efficiency	89.50%

To provide the necessary input power to the N8932A power supply, a bus bar was used within the FMSTL lab that had the specifications of: 3-phase, 208 volts (AC), and 625 amps in total. A quick-disconnect fuse box was connected from the bus bar to the power supply with 100 amp fuses installed per phase. Shown in Figure A.7 is the bus bar and quick-disconnect fuse box that was wired, connected, and turned on, once properly installed.

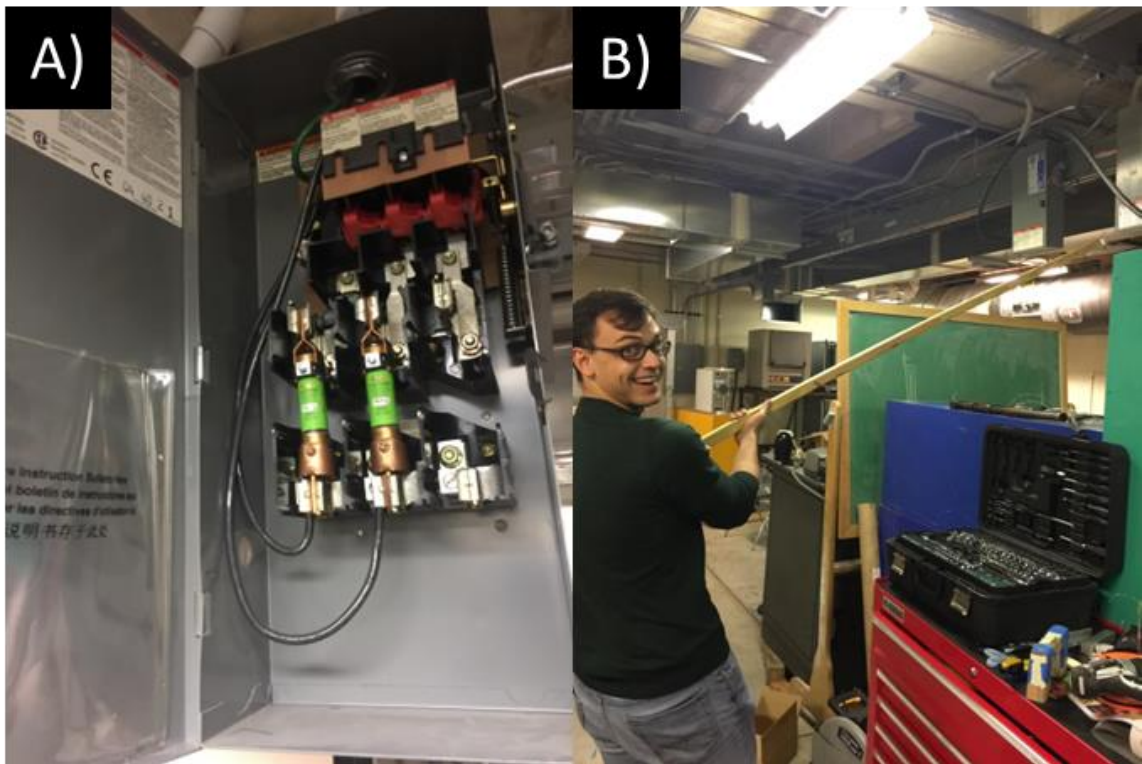


**Figure A.7.** Image of: (A) quick-disconnect fuses being installed, and (B) proper powering on of quick-disconnect fuse box.

#### A.4 APPT Power Resistor Bank Construction

The construction of the 33 parallel-wired WCPRs, which are more commonly water tank heaters, used in the APPT generation apparatus circuit is shown in Figure A.8. It is difficult to find an over the counter or off the shelf, scientifically acceptable, power resistor with the appropriate specifications and ratings that is financially feasible. However, many local hardware stores in the Columbia, MO area did have water tank heaters, each able to withstand 5000W of power, that when wired in parallel, were an appropriately sufficient and acceptable alternative to a high-dollar, custom, “scientific” power resistor.

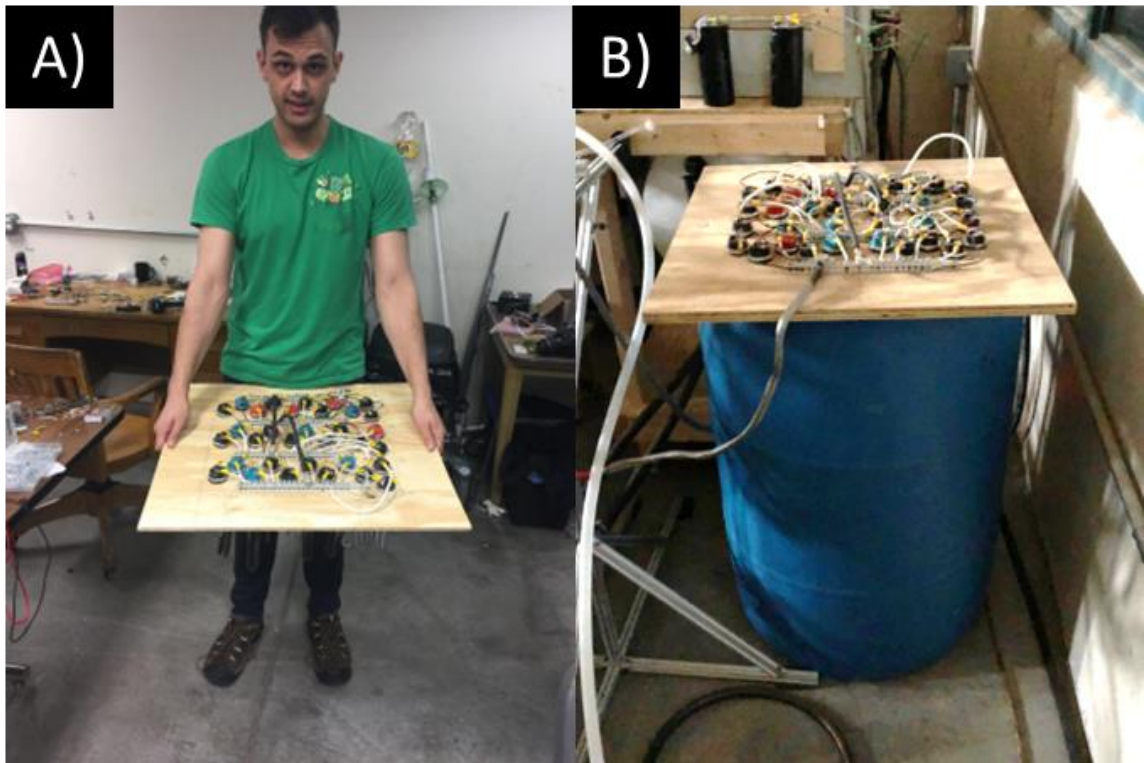


**Figure A.8.** Image of: (A) 33 parallel wired power resistors for APPT’s HCDC circuit, and (B) resistors placed on recirculated water cooling bath tank.

## A.5 LABJACK and LABVIEW DAQ Wiring

Wiring the specific LABJACK DAQ and Insight 4G PXIe 1073 devices proves to be difficult if a formal record is not kept of the specific locations (ports) which wires must “go to”. Thus the following image shown in Figure A.9 serves as a record of the wiring of each of these.

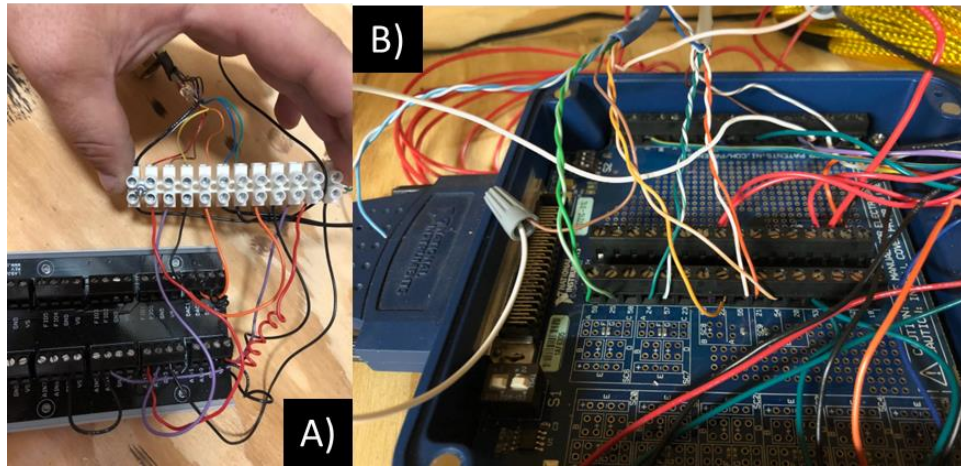


**Figure A.9.** A) LABJACK I/O wiring, B) LabVIEW I/O wiring.

## A.6 PIV Supplementary Data

The additional results of performing the PIV methods discussed in Section 4.3 is provided here since the data was acquired but does not influence discussion within the section. As seen in the histograms present in Figure A.10–Figure A.12, the majority of the particles possess a velocity magnitude equivalent to three meters per second or less with small or trace amounts of particles achieving speeds between 3–25 [m s<sup>-1</sup>].

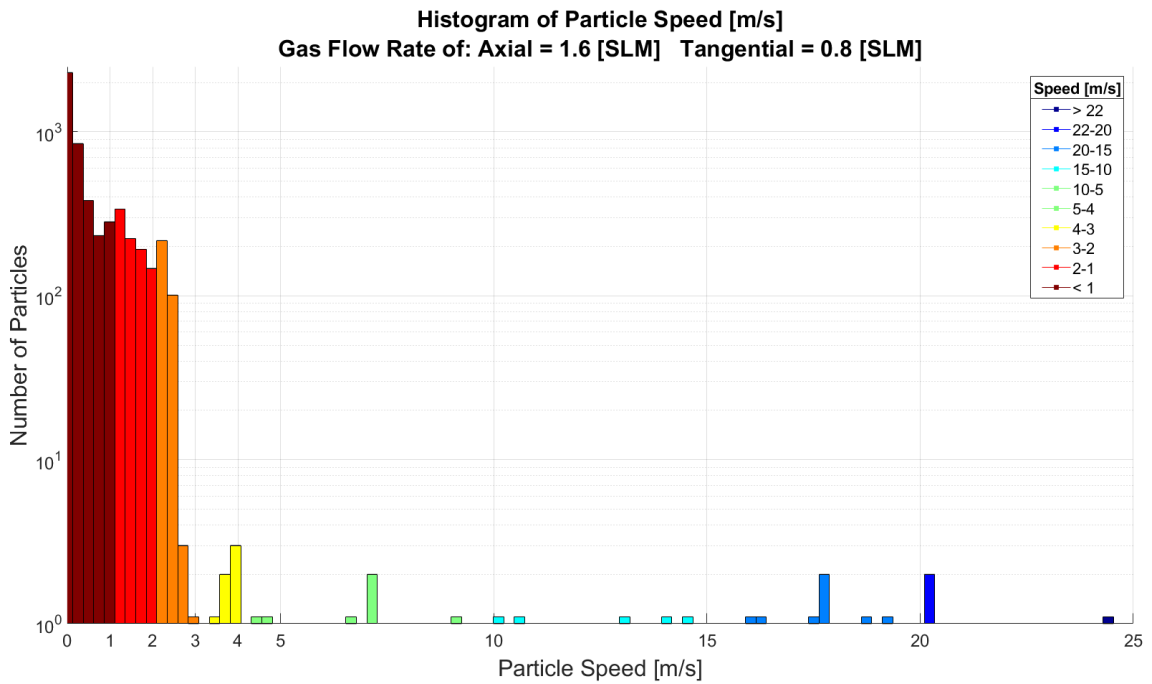


**Figure A.10.** ns-PIV Case 1: 1.6 SLM axial gas flow rate particle speed histogram.

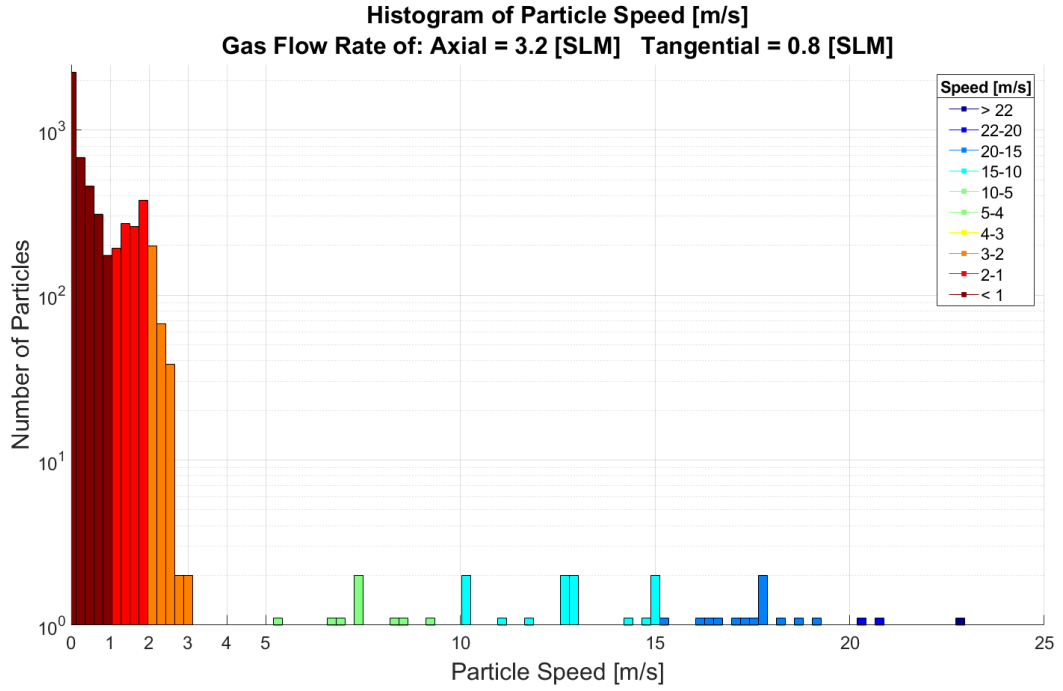


**Figure A.11.** ns-PIV Case 2: 3.2 SLM axial gas flow rate particle speed histogram.

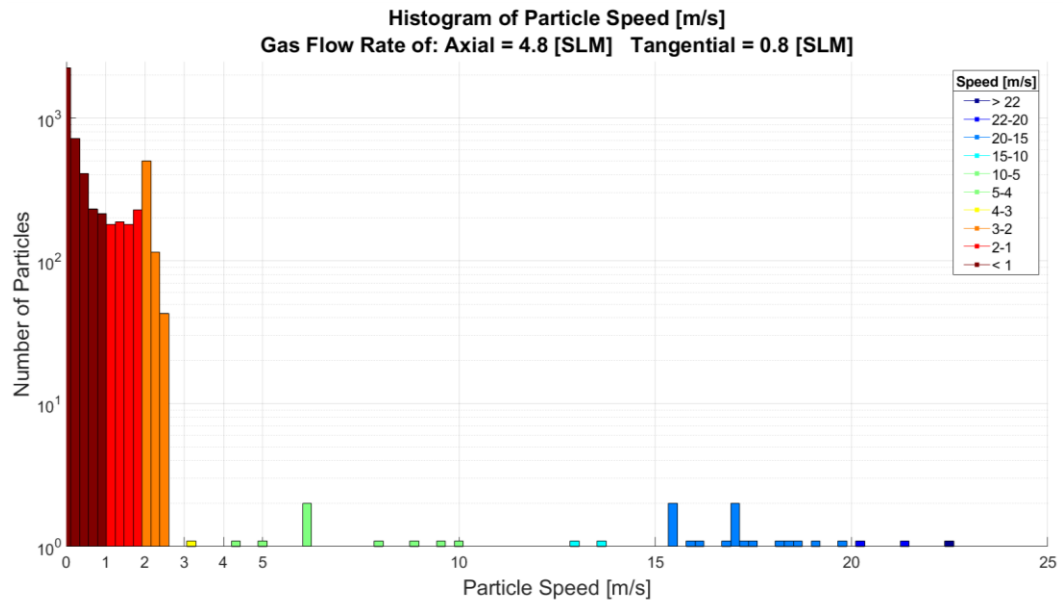


**Figure A.12.** ns-PIV Case 3: 4.8 SLM axial gas flow rate particle speed histogram.

To better analyze the data presented, the following three histograms, with a narrower particle speed range utilized, are presented that show the particle speed distribution from 0–3 [m s<sup>-1</sup>] for each of the three ns-PIV test cases evaluated.

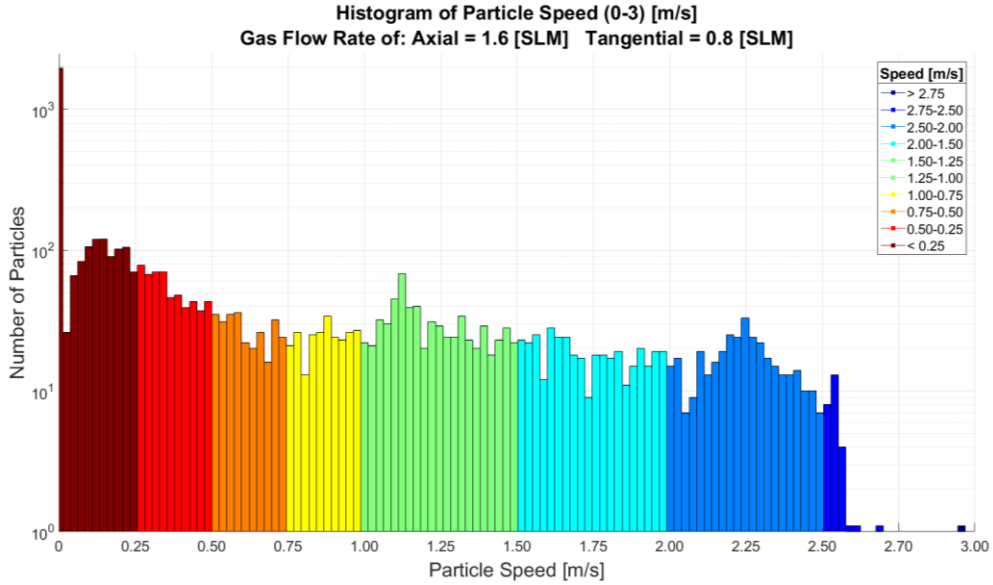


**Figure A.13.** ns-PIV Case 1: 1.6 SLM axial gas flow rate particle speed (0–3 m/s) histogram.

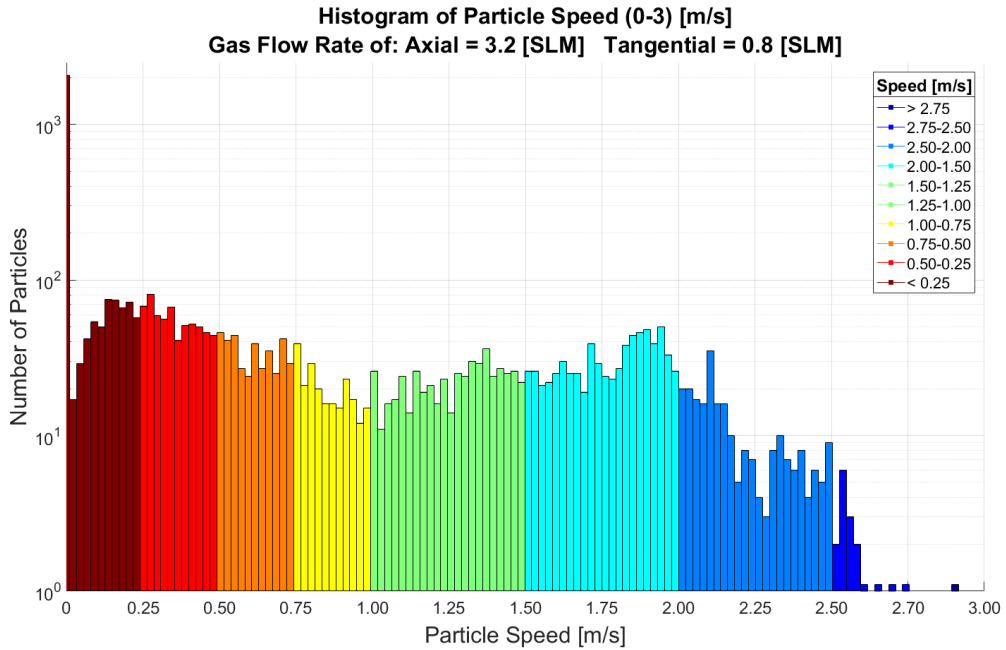


**Figure A.14.** ns-PIV Case 2: 3.2 SLM axial gas flow rate particle speed (0–3 m/s) histogram.

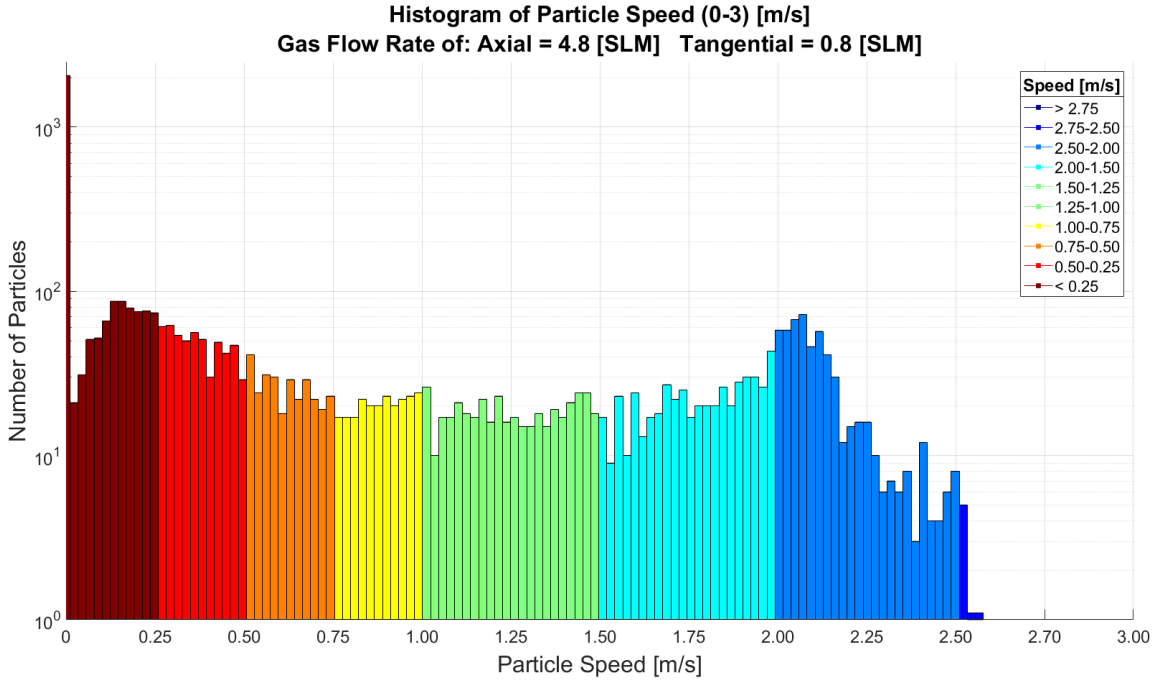


**Figure A.15.** ns-PIV Case 3: 4.8 SLM axial gas flow rate particle speed (0–3 m/s) histogram.

As seen in the histograms in Figure A.13–Figure A.15, as axial gas flow rate increases the number of particles that achieve a speed of  $\geq 2$  [m s<sup>-1</sup>] increases. In Case 1, the slope of the histogram peaks appears to decrease linearly whereas in Case 2 it appears to become more parabolic in nature and increase with Case 3. Analyzing the particle speeds generated by Insight 4G provides the ability to see how the three test cases compare from a statistical quantitative standpoint which is important in ensuring accuracy and consistency is met when processing any PIV data under similar cases or circumstances. The reason for visualizing the more prominent data within the second set of histograms compared to the entirety of the speeds as presented in the first set of histograms is qualitatively visualized when analysing the resulting PIV vector field seen in Figure A.16 for the second test case.

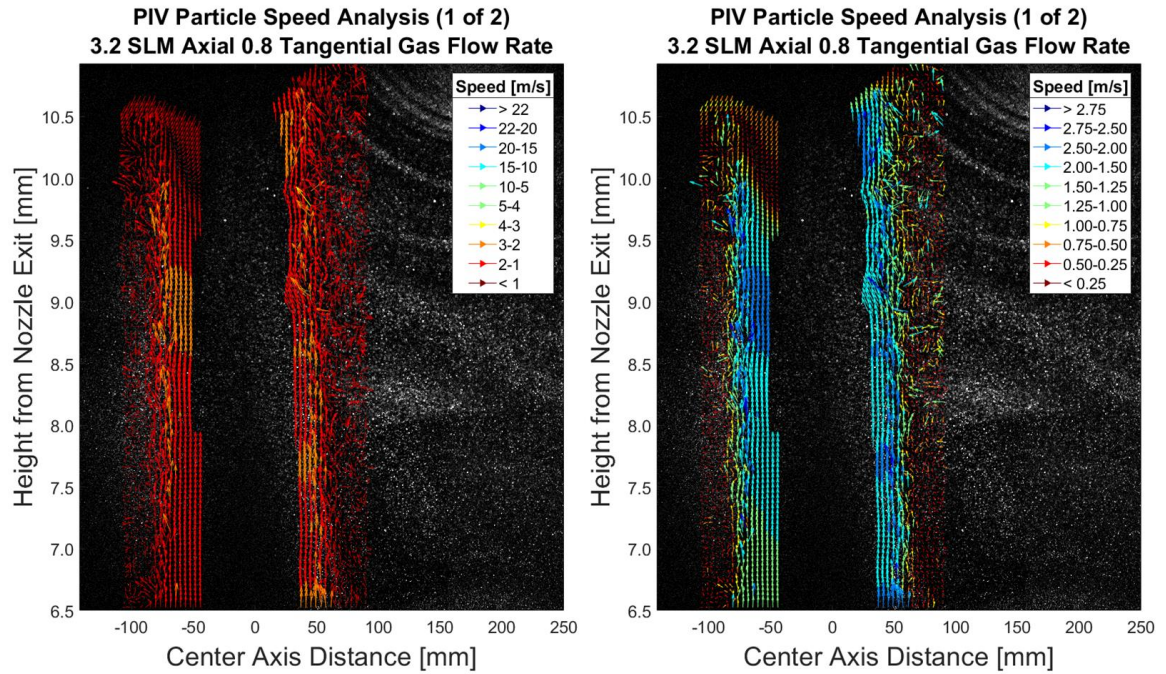


**Figure A.16.** PIV velocity vector field with particle speed from 0–25 m/s (left), 0–3 m/s (right).

In Figure A.16 (left) it is evident that not only are the majority of the particles traveling at similar speeds, but it is not easily discernible which ones are achieving speeds greater than 3 [ $\text{m s}^{-1}$ ]. In the right image, visualizing velocity vectors ranging from 0–3 [ $\text{m s}^{-1}$ ], it is evident that as the particles propagate closer to the plasma flow field, their velocity in the  $y$ -direction increases as expected. Utilizing the same colormap scheme to visualize all three cases of the resulting velocity vector fields obtained through Insight 4G, the following images shown in Figure A.17–Figure A.19 are produced for the three test cases using the author’s custom MATLAB scrip. Following these three images are the resulting velocity vector fields for test Case 1 and test case 3, shown in Figure A.20–Figure A.21, as generated by PIVlab.

PIV Particle Speed Analysis (1 of 2)  
1.6 SLM Axial 0.8 Tangential Gas Flow Rate

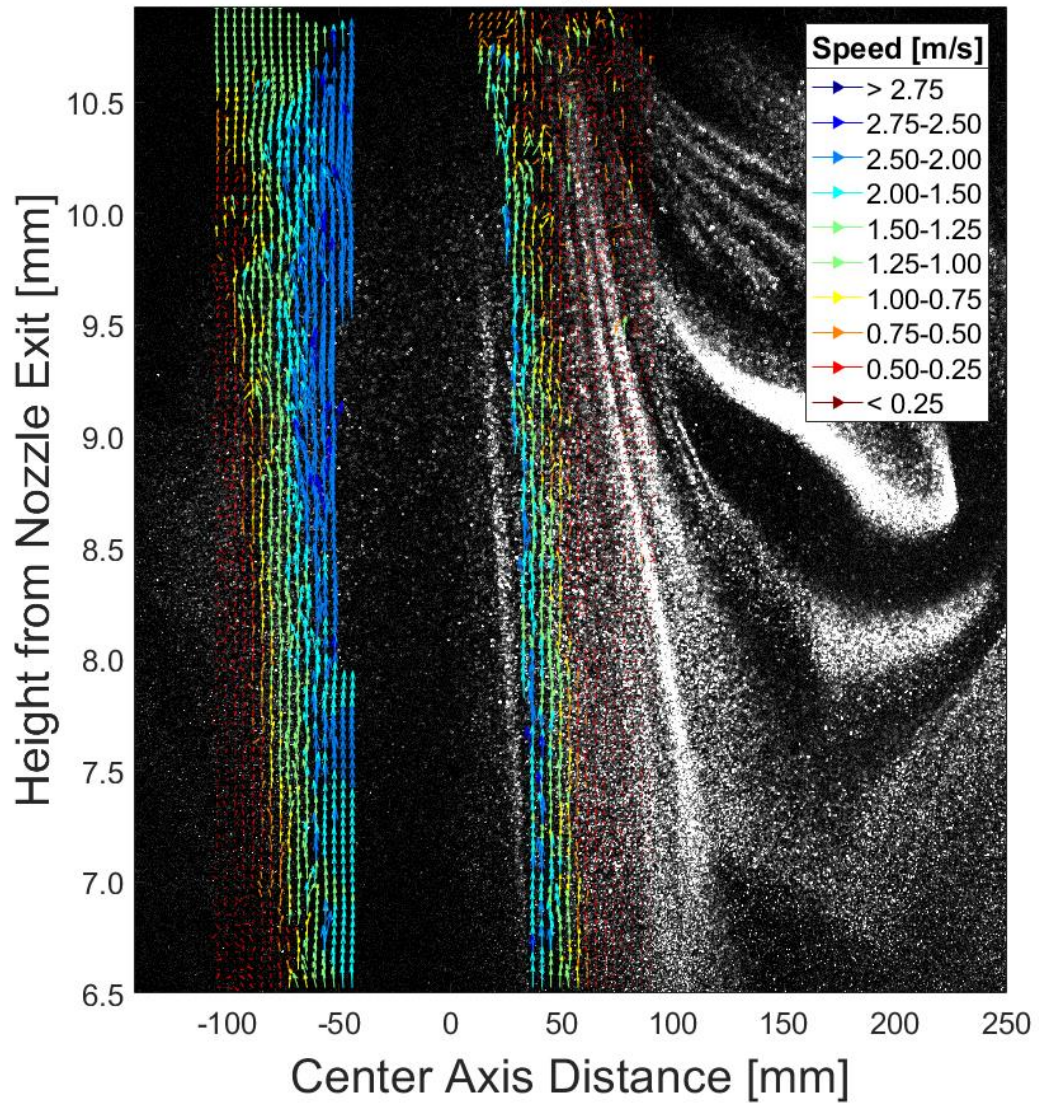


**Figure A.17.** ns-PIV Case 1: 1.6 SLM axial flow rate PIV velocity vector field with particle speed colormap.

### PIV Particle Speed Analysis (1 of 2) 3.2 SLM Axial 0.8 Tangential Gas Flow Rate

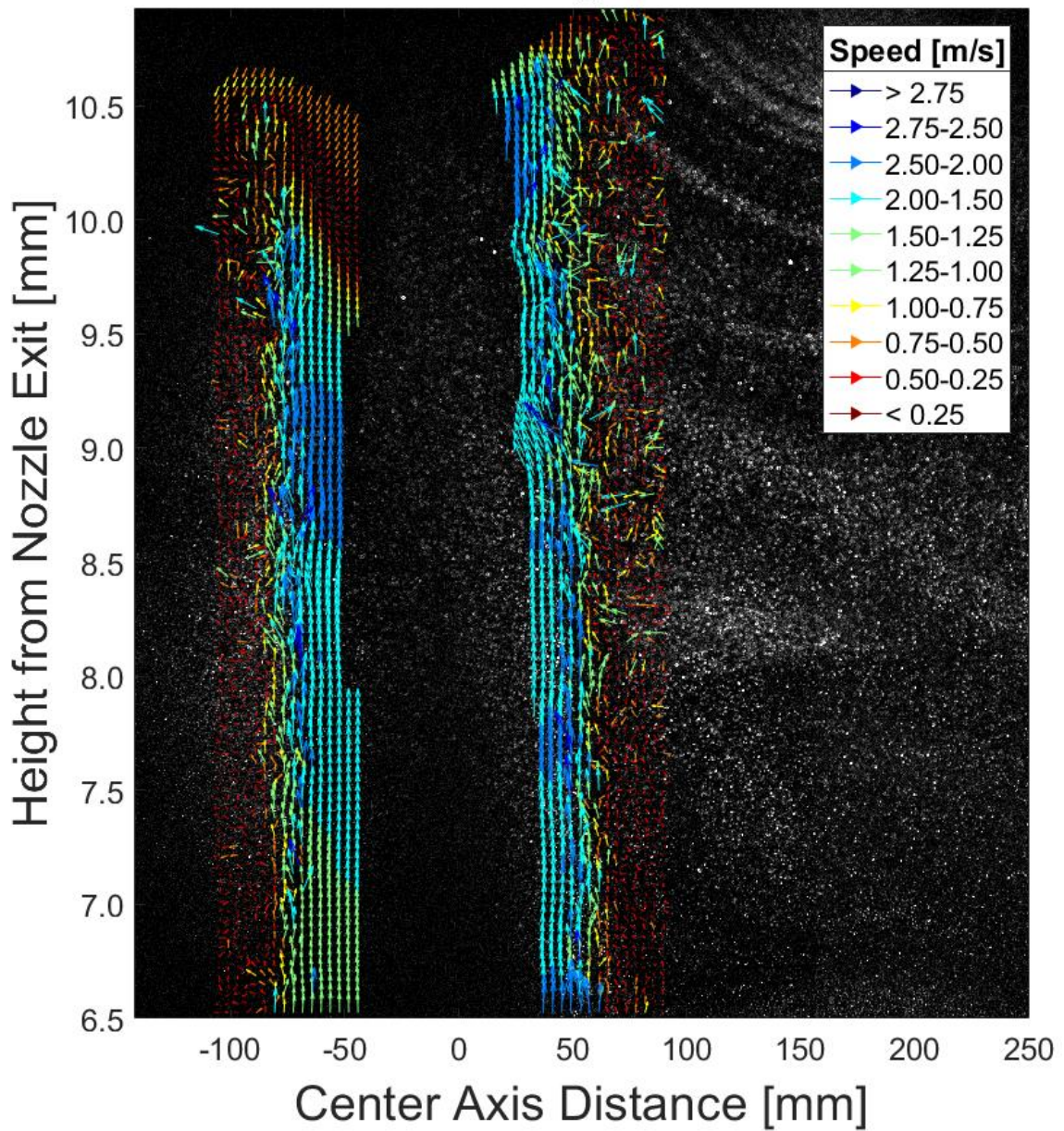


**Figure A.18.** ns-PIV Case 2: 3.2 SLM axial flow rate PIV velocity vector field with particle speed colormap.

**PIV Particle Speed Analysis (1 of 2)**  
**4.8 SLM Axial 0.8 Tangential Gas Flow Rate**

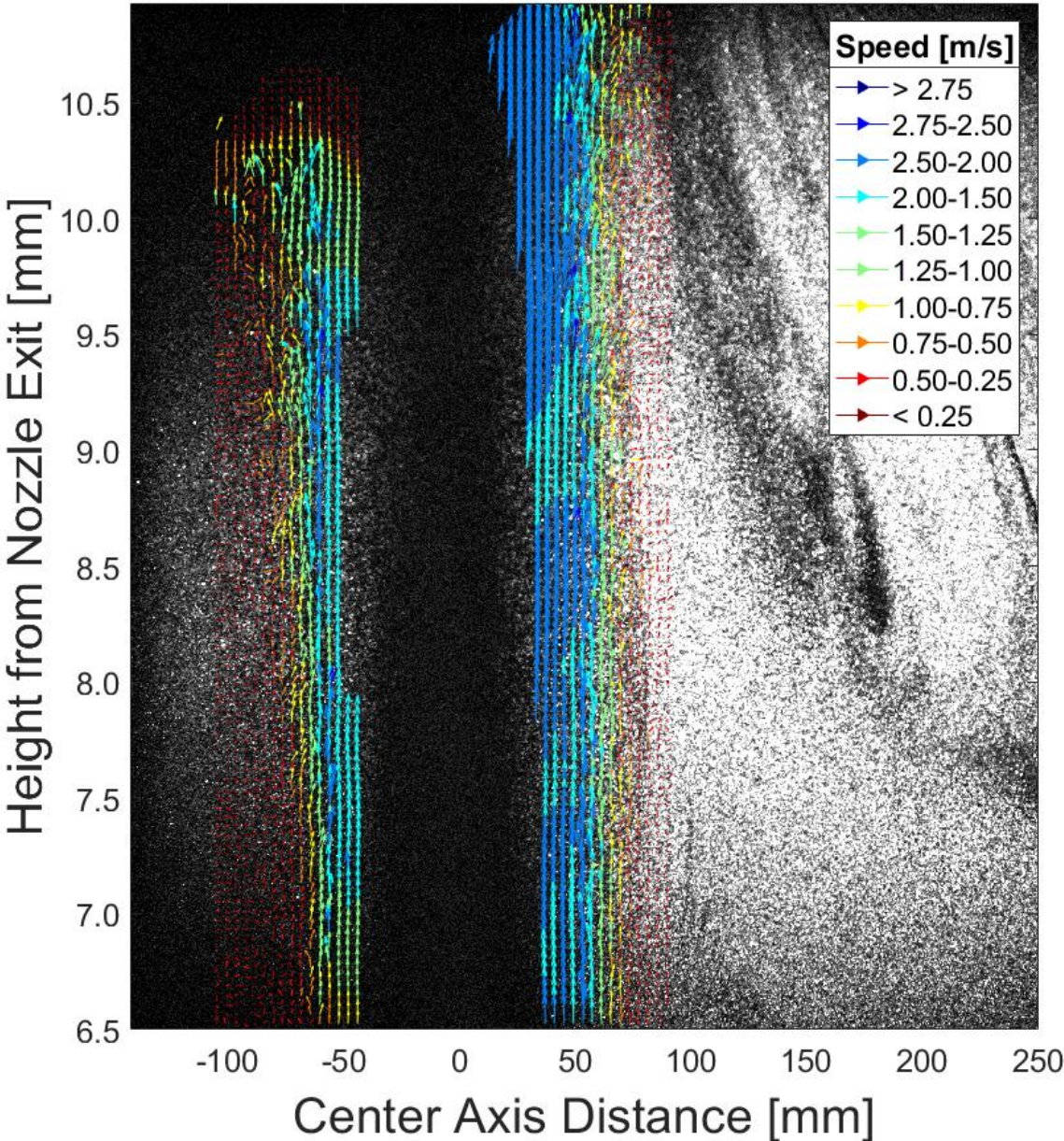


**Figure A.19.** ns-PIV Case 3: 4.8 SLM axial flow rate PIV velocity vector field with particle speed colormap.

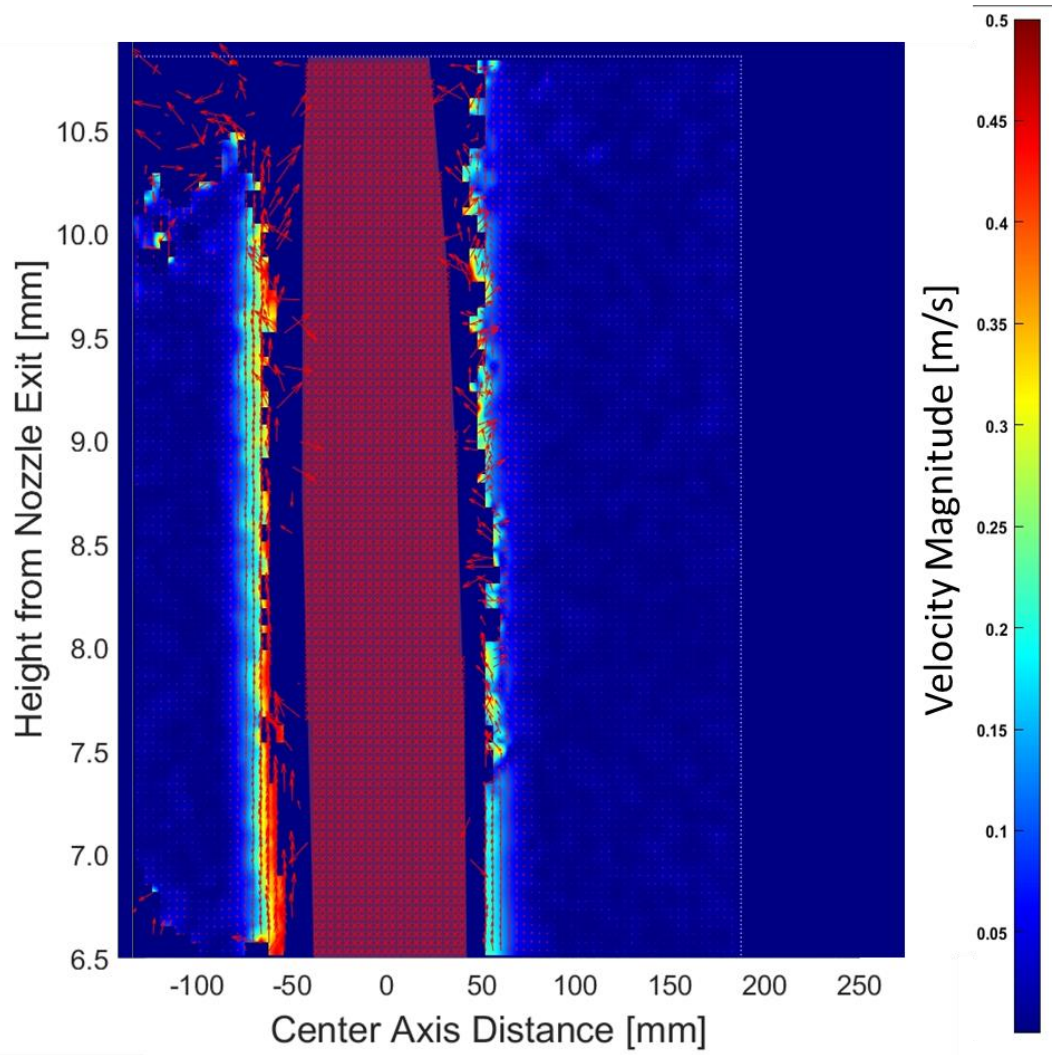


**Figure A.20.** ns-PIV Case 1: 1.6 SLM axial flow rate from PIVlab velocity vector field.

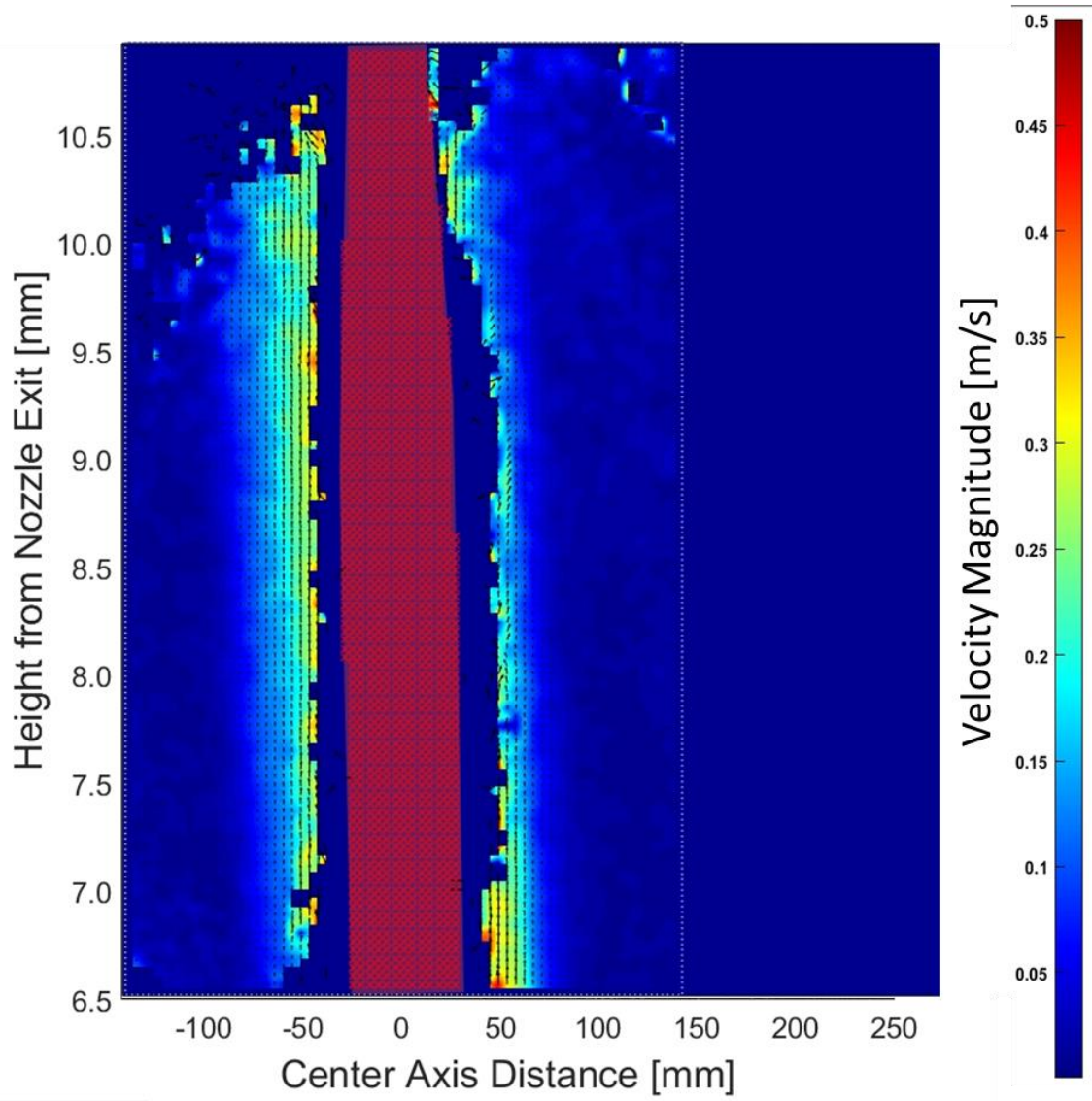


**Figure A.21.** ns-PIV Case 3: 4.8 SLM axial flow rate from PIVlab velocity vector field.

## APPENDIX B. PLASMA TORCH COMPONENTS REPAIR

### B.1 Machining the Anode and Cathode Sections

Machining the cathode and anode sections, specifically the copper press fit pieces is a must to ensure the APPT run stable and laminar. Seen in the left image (A) of Figure B.1 below is the inside of the APPT's copper anode, which has been degraded from arc spot attachment and localization and resulted in the "pitting" that evident. The right image (B) shows what the inside of the anode nozzle looks like when the anode is freshly machined. The difference between the two is clear and why constant care must be performed to ensure that the anode component is adequate to perform diagnostic methods and utilize the APPT itself. All the machining to construct the APPT, components, apparatuses, and custom diagnostic equipment, were completed by the author of this dissertation.

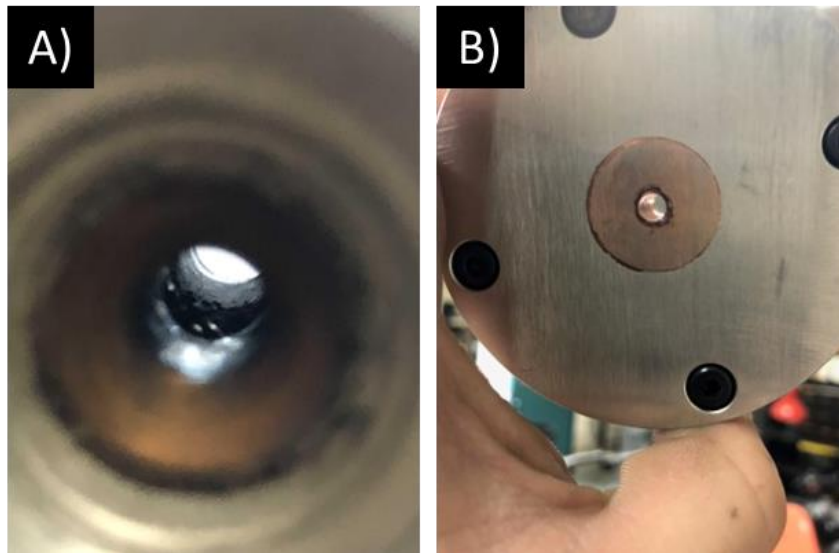


**Figure B.1.** The anode section of the APPT: A) as a used and degraded component and B) as a freshly machined component.

## B.2 Replacement of Tungsten Cathode Rod

Replacing the tungsten rod within cathode of the APPT requires that the APPT be taken apart and the cathode section be disassembled. Although this is not a difficult process, in the future, a new, incrementally increasing cathode tip height system will be used to continuously increase the height of the tungsten rod tip within the APPT, after a certain period of usage has passed. This will allow for more constant initial spark gap distance between the anode and cathode electrodes to be maintained and ensure a greater degree of reproducibility.



**Figure B.2.** Dissassembly of the cathode section from the APPT.

### **B.3 Transferred Arc Plasma Torch for Calibration Purposes**

As discussed in Section 3.3.4, the APPT was temporarily converted into a transferred-arc torch. This temporary conversion was accomplished by effectively flipping over the top half of the anode section, and machining a copper press-fit insert piece without a nozzle port. The manner in which this temporary conversion was performed was also done to ensure the same materials, and components themselves, were used in the non-transferred APPT as well as in the transferred-arc torch setup. By utilizing the same components and materials (post modification), this led to reducing any possibility of error or uncertainty when calibrating the 2DMIM system. The transferred-arc torch setup can be seen in Figure B.3 below.



**Figure B.3.** The transferred arc APPT used for calibrating the imaging system when performing the 2DMIM.

#### B.4 Initial Plasma Torch Operational Results

Since large amount of time went in to redesigning the APPT used in this dissertation's work; some of the preliminary design iterations of the torch led to producing different plasma jet lengths (heights), with the same V-I settings, HVAC starter circuit, and HCDC power supply. This is evident in Figure B.4 below where the overall jet height differs in comparison to the results provided in Section 4.1 where a taller, and more stable plasma flow field was able to be achieved once the APPT design was revised. Namely, the preliminary APPT design used a slightly shorter nozzle length which contributed to the height decrease shown in Figure B.4. This shorter nozzle (~15 mm) resulted in a more undeveloped flow which led to turbulence, as is evident in Figure B.4.

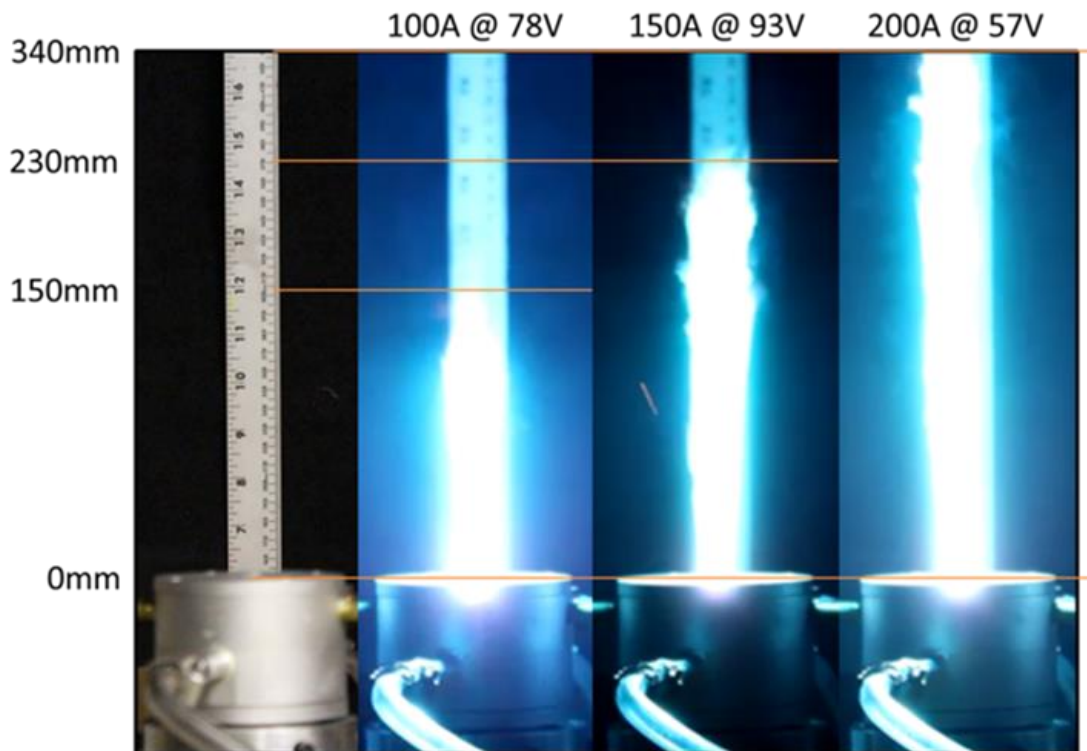


**Figure B.4.** Jet length vs. arc current of the preliminary APPT design that used shorter nozzle length section.

**APPENDIX C. CONSTRUCTION OF SUPPLEMENTARY  
MHD-RMI EXPERIMENTAL COMPONENTS**

**C.1 PIV Solid Particle Seeder and Mock Section Apparatus**

Acquiring the PIV data presented in Section 4.3 required the use of commercially available and custom manufactured components. TSI’s commercially available ns-PIV solid particle seeder is shown in image A) of Figure C.1. The custom manufactured and constructed Mock Test (MT) section is shown in image B) of Figure C.1. Also provided is image C) which is a visual “schematic” portraying where these components are located within the APPT diagnostic PIV apparatus system as a whole.

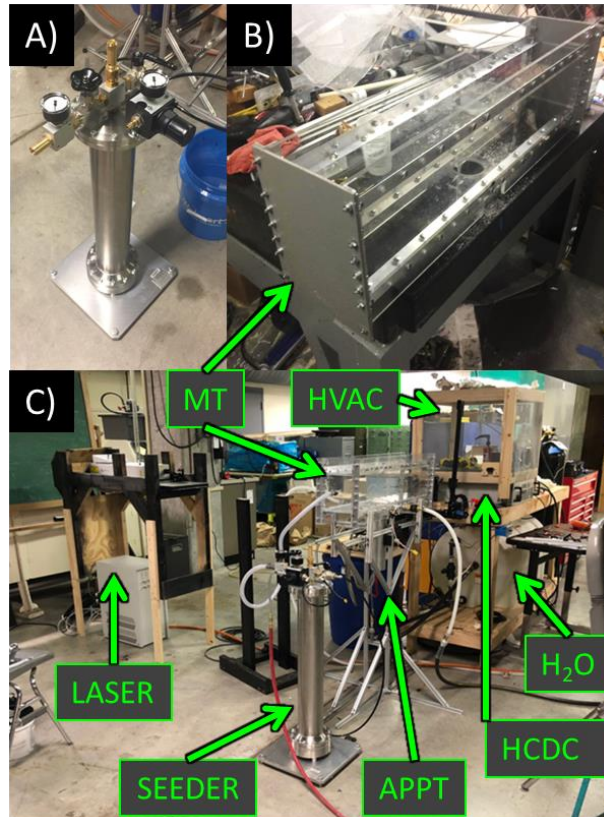


**Figure C.5.** The ns-PIV particle seeder (top left, A), the MT section (top right, B), and a visual schematic of the PIV system apparatus (bottom, C).

As the APPT was operated after the particle-laden flow field was generated during the PIV data acquisition process, some photos were acquired of the setup while operational. Shown in Figure C.2 is: the CCD camera, plasma, and MT in image A), a close-up of the MT in image B), and seen in image C) is the laser illuminated particle-laden flow field in the  $rz$ -plane before the APPT was turned on.

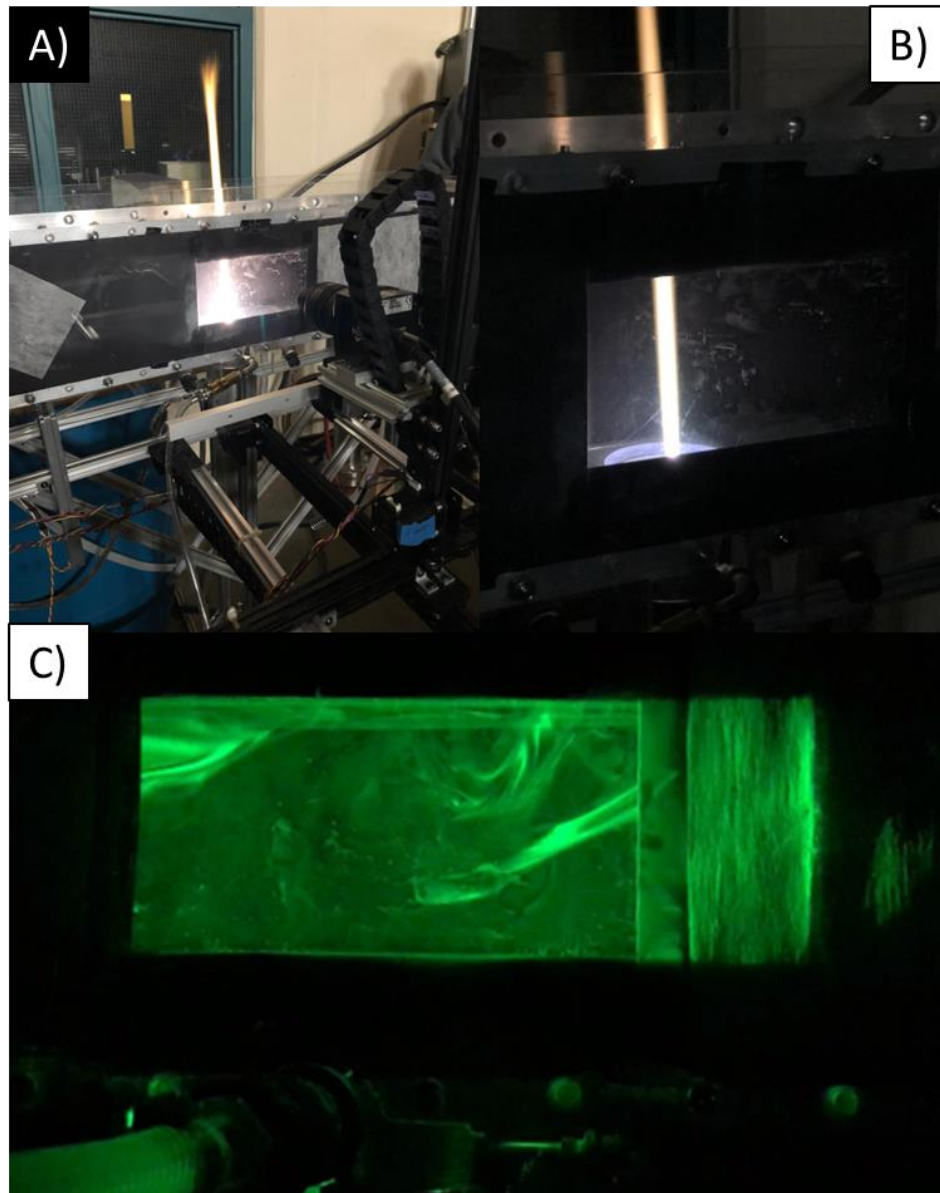


**Figure C.6.** Photographs of the PIV system while operational.

## C.2 Emission Spectrum of the APPT

As discussed in Section 3.3.4, the emissions of the APPT were acquired by a spectrometer as a verification and validation effort when performing the 2DMIM. The spectrometer utilizes a fiber optic cable aimed directly at the centerline of the plasma ejected from the APPT nozzle, (*s.c.*, slightly above the nozzle exit). Once properly aimed, the spectrometer acquires the emission data produced by the APPT as well as any additional emissions present which would otherwise interfere with, and potentially invalidate, the 2DMIM. The spectrometer setup used to do so is shown in Figure C.3.

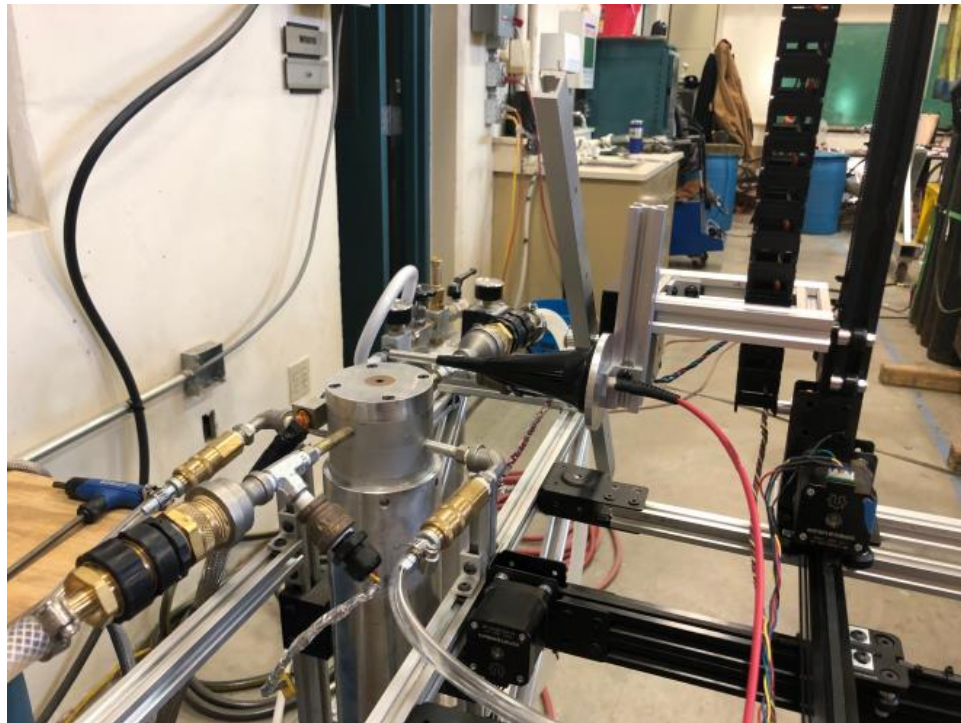


**Figure C.7.** Ocean Optics USB4000 VIS-NIR spectrometer setup to measure emissions present during 2DMIM diagnostic method.

As discussed in Section 3.3.4, validating the emissions present is only one of many validation steps that were taken to perform the 2DMIM. The next effort taken was to validate that the emission line desired to be isolated, was in fact isolated. This was

completed by use of a spectrophotometer to measure the transmittance of the optical bandpass filters used to isolate a specific range of wavelengths near the specified emission line. Specifically, the transmittance vs. wavelength of Andover  $532 \pm 10\text{nm}$  bandpass filter and Thor Labs  $532 \pm 1 \text{ nm}$  laser line filter is shown in Figure C.4 where the solid lines indicate manufacturers' data; data points with corresponding colors indicate measured data as acquired by a Shimadzu UV-2401 $\pm$ 0.3nm spectrophotometer.

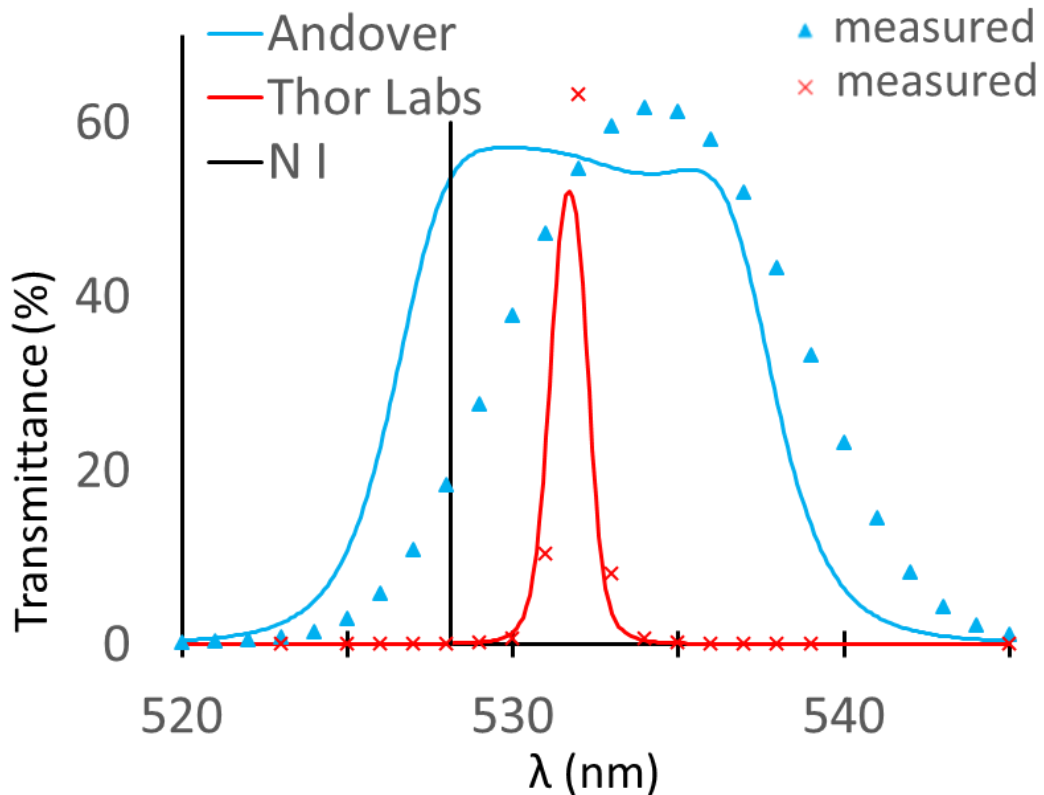


**Figure C.8.** The transmittance vs. wavelength of Andover  $532 \pm 10\text{nm}$  bandpass filter and Thor Labs  $532 \pm 1 \text{ nm}$  laser line filter as acquired by a Shimadzu UV-2401  $\pm 0.3\text{nm}$  spectrophotometer.

The result of acquiring emission spectrum data using the spectrometer setup presented in Figure C.3 and the transmittance data acquired by the spectrophotometer presented in Figure C.4 is combine and shown in Figure C.5. Figure C.5 first shows the torch emission spectrum acquired by an Ocean Optics USB4000 VIS-NIR spectrometer

at the central axis of the torch near the nozzle exit absent of any bandpass filter (purple line). Additionally, the spectrum transmitted by the Andover bandpass filter, used for the 2DMIM, and measured by the spectrometer is shown (blue line) compared to data points from the transmittance (from Figure C.4) measured by the spectrophotometer (red points). The product of the transmittance and torch spectrum (pink dashed line) represents the torch spectrum received at the CCD camera and used for the 2DMIM. The 528.12 N-I emission line is shown as a reference (green line). From this data it can be observed that ~82% of the total light acquired by the CCD camera equipped with the Andover filter, is from the 528.12 nm N-I line. The remainder, in this case, is due to emission continuum, which is expected to also scale with the strength of the adjacent 528.1nm line. No other line emissions are present in this range as must be satisfied when utilizing the 2DMIM method.

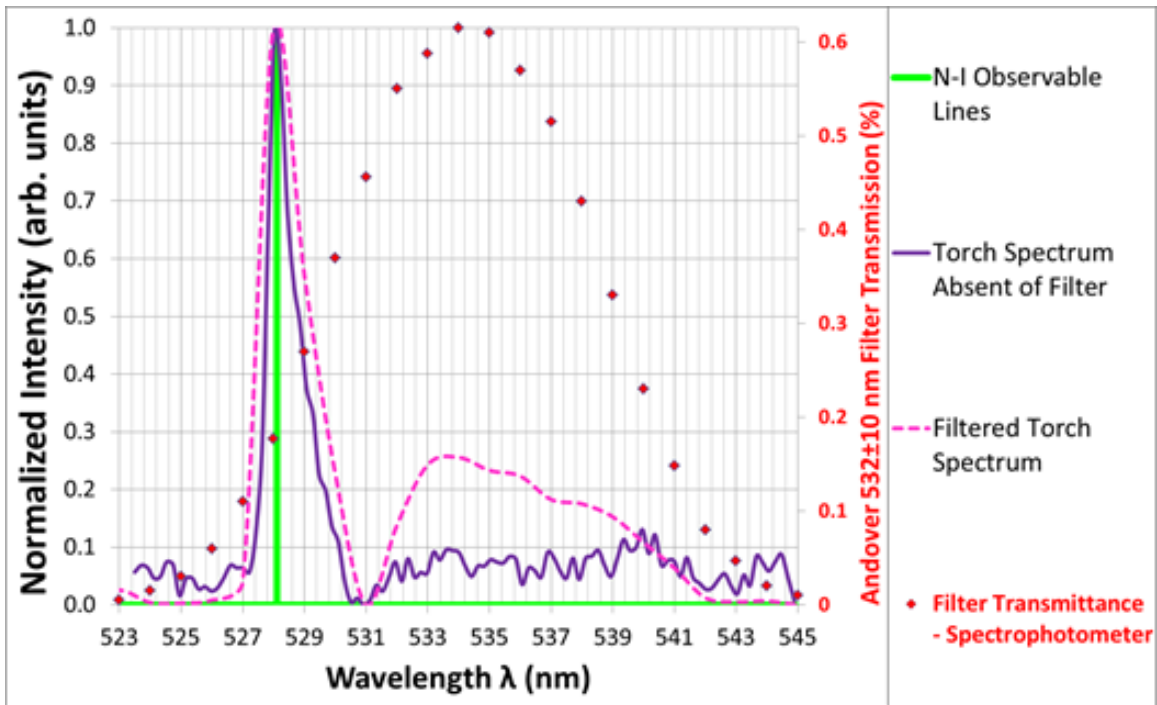


**Figure C.9.** Spectrometer emission measurement of the APPT with and without bandpass filter present accompanied by filter transmittance.

### C.3 The Externally Applied Magnetic Field Apparatus

The magnetic field apparatus used to perform the plasma flow field and magnetic field interaction diagnostics was designed and constructed by the author. The apparatus itself can be traversed in all three Cartesian coordinate directions as well as rotated to set the magnetic field's centerline angle offset from perpendicular, relative to the plasma flow field's centerline. The apparatus is driven (translated and rotated) by NEMA23 stepper motors able to micro-step the magnetic field into, and out of, the plasma flow field along 2020 extruded t-slot linear rail. This ensured that precise positioning of the magnetic field relative to the plasma flow field was achieved. Additionally, tilt angle was able to be specified to a fraction of a degree by the micro-stepped motors. This ensured reliability and repeatability of the magnetic field's position, in reference to the APPT nozzle origin. Custom g-code was developed to operate this system.



**Figure C.10.** Magnetic field apparatus' traversing, positioning, and tilting system.

## C.4 The Missouri Fluid Mixing and Shock Tube Laboratory

The FMSTL's shock tube was initially constructed by the author in the summer of 2015 and Figure C.7 presents the first time it was fully assembled and the lab space that it was done so in.

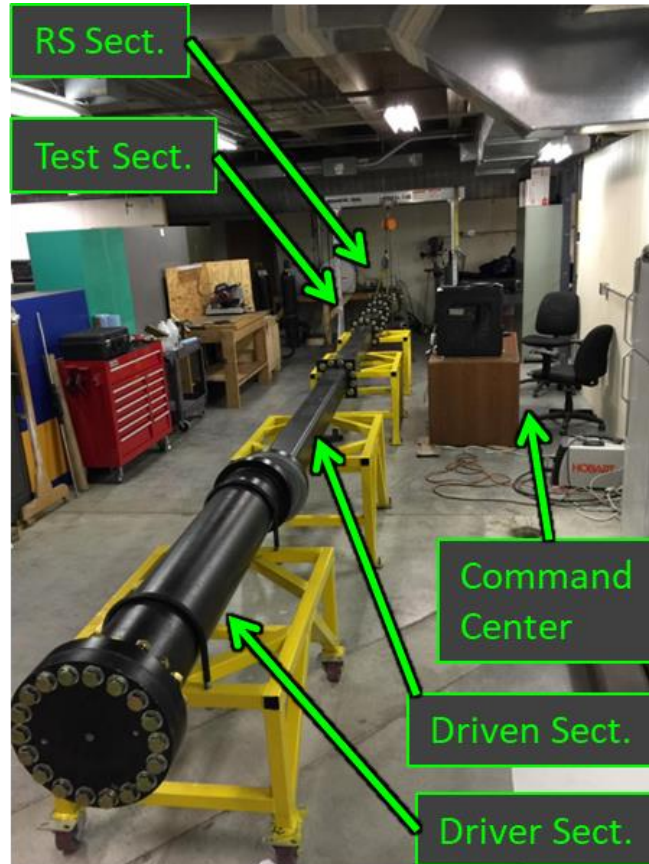


**Figure C.11.** The first complete assembly of the FMSTL's shock tube.

A few years after the shock tube was constructed, the success of the FMSTL lab's research on HIs and MHD grew. This success resulted in a major upgrade of lab space allocation for the FMSTL. Figure C.8 shows the new location of the FMSTL's shock tube and its respective major components, as well as the APPT research control center.

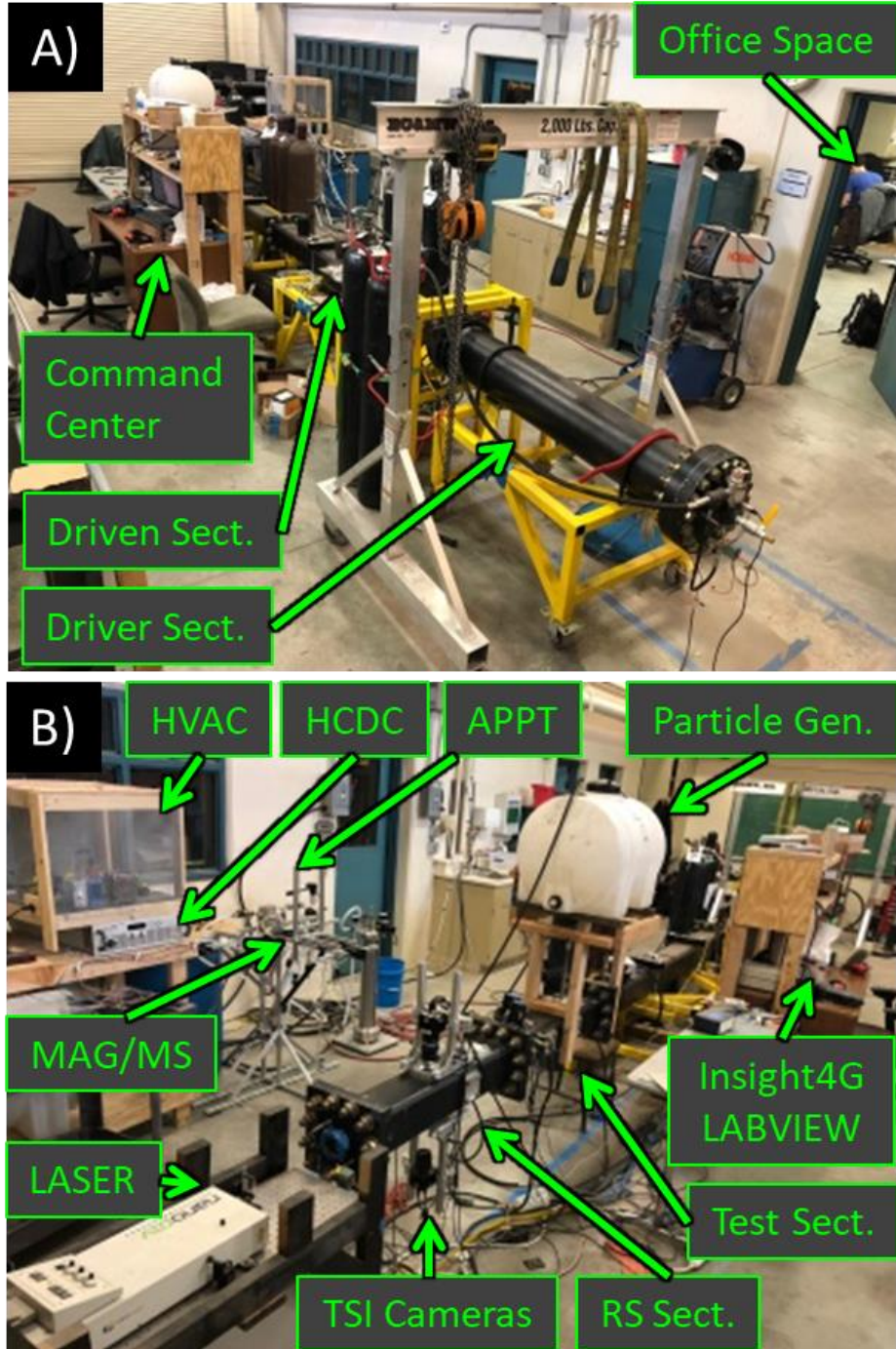


Figure C.12. The Fluid Mixing and Shock Tube Laboratory.

## VITA

From a young age Roy demonstrated an inquisitive interest in building things. One of the first Christmas presents he received from his grandparents around the age 4 or 5 was a set of Lincoln Logs for construction. Next came a set of Tinker Toys and Roy's indoctrination into project management. Before allowing construction to begin, Roy's mom (who is an excellent corporate Project Manager) made him review the plans for what he was building and then lay out all of the pieces required for that job and take a full inventory. Later Roy's parents fueled his interest with a set of K'NEX with which Roy constructed a 3 foot high Ferris wheel that was displayed in his room for years of his childhood. Next were the LEGO bricks with which Roy constructed countless "masterpieces" achieving the pinnacle of LEGO construction with a complete scale version of the 1,300 piece Star Wars 7191 Ultimate Collector Series X-Wing Fighter. Yes the Fighter was also displayed in his room for years. Just a few months before completing his dissertation, Roy reported to his parents that he reconstructed his LEGO "masterpiece" and placed it on display again.

At the age of 10 Roy advanced in scale with his constructions projects. He and his two best childhood friends constructed a Fort using scrap lumber they found from home construction in the neighborhood. Much to the chagrin of Roy's parents, the Fort somehow morphed into a room addition to their home physically attached to the back of their house. Summer had to end and about a month of school had to pass before Roy's father could get away with dismantling that "room addition".

At the age of 12 Roy's passion for building things was further fueled when he began to work for his Uncle Richard re-finishing and staining decks and fences. Not very glamorous but learning processes and procedures and the benefits of hard work were a priority.

Roy developed another passion at about the age of 13 while watching the movie "October Sky", about the early life of NASA engineer, Homer Hickam. Launching smaller-scale rockets and becoming a NASA Astronaut were now on his must do list. That summer Roy convinced his dad to invest in the purchase of a scale Rocket with fuel cartridges that had a capability of reaching about 1,000 feet. Roy spent a few weeks studying and calculating launch position and more importantly landing location just like Homer Hickam. Then the perfect weather day presented itself and Roy and his dad and a couple of friends packed up the rocket and supplies and headed for the baseball and soccer fields near their house for the anticipated lift off. The rocket launch was a huge success and, to the relief of his dad, recovery of the command module was secured without injury to any of the surrounding residences and without the uninvited appearance of the police or homes association patrol.

At the age of 15 Roy further advanced in his construction knowledge and experience when he and began working for his Uncle Richard building new homes. Roy learned how to operate all types of power tools from table saws to nail guns. He also gained invaluable experience reading blueprints and learning the many nuances of framing and finishing construction of a house. Exposure to a continuous concerto of colorful language was also an unexpected experience even if not a valuable one!

Roy's Uncle Richard also had the hobby most boys dream of, racing cars. A fortuitous bit of luck was that the Kansas City International Raceway drag strip was only a few miles from Roy's house. His Uncle Richard actually built his own pro stock race car and ran it at this drag strip on the weekends. Of course Roy was fully immersed in every part of the "racing team" from the car build to manning the pit crew on race nights. A new passion was born in Roy for building engines and racing cars.

Not surprisingly at age 16 Roy's passion for engines and race cars was front and center. When it was time to purchase his first car Roy worked out a deal with his parents getting them to agree to match the money Roy had saved from working for his Uncle Richard. Even less surprising was the car Roy wanted to purchase; a 1993 Mitsubishi 3000 GT-VR4 Twin Turbo, black with chrome wheels and well over 300 horsepower! Now, Roy's dad was and is all about safety and one of the most conservative people you will meet. His dad's plan for the car purchase was something more along the lines of a Ford Taurus. A mighty struggle ensued with Roy spending every waking moment for two weeks trying to convince his dad that somehow a 16 year old kid with a passion for fast cars would have the sense to not race that race car. As a sign of his developing strength of debate and persuasion, somehow Roy convinced his dad.

Over the course of the next few years Roy developed his knowledge and experience of engines and fast cars hanging out and working at the garage of "Mac", a shade-tree mechanic that made repairs exclusively on Mitsubishi cars. Under Mac's tutelage Roy completely tore down and rebuilt the engine and repaired or replaced many

other components of his VR4. To this day Roy still has that Mitsubishi VR4 having never wrecked it and never receiving a speeding ticket while driving it.

Roy got his introduction to traditional engineering his last two years of high school at Summit Technology Academy, a college preparatory program. This Academy combined the traditional technology school hands on approach with the academic instruction of engineering principles. Under the direction of Dr. Paul M. Rutherford (“Doc”), decedent of Ernest Rutherford, and recipient of the 2003 Presidential Award for Excellence in Science Teaching, Roy was fully immersed in the engineering world in an outstanding way. Roy credits Doc for having built the foundations within him to achieve academic and engineering achievements such as his Ph.D. dissertation. It was during this experience at the Academy that Roy decided he wanted to be an engineer and with Doc’s guidance, decided the University of Missouri was the school for him.

Roy has participated in many activities while attending University where he studied mechanical and aerospace engineering. For all three degrees, Roy remained at the University of Missouri – Columbia where he continued to develop his knowledge, skills, and passion for engineering close to his home town. He has always believed that while there are many pleasing qualities to attending other more prestigious collegiate institutions, anyone can excel and thrive at public universities like Mizzou with enough hard work and dedication.

During undergrad, Roy participated in many extra-curricular activities and design teams. One of the main reasons he opted to attend Mizzou was the ASME Formula SAE racecar that is designed and built by engineering students. Since the start of his first

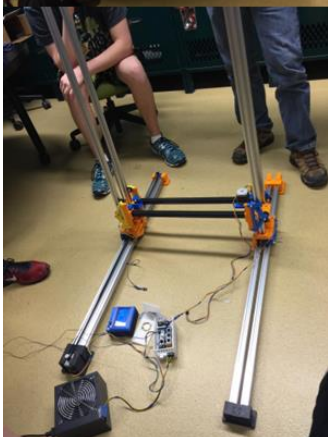
semester Roy spent countless hours learning how to apply his prior knowledge and skills of building race cars towards helping the SAE race team become more successful. Utilizing the same technology applied to his 1993 Mitsubishi 3000gt VR4 and knowledge obtained through MAE coursework, Roy helped the team design and fabricate the first undertray implemented on the SAE racecar and worked on developing a twin turbo system as well. Additionally, the success of the aerodynamic enhancements lead to Roy participating on the design and implementation of the first rear spoiler and front wing utilized on the racecar as well. He met many good friends through this process and got to drive the Formula SAE car around everywhere from the Mizzou Arena parking lot to the competition he attended with the team in Akron Ohio.





Roy's love for aerodynamics was increased inside the classroom where he learned a great deal from Dr. Craig A. Kluever and his friend and mentor Steve P. Nagel, former NASA astronaut and Space Shuttle commander. The knowledge Roy acquired inside the classroom allowed him to work with his friend Zach Blickmann to co-founding the AIAA rocket team. Under the advisement of Steve Nagel, Roy helped lead the team's rocket design and construction to compete in the 7<sup>th</sup> Experimental Sounding Rocket Association's (ESRA) International Rocket Engineering Competition in Green River Utah where the team placed 4<sup>th</sup> overall amongst other universities from around the world. Throughout his undergraduate career, Roy continued to work on AIAA design teams such as the Uninhabited Aerial Vehicle (UAV) team, Satellites Around Mars (SAM), and Students for the Exploration and Development of Space (SEDS) program.

Before starting on his Ph.D. research, Roy also participated in and led many efforts to increase Mizzou's 3D printing capabilities. Roy helped co-found the Print Anything at Mizzou initiative which enables any and all faculty, staff, and students to receive 3D printed parts and objects.



Determined to improve the 3D printing club, Roy assisted in printing prosthetics for military veterans & children locally and abroad. Additionally Roy

participated in the club's "Make Mizzou" project where scaled 3D printed models of the buildings and layouts of the University of Missouri – Columbia campus were made as an effort to assist the visually impaired and handicap as part of the Chancellor's ADA increased awareness initiative. Roy also personally saw to it that Mizzou was one of the few universities across the nation that had a large-scale 3D printer (LS3DP), designed and fabricated by students, with a one cubic meter build volume, which could rival commercial 3D printers at a fraction of the cost. Though his efforts, Roy was able to advise senior capstone design groups to develop sub-components of the LS3DP such as the autonomous heated build plate.

During Roy's Master of Science in Mechanical Engineering degree, he worked under the advisement of Dr. Craig Kluever and Steve Nagel. Roy continued his work on rockets and space technology to complete his thesis on The Conceptual Design of a Satellite Communication Network for supporting the Exploration, Colonization, and Early Development of Mars. Singlehandedly, Roy was able to figure out the means by which humans on earth could commutate with anything, from rovers to astronauts, continuously, on mars. Nearing the completion of his thesis work, CEO of Space-X, Elon Musk announced his plans to funnel millions of dollars into a project that would ultimately achieve the same results.

While performing his graduate studies, Roy was also a Teaching Assistant for multiple engineering classes. Roy was the "TA" of lab sections for MAE 3200 – Engineering Materials for two years during his master's degree, taught by Dr. Robert A. Winholtz. During his Ph.D. program he was the TA for ENGR 1110 – Solid Modeling for Engineering Design, and MAE 1100 – Introduction to Computer Aided Design to which he was awarded the Spring 2019 TA Choice Award for best teaching assistant of the year at Mizzou, by the Missouri Student Association.

Roy's greatest academic achievement is attributed to his work presented in this dissertation. The summer before he began to research plasmas, magnetohydrodynamics, and the Richtmyer–Meshkov instability, Roy proved his worth to his dissertation advisor, Dr. Jacob A. McFarland, by building the Missouri Fluid Mixing Shock Tube Laboratory shock tube with the help of his lab mates. Roy cultivated some of his most significant friendships with the lab personnel who worked in the FMSTL including that with Wolfgang Black, who designed the shock tube. Here Roy learned how to be not only

